
THE MOLECULAR INTERSTELLAR MEDIUM
OF NEARBY STAR-FORMING GALAXIES

D I S S E R T A T I O N

BY

ANDREAS SCHRUBA

HEIDELBERG 2011

INAUGURAL - DISSERTATION
zur
Erlangung der Doktorwürde
der
Naturwissenschaftlich–Mathematischen
Gesamtfakultät
der Ruprecht–Karls–Universität
Heidelberg

Vorgelegt von
Dipl.-Phys. Andreas Schruba
aus Wiesbaden

Tag der mündlichen Prüfung: 24. November 2011

THE MOLECULAR INTERSTELLAR MEDIUM
OF NEARBY STAR-FORMING GALAXIES

Gutacher: Prof. Dr. Hans-Walter Rix
Prof. Dr. Ralf Klessen

Abstract

This thesis presents a comprehensive analysis of the relationship between the star formation rate (SFR) and atomic (H I) and molecular (H₂) gas surface densities — known as the ‘Star Formation Law’. The investigation capitalizes on the HERACLES survey which mapped molecular gas emission with unprecedented resolution and sensitivity across the star-forming disks of 48 nearby spiral and dwarf galaxies. This data is complemented by recent very high quality radio, infrared, and ultraviolet data to form an unmatched multi-wavelength database. We develop a novel method to average spectral data to derive the most sensitive measurements of CO emission to date. In spiral galaxies, we trace > 90% of CO which is located in an exponential disk similar to that of young and old stars. In dwarf galaxies, we derive the first sensitive constraints on the total CO luminosity. With these data we explore the limits of the SF Law in three different regimes: (1) In spiral galaxies, SFR is linearly related with H₂, even in regions that are dominated by the atomic gas phase. The highly non-linear relation between SFR and total gas (H I+H₂) is thus sensitively controlled by the H I–H₂ phase transition. (2) The ratio SFR/CO is approximately constant for massive galaxies but increases strongly in low-mass, low-metallicity dwarf galaxies which suggests a significant (factor 10 – 100) change in the CO-to-H₂ conversion factor. (3) The SF Law shows considerable scatter on small (~ 100 pc) scales, corresponding to the spatial scale of individual star-forming regions and is indicative of their evolution.

Zusammenfassung

Diese Promotionsarbeit stellt eine umfassende Untersuchung des Zusammenhangs von Sternentstehungsrate (SFR) und atomarer (H I) and molekularer (H_2) Gasoberflächendichte dar — bekannt als ‘Sternentstehungsgesetz’. Diese Studie basiert auf der HERACLES Beobachtungskampagne, welche molekulares Gas mit einmaliger Auflösung und Sensitivität über die stellare Scheibe von 48 benachbarten Spiral- und Zweiggalaxien bestimmt hat. Diese Daten werden vervollständigt durch neue Radio, Infrarot, und Ultraviolett Daten von sehr hoher Qualität und bilden eine einzigartige Datenbank des elektromagnetischen Spektrums. Wir haben eine neuartige Methode entwickelt, um Spektren zu mitteln, und bestimmen damit die zur Zeit sensitivsten Messungen von CO Helligkeit. In Spiralgalaxien können wir $> 90\%$ der CO Strahlung ausfindig machen, welche in einer exponentiellen Scheibe verteilt ist, vergleichbar mit der von jungen und alten Sternen. In Zwerggalaxien bestimmen wir die allerersten sensitiven Messungen der gesamten CO Helligkeit. Mit diesen Daten untersuchen wir die Grenzen des Sternentstehungsgesetzes in drei verschiedenen Regionen: (1) In Spiralgalaxien finden wir SFR und H_2 linear verbunden, sogar in Regionen die hauptsächlich aus atomarem Gas bestehen. Die stark nicht-lineare Beziehung zwischen SFR und totaler Gasmasse ($\text{H I} + \text{H}_2$) ist somit empfindlich durch den $\text{H I} - \text{H}_2$ Phasenübergang kontrolliert. (2) Das Verhältnis SFR/CO ist ungefähr konstant in massereichen Galaxien, aber steigt erheblich an in massearmen, metallarmen Zwerggalaxien, was ein stark (Faktor 10 – 100) vergrössertes $\text{CO} - \text{H}_2$ Verhältnis nahelegt. (3) Das Sternentstehungsgesetz beinhaltet grosse Streuung auf kleinen (~ 100 pc) Skalen, entsprechend der Ausdehnung einzelner Sternentstehungsgebiete und mit deren Entwicklung zusammenhängt.

Acknowledgements

There are a number of people that deserve special thanks as they have contributed to the successful completion of this thesis and made the three years that I was allowed to spend at MPIA a wonderful time. In the first place, I would like to thank Fabian Walter for offering me to join his group and get to know the fascinating world of observational astronomy (after spending my previous years with just paper and pencil). His knowledge, advice, support, and guidance have been an invaluable stimulation for my scientific development and I have to say that his dedication clearly exceeded my highest expectations. Second, but to no minor extend, I want to express my thanks to Adam Leroy who has been an inexhaustible source of scientific and technical wisdom and is a wonderful person to work with. This thesis work has gained so much by your participation that I have a hard time to thank you for all of your input. You offered me a most enjoyable visit to Charlottesville with sport and cultural trips which were much fun. I want to thank Frank Bigiel for his advise and collaboration during my thesis work, and a special thank for that one day when we played Innebandy and you mentioned that there may be an opportunity opening up... I want to thank Karin Sandstrom for her participation and valuable comments on my work. Furthermore, I want to express my thanks to Elias Brinks and Erwin de Blok for interesting discussions and helpful comments on my work. I am also thankful for the advice I got from Erik Rosolowsky and Antonio Usero. At the institute, I furthermore enjoyed discussions with Benjamin Moster over galaxy dynamics, with Leonard Burtscher over active galaxies or just astronomy (most enjoyable during a table tennis match), and with Jochen Tackenberg over Galactic star formation. Overall I want to express my gratitude to all members of the MPIA and its directors Hans-Walter Rix and Thomas Henning which form a scientifically and humanely responsible and friendly community. Finally, I would like to thank my thesis committee members Hans-Walter Rix and Ralf Klessen for taking their time to evaluate my thesis work on short notice.

On a private side, I am grateful to the friends I got to know during my years in Heidelberg. This time was wonderful and it would never have been so much fun without you. I was privileged to find friendships that will continue for a lifetime. I am deeply grateful to Jenny Mellberg for her understanding when astronomy once more kept me occupied at times when it actually shouldn't. Finally, I own my parent more than I can say. Your love made me what I am. Your encouragement and assistance made me a privileged person and enabled me to make my dreams come true. Thanks so much!

Contents

Abstract	vii
Acknowledgements	xi
1 Star Formation and the Interstellar Medium	1
1.1 The Observed Star Formation Law	1
1.1.1 Introduction	1
1.1.2 Global SF Law	2
1.1.3 Coarsely Resolved SF Law	4
1.1.4 SF Law at sub-kpc Scale	5
1.1.5 SF Law in Outer Disks	7
1.1.6 SF Law in H I-dominated Galaxies	9
1.1.7 SF Law in Early-Type Galaxies	10
1.1.8 SF Law in Disk vs. Starburst Galaxies	10
1.1.9 Composite SF Law	12
1.2 Physical Processes Underlying the Star Formation Law	14
1.2.1 SF Laws based on Large-Scale Dynamical Processes	15
1.2.2 SF Laws including Stellar Surface Density	17
1.2.3 SF Laws assuming Fixed GMC Efficiencies	17
1.2.4 Thresholds for Star Formation	18
2 Data and Conversion Factors	23
2.1 Multi-Wavelength Surveys	23
2.1.1 SINGS & LVL	23
2.1.2 GALEX NGS	24
2.1.3 THINGS	24
2.1.4 HERACLES	25
2.2 Estimate of SFRs and Gas Masses	29
2.2.1 Star Formation Rates	29
2.2.2 Gas Masses	32
3 The Scale Dependence of the Molecular Gas Depletion Time in M33	35
3.1 Context	35
3.2 Abstract	35
3.3 Introduction	36
3.4 Data	37
3.4.1 Molecular Gas from CO Data	37

3.4.2	Recent Star Formation from H α and IR Data	39
3.5	Methodology	40
3.5.1	Identifying CO and H α Peaks	40
3.5.2	Measuring Depletion Times	41
3.5.3	Uncertainties	41
3.6	Results	42
3.7	Discussion	44
3.7.1	Comparison to a Simple Model	46
3.7.2	τ_{dep} vs. Scale at Different Radii	47
3.8	Conclusions	47
3.9	Appendix	48
4	SF Law in HI-Dominated Regime	51
4.1	Context	51
4.2	Abstract	51
4.3	Introduction	52
4.4	Sample & Data	53
4.5	Methodology	57
4.5.1	Stacking of CO Spectra	58
4.5.2	Fitting the CO Line	59
4.5.3	Stacking as a Function of Radius	61
4.6	Results	62
4.6.1	CO and Star Formation	62
4.6.2	Distribution of Molecular Gas	77
4.7	Summary	84
5	Low CO Luminosities in Dwarf Galaxies	87
5.1	Context	87
5.2	Abstract	87
5.3	Introduction	88
5.4	Data	89
5.4.1	CO Data	92
5.4.2	HI Data	93
5.4.3	Star Formation Tracers	93
5.4.4	Metallicities	93
5.4.5	Sampling	93
5.4.6	Literature Sample	94
5.5	CO Emission in HERACLES Dwarf Galaxies	94
5.5.1	Individual Lines of Sight	94
5.5.2	Improve Sensitivity by Stacking	97
5.6	Scaling Relations for CO Luminosity	101
5.6.1	Comparison to Magellanic Clouds	101
5.6.2	Scaling Relations of L_{CO} with M_{B} and Metallicity	103
5.6.3	CO and Tracers of Star Formation	103

5.7	Implications for CO-to-H ₂ Conversion Factor	107
5.7.1	Different Methods to Estimate the CO-to-H ₂ Conversion Factor . .	108
5.7.2	New & Literature Measurements	109
5.7.3	Comparison	112
5.8	Summary	114
6	Concluding Remarks & Outlook	117
6.1	Concluding Remarks	117
6.2	Outlook	119
	Atlas of Galaxies and Radial Profiles	125
	Bibliography	171
	Curriculum Vitae	187
	List of Publications	191

List of Figures

1.1	Global SF Law	3
1.2	SF law at sub-kpc Scales	6
1.3	SF law in Outer Disks	8
1.4	SF Law in Disk vs. Starburst Galaxies	11
1.5	Composite SF Law	13
2.1	IRAM 30m	25
2.2	HERACLES Observing Strategy	26
2.3	HERACLES Baseline Fitting	28
3.1	CO and H α in M33	38
3.2	SF Relation on kpc-scale	42
3.3	Scale Dependence of Depletion Times	43
3.4	SF Relation for Median Measurements	43
3.5	Simulated Scale Dependence of Depletion Times	49
4.1	Different between H I and CO mean velocities	58
4.2	Stacked Spectra with and without velocity alignment	59
4.3	Example of Stacked Spectra	60
4.4	IR-CO Intensity Relations	63
4.5	SFR Tracer-CO Intensity Relations	64
4.6	Normalized SFR Tracer-CO Intensity Relations	67
4.7	SFR(FUV+IR)-H $_2$ Relation	68
4.8	SFR(H α +IR)-H $_2$ Relation	69
4.9	Metallicity Dependence of Depletion Times	71
4.10	SF Relation for different Gas Components	72
4.11	CO Radial Profiles	78
4.12	H $_2$ -H I Ratio	80
4.13	Radial Dependence of the H $_2$ -H I Ratio	82
4.14	SFR/total Gas - H $_2$ /H I Relation	83
5.1	Coverage of HERACLES dwarf maps	90
5.2	CO Intensity Maps	96
5.3	Stacked CO Spectra	98
5.4	Scaling Relations for L_{CO}	104
5.5	Metallicity Dependence of L_{CO}/L_B	105
5.6	SF Relation for Dwarfs	106
5.7	Metallicity Dependence of α_{CO}	110

List of Figures

5.8 Trends for Metallicity Dependence of α_{CO} 113

6.1 M31 CARMA Map 120

6.2 ALMA map of the Antennae galaxy 121

A.1 Atlas of Galaxy Poster Stamps 126

List of Tables

3.1	τ_{dep} as Function of Peak and Scale	41
4.1	Properties of Galaxy Sample	55
4.2	Relation of IR Emission and SFR Tracers to CO	65
4.3	Relation of SFR to Different Gas Phases	73
5.1	Properties of Galaxy Sample	92
5.2	Properties of Literature Galaxy Sample	95
5.3	CO Luminosities of Molecular Clouds	97
5.4	Stacking of Whole Galaxy	99
5.5	Stacking of $24\mu\text{m}$ -bright Regions ^a	100
5.6	Previous CO Observations of our Galaxy Sample	102
5.7	Metallicity Dependence of α_{CO} assuming constant SFE ^a	111

1 Star Formation and the Interstellar Medium

The night sky, populated with millions of light sources, has inspired humans to think about the Universe, its constituents, and their origin and fate ever since. The visible light originates from stars and they are found in complex distributions forming galaxies of most spectacular shapes. Since a considerable amount of the (baryonic) mass of a galaxy is in stars, their formation and evolution plays a key role in the evolution of galaxies. This makes empirical prescriptions of the star formation rate in galaxies an essential measurement in our attempt to understand galaxy evolution.

First attempts to constrain such empirical laws now date back more than half a century but have remained subject of intensive study. Throughout the decades observational studies have been stimulated by technical innovations which opened our view to larger and larger parts of the electromagnetic spectrum and to an increasing number of observable galaxies of all types in the local and distant Universe. These observations form the fundamental input to distinguish the relative importance of the large number of physical process at work in star formation. In the following, I will give an overview of the current observational picture of the star formation law and various physical processes that lie at the heart of proposed models.

1.1 The Observed Star Formation Law

1.1.1 Introduction

Dating back to the seminal work by Schmidt (1959, 1963), the relationship between star formation rate (SFR) and interstellar medium (ISM) gas mass has been parametrized by power laws, either relating volume densities, which are the relevant physical quantities,

$$\rho_{\text{SFR}} = \epsilon \rho_{\text{Gas}}^n, \quad (1.1)$$

or surface densities, quantities that are directly measurable in external galaxies,

$$\Sigma_{\text{SFR}} = A \Sigma_{\text{Gas}}^N. \quad (1.2)$$

The power law indices n or N govern at which gas densities stars form, the normalizations ϵ or A set the efficiency of the conversion. In the remaining text, I do not always refer to the two relations separately but use the common term — “star formation relation” (or

“SF law”) — for both relations and use only one set of parameters, ϵ and n . In most cases, at least in all observational studies, the latter relation is meant.

A caveat of the whole field is that the two relations are fundamentally different. The relation between volume densities extends from the low density diffuse ISM to individual high density cores of giant molecular clouds (GMCs) where stars actually form. The relation between surface densities operates on significantly larger scales, namely the average over a wide range of local conditions extending up to the whole galaxy. Because the processes that govern the evolution of the ISM and star formation are highly non-linear, it can neither be expected that the two relations are equal nor that one relation can be inferred from the other. The dilemma is that observations probe generally surface densities while the physical processes and theoretical models involve volume densities. The two regimes can however be linked by simulations. In these the relevant physical processes can be implemented for local volume densities (though often not resolved to the fundamental scales of GMCs and star), and they also provide us with an “external” view which can then be tested against observations.

Schmidt estimated the slope of the SF law from the scale heights of atomic (H I) gas and Cepheid variable stars near the Sun and found $n \approx 2 - 3$. From a self-consistent model for the time-evolution of stellar and gas mass, he inferred from the number of known white dwarfs $n \approx 2$, and from the present day helium abundance $n > 1$. He concluded that for $n = 2$, giant ellipticals, because of their high densities, should have low gas mass, high helium abundance, and red color — the opposite of galaxies with low density like the Magellanic Clouds which should be gas rich, have low helium abundance, and bluish color. Schmidt closed with the words “It is hoped to study the evolution of galaxies more in detail in the future”, a hope that has been inspiring astronomers ever since.

1.1.2 The Global Star Formation Law

Following Schmidt, many such studies have been performed to constrain the SF law in our Galaxy and Local Group (LG) galaxies: e.g., SMC by Sanduleak (1969), M31 by Hartwick (1971), M33 by Madore et al. (1974), and seven LG galaxies by Hamajima & Tosa (1975). In a seminal work, Kennicutt (1989) performed the first comprehensive study for a large set of nearby galaxies, a study which was expanded in Kennicutt (1998b) to include 61 “normal” spiral galaxies and 36 (nuclear) starbursts. Kennicutt found a strong correlation between the disk-averaged surface densities of star formation rate, Σ_{SFR} , and total gas, $\Sigma_{\text{gas}} = \Sigma_{\text{HI}} + \Sigma_{\text{H}_2}$, with slope $n \approx 1.4$ (see Figure 1.1) — a relation that holds over more than 5 orders of magnitude. The non-linear nature of the relation meant that the star formation efficiency, $\text{SFE} \equiv \Sigma_{\text{SFR}}/\Sigma_{\text{gas}}$, or its inverse, the (total) gas depletion time, $\tau_{\text{dep}} \equiv \Sigma_{\text{gas}}/\Sigma_{\text{SFR}}$, is not constant but SFR is enhanced in regions of high gas density. Kennicutt’s measured slope is close to $n = 1.5$, a value that naturally arises if large-scale gravitational disk instabilities define the timescale of star formation. However, a similar super-linear scaling can arise if dynamical timescales are considered. In Section 1.2 the reader will find an overview of physical processes proposed to govern the SF law and resulting parametrizations.

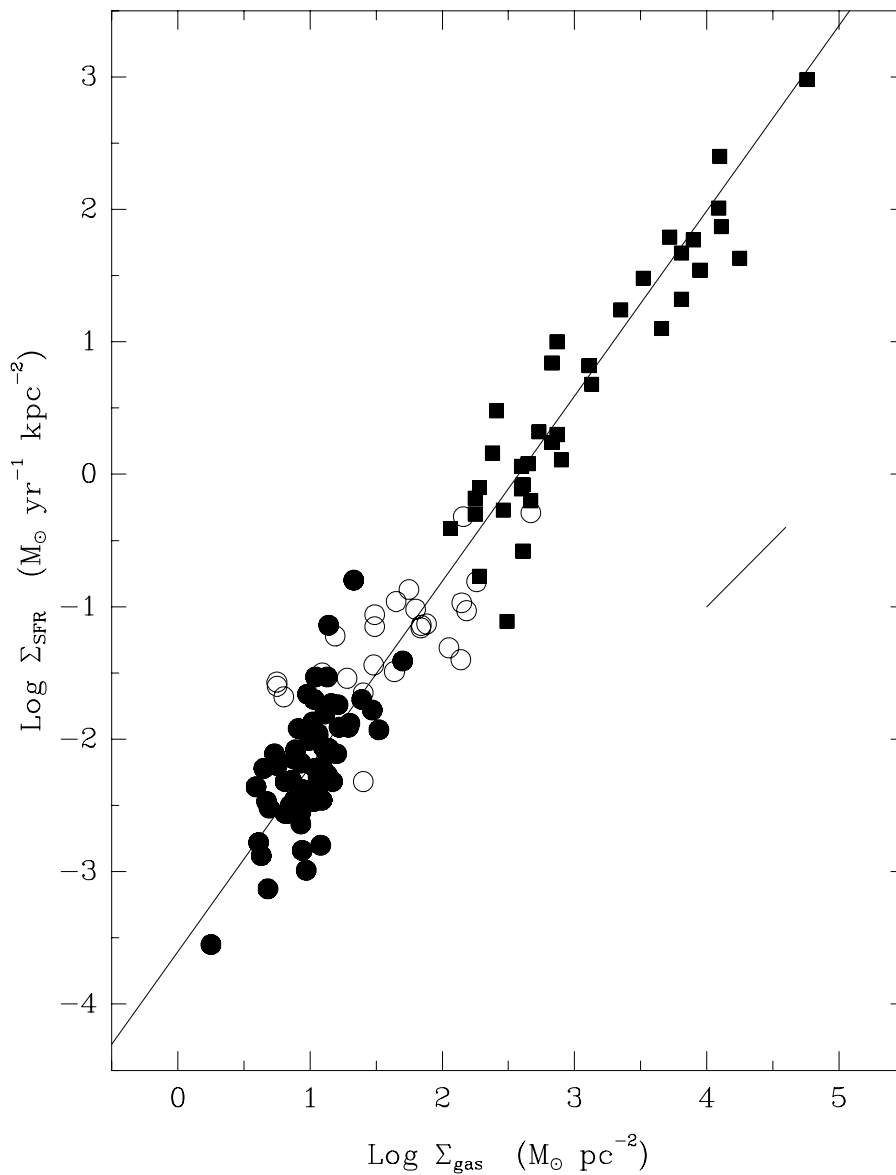


Figure 1.1 Global star formation law for disk-averaged Σ_{SFR} and $\Sigma_{\text{gas}} = \Sigma_{\text{HI}} + \Sigma_{\text{H}_2}$ for normal spiral galaxies (filled circles) and starburst galaxies (squares). Open circles show SFRs and gas surface densities for the centers of normal disk galaxies. The line shows a least-squares fit with index $n = 1.4$. [Figure taken from Kennicutt 1998b]

1.1.3 The Coarsely Resolved Star Formation Law

While disk-averaged studies have the potential to reveal differences in the global ratio of gas mass and SFR as function of galaxy type, they have limited ability to constrain the underlying physical processes. Studies following Kennicutt’s work aimed at resolving the SF law inside of galaxies. Rownd & Young (1999) and Murgia et al. (2002) targeted ~ 300 galaxies in which they studied ~ 1000 regions of $\sim 45''$ in size (limited by the resolution of their single dish CO data). They found strong correlations between CO surface brightness and tracers of SFR ($H\alpha$ or radio continuum emission) inside individual galaxies. For the complete sample they determined a median molecular depletion time of $\tau_{\text{dep}} \approx 2 - 3$ Gyr and a slope of $n \approx 1.2 - 1.4$. They found little (less than 25%) variation in the mean SFE within spirals of different Hubble type with the exception of Sd-Sm/Irr galaxies and mergers which both showed enhanced SFR for their CO luminosity.

The majority of studies analyzing the SF law inside of galaxies used azimuthally averaged radial profiles. The first large sample of radial profiles for 32 galaxies was compiled by Kennicutt (1989, 1998b) and Martin & Kennicutt (2001). They found a strongly non-uniform relation between Σ_{SFR} as traced by $H\alpha$ and Σ_{gas} . While the relation had a uniform slope of $n \approx 1.4$ at high gas densities, $\Sigma_{\text{gas}} \gtrsim 30 M_{\odot} \text{pc}^{-2}$, the $H\alpha$ profiles showed an abrupt cutoff at a threshold density, $\Sigma_{\text{thresh}} \sim 3 - 30 M_{\odot} \text{pc}^{-2}$, which however varied by galaxies by up to one order of magnitude. By considering the critical gas density, Σ_{crit} , at which a rotating gas disk becomes unstable for large-scale gravitational collapse (Toomre, 1964; Quirk, 1972), they found that the ratio $\alpha_{\text{Q}} \equiv \Sigma_{\text{thresh}}/\Sigma_{\text{crit}}$ was much more uniform, $\alpha_{\text{Q}} = 0.69 \pm 0.2$. The scatter in α_{Q} was further decreased when the data were not azimuthally averaged but considered inside wedges of an azimuthal ring. In regions where $\Sigma_{\text{gas}} \gtrsim \alpha_{\text{Q}}\Sigma_{\text{crit}}$, the disk will be unstable and thus is expected to form stars, in regions where $\Sigma_{\text{gas}} \lesssim \alpha_{\text{Q}}\Sigma_{\text{crit}}$, star formation is expected to be strongly suppressed. Although the correspondence was compelling, Martin & Kennicutt (2001) noticed a failure for two low-mass spirals, NGC 2403 and M 33, which have Σ_{gas} significantly below $\alpha_{\text{Q}}\Sigma_{\text{crit}}$ throughout the disk though they are actively forming stars. Hunter et al. (1998) and later Wyder et al. (2009) showed that this a general feature of late-type low-surface brightness galaxies which strongly suggested that large-scale gravitational instabilities are not the (only) triggering mechanism of star formation.

Other studies analyzing radial profiles have been those by Wong & Blitz (2002) that determined for 7 CO-bright spirals a strong correlation between Σ_{SFR} from $H\alpha$ and Σ_{H_2} with $n \approx 1.4$; those by Boissier et al. (2003, 2007) that studied 43 spiral galaxies and determined a slope $n \approx 2$ between Σ_{SFR} from FUV and Σ_{gas} ; and those by Schuster et al. (2007) that studied M 51 and found only a strong correlation between Σ_{SFR} from RC and Σ_{gas} with $n = 1.4 \pm 0.6$, and only a weak sub-linear correlation between Σ_{SFR} and Σ_{H_2} . These studies also tested the validity of the large-scale gravitational instability criterion to regulate star formation. For that they included the gravitational potential from stars into the calculation of Σ_{crit} , however, the resulting α_{Q} values showed large scatter providing no evidence for such a theory.

In summary, different studies derived power law slopes in the range of $n \approx 1 - 2$ leaving it unclear if a universal relation exists and which gas component — H I, H₂, or total gas — should correlate best with SFR.

1.1.4 The Star Formation Law at sub-kiloparsec Scales

One likely reason why different studies returned different scaling relations lies in the inhomogeneous set of SFR tracers — FUV, $H\alpha$, IR, RC — and adopted methodologies to correct them for dust attenuation and emission not related to recent star formation. Because these corrections can be significant (larger than a factor of 2), it is easy to believe that they can obscure an existing underlying relationship. This situation has improved significantly in the last years. With the launch of the *GALEX* Satellite and the *Spitzer* Space Telescope, it became feasible to obtain maps of UV and IR emission for a large set of nearby and distant galaxies. The SINGS (*Spitzer* Infrared Nearby Galaxy Survey; Kennicutt et al., 2003a) and the LVL (Local Volume Legacy; Dale et al., 2009) survey have obtained IR maps of several hundred nearby galaxies. The *GALEX* NGS (Nearby Galaxy Survey; Gil de Paz et al., 2007) obtained UV maps of ~ 1000 nearby galaxies. These datasets, in conjunction of ground-based $H\alpha$ maps, have proven as robust tracers of unobscured and embedded star formation (Calzetti et al., 2005, 2007; Leroy et al., 2008; Kennicutt et al., 2009).

At the same time coordinated surveys tracing the atomic and molecular ISM have been executed. The VLA large program THINGS (The H I Nearby Galaxy Survey; Walter et al., 2008) obtained 21cm data for 34 nearby galaxies, and the large IRAM program HERACLES (Heterodyne Receiver Array CO Line Extragalactic Survey; Leroy et al., 2009, and in prep.) obtained CO observations for 48 nearby galaxies. The combination of these surveys now allowed to study the relationship between ISM and star formation for a large sample of galaxies, each resolved by hundreds of resolution elements, and performing a homogeneous analysis. This has the potential to sensitively constrain the SF law on sub-galactic scales and test proposed theories of the underlying physics in a wide range of environments both inside of galaxies as well as between galaxies.

Bigiel et al. (2008) used the first available HERACLES data to study the relationship between H I, H_2 , and SFR at 750 kpc resolution in seven H_2 -dominated spirals. The resulting $\Sigma_{\text{SFR}} - \Sigma_{\text{gas}}$ relation (see Figure 1.2) has shown to consist of two, quite distinct scaling relations. The relation between Σ_{SFR} and Σ_{H_2} was observed to be about linear ($n = 1.0 \pm 0.1$) with mean molecular gas depletion time, $\tau_{\text{dep}} = 2.0$ Gyr. The relation between Σ_{SFR} and Σ_{HI} however was very steep with Σ_{HI} saturating at $\sim 10 M_{\odot} \text{ pc}^{-2}$ and Σ_{SFR} varying by more than 2 orders of magnitude over a small range of Σ_{HI} . This suggested that SFE, i.e., the ratio $\Sigma_{\text{SFR}}/\Sigma_{H_2}$, is constant throughout a large range of environments. Leroy et al. (2008) tested if SFE shows dependencies on ISM pressure, dynamical time, galactocentric radius, stellar and gas mass but found none. On the other hand, the ratio $\Sigma_{H_2}/\Sigma_{\text{HI}}$ correlated with many of these parameters. This suggested that the formation of stars from H_2 (inside of GMCs) thus is largely independent of environments while the formation of H_2 out of H I depends strongly on environment.

The value of a comprehensive and homogeneous analysis of a large set of galaxies became obvious as other studies targeting single galaxy continued to indicate different results as long as they were not treated with exactly the same methodology and analyzed together. Crosthwaite & Turner (2007) studied H I, CO, and SFR traced by $100\mu\text{m}$ or 1.4 GHz continuum emission in NGC 6946. They found the highest correlation for $\Sigma_{\text{SFR}} - \Sigma_{H_2}$ but with a radial change of factor ~ 10 , while $\Sigma_{\text{SFR}} - \Sigma_{\text{gas}}$ was about constant with

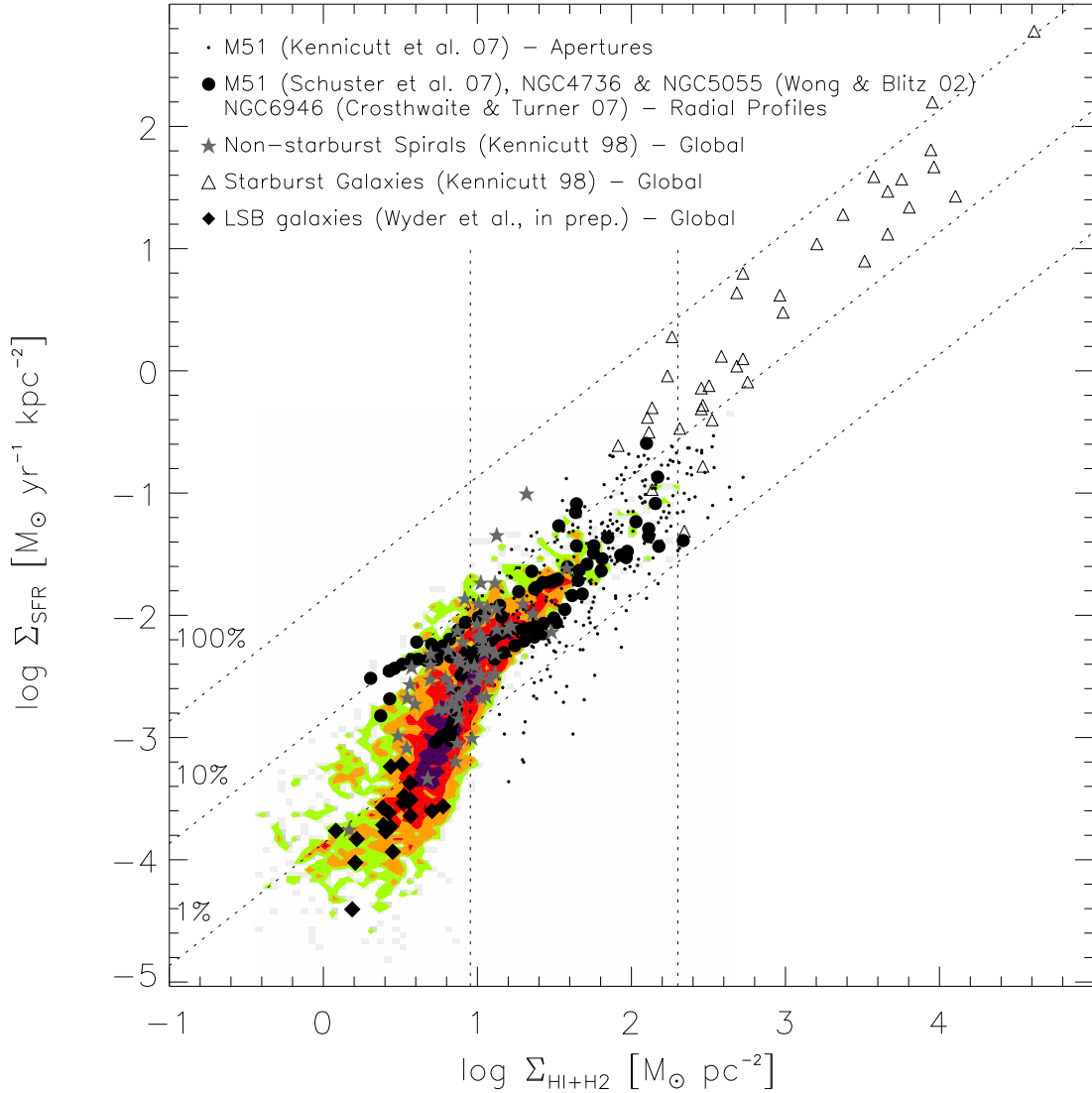


Figure 1.2 The resolved star formation law in nearby galaxies. Colored regions show data density of 750 kpc sized regions in seven spiral galaxies (Bigiel et al., 2008). Black dots show individual apertures in M 51 (Kennicutt et al., 2007). Black circles show radial profiles from M 51 (Schuster et al., 2007), NGC 4736 and NGC 5055 (Wong & Blitz, 2002), and from NGC 6946 (Crosthwaite & Turner, 2007). Filled gray stars show global measurements of 61 normal spiral galaxies and triangles of 36 starburst galaxies (Kennicutt, 1998b). Black filled diamonds show global measurements from 20 LBS galaxies (Wyder et al., 2009). All data have been adjusted to a common IMF, CO line ratio, CO-to-H₂ conversion factor, and galaxy inclination. [Figure taken from Bigiel et al. 2008]

$\tau_{\text{dep}} \approx 2.8$ Gyr. Thilker et al. (2007b) determined SFR from the bolometric luminosity and found for the H_2 -dominated part of NGC 7331 strong correlations between Σ_{SFR} and Σ_{H_2} with slope of $n = 1.64$ and Σ_{gas} with $n = 1.87$. Kennicutt et al. (2007) studied H I, CO, $\text{H}\alpha$, and $24\mu\text{m}$ emission for 250 apertures of 500 pc diameter in M 51 and found the best correlation for $\Sigma_{\text{SFR}} - \Sigma_{\text{H}_2}$ with slope $n = 1.4 - 1.6$. All three studies determined a non-linear $\Sigma_{\text{SFR}} - \Sigma_{\text{H}_2}$ relation, but once they were adjusted to the same conversion factors, Bigiel et al. (2008) showed that they all overlap with the linear relation found for their large sample (see Figure 1.2).

Further evidence highlighting the importance of a clear and homogeneous analysis came from Blanc et al. (2009). They also studied M 51 and resolved the inner 4 kpc into 735 regions of 170 pc in size. They performed integral field spectroscopy and were thus able to measure the $\text{H}\alpha$ flux free of the neighboring [N II] line, stellar absorption and continuum emission, and the Balmer decrement (i.e., $\text{H}\alpha/\text{H}\beta$ line flux) provided a robust measurement of internal extinction. When studying the relationship between Σ_{SFR} and Σ_{H_2} , they determined the best fit by modeling the data with the scatter in x - and y -axis measurements as free parameter and accounting for upper limits; for $\Sigma_{\text{SFR}} - \Sigma_{\text{H}_2}$ they determined $n = 0.82 \pm 0.05$ with an intrinsic scatter of 0.43 ± 0.02 dex. (Not) properly accounting for the intrinsic scatter can significantly affect the measured slope of the SF law. The slope determined by Blanc et al. (2009) is a factor ~ 2 shallower than the result of a linear regression performed in log-log space and neglecting upper limits (the method used by Kennicutt et al., 2007, and many other studies). Rahman et al. (2011) recently tested the influence of different sampling methods (pixel, apertures, rings), spatial resolution, various fitting techniques, and diffuse fractions of different SFR tracers on the determined SF law in NGC 4254. They found that the results were robust in the high surface brightness regime. However, methodology generally affected the result when including regions of lower surface brightness.

1.1.5 The Star Formation Law in the Outer Disk

The extended nature of H I disks and the dearth of $\text{H}\alpha$ emission at large radii has long been interpreted that star formation is strongly (or completely) suppressed. Deep observations with *GALEX* however revealed low but widespread star formation in these regimes (e.g., Thilker et al., 2005, 2007a; Gil de Paz et al., 2007; Bigiel et al., 2010a,b). The conditions for star formation in the outer disks are significantly different than in the inner disk of spirals as these regions have lower heavy element and dust abundance, lower stellar and gas density, flat rotation curves and thus less shear. Bigiel et al. (2010a) studied the SF law outside the optical radius, i.e., in the H I-dominated regime, at $15''$ resolution (corresponding to $0.2 - 1$ kpc) in a sample of 17 galaxies. In the outer disks, Σ_{SFR} is found to scale with $\Sigma_{\text{gas}} \approx \Sigma_{\text{HI}}$, though with a steeper slope, significantly larger scatter, and gas depletion times about 10 times the Hubble time (see Figure 1.3). The SF law in the far outer disk and the central disk is connected by a regime in which $\Sigma_{\text{gas}} \approx 5 - 10 M_{\odot} \text{pc}^{-2}$ varies little but Σ_{SFR} steeply increases by ~ 2 orders of magnitude. In the outer disk, the local amount of H I seems to be the limiting factor of star formation and H I density seems to depend strongly on environment. In the inner disk, the same environmental

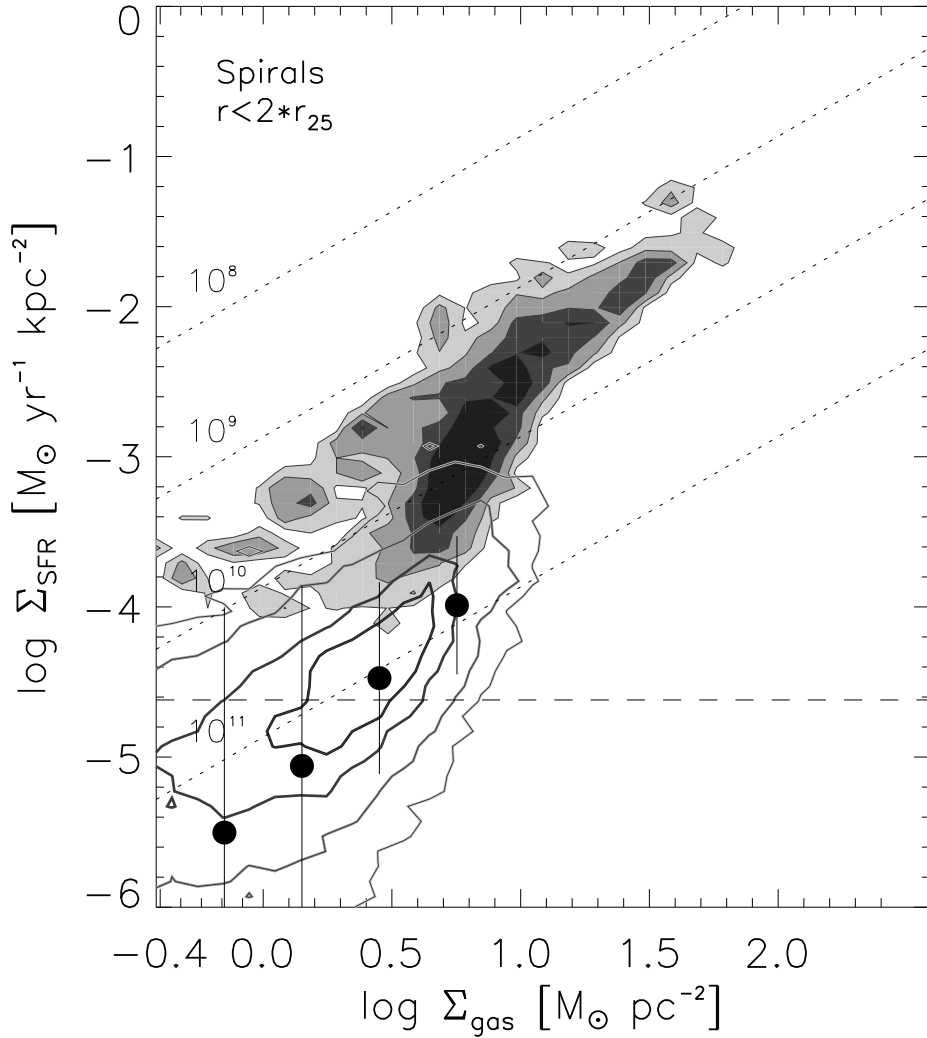


Figure 1.3 The resolved star formation law in spiral galaxies inside the optical radius (filled contours) and outside the optical radius (line contours). Multiple regions are visible: In the inner disk at high densities, Σ_{SFR} scales about linearly with $\Sigma_{\text{gas}} \approx \Sigma_{\text{H}_2}$ and has a gas depletion time of ~ 2 Gyr. At large radii and low densities, Σ_{SFR} scales with $\Sigma_{\text{gas}} \approx \Sigma_{\text{HI}}$, though with large scatter in Σ_{SFR} per unit Σ_{gas} and gas depletion times about 10 times the Hubble time. The transition between the two regimes happens at $\Sigma_{\text{gas}} \approx 3 - 10 M_{\odot} \text{pc}^{-2}$ where the relation is very steep. [Figure taken from Bigiel et al. 2010b]

parameters have basically no effect on the molecular SFE but they seem to control the conversion of H I to H₂.

1.1.6 The Star Formation Law in H I-dominated Galaxies

The SF law in dwarf galaxies and low surface brightness (LSB) galaxies has been of interest due to the unique parameter space these galaxies inhabit compared to typical star-forming galaxies. Hunter et al. (1998) performed an in depth study of H I and H α in a large sample of dwarf galaxies testing various models of dynamical instabilities controlling star formation. They found no evidence that star formation in dwarf galaxies is controlled by large-scale gravitational instabilities as dwarfs have gas densities a factor of ~ 2 below the critical density though they are often vigorously forming stars. Also the inclusion of the gravitational potential from dark matter did not improve consistency between models and observation. The only (azimuthally averaged) quantity that correlated with SFR is the stellar surface density, suggesting that star formation may be triggered and thus controlled by feedback processes.

Leroy et al. (2005) performed an extensive search for CO emission in 121 dwarf galaxies, though detected CO only in 28 galaxies. The $\Sigma_{\text{SFR}} - \Sigma_{\text{H}_2}$ relation, with SFR traced by radio continuum emission, showed no fundamental difference to the SF law of more massive spirals. Both dwarfs and spirals were well fit by a single SF law with slope of $n = 1.3 \pm 0.1$. However, because dwarfs have average surface density of $\Sigma_{\text{H}_2} \approx 3 M_{\odot} \text{ pc}^{-2}$ while spirals have $\Sigma_{\text{H}_2} \approx 10 M_{\odot} \text{ pc}^{-2}$, this would suggest that stars form less efficiently from H₂ in dwarfs because of the non-linearity of the best-fit power law. This result is puzzling because the lower metallicities in dwarfs should lead to the opposite trend. CO emission is found to be underluminous in dwarfs as function of optical luminosity (e.g., Young et al., 1995) and it is thought that CO gets dissociated in lower density regions due to stronger radiation fields such that the remaining CO luminosity does not trace H₂ mass as in higher metallicity regimes. However, increasing the CO-to-H₂ conversion factor in dwarfs would further increase the difference in depletion times. The connection between molecular gas and star formation in low metallicity environments will be discussed in greater detail in Chapter 5.

Wyder et al. (2009) tested the SF law in 19 LSB galaxies. These galaxies can have substantial gas disks which consist predominantly of atomic gas, $\Sigma_{\text{gas}} \approx \Sigma_{\text{HI}}$, but they have relatively low stellar surface densities. These galaxies have $\Sigma_{\text{SFR}}/\Sigma_{\text{HI}}$ about a factor 5 smaller than expected from the relation in Kennicutt (1998b) for massive galaxies. Instead it resemble that found in the outer disks of spirals (Bigiel et al., 2010a, see Figure 1.2). Roychowdhury et al. (2009) extended these studies by comparing H I and FUV in 23 extremely faint dwarf galaxies (median $M_B \sim -13.2$). The disk-averaged $\Sigma_{\text{SFR}}/\Sigma_{\text{HI}}$ is low and comparable to that found in LSB galaxies and the outer disks. In regions of higher gas density, $\Sigma_{\text{HI}} \gtrsim 1 M_{\odot} \text{ pc}^{-2}$, Σ_{SFR} scales with Σ_{HI} but in regions with lower gas density Σ_{SFR} is basically constant and unrelated to Σ_{HI} . Similar extended UV disks have been reported by Thilker et al. (2005, 2007a,b); Boissier et al. (2007) and Bigiel et al. (2010b). As of today it is still unclear which processes trigger and control star formation in those regimes.

1.1.7 The Star Formation Law in Early-Type Galaxies

The SF law in early-type galaxies has recently gained much attention. Observations by *Spitzer* and *GALEX* have shown that star formation is occurring in a significant fraction of early-type galaxies (e.g., Yi et al., 2005; Temi et al., 2009; Young et al., 2009). Targeted follow-up observations and subsequent large volume-limited surveys revealed that these star-forming early-type galaxies also contain substantial amounts of atomic and molecular gas (e.g., Morganti et al., 2006; Combes et al., 2007; Young et al., 2011). Shapiro et al. (2010) studied 48 early-type galaxies (E, S0), 8 of these galaxies show significant evidence of ongoing star formation at multiple wavelengths and all of them have been detected in CO. These galaxies have gas densities of $\Sigma_{\text{gas}} \approx 10 - 200 M_{\odot} \text{ pc}^{-2}$ and SFE comparable to spiral galaxies or nuclear starbursts. Crocker et al. (2011) performed follow-up observations on 12 star-forming early-type galaxies and also found these galaxies to coincide with the SF law of Kennicutt (1998b) or Bigiel et al. (2008) within the 1σ bound. Wei et al. (2010) studied 19 lower-mass early-type galaxies ($M_{\star} < 4 \times 10^{10} M_{\odot}$) with an emphasis on early-type galaxies overlapping the blue sequence. For a subsample of 8 resolved galaxies they measured slopes of $n = 0.6 - 1.9$ (median 1.2), and for the complete average molecular gas depletion times, $\tau_{\text{dep}} = 0.1 - 2.3$ Gyr (median 0.5 Gyr). This suggests that star formation in early-type galaxies is not significantly different than star formation in disks of late-type galaxies, though often a scaled down version to smaller gas masses and SFRs.

1.1.8 The Star Formation Law in Disk and Starburst Galaxies

By the 1960's it was known that many spiral galaxies host nuclear starbursts, i.e., regions with bright emission lines similar to those of H II regions. The distinct nature of these nuclear regions was fully revealed by infrared observations which showed nuclear SFRs of up to $100 M_{\odot} \text{ yr}^{-1}$ in some nearby galaxies, and up to $1000 M_{\odot} \text{ yr}^{-1}$ in (ultra) luminous infrared galaxies (see reviews by Sanders & Mirabel, 1996; Kennicutt, 1998a; Soifer et al., 2008). The study of Kennicutt (1998b) included 36 such nuclear starburst regions. They have gas densities, $\Sigma_{\text{gas}} = 100 - 10^4 M_{\odot} \text{ pc}^{-2}$, in large excess of those found in disks of nearby spiral galaxies, and $\Sigma_{\text{SFR}}/\Sigma_{\text{gas}}$ in excess by factor ~ 10 such that at the current SFR the molecular gas reservoir would be completely exhausted within ~ 100 Myr. Kennicutt (1998b) found that both the nuclear starbursts as well as the disk-averaged values of normal spiral galaxies were well fitted by a unique power law with slope $n = 1.4$. However, not all galaxies with high Σ_{gas} in their centers have Σ_{SFR} in significant excess as compared to average disk values. Komugi et al. (2005) used interferometric CO and (extinction corrected) H α data of 23 nearby normal spiral galaxies to study the SF law at the central $3''$ (< 100 pc) and found these centers to be systematically (~ 0.5 dex) below the starburst sample of Kennicutt (1998b) leaving the exact scaling at high gas densities uncertain. Jogee et al. (2005) considered the gravitational instability criterion for the nuclear regions of 10 barred starburst galaxies and found that the observed gas densities are within a factor ~ 2 of Σ_{crit} predicted by gravitational instabilities, though Σ_{crit} can be very large ($\sim 1000 M_{\odot} \text{ pc}^{-2}$) due to high epicyclic frequencies and high gas velocity dispersions, $\sigma_{\text{gas}} \sim 10 - 40 \text{ km s}^{-1}$. Thus galaxies can assemble large gas masses at their centers

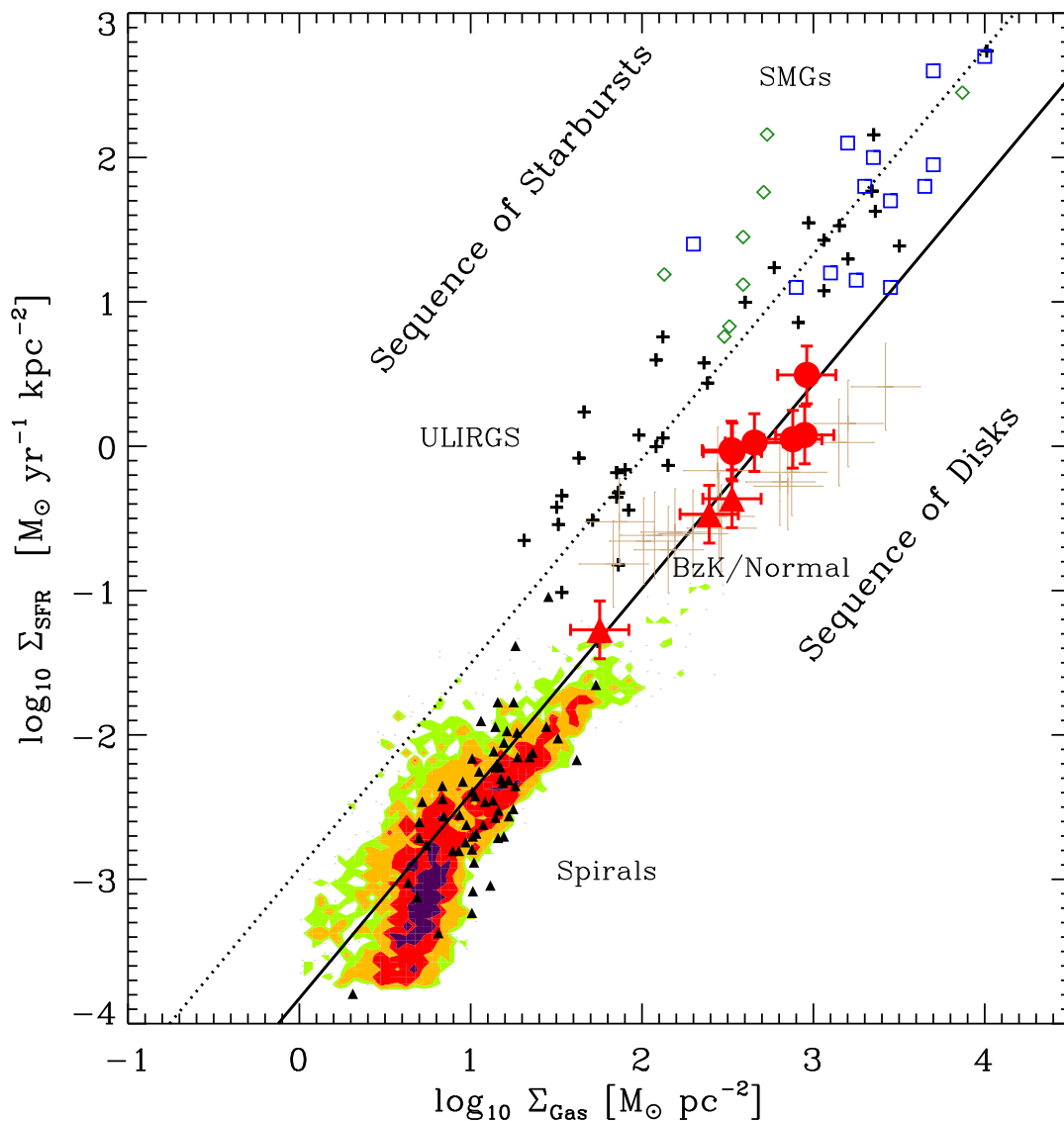


Figure 1.4 The star formation law shows two distinct sequences at high densities: one sequence for disk galaxies including both local spiral galaxies (black triangles, colored contours) and distant normal star-forming (BzK) galaxies (red and brown symbols). Another sequence includes local (nuclear) starbursts, (U)LIRGs, and SMGs (black crosses, open symbols). The lower solid line is a fit to local spirals and $z = 1.5$ BzK galaxies (slope of 1.42), and the upper dotted line is the same relation shifted up by 0.9 dex to fit local (U)LIRGs and SMGs. [Figure taken from Daddi et al. 2010]

and once instabilities are triggered they would grow on very short timescales (few Myrs) resulting in a starburst.

In the last years our observational insight of the SF law at high densities has significantly expanded by new CO observations of distant galaxies. Daddi et al. (2010) and Genzel et al. (2010) showed by a comprehensive compilation of literature data that the SF law at high densities shows a bimodal distribution that cannot be described by a single parametrization (see Figure 1.4). Two distinct sequences have been revealed which are characterized by gas depletion times ($\Sigma_{\text{gas}}/\Sigma_{\text{SFR}}$) which are relatively long in quiescent star-forming galaxies and roughly a factor 10 shorter in violent starbursts. One sequence is that of “normal” disk galaxies including both nearby spiral galaxies as well as distant BzK¹ galaxies which consume their current reservoir of (molecular) gas on ~ 1 Gyr timescale. Another sequence is formed by the nearby (nuclear) starbursts studied by Kennicutt (1998b) and extending to more distant (ultra) luminous infrared galaxies (LIRGs & ULIRGs) and the even more luminous sub-millimeter galaxies (SMGs) — the latter populations are likely major mergers — which consume their gas in ~ 100 Myrs. Both sequences have approximately the same slope ($n \approx 1.2 - 1.4$) but systematically offset (by factor ~ 10) from each other.

Daddi et al. (2010) and Genzel et al. (2010) suggested that the strongly enhanced SFR in starbursts is driven by global processes and likely linked to their short dynamical times ($\tau_{\text{dyn}} \sim 40$ Myr for ULIRGs and SMGs and $\tau_{\text{dyn}} \sim 400$ Myr for spirals) because the two sequences roughly overlap in $\Sigma_{\text{SFR}} - \Sigma_{\text{gas}}/\tau_{\text{dyn}}$ space. The shorter dynamical timescales compress gas clouds more effectively leading to more efficient star formation per unit (molecular) gas mass. This suggestion is motivated by observations of a similar bimodal trend seen for the dense gas fraction traced by the ratio of HCN / CO — where HCN traces dense gas with volume densities $\rho > 10^4 \text{ cm}^{-3}$ — while the ratio SFR / HCN is roughly constant for all galaxies (e.g., Gao & Solomon, 2004; Juneau et al., 2009). Numerical work on the gas dynamics in merging systems also provide evidence for high dense gas though they suggest that these are caused by local processes of increased ISM turbulence and fragmentation (Teyssier et al., 2010). Further observational evidence that starbursts are triggered on sub-galactic scales and are not related to the galaxies global mass or size comes from first spatially resolved studies of merging galaxies (e.g., Boquien et al., 2011). These reveal starburst activity on (sub-) kiloparsec scale while most of the galaxy is forming stars in the quiescent disk mode. Despite these observational and theoretical advances, our current understanding of the nature of starburst is this in its infancy and much remains to be learned by the global and local processes triggering (and quenching) of starbursts.

1.1.9 The Composite Star Formation Law

Detailed observations in the last few years have shown that the SFR is not a simple function of the total gas mass but has a much more complex behavior. Figure 1.5 tries to highlight different regimes, though in a much oversimplified format. In regions of low gas

¹ A two-color selection based on B -, z -, and K -band photometry used to classify galaxies as star-forming or passive systems (Daddi et al., 2004).

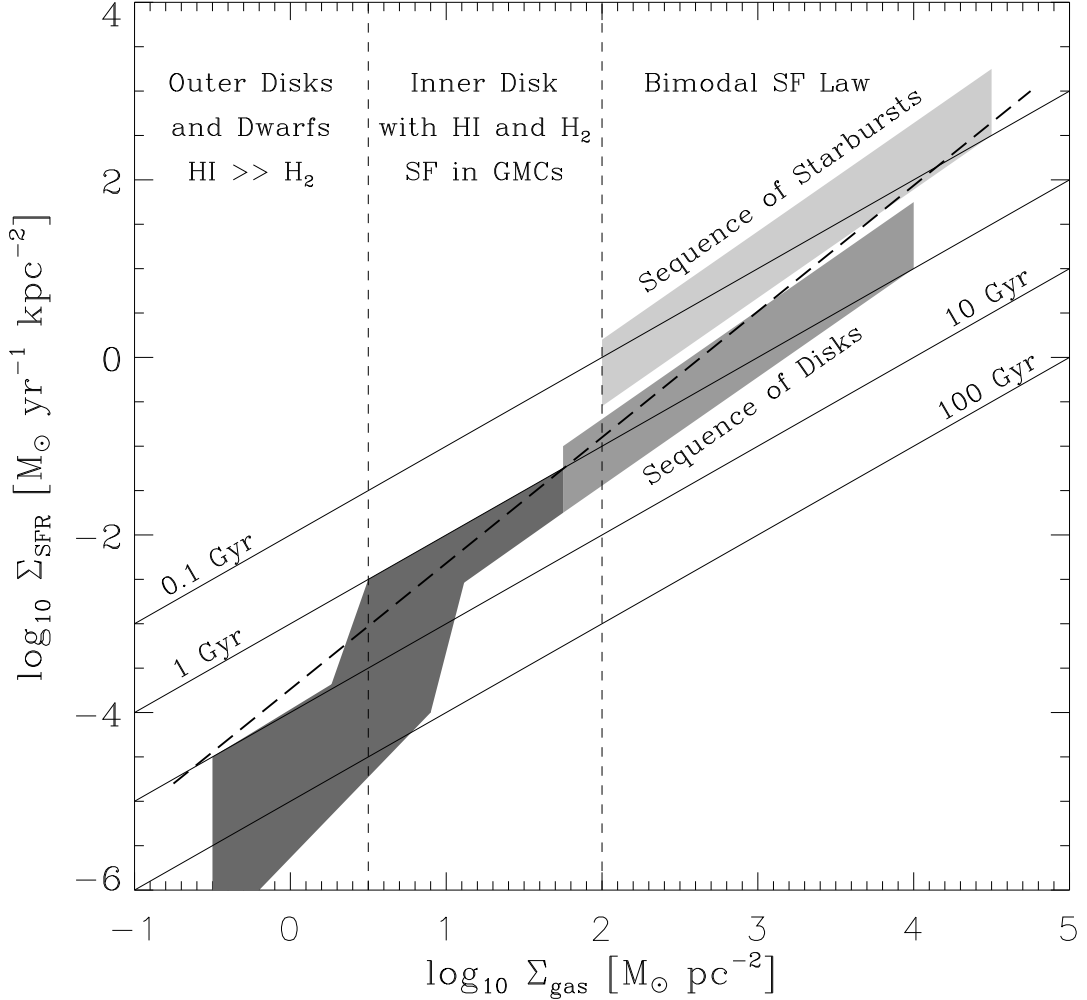


Figure 1.5 A cartoon of the star formation law breaking up into three distinct regimes: Normal disk galaxies form a sequence of $\Sigma_{\text{SFR}} \propto \Sigma_{\text{gas}} \approx \Sigma_{\text{H}_2}$ with gas consumption times of 0.5 – 2 Gyr. At $\Sigma_{\text{gas}} \lesssim 10 \text{ M}_{\odot} \text{ pc}^{-2}$ star formation depends strongly on ISM phase. Σ_{SFR} begins to scale with $\Sigma_{\text{gas}} \approx \Sigma_{\text{HI}}$ where HI becomes rare and gas consumption times exceed the Hubble time. Luminous merging galaxies form a second sequence of $\Sigma_{\text{SFR}} \propto \Sigma_{\text{gas}} \approx \Sigma_{\text{H}_2}$ but offset to gas consumption times ~ 0.1 Gyr. Star formation in both sequences seems to be independence for cosmic lookback time $\lesssim 10$ Gyr. The diagonal dashed line shows the power law $\Sigma_{\text{SFR}} \propto \Sigma_{\text{gas}}^{1.4}$ from Kennicutt (1998b) — clearly insufficient to fit all regimes.

surface densities, $\Sigma_{\text{gas}} \lesssim 1 - 5 M_{\odot} \text{ pc}^{-2}$, as found in the outer disks of spiral galaxies and in dwarf galaxies, Σ_{SFR} scales with Σ_{gas} with gas consumption times much larger than the Hubble time. Star formation is limited by the availability of its raw material but the large scatter in the relation indicates that the ability of the ISM to form overdense, gravitational-unstable regions strongly depends on environment. Towards smaller radii and higher gas surface densities, $\Sigma_{\text{gas}} \sim 5 - 10 M_{\odot} \text{ pc}^{-2}$, the SFR increases steeply and is no longer predictable from the total gas mass. In this range the ISM consists both of atomic and molecular gas and its phase balance is a sensitive function of gas density, metallicity, and potentially other parameters. In Chapter ?? we show that $\Sigma_{\text{SFR}} \propto \Sigma_{\text{H}_2}$ independent of the local atomic gas mass suggesting that the SFR per total gas mass is solely controlled by the formation of a molecular gas phase. In the inner disks of spirals where $\Sigma_{\text{gas}} \gtrsim 10 M_{\odot} \text{ pc}^{-2}$ and the ISM is predominantly molecular, the SFR scales linearly with the available gas mass showing no significant dependence of galaxy type and/or global galaxy properties. At surface densities of $\Sigma_{\text{gas}} \gtrsim 100 M_{\odot} \text{ pc}^{-2}$ — exceeding the surface density of GMCs — the relation begins to steepen again but the uniform trend is broken. Instead the SF relations shows a bimodal form and Σ_{SFR} can vary by factor ~ 10 at fixed gas surface density. It seems likely that the increased SFR per total gas mass represent a transient phase during galaxy evolution (most likely induced by mergers) at which the distribution of gas volume densities is shifted toward significantly higher values than normal in spirals.

1.2 Physical Processes Underlying the Star Formation Law

The following presentation gives an overview of physical processes that have been invoked to underly the observed relation between SFR and gas density. These models typically consist of two elements: (1) a model which describes how SFR depends on ISM density and potentially other parameters, and (2) a prescription which ISM material is participating in the star formation process. The former is often described by the following formula,

$$\Sigma_{\text{SFR}} = \epsilon \frac{\Sigma_{\text{gas}}}{\tau}, \quad (1.3)$$

with relates the SFR surface density, Σ_{SFR} , and the gas surface density, Σ_{gas} , with a timescale τ at which the physical process assembles dense star-forming gas structures, and an efficiency ϵ that defines the fraction of gas that is converted into stars per unit timescale. The requirement from observation is that $\tau/\epsilon = \tau_{\text{dep}} = \Sigma_{\text{gas}}/\Sigma_{\text{SFE}}$ and ~ 2 Gyr for the range $\Sigma_{\text{gas}} = 10 - 100 M_{\odot} \text{ pc}^{-2}$. The latter is used to set additional requirements for the ISM material that can form stars, either by invoking a critical gas density “threshold” for a one phase ISM model or by selecting a specific ISM phase in a multi-phase ISM model ideally in combination with a prescription of ISM phase balance.

1.2.1 SF Laws based on Large-Scale Dynamical Processes

Disk Free-Fall Timescale

A basic class of models are those that consider large-scale dynamical processes as relevant for setting the timescale of gas assembly and star formation. These models typically assume a single gas component (and stars) in an axially symmetric rotating thin disk. Several related timescales have been proposed. Madore (1977) proposed the (vertical) free-fall time, τ_{ff} , of a self-gravitating gas disk to be the relevant timescale,

$$\tau_{\text{ff}}^{-1} \propto (G\rho_0)^{1/2} \sim (G\Sigma_{\text{gas}}/H)^{1/2}, \quad (1.4)$$

with the midplane gas density, ρ_0 , the gravitational constant, G , and the scale height, H , of the gas disk. For a fixed scale height the star formation relation is

$$\Sigma_{\text{SFR}} \propto \Sigma_{\text{gas}}^{1.5}, \quad (1.5)$$

The resulting power-law slope of $n = 1.5$ is similar to the widely adopted slope of $n = 1.4$ determined by Kennicutt (1998b) and many previous and following studies. Though numerous recent studies confirmed that a single power-law is a gross oversimplification of the complex observational picture of the SF law especially in the low and high density regime (see Figure 1.5).

Alternatively, for a varying scale height $H = \sigma_{\text{gas}}^2/\pi G\Sigma_{\text{gas}}$ that depends on the velocity dispersion of the gas, σ_{gas} , (e.g., Krumholz & McKee, 2005) gives

$$\Sigma_{\text{SFR}} \propto \frac{\Sigma_{\text{gas}}^2}{\sigma_{\text{gas}}}, \quad (1.6)$$

a model that is however hampered by the observational difficulty to determine (local) velocity dispersions. For spiral galaxies in THINGS and HERACLES, the H I velocity dispersion decreases by a factor ~ 2 over the inner $\sim 2 - 5 R_{25}$ with an average value of $\sim 10 \text{ km s}^{-1}$ (Tamburro et al., 2009). H₂ can however have significantly (factor ~ 10) larger velocity dispersion near galaxy centers. The above equation is fulfilled with average scatter ~ 0.5 dex with no systematic correlation with galactocentric radius but with galaxy inclination (Spearman rank correlation coefficient of 0.3 and $\Sigma_{\text{SFR}}/(\Sigma_{\text{gas}}^2/\sigma_{\text{gas}})$ factor ~ 2.5 higher on average for galaxies with inclination $i > 40$).

If the stellar gravitational potential is non-negligible, then the midplane gas density depends on the midplane pressure of the gaseous and stellar disk in hydrostatic equilibrium (Elmegreen, 1989), which adds a correction factor to the above star formation relation,

$$\Sigma_{\text{SFR}} \propto \frac{\Sigma_{\text{gas}}^2}{\sigma_{\text{gas}}} \left(1 + \frac{\Sigma_* \sigma_{\text{gas}}}{\Sigma_{\text{gas}} \sigma_*} \right)^{1/2}, \quad (1.7)$$

that depends in addition on the stellar (vertical) velocity dispersion, σ_* , and the stellar mass surface density, Σ_* .

Orbital Timescales

An alternative approach to characterize the (global) SFR in galaxies, from Shu et al. (1973), is based on the orbital timescale τ_{orb} given by

$$\tau_{\text{orb}}^{-1} = \frac{\Omega}{2\pi} = \frac{v(r_{\text{gal}})}{2\pi r_{\text{gal}}}, \quad (1.8)$$

with orbital rotational velocity $v(r_{\text{gal}})$ at galactocentric radius r_{gal} and orbital rotation frequency Ω . The star formation relation can be parametrized as

$$\Sigma_{\text{SFR}} = \epsilon_{\text{orb}} \Sigma_{\text{gas}} \Omega. \quad (1.9)$$

Such a dependence is appropriate if spiral arms are the key factor for triggering cloud and thus star formation (e.g., Wyse & Silk, 1989) or if star formation is self-regulated to retain a constant value (e.g., Silk, 1997). Many studies have shown that such a relation performs equally well as a relation of the form $\Sigma_{\text{SFR}} \propto \Sigma_{\text{gas}}^n$ when disk-averaged quantities in spiral and starburst galaxies are considered (e.g., Kennicutt, 1998b). The normalization of the order $\epsilon_{\text{orb}} \approx 0.017$ suggests that $\sim 10\%$ of the star-forming ISM is converted to stars per orbital time τ_{orb} .

Daddi et al. (2010) and Genzel et al. (2010) tested the dynamical SF law of the form $\Sigma_{\text{SFR}} \propto (\Sigma_{\text{H}_2}/\tau_{\text{dyn}})^n$ for disk-averaged measurements of low- z and high- z normal star-forming and star-bursting galaxies. They determined a best fit relation with $n \approx 1.1 \pm 0.1$ but large scatter (~ 0.55 dex). Interestingly they found that the bimodality of the SF law seen in the $\Sigma_{\text{SFR}} - \Sigma_{\text{gas}}$ plane (see Figure 1.4) is removed (or at least diminished) when parametrized this way. Thus global galaxy properties (which set τ_{dyn}) seem to regulate at least in part local processes like star formation. The physical process underlying this connection however remains unclear. On global scales the disk-averaged $\langle \tau_{\text{orb}} \rangle$ may just reflect the galaxy's dynamical mass. Krumholz & McKee (2005) found for spiral and starburst galaxies that Σ_{gas} and Ω are correlated by $\Omega \propto \Sigma_{\text{gas}}^{0.49}$, explaining why the two SF relations both work equally well. On the other hand, Daddi et al. (2010) noted that the dynamical time may be expected to scale with the gas volume density as $\tau_{\text{dyn}}^{-1} \propto \rho^{0.5}$ (Silk, 1997) such that in some galaxies gas can reach high densities and the system gets short dynamical timescales so that the gas is consumed more rapidly — a suggestion that is consistent with the higher dense gas fractions found in merging galaxies.

Another ambiguity for which process τ_{orb} should be the relevant timescale arises for galaxies (regions inside galaxies) that are predominantly molecular. It seems more reasonable that τ_{orb} is related to the H_2/HI ratio than defining the timescale at which already existing molecular gas (mostly likely in GMCs) forms stars. Leroy et al. (2008) tested both for correlations between τ_{orb} and $\Sigma_{\text{SFR}}/\Sigma_{\text{gas}}$ and $\Sigma_{\text{H}_2}/\Sigma_{\text{HI}}$ inside of galaxies but found for neither an efficiency factor ϵ_{orb} that did performed reasonably well from the centers to the outer disks. A similar result was noted by Wyder et al. (2009) for radial profiles in LSB galaxies.

Other models that also depend on the orbital frequency Ω emerge if the rate of collisions between gas clouds is considered to set the timescale for star formation. Wyse (1986)

suggested that GMCs and thus stars result from atomic cloud-cloud collisions at a rate proportional to $\Sigma_{\text{HI}}^2(\Omega(r) - \Omega_{\text{P}})$ where Ω_{P} is the constant pattern speed. Tan (2000) suggested the slightly different scaling $\Sigma_{\text{SFR}} \propto \Sigma_{\text{gas}}\Omega(1 - 0.7\beta)$ where $\beta = d \ln v(r_{\text{gal}})/d \ln r_{\text{gal}}$ and $v = v_{\text{rot}}$ the circular rotation velocity. The dependence on β captures the importance of shear for cloud-cloud collisions. For a flat rotation curve, $\beta = 0$, and for solid body rotation, $\beta = 1$, such that Σ_{SFR} is reduced toward the galaxy centers. Tan (2010) tests this model in the H_2 -dominated regions of 12 spiral galaxies and finds it a better parametrization of the radial profile of Σ_{SFR} than provided by $\Sigma_{\text{gas}}\Omega$ or Σ_{gas}^n .

1.2.2 SF Laws including Stellar Surface Density

Dopita & Ryder (1994) suggested a generalized SF law of the following form inspired by the observational relation between stellar surface brightness and surface brightness of $\text{H}\alpha$

$$\Sigma_{\text{SFR}} \propto \Sigma_{\text{gas}}^n \Sigma_{\text{gas+stars}}^m . \quad (1.10)$$

They also noted that observational data was best fit for $1.5 < (n + m) < 2.5$, and that a model of self-regulated star formation including cloud-cloud collisions and stellar feedback predicts $n = 5/3$ and $m = 1/3$. A close association between stellar mass and SFR surface density was also noted by Hunter et al. (1998); Hunter & Elmegreen (2004) and Leroy et al. (2008) but the latter study showed that the relation $\Sigma_{\text{SFR}}/\Sigma_{\text{gas}} \propto \Sigma_{\text{stars}}$, i.e., with a linear dependence on the stellar surface density, performs well in H I -dominated regions while in H_2 -dominated regions $\Sigma_{\text{SFR}}/\Sigma_{\text{gas}} = \text{const.}$ is inevitably independent of Σ_{stars} .

In a recent study, Shi et al. (2011) tested this “extended SF law” for a large compilation of disk-averaged data including nearby early- and late-type / dwarf galaxies and distant normal star-forming and starburst galaxies. Holding $n = 1$ fixed, they determined the best fit as $m = 0.48 \pm 0.04$ and noted that LSB galaxies — those systems that lie systematically below the relation $\Sigma_{\text{SFR}} \propto \Sigma_{\text{gas}}^{1.4}$ (Kennicutt, 1998b) — are now well fit without systematic offset. They also noted that a relation like $\Sigma_{\text{SFR}} \propto \Sigma_{\text{gas}} \Sigma_{\text{stars}}^{0.5}$ does arise from models of (a) large-scale disk instabilities in stellar mass dominated disks, or (b) pressure-regulated H_2 formation in H I -dominated regimes, or (c) the balance between hydrostatic gas pressure and pressure by supernova and radiation from massive stars. Thus globally such a relation may be of value but on local scales it remains ambiguous which physical processes control ISM structure and star formation because stellar surface density does correlate with many other parameters (e.g., potential gravity, radiation field, metallicity).

1.2.3 SF Laws assuming Fixed GMC Efficiencies

A large class of star formation models assumes that the SFR scales directly with the gas mass in gravitational-bound clouds (GBCs). Observations in our galaxy have revealed that most stars are forming in such clouds and that the gas in these clouds is cold and predominantly molecular. In these models, SFR is thus either coupled to the gas mass in a thermally cold ISM phase and/or in GBCs (independent of its chemical state) or associated to the molecular gas mass in GMCs. The resulting SF law is

$$\Sigma_{\text{SFR}} = \epsilon_{\text{ff, GMC}} \frac{f_{\text{H}_2} \Sigma_{\text{gas}}}{\tau_{\text{ff, GMC}}}, \quad (1.11)$$

with an efficiency factor $\epsilon_{\text{ff, GMC}}$ per free-fall time $\tau_{\text{ff, GMC}}$ and a dependence on the molecular fraction, $f_{\text{H}_2} = \Sigma_{\text{H}_2}/\Sigma_{\text{gas}} = R_{\text{H}_2}/(R_{\text{H}_2} + 1)$ or alternatively expressed by the $\text{H}_2/\text{H I}$ ratio $R_{\text{H}_2} = \Sigma_{\text{H}_2}/\Sigma_{\text{HI}}$. Several proposals have been made which physical processes regulate the ISM phase balance (i.e., f_{H_2} or R_{H_2}) and they are summarized below.

Furthermore, it is often assumed that the star formation efficiency per free-fall time, $\epsilon_{\text{ff, GMC}}$, is constant (Krumholz & Tan, 2007). This requires that GMCs are decoupled from their surrounding ISM and that they share uniform properties and mass functions in many different environments. Observations of GMCs in the Milky Way and nearby galaxies strongly suggest such uniform properties (e.g., Bolatto et al., 2008; Fukui & Kawamura, 2010). These include that GMCs seem to have almost constant surface densities of $\sim 85 M_{\odot} \text{ pc}^{-2}$ and that they share universal scaling relations commonly known as Larson laws (Larson, 1981). As long as the external pressure is low, GMCs properties are solely set by internal processes. In the last decade a perception has been developed that GMC properties are governed by the (complex) interplay of turbulence, magnetic fields, and self-gravity (e.g., Mac Low & Klessen, 2004; McKee & Ostriker, 2007; Krumholz, 2011). On large scales (supersonic) turbulence make GMCs stable against gravitational collapse but turbulence also induces a wide distribution of densities with high-density regions susceptible to gravitational collapse. For a long time it has been puzzling why star formation in GMCs performs quite “inefficient”, i.e., why on global scales the (molecular) gas consumption time is ~ 2 Gyr while the free-fall timescale of a typical GMC with mass $M_{\text{H}_2} \sim 10^6 M_{\odot}$ and mean density $\rho_{\text{H}} = 100 \text{ cm}^{-3}$ is only $\tau_{\text{ff, GMC}} \sim 4$ Myr. However, by assuming that GMCs are dominated by supersonic turbulence, Krumholz & McKee (2005) were able to derive $\epsilon_{\text{ff, GMC}} \sim 0.01$ to first order constant for all virialized clouds such that $\sim 1\%$ of a GMCs mass is converted into stars per free-fall time.

1.2.4 Thresholds for Star Formation

The above models provide parametrizations at which rate gas can be converted into stars, however, they do not define which gas actively participates in the star formation process. The fact that pure self-gravity will render every large and massive enough region unstable, and hence star-forming, is in contradiction to observations of extended H I disks with little star formation. This suggests that there have to be processes that can prevent the gas from forming stars. Many proposals have been put forward which define such a “threshold” for star formation either by referring to a critical minimal gas surface density required for gravitational instabilities to grow or related to thermal and/or phase transitions in the ISM required to form gravitational-bound gas clouds. In the following, I will describe several such thresholds.

The Q Threshold

One such mechanism which can stabilize the gas disks against gravitational collapse is provided by rotation and shear in galactic disks which disrupts large gas clouds before they can gravitationally contract. Toomre (1964) and Quirk (1972) suggested the Q parameter to define the threshold when self-gravity can overcome shear disruption,

$$Q_{\text{gas}} = \frac{\kappa \sigma_{\text{gas}}}{\pi G \Sigma_{\text{gas}}} , \quad (1.12)$$

where Σ_{gas} is the gas surface density, κ the epicyclic frequency $\kappa^2 \equiv R^{-3} \partial(\Omega^2 R^4) / \partial R$ (with $\kappa = 2\Omega = \text{const.}$ for solid body rotation and $\kappa = \sqrt{2}\Omega \propto r_{\text{gal}}^{-1}$ for a flat rotation curve), and σ_{gas} is the (vertical) gas velocity dispersion (either thermal or turbulent). For $Q > 1$ gas should be stable on all spatial scales either by pressure forces on small scales or by shear on large scales. For $Q < 1$ gas should become unstable on large scales, collapse and form dense star-forming clouds. Thus, $Q = 1$ defines the critical surface density for large-scale collapse,

$$\Sigma_{\text{crit}, Q} = \alpha_Q \frac{\kappa \sigma_{\text{gas}}}{\pi G} . \quad (1.13)$$

The factor $\alpha_Q = Q^{-1}$ has been added to account for small deviations from the theoretical prediction of $Q = 1$. Kennicutt (1998b) and Martin & Kennicutt (2001) showed that the density of H II regions significantly drops at a threshold radius, r_{thresh} , corresponding to $\Sigma_{\text{gas}}(r_{\text{thresh}}) = \Sigma_{\text{crit}, Q}$ with $\alpha_Q \approx 0.65$. In dwarf galaxies with active star formation α_Q is however required to be significantly (factor ~ 2) smaller to get the observed Σ_{gas} close to $\Sigma_{\text{crit}, Q}$ (e.g., Hunter et al., 1998; Wyder et al., 2009). Thus, providing evidence against a unique relationship.

Hunter et al. (1998) performed a detailed study of other factors that could affect α_Q including disk thickness, stellar and dark matter potentials, thermal properties of the gas, and shear regulated cloud formation but found no model (with the marginal exception of the shear regulated one) that was able to predict the (non) occurrence of star formation with appreciated accuracy. For all galaxies, stellar potential wells may significantly influence the stability of the gas disk. Wang & Silk (1994) defined

$$Q_{\text{stars}} = \frac{\kappa \sigma_*}{\pi G \Sigma_*} , \quad (1.14)$$

with the surface density of stars, Σ_* , and the stellar velocity dispersion, σ_* . The approximate instability criterion becomes then

$$Q_{\text{eff}} = \left(\frac{1}{Q_{\text{gas}}} + \frac{1}{Q_{\text{stars}}} \right)^{-1} = \frac{\kappa \sigma_{\text{gas}}}{\pi G \Sigma_{\text{gas}}} \left(1 + \frac{\Sigma_{\text{gas}} \sigma_*}{\Sigma_* \sigma_{\text{gas}}} \right)^{-1} . \quad (1.15)$$

Leroy et al. (2008) found that by including the stellar potential Q is reduced from $Q_{\text{gas}} \sim 4$ to $Q_{\text{eff}} \sim 1.5$ throughout the disk of 23 spiral and dwarf galaxies.

Formation of a Cold ISM Phase

The various studies that cast doubt on utility of the Toomre Q parameter as a general threshold for star formation made Elmegreen (1994) suggest that the need of a cold ISM phase to form stars may define the relevant threshold for star formation. Elmegreen found that the formation of a cold phase requires a minimal critical pressure (correlated with a minimal gas column density) which itself depends on radiation field and metallicity. Schaye (2004) followed up on this idea and studied a model gaseous disk containing metals and dust and that is embedded in a dark matter halo and an external radiation field. From that Schaye derived a critical surface density at which the ISM temperature is $T < 1000$ K allowing for the formation of molecular gas and rendering the disk gravitational unstable. The critical surface density where $T \sim 500$ K, the molecular fraction is $f_{\text{H}_2} \sim 10^{-3}$, and $Q \sim 1$ is approximately given by (neglecting higher order terms)

$$\Sigma_{\text{crit}} \approx \frac{6.1}{\text{M}_{\odot} \text{ pc}^{-2}} f_{\text{gas}}^{0.3} \left(\frac{Z}{0.1 Z_{\odot}} \right)^{-0.3} \left(\frac{I}{10^6 \text{ cm}^{-2} \text{ s}^{-1}} \right)^{0.23}, \quad (1.16)$$

where $f_{\text{gas}} \approx \Sigma_{\text{gas}}/\Sigma_{\text{gas+stars}}$, Z is the metallicity, and I is the ionizing radiation field (see also Leroy et al., 2008). The idea that the thermal/chemical phase of the ISM is important in determining the critical threshold is the basis of many recent theories of star formation but it does not render galactic rotation (and thus Toomre's Q) completely irrelevant as it controls where global perturbations like spiral arms can form which also affect the phase balance.

H₂/H I Ratio set by Midplane Pressure

Several authors have suggested that R_{H_2} is set by the ambient hydrostatic pressure, P_{h} , at the midplane,

$$R_{\text{H}_2} = \frac{\Sigma_{\text{H}_2}}{\Sigma_{\text{HI}}} \propto P_{\text{h}}^{\gamma}. \quad (1.17)$$

The reasoning is that because pressure is proportional to the midplane volume density, $P_{\text{h}} = \rho_0 \sigma_{\text{gas}}^2$, high pressure and hence high gas densities enhance H₂ formation, increasing the column densities and shielding from the interstellar radiation field. Thus causing increased gravitational instability. Elmegreen (1989) gives an approximate formula for P_{h} for a gaseous and stellar disk in hydrostatic equilibrium,

$$P_{\text{h}} \approx \frac{\pi}{2} G \Sigma_{\text{gas}}^2 \left(1 + \frac{\Sigma_{*} \sigma_{\text{gas}}}{\Sigma_{\text{gas}} \sigma_{*}} \right). \quad (1.18)$$

On theoretical grounds, Elmegreen (1993) suggested that $R_{\text{H}_2} \propto P_{\text{h}}^{2.2} j^{-1}$ depends steeply on P_{h} and to a minor extent on the strength of the radiation field, j . This leads to $R_{\text{H}_2} \propto P_{\text{h}}^{1.2}$ if $j \propto \Sigma_{\text{SFR}} \propto \Sigma_{\text{H}_2}$. Wong & Blitz (2002) tested this dependence using

azimuthally averaged radial profiles in H₂-dominated regions of 12 spiral galaxies and found $\gamma = 0.8$. Leroy et al. (2008) tested the dependence of Σ_{SFR} on P_{h} both for a scaling via the disk free-fall time ($\tau_{\text{ff}}^{-1} \propto \rho_0^{1/2} \propto P_{\text{h}}^{1/2}$, i.e., Equation 1.7) as well as via the scaling $R_{\text{H2}} \propto P_{\text{h}}^{\gamma}$. Throughout the disks of spirals and dwarfs the latter parametrization with a steep exponent of $\gamma \sim 1.2$ provided a good description of the data while the former predicts a dependence of SFE on P_{h} in the inner H₂ dominated regions of spirals which is not observed (but SFE is constant).

Blitz & Rosolowsky (2004) and Blitz & Rosolowsky (2006) derived a similar expression of P_{h} that is valid for an infinite, two-fluid disk with locally isothermal stellar and gas layers. Under the assumption that the gas scale height is much less than the stellar scale height and that stellar scale height and gas velocity dispersion are constant, this leads to

$$P_{\text{h}} \propto \Sigma_{\text{gas}} \Sigma_{*}^{1/2}, \quad (1.19)$$

and they determined for a pixel-by-pixel analysis of 14 galaxies $\gamma = 0.92$ for $R_{\text{H2}} \propto P_{\text{h}}^{\gamma}$.

H₂/HI Ratio set by Photodissociation Model

In a series of papers, Krumholz & McKee (2005); Krumholz et al. (2008, 2009a,b); McKee & Krumholz (2010) developed a model for the star formation law from first principles. They assume that star formation is directly coupled to the molecular gas which resides exclusively in GMCs and the SFR per total gas is controlled by three factors: (1) The fraction of gas that is in the molecular phase determined by the balance between H₂ formation and dissociation which itself depends on gas density, metal abundance, and the ambient radiation field. (2) GMCs are virialized and supersonically turbulent which renders the SFE per free-fall time low. (3) GMCs are decoupled from the surrounding ISM as long as the ambient pressure is low.

In detail, they consider a spherical cloud of atomic and molecular gas mixed with dust in an ambient radiation field with photons in the Lyman-Werner band². They then model the balance between H₂ dissociation (from a radiative transfer calculation) and H₂ formation (from chemistry). For an idealized cloud where the transition from a fully molecular core to a fully atomic envelope happens in a thin shell, they find that the total H₂ fraction depends only on two dimensional parameters: χ , the radiation field strength normalized by the gas density, and τ_{R} , a measure of the dust optical depth of a cloud. They further assume that gas density in the shielding envelope is set by pressure balance in a two-phase atomic ISM which makes $\chi \approx 1$ and only weakly dependent on metallicity. From that follows that the atomic envelopes have a characteristic visual extinction $A_{\text{V}} \approx 0.2$ at solar metallicity and that the transition from atomic to molecular gas occurs at a characteristic shielding column of $\Sigma_{\text{HI}} \approx 10 M_{\odot} \text{ pc}^{-2}$ — varying inversely

² The Lyman-Werner band includes ultraviolet photons in the wavelength range 912 – 1120 Å that can excite electric-dipole transitions of H₂ from the ground state to the next two lowest singlet levels with projected total momentum quantum number unchanged (Lyman band) or changed (Werner band), both with a large number of sublevels. Higher energetic photons mostly ionize atomic hydrogen and are negligible for excitation of H₂.

with metallicity. The molecular fraction is defined by the following set of equation and depends to first order on the surface density of the atomic-molecular complex Σ_{comp} and to second order on metallicity Z ,

$$\begin{aligned}\chi &\approx 2.3 \frac{1 + 3.1(Z/Z_{\odot})^{0.365}}{3} \\ \psi &= \chi \frac{2.5 + \chi}{2.5 + \chi e} \\ s &= \frac{Z/Z_{\odot}}{\psi} \frac{\Sigma_{\text{comp}}}{1 \text{ M}_{\odot} \text{ pc}^{-2}} \\ R_{\text{H}_2} &\approx \left[1 + \left(\frac{s}{11} \right)^3 \left(\frac{125 + s}{96 + s} \right)^3 \right]^{-1/3} - 1\end{aligned}\quad (1.20)$$

The SFR is then given by the molecular gas surface density $f_{\text{H}_2} \Sigma_{\text{gas}}$ (Equation 1.11) and the proportionality constant, i.e., the SFE per free-fall time,

$$\frac{\epsilon_{\text{ff, GMC}}}{\tau_{\text{ff, GMC}}} = \frac{M_6^{-1/3}}{0.8 \text{ Gyr}} \max \left[1, \left(\frac{\Sigma_{\text{gas}}}{85 \text{ M}_{\odot} \text{ pc}^{-2}} \right)^{2/3} \right] \quad (1.21)$$

where M_6 is the cloud mass in units of $10^6 M_{\odot}$ estimated as $M_6 = 37 \Sigma_{\text{gas}} / (85 \text{ M}_{\odot} \text{ pc}^{-2})$ from the galaxy Jeans mass. This equation introduces a break into the SF relation at high surface densities. Where that large-scale averaged gas surface density Σ_{gas} is below the typical surface density of GMCs ($\sim 85 \text{ M}_{\odot} \text{ pc}^{-2}$), the clouds are decoupled from the ambient ISM, have uniform pressure, and form stars at a constant rate. If the galactic Σ_{gas} exceeds the surface density of a GMC, the cloud's pressure equals the galactic pressure leading to higher densities in the cloud and increased SFRs.

Comparison with observations is however complicated by two facts: (a) the finite spatial resolution of extragalactic observations, and (b) a warm atomic ISM not associated with the atomic-molecular complexes modeled here. The finite spatial resolution corresponds to measurements of the total gas surface density Σ_{obs} which are a lower limit on the surface density of the atomic-molecular complexes Σ_{comp} . The higher Σ_{comp} is and thus the ‘‘clumpiness’’ of the gas, the better it is able to shield itself against dissociating radiation. Therefore, a clumping factor c has to be introduced which links $\Sigma_{\text{comp}} = c \Sigma_{\text{obs}}$. The second concern arises that the warm atomic ISM between (and before/behind) individual atomic-molecular complexes is neglected which will introduce an overestimate of Σ_{comp} and hence of the H_2 fraction especially in low column density regions. Despite these limitations, the model performs well to predict the H I to H_2 transition as function of total gas and metallicity. They further confirm that their model follows the molecular fraction–pressure relation $R_{\text{H}_2} \propto P_{\text{h}}^{\gamma}$ found by Blitz & Rosolowsky (2004, 2006, see above) though they argue that surface density and metallicity are the physical variables that control the molecular fraction.

In Chapter 4 we test the model's predictions of the H I to H_2 transition as function of total gas surface density and metallicity against sensitive measurements in the disks of spiral galaxies ranging from the H_2 -dominated centers to the H I-dominated outskirts.

2 Data and Conversion Factors

2.1 Multi-Wavelength Surveys

In our attempt to learn about the SF Law we have to bring together as much information as possible about the properties and constituents of a large set of galaxies. We need to know about the constituents of the ISM — the neutral atomic and molecular ISM, the ionized ISM, and heavy elements (i.e., metals) in dust grains and the gas phase. We need to know about the stars in galaxies, ideally their detailed star formation history with an particular emphasise on stars that have just recently formed. We further need to know about the spatial distribution of these components and have an estimate about their dynamics. To accomplish this heroic goal, several large groups have coordinated their efforts within the last years to build the most comprehensive multi-wavelength database of nearby galaxies to date. This work would not have been possible without the tremendous work of these groups and I would like to acknowledge their efforts by presenting their key products — maps of multi-wavelength emission for all galaxies in the HERACLES survey and considered in this work can be found in the Appendix A.1.

In the following, I will highlight the multi-wavelength surveys which form the cornerstones of this work with an emphasis on the HERACLES survey in which I have been a key contributor and core member during my thesis years. Then I describe how we use them to estimate physical quantities such as SFRs and gas masses.

2.1.1 SINGS & LVL

The *Spitzer* Infrared Nearby Galaxies Survey (SINGS; Kennicutt et al., 2003a) and the Local Volume Legacy (LVL; e.g., Dale et al., 2009) are two Legacy programs which used the *Spitzer* Space Telescope¹ to obtain photometry and spectroscopy of the mid- and far-infrared continuum and line emission over large parts of many nearby galaxies. The SINGS survey includes 75 galaxies of all Hubble types within a distance of $D < 30$ Mpc. The LVL survey extended this sample by photometric observations of 258 galaxies within $D < 11$ Mpc. In this work we use photometric data taken with the MIPS instrument (Rieke et al., 2004) in three broadband filters in far-infrared wavelength range: centered at $24\mu\text{m}$, $70\mu\text{m}$, and $160\mu\text{m}$. The processing of the data is described in Gordon et al. (2005), the final data have point spread functions (PSFs) with full-width half maxima of $\sim 6''$, $18''$, and $40''$ at 24, 70, $160\mu\text{m}$, respectively. The MIPS PSF have a complex structure at low intensity levels, but we will mostly use the $24\mu\text{m}$ data at coarser ($13''$) resolution after convolving the PSF to Gaussian shape by special kernels. The sensitivity is $\sim 0.2 \text{ MJy sr}^{-1}$ at $24\mu\text{m}$ and $\sim 0.5 \text{ MJy sr}^{-1}$ at 70 and $160\mu\text{m}$, which is sufficient to

¹ <http://www.spitzer.caltech.edu/>

detect IR emission in all bands at $\text{SNR} \gtrsim 3$ at $R \sim 1 R_{25}$. These maps represent the most sensitive IR photometric imaging data of such a large sample of galaxies today.

We furthermore use ancillary data obtained by the SINGS & LVL teams, in particular maps of $\text{H}\alpha$ emission (Kennicutt et al., 2008). These have been obtained at the KPNO 2.1 m and the CTIO 1.5 m telescopes and from an extensive literature compilation. Because the $\text{H}\alpha$ data have been taken with narrowband filters, they contain non-negligible flux from the neighboring $[\text{N II}]$ line and underlying stellar continuum. The continuum emission can be subtracted by scaling broadband R -band flux, the $[\text{N II}]/\text{H}\alpha$ ratio is estimated by scaling the B -band flux for a formula that has been calibrated in a subsample of spectroscopically observed galaxies. As a result, this processing makes the $\text{H}\alpha$ maps uncertain at fluxes $I_{\text{H}\alpha} \lesssim 10^6 \text{ erg s}^{-1} \text{ cm}^{-2} \text{ sr}^{-1}$ ($\approx 2.2 \cdot 10^{-4} \text{ MJy sr}^{-1}$) which encompasses radii $R \sim 0.5 - 1.5 R_{25}$.

2.1.2 GALEX NGS

The *GALEX* Nearby Galaxy Survey (NGS; Gil de Paz et al., 2007) is a comprehensive photometric imaging survey in the ultraviolet of 1034 nearby galaxies using the *Galaxy Evolution Explorer* (GALEX) satellite². Images have been taken with two broadband filters covering in the FUV a wavelength range of $\lambda = 1350 - 1750 \text{ \AA}$ with angular resolution of $\sim 4.5''$ and in the NUV for $\lambda = 1750 - 2750 \text{ \AA}$ with $\sim 5.6''$ resolution. The large (1.2° diameter) field-of-view and the high sensitivity make the *GALEX* satellite the instrument of choice to obtain UV maps for huge numbers of galaxies. The *GALEX* NGS survey provided these UV maps for most of the SINGS / LVL sample.

2.1.3 THINGS

The H I Nearby Galaxy Survey (THINGS; Walter et al., 2008) used the Very Large Array³ (VLA) to obtain 21cm observations of 34 nearby galaxies ($D = 2 - 15 \text{ Mpc}$) that are subsample to the SINGS sample. These data formed the first comprehensive set of 21cm data with high spectral (2.6 or 5.2 km s^{-1}) and high angular ($\sim 6''$) resolution for such a large sample of nearby galaxies. These data have sufficient sensitivity, $N_{\text{HI}} \sim 4 \times 10^{19} \text{ cm}^{-2}$ on scales of $30''$, to detect H I emission in the outer disks out to several optical radii.

Following up on this survey, the LITTLE THINGS survey⁴ (Local Irregulars That Trace Luminosity Extremes; Hunter et al. 2011, in prep.) with an emphasize on low mass galaxies has been initiated. This program also used the VLA to obtain 21cm data with similar high angular ($\sim 6''$) resolution as THINGS and spectral resolution of 1.3 or 2.6 km s^{-1} . As part of my PhD time I actively participated in the data reduction and quality assessment of the final data products (though their data are not used in the analysis presented here).

During the last years, the coverage of HERACLES galaxies with 21cm observations has further been increased by follow-up observations at the VLA (PI.: Adam Leroy) and an

²<http://www.galex.caltech.edu/>

³<http://www.vla.nrao.edu/>

⁴<http://www2.lowell.edu/users/dah/littlethings/>



Figure 2.1 IRAM 30m [Figure taken from IRAM webpage]

extensive compilation of data from the archive. These data do not reach the high spectral and angular resolution of THINGS and LITTLE THINGS. They have PSFs of $\sim 15 - 25''$ and spectral resolutions of $\sim 10 \text{ km s}^{-1}$ with about equal sensitivity. We thus have been able to construct an HI database of ~ 100 nearby galaxies.

2.1.4 HERACLES

The Heterodyne Receiver Array CO Line Extragalactic Survey (HERACLES; Leroy et al., 2009) is a survey of CO $J = 2 - 1$ in 48 nearby galaxies using the IRAM⁵ 30m telescope. This survey forms the heart of my thesis work, I have spent 10 weeks at the telescope to take a significant fraction of the data and was actively involved in reducing the data and testing possible improvements in the reduction process. In the following I will describe the setup of the survey, the observing strategy, and the essential steps of data reduction (partly outlined in Leroy et al. 2009).

IRAM 30m Telescope

The IRAM 30m telescope (see Figure 2.1) is one of today's largest single dish telescopes operating in the millimeter wavelength regime. It is located at an altitude of 2850 m on Pico Veleta in the Spanish Sierra Nevada. The telescope is equipped with several heterodyne receivers and a bolometer camera operating at 3, 2, 1, and 0.9 mm wavelength.

HERA Receiver

With the HERACLES survey we used the HERA receiver (Schuster et al., 2004) which is a heterodyne receiver array consisting of two arrays of 3×3 pixels. The two arrays have orthogonal polarization pointing at the same position on sky. HERA is equipped with a derotator that holds the array pattern fixed with respect to the source allowing homogeneous mapping. The receiver is tunable in the frequency range 215 – 272 GHz which is rich in molecular lines⁶ (e.g., ^{12}CO and its isotopologues, HCN, HCO^+ , CS, etc.).

⁵ <http://www.iram-institute.org/>

⁶ See also <http://www.splatalogue.net/>

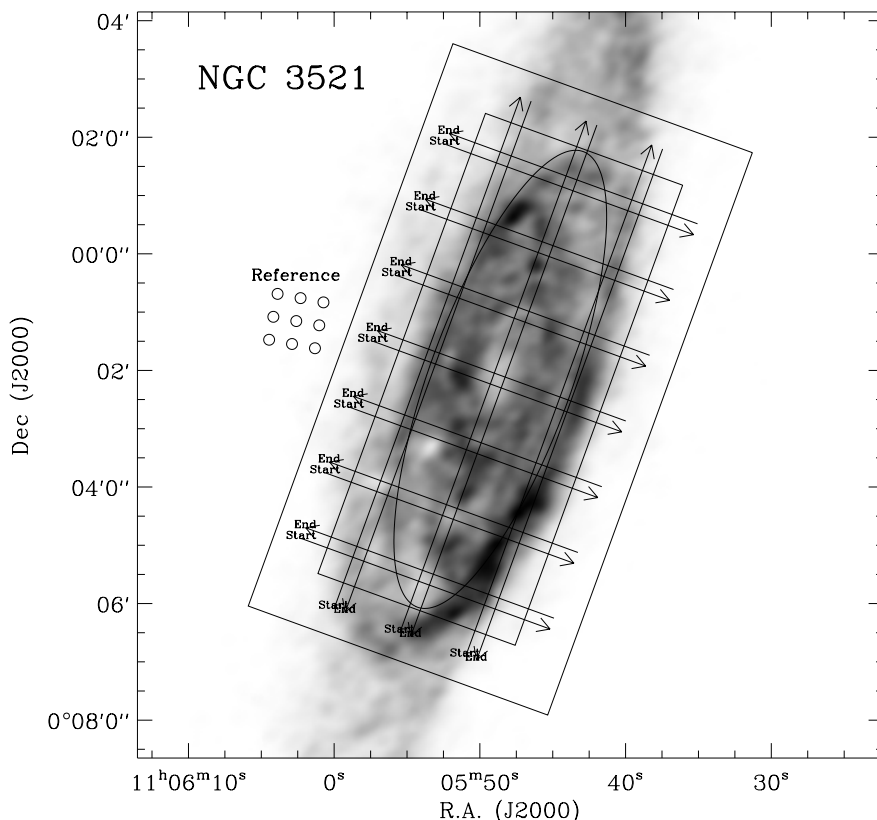


Figure 2.2 HERACLES observing strategy illustrated for NGC 3521. The grayscale image shows an HI column density map; the oval indicates R_{25} , the target area. Arrows indicate the length and orientation of individual scan legs which fully sample the area inside the inner rectangle. The beam print of HERA is shown at the reference position which is chosen to be free of gas but near the galaxy. [Figure taken from Leroy et al. 2009]

We tuned HERA to 230.538 GHz, the rest frequency of the $^{12}\text{CO } J = 2 - 1$ rotational line transition. At this frequency the 30m has a beam FWHM of $\sim 11''$. For signal processing, we used the Wideband Multiline Autocorrelator (WILMA) which can process the signal from all 18 pixel over a bandwidth of 930 MHz with 2 MHz wide channels. At 230 GHz this corresponds to a channel width of 2.6 km s^{-1} with total bandwidth of 1200 km s^{-1} .

Observing Strategy

The basic observing strategy of the HERACLES survey is to perform *on-the-fly* mapping, i.e., moving the HERA receiver array over the source and integrate and record the observed spectra during scanning. The observations are executed along scan legs which are offset parallel to each other to cover the whole galaxy. The observations are repeated in orthogonal direction to reduce artifacts in the final data. Figure 2.2 shows our observing strategy.

Calibration (and some Basics of Radio Astronomy)

Intensities in radio astronomy are often expressed in temperature units. For that one assumes (pretends) that the source emits radiation with intensity I_ν according to a black body with (brightness) temperature T_B . The intensity is then given by Planck's law. In radio (and millimeter) astronomy, frequencies are low such that I_ν can be approximated by the Rayleigh-Jeans formula,

$$I_\nu = B_\nu(T_B) \approx \frac{2kT_B}{\lambda^2} \quad (2.1)$$

The power measured by the telescope is however not only due to the source but includes power from several (noise) sources and the measured output is the system temperature

$$T_{\text{sys}} = T_{\text{rec}} + T_{\text{scat}} + T_{\text{atm}} + T_{\text{cmb}} + T_A \quad (2.2)$$

where T_{rec} is receiver temperature, T_{scat} accounts for emission scattered from the ground into the beam path / receiver, T_{atm} is the temperature of the atmosphere, T_{cmb} is the temperature of the Cosmic Microwave Background, and finally T_A is the antenna temperature (closely related to the source brightness T_B).

Unfortunately, the astronomical source signal T_A contributes the smallest (i.e., a tiny) fraction to the measured T_{sys} . The typical observing strategy is to make repeated *On-Off* observations by switching between the sky position of the source and a nearby reference position assumed to be free of astronomical signal. The astronomical signal is then in the difference *On-Off*, though buried under lots of noise which has to be reduced by long integration times. To set an absolute temperature scale, observations are repeatedly switched by a ‘‘chopper wheel’’ between sky observations (the *On*'s and *Off*'s) and an internal *Hot* load. The brightness temperature of the source (filling the entire 2π steradians of the forward beam pattern) is then

$$T_A^* = T_{\text{cal}} \frac{\text{On} - \text{Off}}{\text{Hot} - \text{Off}} \quad (2.3)$$

where T_{cal} is a calibration factor determined separately. T_A^* and T_A are connected by

$$F_{\text{eff}} T_A^* = T'_A = T_A e^{\tau A} \quad (2.4)$$

where F_{eff} ($= 0.91$) is the forward efficiency correcting for rearward losses, and the factor $\exp(\tau A)$ corrects for the atmospheric attenuation measured by a weather station. Finally, the brightness temperature T_{mb} of a source filling just the main beam is given by

$$T_{\text{mb}} = \frac{B_{\text{eff}}}{F_{\text{eff}}} T_A^* \quad (2.5)$$

where $B_{\text{eff}} = \Omega_{\text{mb}}/\Omega_{4\pi}$ ($= 0.58$) is the main beam efficiency. Under reasonable conditions (i.e., the source extend is not much smaller than the beam size) T_{mb} is a good approximate of the source brightness T_B . The remainder of the text, we work in units of T_{mb} .

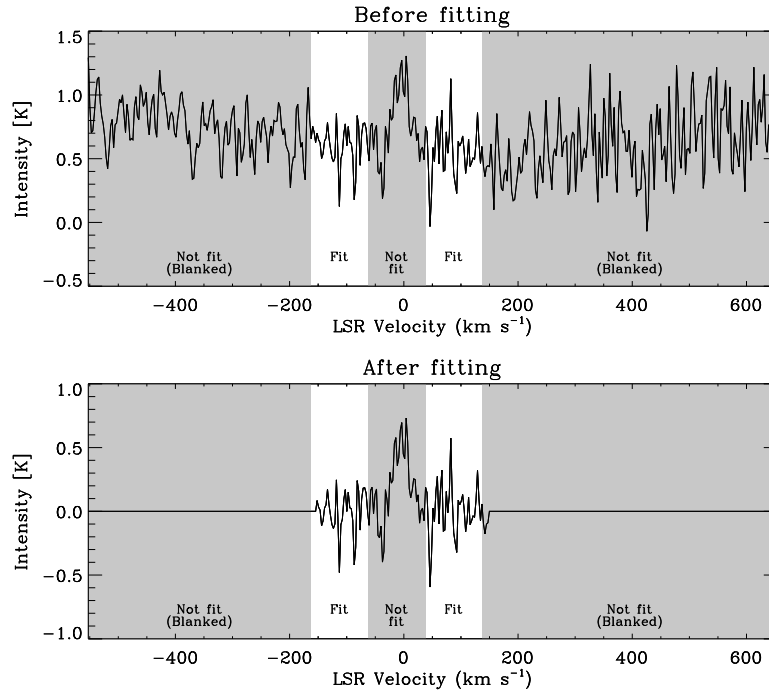


Figure 2.3 Our approach to fit baselines is to define two fitting windows close to the local CO line velocity which we estimate from HI data. We then fit and subtract a linear function from the observed spectrum. [Figure taken from Leroy et al. 2009]

Baseline Fitting

The observed spectra, which are calibrated as described above, can will show variations in the total power and/or non-linear variations over the bandpass due to receiver and/or atmospheric instabilities. These need to be adjusted before construction of the final data cube. Figure 2.3 shows an example of our baseline fitting approach. The upper spectrum shows the calibrated spectrum before baseline fitting. We define two fitting windows which are positioned close to the local HI systemic velocity (which assumes that HI and CO align at the same velocity; see Section 4.5 where we verify this assumption) and fit and subtract linear function from the original spectrum.

Constructing the Final Data Cube

Finally we have to average the individual spectra taken at irregular positions into a data cube which we choose to have $2''$ pixel size and 2.6 km s^{-1} channel width. For each pixel we perform a weighted average where the weight is defined by a “gridding kernel” of $7''$ FWHM yielding a final resolution of $13''$. In the final data cube an individual resolution element contains $\sim 2 - 3$ min of on-source integration time. The average noise level of all galaxies is $\sigma_{\text{rms}} = 23 \text{ mK}$ per channel and 68% of all galaxies have σ_{rms} within $19 - 27 \text{ mK}$.

Constructing Velocity-Integrated Maps

We determine velocity-integrated (moment 0) maps by integrating the cube inside a given (3D) mask region. The mask is the sum of three individual masks: (1) a mask containing regions with significant emission over a narrow range of consecutive channels, (2) a mask containing regions within a galaxy-adjusted velocity window (at least $\pm 25 \text{ km s}^{-1}$) around the local H I mean velocity, (3) a mask containing regions of significant emission as found in data from the literature. The resulting moment 0 maps for the HERACLES galaxies are shown in the upper right panels of Figure A.1. This presents a complete presentation of the HERACLES data as compared to the subsample presented in Leroy et al. (2009). For a given galaxy, the combined mask contains at different positions varying numbers of channels which makes the uncertainty in the velocity-integrated intensities position dependent. Typical (1σ) uncertainties are $I_{1\sigma} \sim 0.5 \text{ K km s}^{-1}$ which translates to an uncertainty in the H₂ surface density of $\Sigma_{\text{H}_2, 1\sigma} \sim 2.2 \text{ M}_\odot \text{ pc}^{-2}$ for a galaxy with 45° inclination (see Section 2.2.2 for details on the conversion factor).

2.2 Estimate of SFRs and Gas Masses

In the section I summarize how (physical) quantities like gas mass or SFR rates have been derived from observed intensities and how these conversion factors are constrained.

2.2.1 Star Formation Rates

Individual stars are unresolved in all but the closest galaxies. We therefore have to infer information on the young stellar population from integrated measurements of emission. This emission may stem directly from the photospheres of bright stars (UV continuum), or from recombination lines emitted in the ISM surrounding bright stars (H α , Pa α , etc.), or from dust processed star light (TIR luminosity or mid-IR intensities) — see Kennicutt (1998a) for a review of SFR tracers. All these tracers are stimulated by young and massive stars though with considerable spread in the lower mass and thus age limit. To determine the appropriate conversion factors to go from measured luminosities to stellar masses, composite spectra of (young) stellar populations have to be modeled using a library of stellar spectra and evolutionary tracks (e.g., Starburst99⁷) and by assuming a star formation history, initial mass function, and metallicity. The modeled spectra are then either convolved with the filter response of a telescope (e.g., UV continuum) or used as input for models of absorption and re-emission processes in the surrounding ISM (e.g., H α , Pa α). The use of indirect tracers of the star formation rate (e.g., IR dust emission) cannot be calculated precisely and hence often rely in empirical calibrations.

Unobscured Star Formation Tracer — H α and FUV

H α and FUV continuum emission are two often used SFR tracers. However, their emission is highly susceptible to dust attenuation and thus (without correction) H α and FUV trace

⁷ <http://www.stsci.edu/science/starburst99/>

only the “unobscured” SFR — the emission absorbed by dust is re-emitted in the IR and is referred to as “obscured” or “embedded” SFR.

The UV continuum is a direct tracer of stellar luminosity as it stems from photospheres of young massive OB stars. In “normal” galaxies, basically all continuum emission at short (UV & optical) wavelengths is stellar light. Toward shorter wavelengths the continuum spectrum becomes more and more dominated by the youngest stellar population, so that SFR is expected to scale linearly with luminosity. This favors the UV wavelength range at 1250–2500 Å but longward of the Ly α forest. These wavelengths cannot be observed from the ground for local galaxies ($z < 0.5$) but are fully accessible by the Hubble telescope or by the *GALEX* satellite. Fortunately, *GALEX* has observed a large number of nearby galaxies, and we frequently use its FUV maps to estimate the SFR.

Throughout this work, we use the conversion factor between (unobscured) SFR and FUV emission derived by Salim et al. (2007),

$$\Sigma_{\text{SFR}} [\text{M}_{\odot} \text{ yr}^{-1} \text{ kpc}^{-2}] = 8.1 \times 10^{-2} I_{\text{FUV}} [\text{MJy sr}^{-1}] . \quad (2.6)$$

This formula has been bootstrapped from SED-derived SFRs determined from SED modeling fitted to photometric data of 50,000 galaxies from *GALEX* and SDSS and assumes a Chabrier (2003) IMF. Most FUV emission is emitted by stars with mass $M > 5 M_{\odot}$ and age $t < 100$ Myr with the bulk of emission coming from stars with age $t < 20 - 30$ Myr (e.g., Salim et al., 2007).

H α emission and other nebular emission lines (e.g., H β , Pa α , Pa β , Br α , Pa γ) re-emit star light shortward of the Lyman limit ($\lambda \ll 912$ Å) inside H II regions surrounding star clusters containing OB stars, and thus are a sensitive probe of the most massive stars ($M > 10 M_{\odot}$) with lifetimes < 30 Myr and most emission associated only a few Myr old. For a given electron temperature (typically $T_e \sim 10,000$ K) and under the assumption that recombining hydrogen atoms have their electron cascading down to the second lowest energy level (i.e., case B recombination), the ionizing photon production can be directly inferred from the observed recombination line strengths. Limitations of this method are that ionizing radiation may leak from H II regions (as evident from the existence of a diffuse H α component containing $\sim 20 - 40\%$ of the total H α luminosity; e.g., Hoopes & Walterbos, 2000, 2003) or ionizing radiation absorbed by dust inside the H II region.

For the relation between SFR and H α we use the calibration from Calzetti et al. (2007),

$$\Sigma_{\text{SFR}} [\text{M}_{\odot} \text{ yr}^{-1} \text{ kpc}^{-2}] = 2.9 \times 10^{-2} I_{\text{H}\alpha} [\text{MJy sr}^{-1}] , \quad (2.7)$$

which is derived from population synthesis modeling and assumes continuous star formation over the past 100 Myr and the default Starburst99 IMF (from 2005).

Embedded Star Formation Tracer — 24 μm

The above SFR formulae predict only the total SFR if the tracer is not significantly attenuated by dust inside the studied galaxy — this is typically not the case. For dusty

galaxies the dominant fraction of emission leave the galaxy not in the UV-optical wavelength regime but in the IR. For these galaxies, the total IR luminosity make a good SFR tracer under the assumption that the total IR luminosity equals the bolometric luminosity emitted from the stellar population. Unfortunately, this method is limited to coarse spatial scales due to the limited angular resolution of current far-IR observatories.

Another approach to correct SFR tracers for dust attenuation has been proposed from the observation that mid-IR emission (e.g., at $\lambda \sim 24\mu\text{m}$ from ISO or *Spitzer*) coincides and scales with $\text{H}\alpha$ emission (Kennicutt et al., 2007; Calzetti et al., 2007) The attenuation-corrected SFR is then specified by a formula combining an “unobscured” SFR tracer (e.g., $\text{H}\alpha$) and an “embedded” SFR tracer (e.g., $24\mu\text{m}$ intensity). The appropriate factor to scale the embedded SFR tracer to account for the dust attenuation is difficult to calculate a priori and hence has to be determined empirically for each unobscured SFR tracer. This is done by adjusting a weight of the embedded SFR tracer such that the combined SFR formula matches a “reference” SFR (that are either little affected by extinction or where we hope to have a better understanding how to correct for extinction). The application of these formulae rely heavily on several assumptions: a reference SFR tracer (which may not exists), that the mid-IR emission is (predominantly) caused by the young stellar population, and that the calibration adjusted in a limited range of environments extends beyond those. Despite those limitations, these “hybrid” SFR formulae may provide a more robust estimate of the total SFR as derived from many other extinction corrections, and are nowadays frequently used in (nearby) galaxy studies.

For the combination of $\text{H}\alpha$ and $24\mu\text{m}$, we use the calibration by Calzetti et al. (2007),

$$\Sigma_{\text{SFR}} [\text{M}_{\odot} \text{ yr}^{-1} \text{ kpc}^{-2}] = (2.9 \times 10^{-2} I_{\text{H}\alpha} + 2.5 \times 10^{-3} I_{24\mu\text{m}}) [\text{MJy sr}^{-1}] , \quad (2.8)$$

which has been calibrated against SFRs derived from $\text{Pa}\alpha$ emission. For the combination of FUV and $24\mu\text{m}$, we use the calibration by Leroy et al. (2008),

$$\Sigma_{\text{SFR}} [\text{M}_{\odot} \text{ yr}^{-1} \text{ kpc}^{-2}] = (8.1 \times 10^{-2} I_{\text{FUV}} + 3.2 \times 10^{-3} I_{24\mu\text{m}}) [\text{MJy sr}^{-1}] , \quad (2.9)$$

which has been calibrated against the SFR from FUV+ $24\mu\text{m}$ using the above calibration. Note that the weighting of the IR term is a factor 1.3 higher for FUV+ $24\mu\text{m}$ than for $\text{H}\alpha$ + $24\mu\text{m}$ which accounts for the increased dust attenuation toward shorter wavelengths. There is however another subtle difference in the two above SFR combinations. While $I_{\text{H}\alpha}$ and $I_{24\mu\text{m}}$ scale roughly linearly over a wide range of luminosities (corresponding to $\Sigma_{\text{SFR}} \approx 0.001 - 0.1 \text{ M}_{\odot} \text{ pc}^{-2}$; see A. Leroy et al. 2011, submitted), the ratio between I_{FUV} and $I_{24\mu\text{m}}$ changes more gradually with luminosity or Σ_{SFR} making it a real hybrid combination where the two components operate in distinct regimes — typically $24\mu\text{m}$ in the inner and FUV in the outer disk of galaxies.

2.2.2 Gas Masses

Atomic Gas

The neutral atomic (H I) hydrogen can be traced by its 21cm hyperfine structure transition ($f = 1.420$ GHz or $\lambda = 21.11$ cm). Though this transition is strongly forbidden, it is relevant due to the large column densities of H I ($N_{\text{HI}} \lesssim 10^{22}$ cm $^{-2}$) and the fact that the first electronically excited level of H I requires an energy of 10 eV and is not metastable. In the optically thin case, the line intensity I_{HI} does not depend on the kinetic temperature of the gas (as the hydrogen atoms are in collisional equilibrium; this makes the same formula applicable to both the warm and cold atomic phase) and I_{HI} is linearly related to N_{HI}

$$N_{\text{HI}} [\text{cm}^{-2}] = 1.823 \times 10^{18} I_{\text{HI}} [\text{K km s}^{-1}] . \quad (2.10)$$

Expressed in units of solar masses and including a factor 1.36 to account for heavy elements, this is equivalent to

$$\Sigma_{\text{HI}} [M_{\odot} \text{ pc}^{-2}] = 0.02 I_{\text{HI}} [\text{K km s}^{-1}] . \quad (2.11)$$

In case of significantly self absorption we could underestimate the true H I column density. Averaged over a statistical sample of galaxies, Zwaan et al. (1997) determined the flux correction due to self absorption to be on average $\sim 10\%$. Braun et al. (2009) studied the amount of self absorption in great detail in the strongly inclined Andromeda galaxy ($i = 78^\circ$) and determined the global opacity correction to be $\sim 30\%$. Because most of our galaxies are seen at much lower inclination, we do not attempt to correct for optical depth effects.

Molecular Gas

The molecular mass is more difficult to measure. Molecular (H_2) hydrogen is a symmetric molecule and has no permanent electric dipole moment which makes rotational and vibrational transitions extremely weak. The lowest ro-vibrational transitions require energies in the IR wavelength regime ($T \gtrsim 1000$ K) that cannot be excited in GMCs ($T \sim 10$ K and $n \gtrsim 100$ cm $^{-3}$) in which most of the molecular gas resides. Therefore, observations of the second most abundant molecule, CO, are used to infer molecular gas masses. The lowest rotational transitions $^{12}\text{CO } J = 1 \rightarrow 0$ ($f = 115.271$ GHz, $\lambda = 2.6$ mm, and $h\nu/k = 5.5$ K) and $^{12}\text{CO } J = 2 \rightarrow 1$ ($f = 230.538$ GHz, $\lambda = 1.3$ mm, and $h\nu/k = 16.6$ K) have a critical density of $n_{\text{crit}} \sim 2 \times 10^3$ cm $^{-3}$ and are thus easily excited in GMCs. Luckily, these CO transitions have frequencies not (strongly) overlapping with water lines which makes them accessible from the ground. Complicating is however that the low- J transitions of ^{12}CO are optically thick in dense environments (e.g., GMCs) and the conversion between integrated intensity and abundance / mass has to be calibrated empirically. The integrated CO intensity, $I_{\text{CO},n \rightarrow n-1}$, for the transition $J = n \rightarrow n - 1$ is related to the H_2 mass surface density by

$$\frac{\Sigma_{\text{H}_2}}{1 \text{ M}_\odot \text{ pc}^{-2}} = 4.4 \left(\frac{X_{\text{CO},1\rightarrow0}}{2.0 \times 10^{20} \text{ cm}^{-2} (\text{K km s}^{-1})^{-1}} \right) \left(\frac{I_{\text{CO},1\rightarrow0}}{I_{\text{CO},n\rightarrow n-1}} \right) \left(\frac{I_{\text{CO},n\rightarrow n-1}}{1 \text{ K km s}^{-1}} \right) \quad (2.12)$$

where $X_{\text{CO},1\rightarrow0}$ (or just X_{CO}) is the CO-to-H₂ conversion factor and $I_{\text{CO},1\rightarrow0}/I_{\text{CO},n\rightarrow n-1}$ is the ratio between the intensities of different rotational transitions. Both factors have to be adjusted for the specific environment studied. Throughout this work, as we work with the HERACLES CO $J = 2 - 1$ data, we assume $I_{\text{CO},1\rightarrow0}/I_{\text{CO},2\rightarrow1} = 1.25$. For the CO-to-H₂ conversion factor we generally use $X_{\text{CO}} = 2.0 \times 10^{20} \text{ cm}^{-2} (\text{K km s}^{-1})^{-1}$. This value is in rough agreement between different studies fitting the diffuse γ -ray background (Strong & Mattox, 1996; Abdo et al., 2010), FIR-dust emission (Bloemen et al., 1990; Dame et al., 2001), and the virial mass of GMCs (Solomon et al., 1987; Heyer et al., 2009) for the Solar Neighborhood and has been shown to hold in nearby galaxies with environments similar to that of the Solar Neighborhood (e.g., Bolatto et al., 2008; Leroy et al., 2011). Despite our choice of a constant X_{CO} factor, we have to warn the reader that the X_{CO} factor is a strong (non-linear) function of, e.g., gas densities, radiation fields, and metallicities and significant variations are expected and in part measured in, e.g., low-metallicity dwarf galaxies and gas-rich starburst galaxies (e.g., Narayanan et al., 2011; Shetty et al., 2011a,b). We will come back to this topic in more detail in Chapter 5 where we study molecular gas in nearby dwarf galaxies and test new methods to constrain the X_{CO} factor from the star formation rate.

3 The Scale Dependence of the Molecular Gas Depletion Time in M33

3.1 Context

The observations presented in Chapter 1 have culminated in a star formation law with a “star-forming sequence” which is a surprisingly tight relation between SFR and gas mass. This relation holds both for global quantities as well as inside of galaxies on \sim kpc scales with only a factor $\sim 2 - 3$ scatter suggesting a close-to one-to-one relationship in the distribution of gas and stars. Observations in the Milky Way however show that the distribution of gas and recently formed stars is far away from being identical. Actually the radiation and momentum feedback of young massive stars make a very hostile environment for their parent cloud and finally dissipates them. This evolution of molecular clouds and massive stars is most evident in our Galaxy but should also show up in the SF law observed in other galaxies, namely by increasing the scatter in the ratio of SFR and gas mass if one considers subsequently smaller spatial scales. This scatter should be large on small scales but average out on large scales once many individual star-forming regions are included. In this Chapter, we study the scale dependence of the scatter in the SF law in the Local Group galaxy M33, which holds the prospect to link Galactic and extragalactic studies: Here, sufficient resolution can be reached to isolate individual molecular clouds and young stars (traced here by H II regions) and at the same time offers the view on the global relationship.

3.2 Abstract¹

We study the Local Group spiral galaxy M33 to investigate how the observed scaling between the (kpc-averaged) surface density of molecular gas (Σ_{H_2}) and recent star formation rate (Σ_{SFR}) relates to individual star-forming regions. To do this, we measure the ratio of CO emission to extinction-corrected H α emission in apertures of varying sizes centered both on peaks of CO and H α emission. We parameterize this ratio as a molecular gas (H $_2$) depletion time (τ_{dep}). On large (kpc) scales, our results are consistent with a molecular star formation law ($\Sigma_{\text{SFR}} \sim \Sigma_{\text{H}_2}^b$) with $b \sim 1.1 - 1.5$ and a median $\tau_{\text{dep}} \sim 1$ Gyr, with no dependence on type of region targeted. Below these scales, τ_{dep} is a strong function of

¹ This Chapter has been published as: Schrubba, A., Leroy, A. K., Walter, F., Sandstrom, K., Rosolowsky, E., 2010, ApJ, 722, 1699

adopted angular scale and the type of region that is targeted. Small ($\lesssim 300$ pc) apertures centered on CO peaks have very long τ_{dep} (i.e., high CO-to-H α flux ratio) and small apertures targeted toward H α peaks have very short τ_{dep} . This implies that the star formation law observed on kpc scales breaks down once one reaches aperture sizes of $\lesssim 300$ pc. For our smallest apertures (75 pc), the difference in τ_{dep} between the two types of regions is more than one order of magnitude. This scale behavior emerges from averaging over star-forming regions with a wide range of CO-to-H α ratios with the natural consequence that the breakdown in the star formation law is a function of the surface density of the regions studied. We consider the evolution of individual regions the most likely driver for region-to-region differences in τ_{dep} (and thus the CO-to-H α ratio).

3.3 Introduction

The observed correlation between gas and star formation rate surface densities (the ‘star formation law’) is one of the most widely used scaling relations in extragalactic astronomy (e.g., Schmidt, 1959; Kennicutt, 1998b). However, its connection to the fundamental units of star formation, molecular clouds and young stellar clusters, remains poorly understood. On the one hand, averaged over substantial areas of a galaxy, the surface density of gas correlates well with the amount of recently formed stars (e.g., Kennicutt, 1998b). On the other hand, in the Milky Way giant molecular clouds (GMCs), the birthplace of most stars, and H II regions, the ionized ISM regions around (young) massive stars, are observed to be distinct objects. While they are often found near one another, the radiation fields, stellar winds, and ultimately supernovae make H II regions and young clusters hostile to their parent clouds on small (~ 10 pc) scales. Thus, while correlated on galactic scales, young stars and molecular gas are in fact anti-correlated on very small scales. The details of the transition between these two regimes remain largely unexplored (though see Evans et al., 2009).

Recent observations of nearby galaxies have identified a particularly tight correlation between the distributions of *molecular* gas (H $_2$) and recent star formation on \sim kpc scales (Murgia et al., 2002; Wong & Blitz, 2002; Kennicutt et al., 2007; Bigiel et al., 2008; Leroy et al., 2008; Wilson et al., 2008). While the exact details of the relation are still somewhat uncertain, in the disks of spiral galaxies the parametrization seems to be a power law, $\Sigma_{\text{SFR}} = a\Sigma_{\text{H}_2}^b$, with power law index $b \approx 1 - 1.7$ and coefficient a corresponding to H $_2$ depletion times of ~ 2 Gyr in normal spirals.

Both parts of this relation, the surface densities of H $_2$ and recent star formation, resolve into discrete objects: GMCs and H II regions, young associations, and clusters. In this paper, we investigate whether the \sim kpc H $_2$ -SFR relation is a property of these individual regions or a consequence of averaging over large portions of a galactic disk (and the accompanying range of evolutionary states and physical properties). To do so, we compare CO and extinction-corrected H α at high spatial resolution in the nearby spiral galaxy M33. We examine how the ratio of CO-to-H α changes as a function of region targeted and spatial scale. M33 is a natural target for this experiment: it has favorable orientation and is close enough that peaks in the CO and H α maps approximately correspond to individual massive GMCs (Rosolowsky et al., 2007) and H II regions (Hodge et al., 2002).

Perhaps not surprisingly, we find that the ratio of CO luminosity (a measure of the molecular gas mass) to extinction-corrected H α flux (a measure of the star formation rate) depends on the choice of aperture and spatial scale of the observations. After describing how we estimate H $_2$ masses and the recent star formation rate (Section 3.4) and outlining our methodology (Section 3.5), we show the dependence of the depletion times on spatial scale and region targeted (Section 3.6). Then we explore physical explanations for these results (Section 3.7).

3.4 Data

We require the distributions of H $_2$ and recently formed stars which we trace via CO emission and a combination of H α and IR emission, respectively.

3.4.1 Molecular Gas from CO Data

Star-forming clouds consist mainly of H $_2$, which cannot be directly observed under typical conditions. Instead, H $_2$ is usually traced via emission from the second most common molecule, CO. We follow this approach, estimating H $_2$ masses from the CO $J = 1 - 0$ data of Rosolowsky et al. (2007), which combines the BIMA (interferometric) data of Engargiola et al. (2003) and the FCRAO 14 m (single-dish) data of Heyer et al. (2004). The resolution of the merged data cube is $13'' \times 2.03 \text{ km s}^{-1}$ with a median 1σ noise of 240 mK ($\sim 2.1 M_\odot \text{ pc}^{-2}$ for our adopted X_{CO}). Rosolowsky et al. (2007) showed that this combined cube recovers the flux of the Heyer et al. (2004) FCRAO data.

We convert integrated CO intensities into molecular gas surface densities assuming $X_{\text{CO}} = 2.0 \times 10^{20} \text{ cm}^{-2} (\text{K km s}^{-1})^{-1}$. This is approximately the Milky Way conversion factor and agrees well with work on M33 by Rosolowsky et al. (2003). For this X_{CO} :

$$\Sigma_{\text{H}_2} [M_\odot \text{ pc}^{-2}] = 4.4 I_{\text{CO}} [\text{K km s}^{-1}] , \quad (3.1)$$

where I_{CO} is the integrated CO intensity over the line of sight and Σ_{H_2} is the mass surface density of molecular gas, including helium.

The data cover a wide bandpass, only a small portion of which contains the CO line. As a result, direct integration of the cube over all velocities produces an unnecessarily noisy map. Therefore, we “mask” the data, identifying the velocity range likely to contain the CO line along each line of sight. We integrate over all channels with $\pm 25 \text{ km s}^{-1}$ of the local mean HI velocity (using the data from Deul & van der Hulst, 1987). To ensure that this does not miss any significant emission, we also convolve the original CO cube to $30''$ resolution and then identify all regions above 3σ in 2 consecutive channels. Any region within or near such a region is also included in the mask. We blank all parts of the data cube that do not meet either criteria and then integrate along the velocity axis to produce an integrated CO intensity map. Figure 3.1 shows this map at full resolution (*middle left*) and smoothed to $\sim 45''$ resolution (*top left*) to increase the SNR and highlight extended emission. The noise in the integrated intensity map varies with position but typical 1σ values are $8 - 10 M_\odot \text{ pc}^{-2}$; the dynamic range (peak SNR) is ~ 20 . The 3σ mass sensitivity in an individual resolution element is $\sim 10^5 M_\odot$.

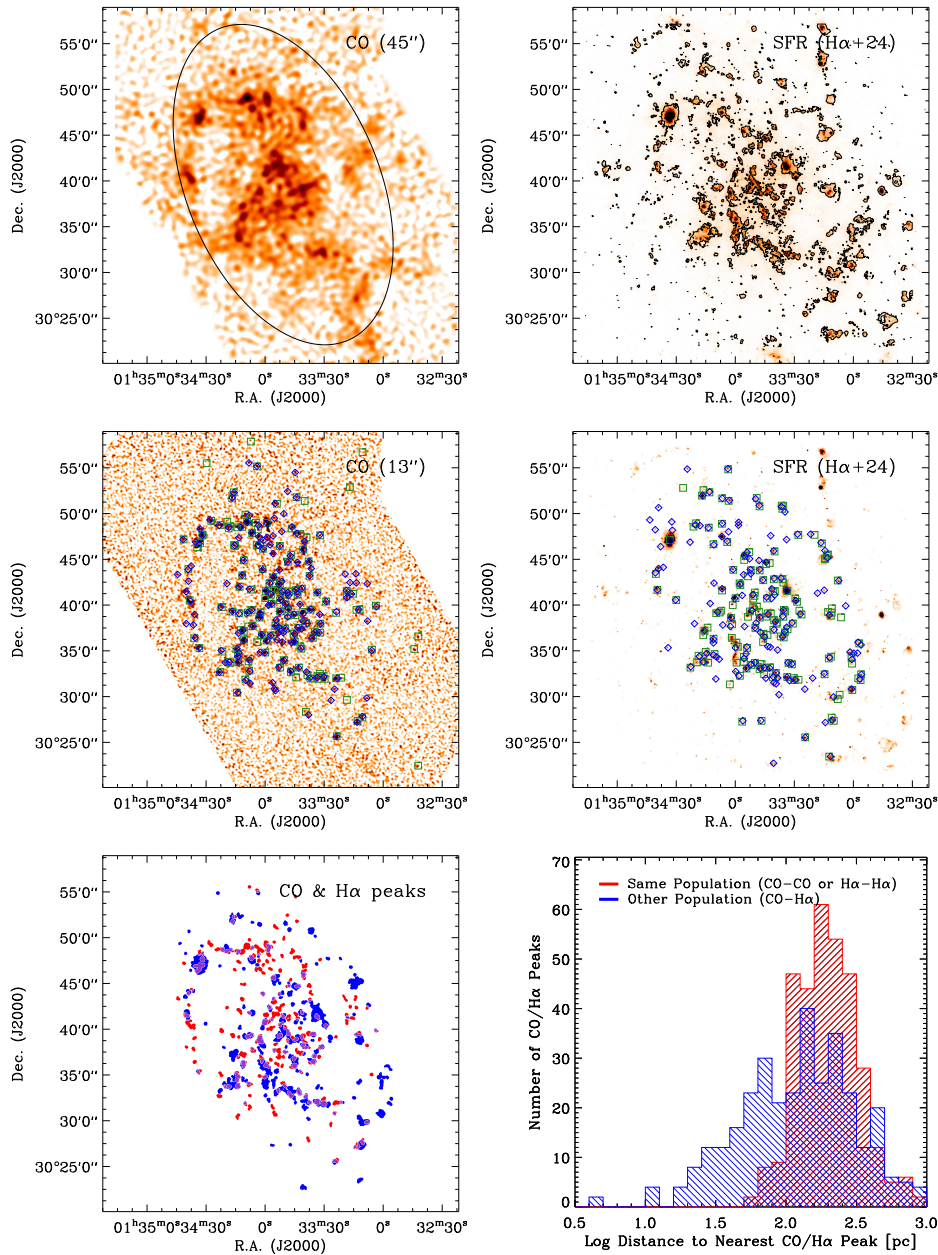


Figure 3.1 CO and recent star formation in M33. *Top left*: Masked, integrated CO intensity smoothed to $\sim 45''$ resolution to enhance the SNR. The black ellipse shows $R_{\text{gal}} = 4.5$ kpc ($\sim 0.6 r_{25}$); we carry out our analysis inside this radius. *Top right*: $\text{H}\alpha$ emission corrected for extinction via combination with mid-IR emission. A black contour outlines regions that remain after the subtraction of the diffuse ionized gas (see text). *Middle left*: Positions of our CO peaks (blue diamonds) plotted on the full resolution CO map along with the cataloged positions of GMCs from Rosolowsky et al. (2007, green squares). *Middle Right*: Positions of our $\text{H}\alpha$ peaks (blue diamonds) along with the 150 most luminous H II regions cataloged by Hodge et al. (2002, green squares). *Bottom left*: Relative distributions of bright CO (red) and $\text{H}\alpha$ (blue) emission and the area of overlap (purple), inflated by $6''$ for display reasons. *Bottom right*: Histograms of distance from each peak to the nearest peak of the same type (red, i.e., $\text{H}\alpha$ to $\text{H}\alpha$ or CO to CO) and of the other type (blue, CO to $\text{H}\alpha$ and vice versa).

3.4.2 Recent Star Formation from H α and IR Data

We trace the distribution of recent star formation using H α emission, which is driven by ionizing photons produced almost exclusively in very young (massive) stars. We account for extinction by combining H α and infrared (24 μ m) emission, a powerful technique demonstrated by Calzetti et al. (2007) and Kennicutt et al. (2007, 2009). Assuming continuous star formation over the past 100 Myr and studying a set of extragalactic star-forming regions, Calzetti et al. (2007) found the recent star formation rate (SFR) to be

$$\text{SFR} [\text{M}_{\odot} \text{ yr}^{-1}] = 5.3 \times 10^{-42} [L(\text{H}\alpha) + 0.031 L(24\mu\text{m})] , \quad (3.2)$$

where $L(\text{H}\alpha)$ and $L(24\mu\text{m}) = \nu L_{\nu}(24\mu\text{m})$ are the luminosities of a region in H α emission and at 24 μ m, measured in erg s^{-1} .

The assumption of continuous star formation is certainly inapplicable to individual regions, which are better described by instantaneous bursts (e.g., Relaño & Kennicutt, 2009). We only report averages of a large set (~ 150) of regions, which together constitute a large part of M33’s total H α , and argue that this justifies the application of Equation 3.2 (see Section 3.5.2). In any case SFR units allow ready comparison to previous work.

H α Data

We use the narrow-band H α image obtained by Greenawalt (1998) with the KPNO 0.6 m telescope. The reduction, continuum subtraction, and other details of these data are described by Hoopes & Walterbos (2000). Before combination with the IR map, we correct the H α map for Galactic extinction using a reddening of $E(\text{B}-\text{V}) = 0.042$ (Schlegel et al., 1998) and a ratio of H α narrow band extinction to reddening of $R(\text{H}\alpha) = 2.33$.

Studies of M33 and other nearby galaxies find typically $\sim 40\%$ of the H α emission to come from “diffuse ionized gas” (DIG, Hoopes & Walterbos, 2000; Thilker et al., 2002; Hoopes & Walterbos, 2003; Thilker et al., 2005). The origin of this emission is still debated; it may be powered by leaked photons from bright H II regions or it may arise “in situ” from isolated massive stars. We choose to remove this diffuse component from the H α map and any discussion of H α emission in the following analysis refers to this DIG-subtracted map (we assess the impact of this step in the Appendix). We do so using the following method from Greenawalt (1998). We begin by median filtering the H α map with a 900 pc kernel. We then identify H II regions as areas in the original map that exceed the median-filtered map by an emission measure of 50 pc cm^{-6} (outlined by black contours in the top right panel of Figure 3.1). We blank these regions in the original map and smooth to get an estimate of DIG emission towards the H II regions. Our working map consists of only emission from the H II regions after the DIG foreground has been subtracted. The integrated H α flux (inside $R_{\text{gal}} = 4.5 \text{ kpc}$) allocated to the diffuse map is $1.05 \times 10^{40} \text{ erg s}^{-1}$ (44%) while the part allocated to the DIG-subtracted, H II-region map is $1.35 \times 10^{40} \text{ erg s}^{-1}$ (56%), in good agreement with previous results on M33 and other nearby galaxies.

IR Data

We measure IR intensities from 24 μm maps obtained by the *Spitzer* Space Telescope (PI: Gehrz et al. 2005, see also Verley et al. 2007). The data were reduced by K. Gordon (2009, private communication) following Gordon et al. (2005). *Spitzer*'s point spread function at 24 μm is $\sim 6''$, well below our smallest aperture size ($\sim 18''$) and so is not a large concern.

As with the $\text{H}\alpha$ image, the 24 μm map includes a substantial fraction of diffuse emission — infrared cirrus heated by an older population, emission from low-mass star-forming regions, and dust heated leakage from nearby H II regions, with a minor contribution from photospheric emission of old stars. Verley et al. (2007) argue that this diffuse emission accounts for $\sim 2/3$ of all 24 μm emission in M33. To isolate 24 μm emission originating directly from H II regions, we follow a similar approach to that used to remove DIG from the $\text{H}\alpha$ map. The key difference is that instead of trying to identify all 24 μm bright sources by filtering and applying a cut-off to the 24 μm emission, we use the existing locations of H II regions to isolate any local 24 μm excess associated with H II regions. We extinction-correct the DIG-subtracted $\text{H}\alpha$ emission using only this local excess in 24 μm emission. The total integrated flux at 24 μm ($R_{\text{gal}} \leq 4.5$ kpc) is 3.92×10^{41} erg s $^{-1}$, the fraction of DIG-subtracted 24 μm inside the H II region mask is 1.63×10^{41} erg s $^{-1}$ (42%). The 24 μm correction implies $\text{H}\alpha$ extinctions of $A_{\text{H}\alpha} \sim 0.3 - 0.4$ magnitudes.

3.5 Methodology

To quantify the scale-dependence of the molecular star formation law, we measure the H_2 depletion time², $\tau_{\text{dep}} = \Sigma_{\text{H}_2} / \Sigma_{\text{SFR}}$, for apertures centered on bright CO and $\text{H}\alpha$ peaks. We treat the two types of peaks separately and vary the sizes of the apertures used. In this way we simulate a continuum of observations ranging from nearly an entire galaxy (> 1 kpc apertures) to studies of (almost) individual GMCs or H II regions (75 pc apertures). The CO data limit this analysis to galactocentric radius < 4.5 kpc ($\sim 0.6 r_{25}$).

3.5.1 Identifying CO and $\text{H}\alpha$ Peaks

We employ a simple algorithm to identify bright regions in the DIG-subtracted, extinction-corrected $\text{H}\alpha$ map and the integrated CO intensity map. This automated approach allows us to use the same technique on both maps to find peaks matched in scale to our smallest aperture (75 pc). It is also easily reproducible and extensible to other galaxies.

This algorithm operates as follows: We identify all contiguous regions above a certain intensity — the local 3σ in the CO map and $\sim 1.9 \times 10^{40}$ erg s $^{-1}$ kpc $^{-2}$ in the corrected $\text{H}\alpha$ map ($\sim 0.1 M_{\odot}$ yr $^{-1}$ kpc $^{-2}$ following Equation 3.2). We reject small regions (area less than ~ 110 arcsec 2 , which correspond to ~ 1800 pc 2 at the distance of M33) as potentially spurious; the remaining regions are expanded by $20''$ (~ 80 pc) in radius to include any low intensity envelopes. The positions on which we center our apertures are then the intensity-weighted average position of each distinct region.

² We emphasize that τ_{dep} maps directly to observables. It is proportional to the ratio of CO to extinction-correct $\text{H}\alpha$ emission.

Table 3.1. τ_{dep} as Function of Peak and Scale

Scale (pc)	Depletion Time (Gyr)		$\langle N \rangle^{\text{a}}$
	centered on CO	centered on H α	
1200	1.1 ± 0.1	0.9 ± 0.1	16.2
600	1.2 ± 0.3	1.0 ± 0.1	5.2
300	2.5 ± 0.5	0.64 ± 0.05	2.1
150	4.9 ± 0.9	0.41 ± 0.04	1.4
75	8.6 ± 2.1	0.25 ± 0.02	1.1

Note. — (a) Typical number of individual CO or H α peaks inside an aperture.

We find 172 CO regions and 154 H α regions. Strictly speaking, these are discrete, significant emission features at ~ 50 pc resolution. At this resolution, there is a close but not perfect match between these peaks and the real physical structures in the two maps — GMCs and H II regions. Figure 3.1 (*middle panels*) shows our peaks along with the cataloged positions of GMCs (Rosolowsky et al., 2007) and H II regions (Hodge et al., 2002). There is a good correspondence, with $> 80\%$ of the 149 known GMCs and the 150 brightest H II regions lying within $\sim 6''$ (3 pixels) of one of our regions.

3.5.2 Measuring Depletion Times

For a series of scales d , we center an aperture of diameter d on each CO and H α peak and then measure fluxes within that aperture to obtain a mass of H $_2$ (M_{H_2}) and a star formation rate (SFR). We then compute the median H $_2$ depletion time for the whole set of apertures. We do this for scales $d = 1200, 600, 300, 150$ and 75 pc and record results separately for apertures centered on CO and H α peaks.

At larger spatial scales, apertures centered on different peaks overlap (because the average spacing between CO and H α peaks is less than the aperture size). To account for this, we measure only a subset of apertures chosen so that at least 80% of the selected area belongs only to one aperture targeting a given peak type (CO or H α) at one time.

While we center on particular peaks, we integrate over all emission in our maps within the aperture. At the smallest scales we probe (75 pc), this emission will arise mostly — but not exclusively — from the target region. At progressively larger scales, we will integrate over an increasing number of other regions.

3.5.3 Uncertainties

We estimate the uncertainty in our measurements using a Monte-Carlo analysis. For the high-SNR H α and 24 μm maps, we add realistic noise maps to the observed “true” maps and repeat the identification and removal of DIG emission using smoothing kernels and

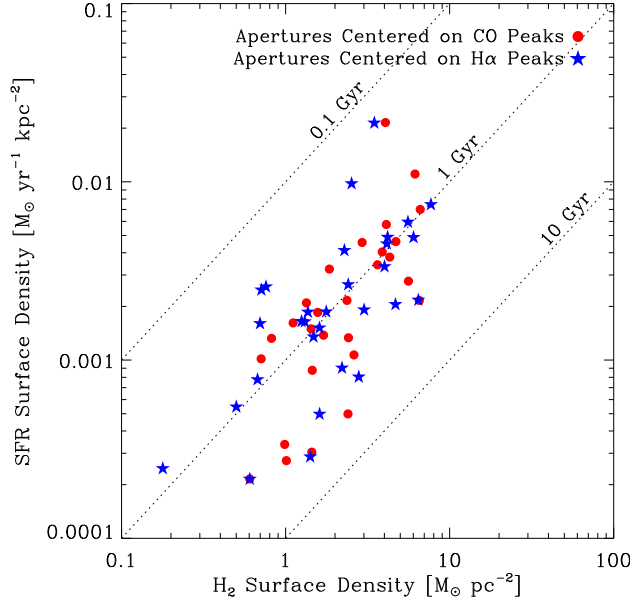


Figure 3.2 The relationship between SFR surface density (y -axis) and H_2 surface density (x -axis) at large spatial scales. Red points show measurements integrated over (one independent subset of) 1200 pc apertures centered on CO peaks. Blue points show similar measurements centered on $H\alpha$ peaks. Dashed lines indicate fixed H_2 depletion times ranging from 0.1 Gyr in the upper left to 10 Gyr in the lower right.

emission measure cuts perturbed from the values in Section 3.4.2 by $\pm 25\%$. The low SNR of the CO data requires a more complex analysis. We assume that all regions with surface densities above $10 M_\odot \text{ pc}^{-2}$ ($\sim 1.5 \sigma$) in the integrated CO map contain true signal. We generate a noise map correlated on the ($13''$) spatial scale of our CO data and scale this noise map according to the square root of the number of channels along each line of sight in our masked CO cube (typically 5–7). Then we add all emission from the pixels above $10 M_\odot \text{ pc}^{-2}$. Finally, we re-identify peaks in the new maps and re-measure M_{H_2} and SFR in each region. We repeat this process 100 times; the scatter in τ_{dep} across these repetitions is our uncertainty estimate.

3.6 Results

Figure 3.2 shows a well-known result for M33. There is a strong correlation (rank correlation coefficient of $r \approx 0.8$) between the surface densities of SFR and H_2 at 1200 pc scales. Power law fits to the different samples (types of peaks) and Monte Carlo iterations yield H_2 depletion times, $\tau_{\text{dep}} = M_{H_2}/\text{SFR}$, of ~ 1 Gyr (at H_2 surface densities of $3 M_\odot \text{ pc}^{-2}$) and power law indices of $\sim 1.1 - 1.5$. These results (modulo some renormalization due to different assumptions) match those of Heyer et al. (2004) and Verley et al. (2010) in their studies of the star formation law in M33. The important point here is that there is good evidence for an internal H_2 -SFR surface density relation in M33.

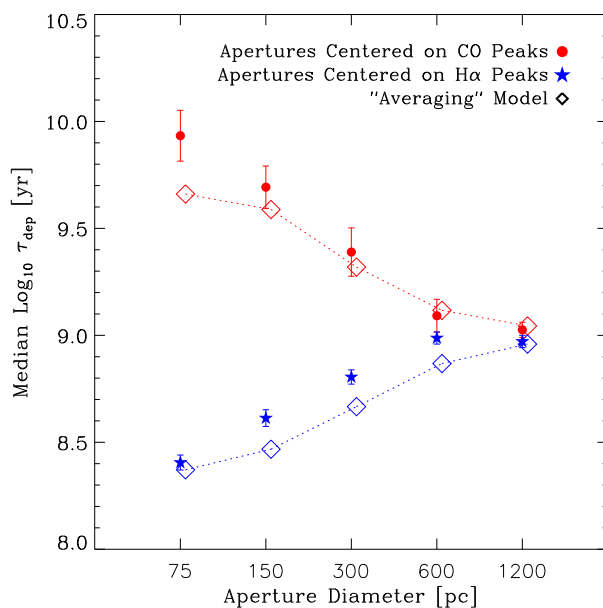


Figure 3.3 Scale dependence of the H_2 depletion time, τ_{dep} , in M33. The y -axis shows the logarithm of the median H_2 depletion time for apertures of different diameters (x -axis) centered on CO peaks (red) and $\text{H}\alpha$ peaks (blue). Error bars correspond to uncertainty in the median estimated via a Monte-Carlo analysis. Dashed lines show expectation for simply averaging together two populations of regions in different states (Section 3.7).

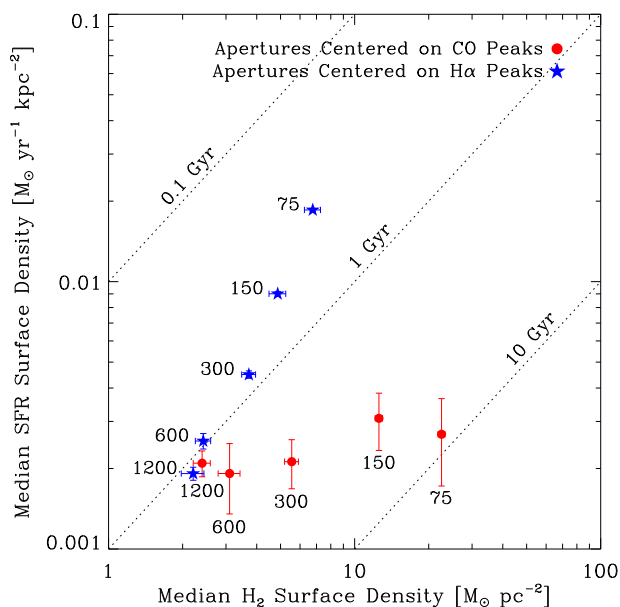


Figure 3.4 Scale dependence of the location of data in the star formation law parameter space. Red points show the median Σ_{SFR} (y -axis) and Σ_{H_2} (x -axis) for apertures centered on CO peaks. Blue stars show the same for apertures centered on $\text{H}\alpha$ peaks. Dashed lines as in Figure 3.2.

We plot the median τ_{dep} as a function of scale (aperture size) in Figure 3.3, giving results for apertures centered on CO (red circles) and H α (blue stars) peaks separately. For the largest scales, we find a similar τ_{dep} for both sets of apertures (as was evident from Figure 3.2). Going to smaller aperture sizes, τ_{dep} becomes a strong function of scale and type of peak targeted. Small apertures centered on CO peaks have very long τ_{dep} (up to 10 Gyr). Small apertures targeted toward H α peaks have very short τ_{dep} (0.3 Gyr). This may not be surprising, given the expectations that we outlined in Section 4.3 and the distinctness of the bright H α and CO distributions seen in the lower left panel of Figure 3.1, but the dramatic difference as one goes from \sim kpc to \sim 100 pc scales is nonetheless striking.

A few caveats apply to Figure 3.3. First, in subtracting the diffuse emission (DIG) from the H α map, we removed \sim 40% of the flux. This could easily include faint regions associated with CO peaks, which instead show up as zeros in our map. Perhaps more importantly, we use the 24 μm map *only* to correct the DIG-subtracted H α map for extinction. Any completely embedded star formation will therefore be missed. For both of these reasons, the SFR associated with the red points, while it represents our best guess, may be biased somewhat low and certainly reflects emission from relatively evolved regions — those regions that have H α fluxes above our DIG-cutoff value. There is no similar effect for the CO map.

Figure 3.3 implies that there is substantial movement of points in the star formation law parameter space as we zoom in to higher resolution on one set of peaks or another. Figure 3.4 shows this behavior, plotting the median Σ_{SFR} and median Σ_{H_2} for each set of apertures (N.B., the ratio of median Σ_{H_2} to median Σ_{SFR} does not have to be identical to the median τ_{dep} ; the difference is usually \lesssim 30%). We plot only medians because individual data are extremely uncertain, include many upper limits, and because we are primarily interested in the systematic effects of resolution on data in this parameter space.

Apertures centered on CO peaks (red points) have approximately constant Σ_{SFR} , regardless of resolution. This can be explained if emission in the H α map is homogeneously distributed as compared to the position of CO peaks. Meanwhile there is a strong change in Σ_{H_2} for decreasing aperture sizes on the same peaks; Σ_{H_2} goes up as the bright region fills more and more of the aperture. A similar effect can be seen for the H α (blue stars), though there is more evolution in Σ_{H_2} with increasing resolution because most bright H α regions also show some excess in CO emission.

3.7 Discussion

Figure 3.3 shows that by zooming in on an individual star-forming region, one loses the ability to recover the star formation law observed on large scales. For apertures \lesssim 300 pc in size, the relative amounts of CO emission and H α intensity vary systematically as a function of scale and what type of region one focuses on. Another simple way to put this, demonstrated in Figure 3.4, is that scatter orthogonal to the SFR-H $_2$ relation increases with increasing resolution. Eventually this washes out the scaling seen on large scales and the star formation law may be said to “break down”.

What is the origin of this scale dependence? In principle one can imagine at least six sources of scale dependence in the star formation law:

-
1. Statistical fluctuations due to noise in the maps.
 2. Feedback effects of stars on their parent clouds.
 3. Drift of young stars from their parent clouds.
 4. Region-to-region variations in the efficiency of star formation.
 5. Time-evolution of individual regions.
 6. Region-to-region variations in how observables map to physical quantities.

Our observations are unlikely to be driven by any of the first three effects. In principle, statistical fluctuations could drive the identification of H α and CO peaks leading to a signal similar to Figure 3.3 purely from noise. However, our Monte Carlo calculations, the overall SNR in the maps, and the match to previous region identifications make it clear that this is not the case.

Photoionization by young stars can produce CO shells around H II regions inside of a larger cloud or complex. This is a clear case of a small-scale offset between H α and CO. However, the physical scales in Figure 3.3 are too large for this effect to have much impact, it should occur on scales more like ~ 10 pc.

Similarly, the scales over which τ_{dep} diverges between CO and H α peaks (75–300 pc) are probably too large to be produced by drift between young stars and their parent cloud. A typical internal GMC velocity dispersion in M33 is a few km s $^{-1}$ (1σ ; Rosolowsky et al., 2003). Over an average cloud lifetime (~ 30 Myr; Blitz et al., 2007; Kawamura et al., 2009), this implies a drift of at most 100 pc. This extreme case is just large enough to register in our plot but unlikely to drive the signal we see at scales of 150 – 300 pc. See Engargiola et al. (2003) for a similar consideration of GMCs and H I filaments.

Instead of drifts or offsets, what we observe is simply a lack of direct correspondence between the CO and H α luminosities of individual star-forming regions. The brightest 150 CO peaks are simply not identical to the brightest 150 H α peaks. The bottom right panel of Figure 3.1 shows this clearly; about a third of the peaks in M33 are nearer to another peak of their own type (i.e., CO to CO or H α to H α) than to a peak of the other type. Thus Figure 3.3 shows that the ratio of CO to H α emission varies dramatically among star-forming regions. In this case the size scale on the x -axis in Figure 3.3 is actually a proxy for the number of regions inside the aperture. In M33, apertures of 75 pc diameter usually contain a single peak. At 150 pc, this is still the case $\sim 70\%$ of the time, and at 300 pc only a few regions are included in each aperture.

Why does the ratio of CO-to-H α vary so strongly from region-to-region? The efficiency with which gas form stars may vary systematically from region to region (with high H α peaks being high-efficiency regions), star-forming regions may undergo dramatic changes in their properties as they evolve (with H α peaks being evolved regions), or the mapping of observables to physical quantities (Equations 3.1 and 3.2) may vary from region to region.

It is difficult to rule out region-to-region efficiency variations, but there is also no strong evidence for them. Leroy et al. (2008) looked for systematic variations in τ_{dep} as a function

of a number of environmental factors and found little evidence for any systematic trends. Krumholz & McKee (2005); Krumholz & Tan (2007) suggested that the cloud free-fall time determines τ_{dep} to first order, but based on Rosolowsky et al. (2003), the dynamic range in free-fall times for M33 clouds is low. On the other hand, Gardan et al. (2007) found unusually low values of τ_{dep} in the outer disk of M33.

There is strong evidence for evolution of star-forming regions. Fukui et al. (1999), Blitz et al. (2007), Kawamura et al. (2009), and Chen et al. (2010) showed that in the LMC, the amount of H α and young stars associated with a GMC evolves significantly across its lifetime. In our opinion this is the most likely explanation for the behavior in Figure 3.3. Star-forming regions undergo a very strong evolution from quiescent cloud, to cloud being destroyed by H II region, to exposed cluster or association. When an aperture contains only a few regions, τ_{dep} for that aperture will be set by the evolutionary state of the regions inside it. That state will in turn determine whether the aperture is identified as a CO peak or an H α peak. CO peaks will preferentially select sites of heavily embedded or future star formation while H α peaks are relatively old regions that formed massive stars a few Myr ago.

Region-to-region variations in the mapping of observables (CO and H α) to physical quantities (H $_2$ mass and SFR) are expected. Let us assume for the moment that the ratio of H $_2$ to SFR is constant and independent of scale. Then to explain the strong scale dependence of the ratio of CO to H α in Figure 3.3 there would need to be much more H $_2$ per unit CO near H α peaks and many more recently formed stars per ionizing photon near the CO peaks. At least some of these effects have been claimed: e.g., Israel (1997) find a strong dependence of X_{CO} on radiation field and Verley et al. (2010) suggest that incomplete sampling of the IMF in regions with low SFRs drive the differences they observe between star formation tracers. However, both claims are controversial and it seems very contrived to invoke a scenario where only this effect drives the breakdown in Figure 3.3. It seems more plausible that the mapping of observables to physical quantities represents a secondary source of scatter correlated with the evolutionary state of a region (e.g., the age of the stellar population).

3.7.1 Comparison to a Simple Model

We argue that the behavior seen in Figures 3.3 and 3.4 comes from averaging together regions in different states. Here we implement a simple model to demonstrate that such an effect can reproduce the observed behavior.

The model is as follows: we consider a population of regions. We randomly assign each region to be an ‘‘H α peak’’ or a ‘‘CO peak’’ with equal chance of each. CO peaks have 5 times as much CO as H α and H α peaks have 5 times as much H α as CO (roughly driven by the difference between the results for 75 pc apertures in Table 3.1). Physically, the idea is simply to build a population of regions that is an equal mix ‘‘young’’ (high CO-to-H α) and ‘‘old’’ (low CO-to-H α). Dropping an aperture to contain only a young (CO peak) or old (H α peak) region will recover our results at 75 pc scales by construction. Next we average each of our original region with another, new region (again randomly determined to be either a CO or H α peak). We add the CO and H α emission of the two

region together, record the results. We then add a third region (again randomly young or old), and so on.

The result is a prediction for the ratio of CO to H α as a function of two quantities: 1) the number of regions added together and 2) the type of the first region (CO or H α peak). Using the average number of regions per aperture listed in Table 3.1 and normalizing to an average depletion time of 1 Gyr, we then have a prediction for τ_{dep} as a function of scale. This appears as the diamond symbols and dashed lines in Figure 3.3.

Given the simplicity of the model, the agreement between observations and model in Figure 3.3 is good. Our observations can apparently be explained largely as the result of averaging together star-forming regions in distinct evolutionary states. At scales where a single region dominates, the observed τ_{dep} is a function of the state of that region. As more regions are included, τ_{dep} just approaches the median value for the system.

3.7.2 τ_{dep} vs. Scale at Different Radii

The star formation law apparently breaks down (or at least includes a large amount of scatter) on scales where one resolution element corresponds to an individual star-forming region. The spatial resolution at which this occurs will vary from system to system according to the space density of star-forming regions in the system.

The surface densities of star formation and H $_2$ vary with radius in M33 (Heyer et al., 2004). This allows us to break the galaxy into two regions, a high surface density inner part ($r_{\text{gal}} = 0 - 2.2$ kpc) and a low surface density outer part ($r_{\text{gal}} = 2.2 - 4.5$ kpc). We measure the scale dependence of τ_{dep} for each region in the same way that we did for all data. An important caveat is that the DIG subtraction becomes problematic for the outer region, removing a number of apparently real but low-brightness H II regions from the map. We achieve the best results for large radii with the DIG subtraction is turned off and report those numbers here. The basic result of a larger-scale of divergence in the outer disk remains the same with the DIG subtraction on or off.

We find the expected result, that τ_{dep} for CO and H α peaks diverges at larger spatial scales in the outer disk than the inner disk. In both cases the ratio of τ_{dep} at CO peaks to τ_{dep} at H α peaks is ~ 1 for 1200 pc apertures. For 600 pc apertures that ratio remains ~ 1 in the inner disk but climbs to ~ 2 in the outer disk, suggesting that by this time there is already some breakdown in the SFR-H $_2$ relation. For 300 pc apertures, the same ratio is ~ 1.7 in the inner disk and ~ 3 in the outer disk. It thus appears that at large radii in M33 the star formation law breaks down on scales about twice that of the inner disk, though the need to treat the DIG inhomogeneously means that this comparison should not be overinterpreted.

3.8 Conclusions

Our main conclusion is that the molecular star formation law observed in M33 at large scales (e.g., Heyer et al., 2004; Verley et al., 2010) shows substantial scale dependence if one focuses on either CO or H α peaks. The median depletion time (or CO-to-H α ratio) measured in a 75 pc diameter aperture (derived from averaging ~ 150 such apertures)

varies by more than an order of magnitude between CO and H α peaks. At large (\sim kpc) scales this difference mostly vanishes. We argue that the scale for the breakdown is set by the spatial separation of high-mass star-forming regions, with the breakdown occurring when an aperture includes only a few such regions in specific evolutionary states (a scale that corresponds to \sim 300 pc in M33).

In this case the scaling relation between gas and star formation rate surface density observed at large scales does not have its direct origin in an instantaneous cloud-scale relation. Individual GMCs and H II regions will exhibit a CO-to-H α ratio that depends on their evolutionary state (likely with significant additional stochasticity) and as a result the \sim 150 brightest objects at a given wavelength will be a function of what evolutionary state that observation probes. This divergence is consistent with recent results from the LMC (Kawamura et al., 2009) indicating that individual GMCs exhibit a range of evolutionary states over their 20 – 30 Myr lifetime.

This does not mean that comparisons of tracers of recent and future star formation on small scales are useless. To the contrary, such observations contain critical information about the evolution of individual clouds as a function of time and location that is washed out at large scales (\gtrsim 300 pc in M33). However, once one moves into the regime where a single object contributes heavily to each measurement, it is critical to interpret the results in light of the evolution of individual clouds.

3.9 Appendix

Here we test how our method of selecting peaks and the removal of a diffuse ionized component affect our results.

First, we repeating the analysis on the original maps without any DIG subtraction. We show the results in the left panel of Figure 3.5, along with the original measurements (in gray) from Figure 3.3. To first order, the scale-dependence of τ_{dep} is unchanged, but the H $_2$ depletion are offset; τ_{dep} derived from maps with no DIG subtraction is a factor of \sim 2 smaller from the DIG-subtracted maps.

As a second test we assess the impact of the particular choice of aperture positions. In main text we used a peak-finding algorithm. Here we test the effect of using published positions of GMCs and H II regions instead. The right panel in Figure 3.5 shows our original data in gray while the red and blue points are τ_{dep} derived using the Rosolowsky et al. (2007) and Hodge et al. (2002) catalogs. The median τ_{dep} at large scale is unchanged from Figure 3.3 (gray values). However, for apertures centered on GMCs, τ_{dep} on small scales does change from our analysis. This difference originates in different numbers and locations of the positions that are studied. In our original analysis, we study 172 positions which have CO emission peaks above 3σ . The Rosolowsky catalog, on the other hand, consists of only 140 positions inside a galactocentric radius of 4.5 kpc. In addition, a subset of the two samples targets different regions in M33: First, the catalog positions tend to be more clustered than the “peak” positions which leads to a somewhat larger number (5 – 15%) of objects in the smaller apertures and a smaller deviation in depletion times for CO or H II centered apertures. Second, while the molecular gas surface densities at the positions of the two samples do not differ significantly, the star formation rate surface

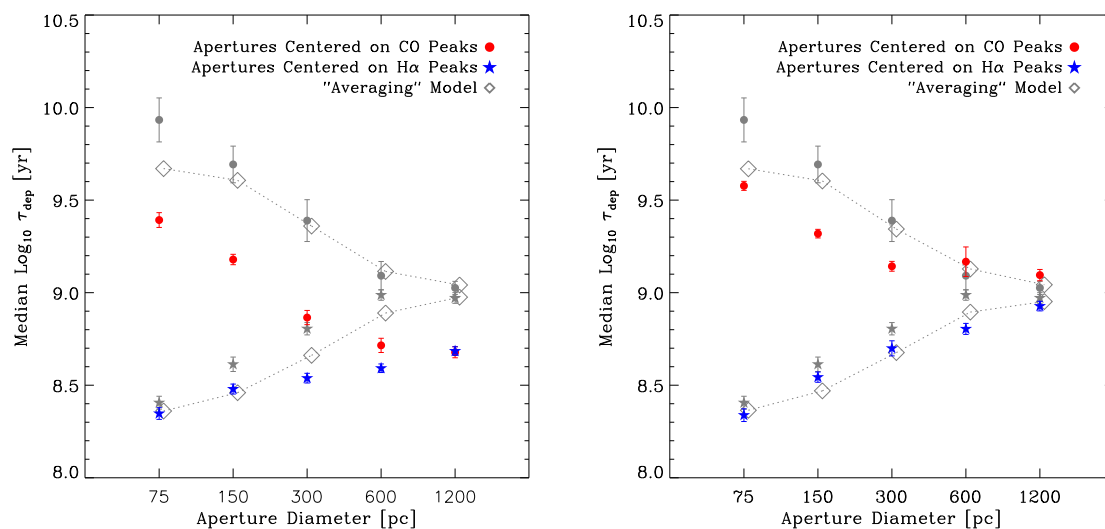


Figure 3.5 Tests of systematics. We repeat the measurement of τ_{dep} and remake Figure 3.3 varying our methodology. *Left:* Results if we perform no DIG-subtraction on the $\text{H}\alpha$ maps. *Right:* Results if we use the known positions of GMCs and H II regions from Rosolowsky et al. (2007) and Hodge et al. (2002). In both panels, our original results using the DIG-subtracted maps and an automated peak finder appear as gray points. Our qualitative conclusions are largely robust to these changes in methodology, though the overall normalization of CO-to- $\text{H}\alpha$ ratio does depend on the DIG subtraction.

densities are a factor of ~ 3 higher for the catalog positions as compared to the (more numerous) “peak” positions. This leads to shorter H_2 depletion times on small scales for the catalog sample.

Both tests show that the analyzed scale dependence of the star formation relation and the determination of its origin is not strongly dependent on the particular methodology chosen in this paper. While global shifts in the derived depletion times can arise due to the subtraction of diffuse $\text{H}\alpha$ emission, we find only small variations in the scale dependence due to different selection of positions where we perform our study.

It is a pleasure to thank my collaborators on this project:

Fabian Walter (MPIA), Adam K. Leroy (MPIA, NRAO), Karin Sandstrom (MPIA), and Erik Rosolowsky (University of British Columbia Okanagan)

We thank Mark Heyer and Edvige Corbelli for providing us the CO data, Rene Walterbos for the $\text{H}\alpha$ image, and Karl Gordon for the *Spitzer* images of M33. We acknowledge the use of the H II region catalog from Hodge et al.

4 A Molecular Star Formation Law in the Atomic Gas Dominated Regime in Nearby Galaxies

4.1 Context

The finding that the atomic and molecular gas phase do act fundamentally different in their relation with star formation rate with a “molecular relation” being approximately linear and basically a non-existence of a “atomic relation” (Bigiel et al., 2008; Leroy et al., 2008) has been a major step forward in our understanding of how gas is turned into stars. However, the limited sensitivity to determine the molecular gas mass enabled these two studies to analyze the molecular relation solely in the regime where the ISM is dominated by molecular gas. This leaves a crucial question unanswered, namely if the general observation of low star formation rates per total gas mass in the outer disks of spirals are an indication of a fundamentally different star formation process in the outer disks and/or atomic gas dominated regions or merely an indication of suppressed formation of “star-forming” molecular gas. To address this fundamental question, we constructed a comprehensive multi-wavelength dataset including all data from the just finished HERACLES CO survey and developed a novel machinery to stack spectra over large regions (e.g., radial annuli) and thus extract the most sensitive CO measurements across the disks of spirals galaxies to date. To discriminate the two scenarios, these measurements had to be sensitive enough to trace the molecular gas far into the atomic gas dominated outer disks. The following Chapter does describe our developed stacking method and presents results concerning the ISM phase balance and their individual role in the (separated and combined) star formation relation. This has been done here for the spiral galaxies in the HERACLES sample, i.e., the galaxies where we could robustly detect CO. The galaxies that remained undetected in this (radial) study, i.e., the dwarf galaxies, are targets of a more in depth search for CO emission in the following Chapter.

4.2 Abstract¹

We use the IRAM HERACLES survey to study CO emission from 33 nearby spiral galaxies down to very low intensities. Using 21-cm line atomic hydrogen (HI) data, mostly from

¹ This Chapter has been published as: Schruba, A, Leroy, A. K., Walter, F., Bigiel, F., Brinks, E., de Blok, W. J. G., Dumas, G., Kramer, C., Rosolowsky, E., Sandstrom, K., Schuster, K., Usero, A., Weiss, A., Wiese Meyer, H., 2011, AJ, 142, 37

THINGS, we predict the local mean CO velocity based on the mean HI velocity. By re-normalizing the CO velocity axis so that zero corresponds to the local mean HI velocity we are able to stack spectra coherently over large regions. This enables us to measure CO intensities with high significance as low as $I_{\text{CO}} \approx 0.3 \text{ K km s}^{-1}$ ($\Sigma_{\text{H}_2} \approx 1 \text{ M}_\odot \text{ pc}^{-2}$), an improvement of about one order of magnitude over previous studies. We detect CO out to galactocentric radii $r_{\text{gal}} \sim r_{25}$ and find the CO radial profile to follow a remarkably uniform exponential decline with scale length of $\sim 0.2 r_{25}$. Here we focus on stacking as a function of radius, comparing our sensitive CO profiles to matched profiles of HI, H α , FUV, and IR emission at $24 \mu\text{m}$ and $70 \mu\text{m}$. We observe a tight, roughly linear relationship between CO and IR intensity that does not show any notable break between regions that are dominated by molecular gas ($\Sigma_{\text{H}_2} > \Sigma_{\text{HI}}$) and those dominated by atomic gas ($\Sigma_{\text{H}_2} < \Sigma_{\text{HI}}$). We use combinations of FUV+ $24\mu\text{m}$ and H α + $24\mu\text{m}$ to estimate the recent star formation rate (SFR) surface density, Σ_{SFR} , and find approximately linear relations between Σ_{SFR} and Σ_{H_2} . We interpret this as evidence for stars forming in molecular gas with little dependence on the local total gas surface density. While galaxies display small internal variations in the SFR-to-H $_2$ ratio, we do observe systematic galaxy-to-galaxy variations. These galaxy-to-galaxy variations dominate the scatter in relationships between CO and SFR tracers measured at large scales. The variations have the sense that less massive galaxies exhibit larger ratios of SFR-to-CO than massive galaxies. Unlike the SFR-to-CO ratio, the balance between atomic and molecular gas depends strongly on the total gas surface density and galactocentric radius. It must also depend on additional parameters. Our results reinforce and extend to lower surface densities a picture in which star formation in galaxies is separable into two processes: the assembly of star-forming molecular clouds and the formation of stars from H $_2$. The interplay between these processes yields a total gas-SFR relation with a changing slope, which has previously been observed and identified as a star formation threshold.

4.3 Introduction

Stars form out of molecular (H $_2$) gas and many recent observations of nearby galaxies have revealed a strong correlation between the surface density of molecular gas, Σ_{H_2} , and the star formation rate (SFR) surface density, Σ_{SFR} (Wong & Blitz 2002; Kennicutt et al. 2007; Bigiel et al. 2008; Leroy et al. 2008; Wilson et al. 2008; Blanc et al. 2009; see also the recent review by Bigiel et al. 2011). These studies show a correlation over several orders of magnitude, but mostly for regions where H $_2$ makes up the majority of the neutral gas, $\Sigma_{\text{H}_2} \gtrsim \Sigma_{\text{HI}}$. The lack of a clear correlation between atomic gas (HI) surface density, Σ_{HI} , and Σ_{SFR} inside galaxy disks (e.g., Bigiel et al., 2008) offers circumstantial evidence that star formation remains coupled to the molecular, rather than total (HI+H $_2$), gas surface density even where HI makes up most of the interstellar medium (ISM). However, the exact relationship between Σ_{SFR} and Σ_{H_2} in the HI-dominated parts of galaxies ($\Sigma_{\text{H}_2} \lesssim \Sigma_{\text{HI}}$) remains largely unexplored.

In this paper we use new, sensitive, wide-field CO maps from the IRAM² HERACLES

² IRAM is supported by CNRS/INSU (France), the MPG (Germany) and the IGN (Spain).

survey (Leroy et al., 2009) to measure correlations between molecular gas and SFR tracers over a large dynamic range. By employing stacking techniques based on H I priors we extend our observations from H₂-dominated galaxy centers to the outer parts of galaxies where the H₂ surface density is much lower than the H I surface density, $\Sigma_{\text{H}_2} \ll \Sigma_{\text{H I}}$.

Deep CO measurements allow us to test if a single “star formation law” applies in both the H₂- and H I-dominated parts of galaxies. Following Schmidt (1959), astronomers have investigated scaling relations linking gas and star formation for decades. Such relations only approximate the complex physical processes involved in star formation but provide useful constraints on theoretical models and important input to simulations. After Kennicutt (1989, 1998b), power laws linking surface densities of gas and SFR are the most common formulation. However, the choice of which gas surface density to use — total or molecular gas — remains controversial, as does the extension of any measured molecular relation to low surface densities. The underlying question is what limits star formation in low column density regions, the formation of molecular gas or the efficiency at which the available molecular gas is converted into stars? Sensitive observations of molecular gas down to low surface densities in a large sample of galaxies are needed to address these questions.

Our CO measurements also allow us to investigate the distribution of molecular gas out to large radii. A characteristic exponential decline has been observed several times (Young et al., 1995; Regan et al., 2001; Leroy et al., 2009), but it is not known if this decline becomes sharper at one point, for example corresponding to claimed star formation thresholds (e.g., Martin & Kennicutt, 2001). We also test how variations in the H₂-to-H I ratio extend to low surface densities. This quantity is a strong and systematic function of environment in nearby galaxies (Wong & Blitz, 2002; Blitz & Rosolowsky, 2006; Leroy et al., 2008; Hitschfeld et al., 2009) but it has been difficult to extend the observed correlations to low surface densities.

In Section 4.4 we describe our sample and data. In Section 4.5 we present the method that we use to extract sensitive CO measurements. In Section 4.6 we present radial profiles of H I, CO, IR, FUV, and H α and use these to relate CO, H I, and tracers of recent star formation. In Section 4.7 we summarize our results.

4.4 Sample & Data

We study 33 nearby, star-forming disk galaxies, the set of HERACLES targets for which we could collect the necessary H I, IR, FUV, and H α data. This is mainly the overlap of several surveys: HERACLES (IRAM 30m CO, Leroy et al., 2009), THINGS (VLA H I, Walter et al., 2008), SINGS or LVL (*Spitzer* IR, Kennicutt et al., 2003a; Dale et al., 2009), and the GALEX NGS (GALEX FUV, Gil de Paz et al., 2007). We supplement these with a combination of archival and new H I data and archival GALEX data. We exclude low mass, low metallicity galaxies with only upper limits on CO emission and nearly edge-on galaxies.

Table 4.1 lists our sample along with adopted morphology, distance, inclination, position angle, optical radius, and metallicity. These values are taken from Walter et al. (2008) if possible and from LEDA and NED in other cases. We quote oxygen abun-

dances (metallicities) from Moustakas et al. (2010, Table 9), averaging the metallicities derived from a theoretical calibration (their KK04 values) and an empirical calibration (their PT05 values). For galaxies without a Moustakas et al. (2010) metallicity, we adopt a metallicity equal to the average of their B-band luminosity–metallicity relations. For NGC 2146 we quote the metallicity given by Engelbracht et al. (2008). For NGC 5457 (M 101) we take a constant metallicity defined by the value at $0.4 r_{25}$ from the gradient fit by Kennicutt et al. (2003b).

We trace molecular hydrogen (H_2) using CO(2→1) line emission observed with the IRAM 30m as part of the HERACLES survey (Leroy et al., 2009). They describe in detail the observations and reduction for the subset of galaxies observed until Summer 2008. The remaining targets were observed and reduced in the same way. The final data cubes have an angular resolution (FWHM) of $13''$ and a spectral resolution (channel separation) of 2.6 km s^{-1} .

Our measurements of atomic hydrogen (HI) come mostly from the THINGS survey (Walter et al., 2008), which used the Very Large Array (VLA) to observe the 21-cm hydrogen line in 34 nearby galaxies. The observing and reduction strategies are described therein. The final data cubes have an angular resolution of $\sim 11''$ (using natural weighting) and a spectral resolution of 2.6 or 5.2 km s^{-1} . THINGS is sensitive to $\Sigma_{\text{HI}} \approx 0.5 M_{\odot} \text{ pc}^{-2}$ on scales of $30''$. Using azimuthal averaging, we reach even better sensitivities at large radii. As a result, the HI sensitivity never limits our analysis.

The HI data for NGC 337, 2146, 2798, 3049, 3938, 4254, 4321, 4536, 4579, 4625, 4725, and 5713 are a combination of new and archival VLA data (the new data are from VLA programs AL731 and AL735). These have been reduced and imaged using the Common Astronomy Software Applications (CASA) following a similar protocol than the THINGS reduction. These supplemental HI cubes include only data from the VLA’s C and D configurations; THINGS also includes B configuration data. For NGC 4559 we take HI data observed with the Westerbork Synthesis Radio Telescope (WSRT) by van der Hulst (2002). The beam sizes (FWHM) of the supplemental HI are $15'' - 25''$ and the velocity resolution is $2.5 - 20 \text{ km s}^{-1}$, usually 10 km s^{-1} .

We derive HI surface densities from 21-cm line intensities and H_2 surface densities from CO(2→1) line intensities following

$$\Sigma_{\text{HI}} = 0.02 I_{\text{HI}} \times \cos i \quad (4.1)$$

$$\Sigma_{\text{H}_2} = 6.25 I_{\text{CO}} \times \cos i \quad (4.2)$$

where Σ_{HI} and Σ_{H_2} have units of $M_{\odot} \text{ pc}^{-2}$ and I_{HI} and I_{CO} are measured in K km s^{-1} . The mass surface densities are projected to face-on values and include a factor of 1.36 to account for heavy elements. For Equation (4.2) we have assumed a CO line ratio of $I_{\text{CO}(2\rightarrow 1)}/I_{\text{CO}(1\rightarrow 0)} = 0.7$ and a CO(1→0)–to– H_2 conversion factor $X_{\text{CO}} = 2.0 \times 10^{20} \text{ cm}^{-2} (\text{K km s}^{-1})^{-1}$ (see Leroy et al., 2009, and references therein).

We use broadband infrared (IR) photometry at $24 \mu\text{m}$ and $70 \mu\text{m}$ obtained by the *Spitzer* legacy surveys SINGS (Kennicutt et al., 2003b) and LVL (Dale et al., 2009). *Spitzer* has angular resolution $\sim 6''$ at $24 \mu\text{m}$ and $18''$ at $70 \mu\text{m}$. The sensitivity of these

Table 4.1. Properties of Galaxy Sample

Galaxy	Morph.	D Mpc	Incl. °	P.A. °	r_{25} '	Metal. ^c 12+logO/H
NGC337	SBd	24.7	51	90	1.48	8.51
NGC628 ^{a,b}	Sc	7.3	7	20	4.92	8.68
NGC925 ^{a,b}	SBcd	9.2	66	287	5.32	8.52
NGC2146	SBab	12.8	54	123	2.69	8.68 ^d
NGC2403 ^a	SBc	3.2	63	124	7.87	8.57
NGC2798 ^a	SBa	24.7	85	152	1.20	8.69
NGC2841 ^{a,b}	Sb	14.1	74	153	3.45	8.87
NGC2903 ^{a,b}	SBd	8.9	65	204	5.92	8.90
NGC2976 ^{a,b}	Sc	3.6	65	335	3.60	8.67
NGC3049	SBab	8.9	58	28	1.04	8.82
NGC3077 ^a	Sd	3.8	46	45	2.70	8.64
NGC3184 ^{a,b}	SBc	11.1	16	179	3.70	8.83
NGC3198 ^{a,b}	SBc	13.8	72	215	3.24	8.62
NGC3351 ^{a,b}	SBb	10.1	41	192	3.60	8.90
NGC3521 ^{a,b}	SBbc	10.7	73	340	4.16	8.70
NGC3627 ^a	SBb	9.3	62	173	5.14	8.67
NGC3938	Sc	12.2	14	15	1.77	8.74
NGC4214 ^{a,b}	Irr	2.9	44	65	3.40	8.25
NGC4254	Sc	20.0	32	55	2.51	8.79
NGC4321	SBbc	14.3	30	153	3.01	8.83
NGC4536	SBbc	14.5	59	299	3.54	8.61
NGC4559	SBcd	11.6	65	328	5.24	8.55
NGC4569	SBab	20.0	66	23	4.56	8.92
NGC4579	SBb	20.6	39	100	2.51	8.88
NGC4625	SBmp	9.5	47	330	0.69	8.70
NGC4725	SBab	9.3	54	36	4.89	8.73
NGC4736 ^{a,b}	Sab	4.7	41	296	3.87	8.66
NGC5055 ^{a,b}	Sbc	10.1	59	102	5.93	8.77
NGC5194 ^a	SBc	8.0	20	172	3.85	8.86
NGC5457 ^a	SBcd	7.4	18	39	11.99	8.46 ^e
NGC5713	Scd	26.5	48	11	1.23	8.64
NGC6946 ^{a,b}	SBc	5.9	33	243	5.70	8.72
NGC7331 ^{a,b}	Scd	14.7	76	168	4.59	8.68

Note. — (a) Targets of THINGS survey (Walter et al., 2008)
(b) Targets in first HERACLES survey paper (Leroy et al., 2009)
(c) Oxygen abundance from Moustakas et al. (2010)
(d) Oxygen abundance from Engelbracht et al. (2008)
(e) Oxygen abundance from Kennicutt et al. (2003b)

data is sufficient to obtain high signal-to-noise measurements when averaging in radial rings (see below) throughout the area that we study ($r_{\text{gal}} \lesssim 1.2 r_{25}$).

The GALEX NGS (Gil de Paz et al., 2007) imaged far- and near-ultraviolet (FUV and NUV) emission for most of our targets. The FUV band covers 1350 – 1750 Å with an angular resolution $\sim 4.5''$. We use these images to trace unobscured emission from young stars. For galaxies not covered by the NGS, we searched the NASA Multimission Archive at STScI and used the FUV image with the longest exposure time. These data also have sufficient sensitivity to determine FUV intensities with high signal-to-noise throughout the star-forming disk.

We draw H α data from the SINGS and LVL surveys, complemented by literature data for NGC 2903, 4214, 4569, 4736, and 5457. For the literature and several problematic SINGS targets, we pin the total H α + [N II] flux to published values, usually those of Kennicutt et al. (2008). Leroy et al. (2011, in prep.) describe the processing of the maps, which involves subtracting a smooth background, masking foreground stars following Muñoz-Mateos et al. (2009), correcting for [N II] contamination following Kennicutt et al. (2008), and correcting for Galactic extinction. The H α maps become uncertain, and likely biased low due to background subtraction, below intensities equivalent to Σ_{SFR} of a few times $10^{-4} M_{\odot} \text{ yr}^{-1} \text{ kpc}^{-2}$, values typically crossed inside the radial range studied here. This, and the declining H α -to-FUV flux ratios which are observed as *Galex* UV disks extending far beyond the H α emission (Thilker et al., 2007a; Meurer et al., 2009), limit the utility of the H α maps to trace star formation in the low brightness regions of outer galaxy disks.

After we examine correlations among observables, we will estimate the star formation rate surface density, Σ_{SFR} , from combinations of H α with 24 μm (Kennicutt et al., 2007) and FUV with 24 μm (Leroy et al., 2008). We adopt the H α +24 μm calibration by Calzetti et al. (2007) and the FUV+24 μm combination from Leroy et al. (2008),

$$\Sigma_{\text{SFR}(\text{H}\alpha+24)} = (2.9 \times 10^{-2} I_{\text{H}\alpha} + 2.5 \times 10^{-3} I_{24\mu\text{m}}) \times \cos i \quad (4.3)$$

$$\Sigma_{\text{SFR}(\text{FUV}+24)} = (8.1 \times 10^{-2} I_{\text{FUV}} + 3.2 \times 10^{-3} I_{24\mu\text{m}}) \times \cos i \quad (4.4)$$

where Σ_{SFR} has units of $M_{\odot} \text{ yr}^{-1} \text{ kpc}^{-2}$ and H α , FUV, and 24 μm intensities are all in MJy sr^{-1} . Both Σ_{SFR} calibrations combine a tracer of the unobscured star formation with infrared (24 μm) emission, which is intended to trace young starlight reprocessed by dust. H α traces O stars with ages $\lesssim 5$ Myrs (Kennicutt et al., 2009) with sensitivity out to ~ 10 Myr (Vacca et al., 1996). FUV traces O and B stars of typical age 20 – 30 Myrs with sensitivity out to ~ 100 Myr (Salim et al., 2007).

Our use of both H α +24 μm and FUV+24 μm emission gives some test of sensitivity to our choice of star formation rate tracer. Several other concerns are worth mentioning. Because dust properties and the stellar populations heating the dust somewhat differ between H II regions and large (kpc) regions in galaxies the appropriate weighting of the 24 μm emission to correct for extinction may be a function of scale and environment. The dust-to-gas ratio, dust size-distribution, ISM geometry, and recent star formation history may also play important roles. The Calzetti et al. (2007) calculation remains state of the art, but there is no definitive consensus about the correct calibration to use outside

bright regions that they study. The reliability of the H α imaging at low surface brightness also represents a concern. Ground based, narrowband H α imaging is challenging and the H α +24 μ m tracer must be considered unreliable where $\Sigma_{\text{SFR}(\text{H}\alpha)} \approx 5 \times 10^{-4} \text{ M}_{\odot} \text{ yr}^{-1} \text{ kpc}^{-2}$. The *Galex* and *Spitzer* maps are better behaved at low surface brightness.

Because of these data quality considerations and our focus on regions with low surface brightness, we emphasize comparisons to FUV+24 μ m. SFR(FUV+24) and SFR(H α +24) give comparable results with scatter of only 0.1 dex ($\sim 25\%$) down to $\Sigma_{\text{SFR}} \approx 5 \times 10^{-4} \text{ M}_{\odot} \text{ yr}^{-1} \text{ kpc}^{-2}$ in an azimuthally averaged ring. Our main method to address these other systematic concerns is to emphasize the observed scaling relations in the first part of the paper. For a more thorough discussion of hybrid SFR tracers see Kennicutt et al. (2009) and for a discussion of their application to gas–SFR comparisons, we refer the reader to Leroy et al. (2011, in prep.).

4.5 Methodology

Our goal is to recover low brightness CO emission from the outer parts of galaxies. CO is very faint in these regions and individual spectra have low signal-to-noise ratios (SNR), requiring us to average many spectra to achieve a detection. Because the velocity of CO emission varies with position, simply averaging spectra spreads the emission across many velocity channels with low SNR in each channel. In principle, this could still yield a high SNR measurement. In practice we wish to maximize SNR by considering only the part of each spectrum likely to contain emission. We must also contend with systematic effects of weather, receiver instabilities, and dish imperfections. These all induce frequency-dependent behavior (“baselines problems”) that make a clear detection of an emission line an important step in a robust analysis.

With these issues in mind, we use the following technique to average CO spectra across large parts of a galaxy. First, we estimate the local mean velocity of CO emission from the H I data. Using this mean velocity, we redefine the velocity axis of each CO spectrum so that the local mean velocity is now zero. We average these shifted CO spectra from across our target region. In the averaged spectra we expect the CO line to emerge at zero velocity with good SNR. The baseline problems described above will not average coherently, allowing a straightforward identification of the line.

This approach hinges on the assumption that the H I mean velocity is a good proxy for the mean velocity of the molecular gas. Figure 4.1 shows that this assumption holds where we detect CO over individual lines of sight, with median $\bar{v}_{\text{CO}} - \bar{v}_{\text{HI}}$ of -0.22 km s^{-1} and a 1σ dispersion of 7.0 km s^{-1} . We expect a similar correspondence in the outer, CO-faint parts of galaxies.

Leveraging H I to detect CO at large radii works because the H I surface densities are essentially constant out to large radii, making H I easily detected across galaxy disks. CO emission, on the other hand, tends to be bright in galaxy centers but declines rapidly with increasing galactocentric radius.

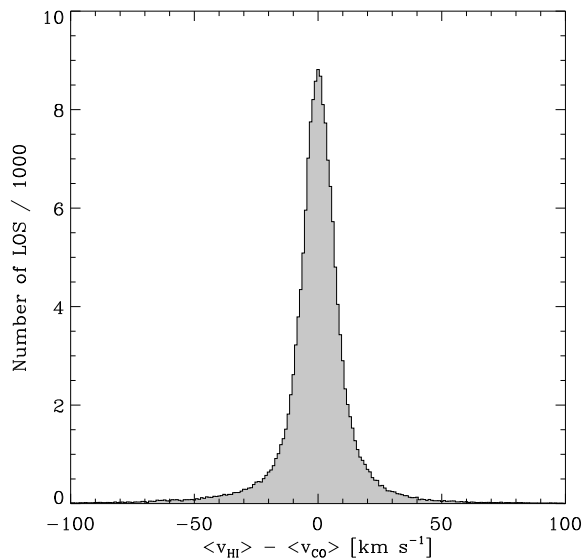


Figure 4.1 The difference between local mean velocities of HI and CO for lines of sight with galactocentric radius smaller than $0.5 r_{25}$. The close correspondence motivates our use of the HI mean velocity to predict the CO velocities in low surface brightness regions.

4.5.1 Stacking of CO Spectra

Predicting the velocity of the CO line from the HI data allows us to increase the SNR when measuring the integrated CO intensity. The HERACLES bandpass is $\sim 1000 \text{ km s}^{-1}$ and a typical CO line width at large galactocentric radii is $\sim 25 \text{ km s}^{-1}$. The HI allows us to restrict our integration to just the relevant part of the spectrum which represents a substantial gain in sensitivity.

Just as important as the increase in SNR, the shifted and stacked spectra allow us to verify that faint emission is actually an astronomical signal. Even for faint CO emission the stacking technique has the potential to reveal a spectral line. Low-level variations due to weather, receiver instabilities, and other systematic effects in the telescope will not create such an effect. Even stray pickup of astronomical emission due to surface imperfections (i.e., error beam effects) will emerge at a low level offset from zero velocity due to galaxy rotation.

Figure 4.2 demonstrates this approach. We plot the averaged CO spectrum of NGC 5055 inside a tilted ring spanning from $0.7 - 0.8 r_{25}$. In the left panel the spectra were averaged as they were observed, whereas in the right panel we first shifted by the local HI mean velocity and then averaged. Both spectra contain the same integrated intensity, however, only the appearance of a clear line feature in the right spectrum at the expected velocity strongly indicates that the signal is not due to baseline features but cannot be anything but CO emission.

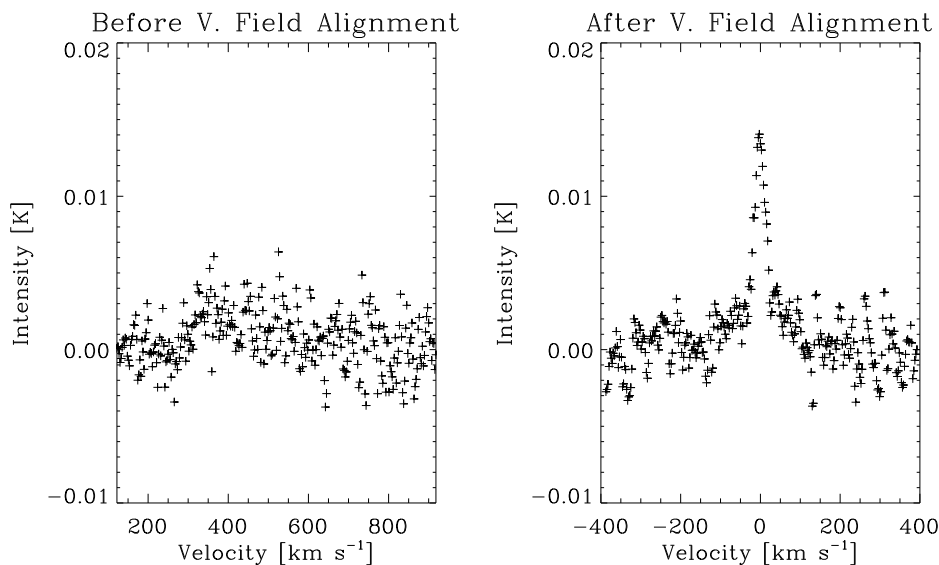


Figure 4.2 Average CO spectrum across tilted ring spanning from $0.7 - 0.8 r_{25}$ in NGC 5055. The left panel shows the result of a simple average of all spectra. The right panel shows the average after each spectrum is shifted so that $v = 0$ corresponds to the local mean H I velocity.

4.5.2 Fitting the CO Line

To extract CO line emission, we perform an automated line fit to each stacked spectrum. This approach picks out spectral line emission rather than baseline structure and does not require us to define an integration window beforehand.

In most regions, the line can be well-approximated by a Gaussian profile with FWHM of $\sim 15 - 40 \text{ km s}^{-1}$ (Figure 4.3 upper right panel). However, in the central regions of some galaxies the line can be very broad with a flattened or double-horned peak (Figure 4.3 upper left panel). These profiles often coincide with central enhancements like bars or molecular rings and are poorly parametrized by a single Gaussian. Instead we fit a double-horn profile, a Gaussian scaled by a symmetric second-order polynomial (functional form from Saintonge, 2007). Based on “by eye” inspection, the asymmetry in these profiles is small enough that a symmetric function is sufficient.

We derive the best fit profile via a non-linear least squares fit³. We constrain the fit parameters so that the center of the profile lies within $\pm 50 \text{ km s}^{-1}$ of zero velocity after shifting, the FWHM is larger than 15 km s^{-1} (to avoid the fit latching onto individual channels), and the amplitude is positive. We always carry out a Gaussian fit first and in those cases where the FWHM exceeds 60 km s^{-1} we switch to a double-horn profile. We verify by eye that this yields sensible results.

The integral of the fitted profile gives us the integrated CO line intensity. We derive

³ We use the IDL procedure `MPFIT.PRO` from Craig Markwardt which performs a Levenberg–Markwardt non-linear least squares minimization and is based on the `MINPACK-1 LMDIF.F` algorithm from More et al. (1978)

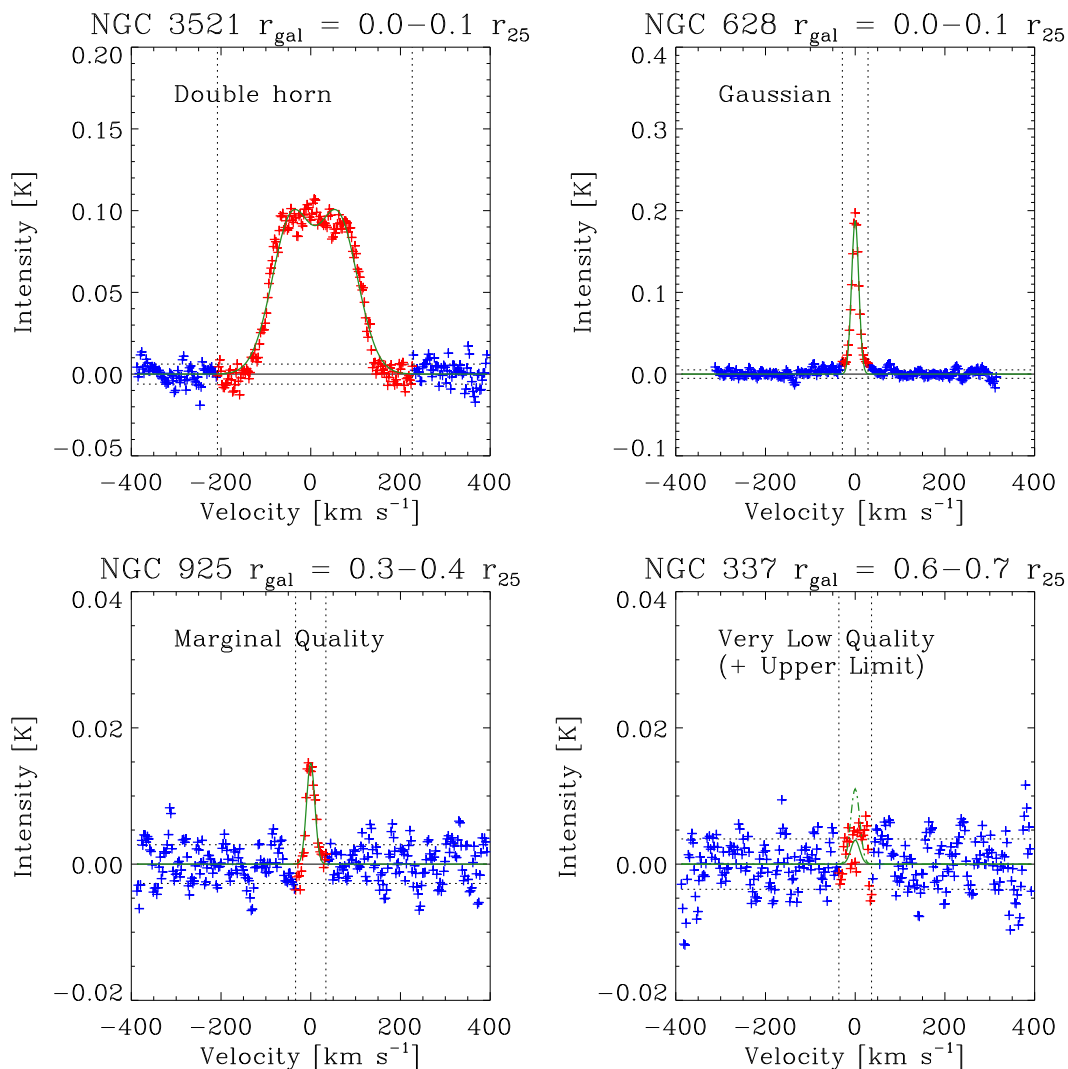


Figure 4.3 Examples of stacked CO spectra with different line shapes. The upper row shows spectra with high quality fits and the lower row shows spectra with low quality fits. The horizontal dotted lines mark the 1σ rms noise of the stacked spectrum. The *upper left* panel shows a broad line approximated by a double-horn profile. The *upper right* panel shows a narrow line fitted by a Gaussian. The *lower left* panel shows a marginal quality fit. The *lower right* panel shows a low quality fit together with the associated upper limit (dashed line).

the uncertainty in this quantity from the noise, estimated from the signal-free part of the spectrum, and the width of the profile. It proved useful to define a quality scale for the fit. The quality is “high” where the peak intensity is larger than 5σ and its integrated intensity is larger than 10 times its uncertainty. In cases where the peak intensity is less than 3σ or the integrated intensity is less than 5 times its uncertainty, we do not trust the fit and instead determine an upper limit. We label cases that fall between these regimes as “marginal”. Figure 4.3 shows examples of our quality measures and line profile fits.

We derive our upper limits integrating over a Gaussian line profile with FWHM set to 18 km s^{-1} , the typical FWHM found for high SNR spectra at $r > 0.5 r_{25}$, and fixed amplitude of 3σ .

4.5.3 Stacking as a Function of Radius

We present our stacking technique applied to radial bins. In principle this method allows us to stack spectra across any region. For example, we could define regions by total gas column, infrared intensity, or features such as spiral arms and bars. In practice, radius makes an excellent ordinate. We wish to study the underlying relationship between CO, HI, IR, FUV, and H α intensity. Stacking with one of these quantities as the ordinate would require carefully modeling the biases involved to measure the underlying relationships. Galactocentric radius is a well-determined, independent quantity that is also highly covariant with these other intensities. This yields a dataset with large dynamic range that is easy to interpret.

Therefore we focus our analysis on data stacked in bins of galactocentric radius. We average over tilted rings $15''$ wide, comparable to the angular resolution of our data. This width corresponds to $\sim 220 \text{ pc}$ for our nearest targets (3 Mpc) and $\sim 1800 \text{ pc}$ for our most distant targets (25 Mpc). We construct the rings assuming that each galaxy is a thin disk with the inclination and position angle given in Table 4.1. To measure CO with highest sensitivity we construct stacked CO spectra using the procedure described above and fit those to determine the integrated CO line intensities. For the other observables — HI, IR, FUV, and H α intensities — we use two-dimensional maps of intensity and determine the mean intensity for each tilted ring.

Error bars on the HI, IR, FUV, and H α intensities show the 1σ scatter within that tilted ring, capturing both statistical noise and deviations from axial symmetry. We estimate the 1σ scatter for our CO measurements by integrating the CO cube over a velocity window that is adjusted for each line of sight such that it includes all channels of significant CO emission but at least all channels with velocities within 25 km s^{-1} of the local mean HI velocity. Note that our 1σ values reflect the scatter in (integrated) intensities of individual lines of sight inside a ring. They should not be confused with the uncertainty in the determination of the mean intensity inside a ring which is typically much smaller.

4.6 Results

In the Appendix Figures A.1 we present stacked radial profiles of integrated CO intensity along with profiles of H I, infrared intensity at 24 μm and 70 μm , FUV, and H α intensity for all galaxies considered here. Following Equations (4.3) we combine H α and 24 μm intensities to estimate the star formation rate surface density SFR(H α +24) and compare those to SFR(FUV+24) derived from FUV and 24 μm intensities using Equation (4.4).

For each galaxy there are two plots: The left panel shows H I, H₂ (from CO), and SFR for both FUV+24 μm and H α +24 μm . The right panel shows our SFR tracers — H α , FUV, 24 μm and 70 μm emission. We present the profiles in both observed intensity⁴ (left hand y -axis) and units of surface density (right hand y -axis of the left panel) — Σ_{H_2} , $\Sigma_{\text{H I}}$, and Σ_{SFR} . Note that we have projected (only) the surface densities of H I, H₂, and SFR to face-on values (i.e., we corrected for inclination). The observed surface brightnesses are not corrected for the effect of inclination. Such a correction will just move each galaxy up and down in lockstep and we find it more useful to report the observed values. The color of a point in the CO profile indicates the significance of the fit to the stacked spectrum: green for high significance, orange for marginal significance, and red for upper limits, these correspond to 3σ upper limits on the fitted intensity (see Section 4.5.2).

4.6.1 CO and Star Formation

With these azimuthally averaged data we are able to compare CO to tracers of recent star formation across a large range of H₂-to-H I ratios. In this subsection, we make empirical comparisons between measured intensities, examine the relative roles of H₂ and H I in the “star formation law,” and investigate the origin of the scatter in these relations.

Scaling Relations between CO and IR, FUV, and H α

Figures 4.4 & 4.5 show scaling relations between observed intensities of CO (x -axis) and different tracers of recent star formation (y -axis). Figure 4.4 shows infrared intensities at 24 μm (top panels) and 70 μm (bottom panels) and Figure 4.5 shows intensities of FUV (top panels) and H α (bottom panels). The left hand panels show the relations for all galaxies and all radii. The panels on the right hand side show only radii $r > 0.5 r_{25}$. H₂ and H I make up roughly equal parts of the ISM near this radius (see the left panel of Figure 4.12), so most of the points in the right hand panels are H I-dominated. A dotted vertical line shows an integrated CO intensity of 2.2 K km s⁻¹, which corresponds to $\Sigma_{\text{H}_2} \approx 10 M_{\odot} \text{ pc}^{-2}$ (assuming $i = 45^\circ$), which is about the surface density at which H₂ and H I make up equal parts of the ISM. A dashed vertical line at $I_{\text{CO}} = 0.3 \text{ K km s}^{-1}$ ($\Sigma_{\text{H}_2} \approx 1 M_{\odot} \text{ pc}^{-2}$ for $i = 45^\circ$) shows a conservative sensitivity limit for the whole sample. Typically our upper limits, which are not displayed in these plots, lie to the left of this line. They will be systematically higher at large radii when radial rings partially exceed the coverage of our CO maps.

⁴ In order to have H I and H₂ comparable in units of mass surface density we scale the observed H I intensity by a factor of 312.5; the ratio of Equation (4.1) and (4.2).

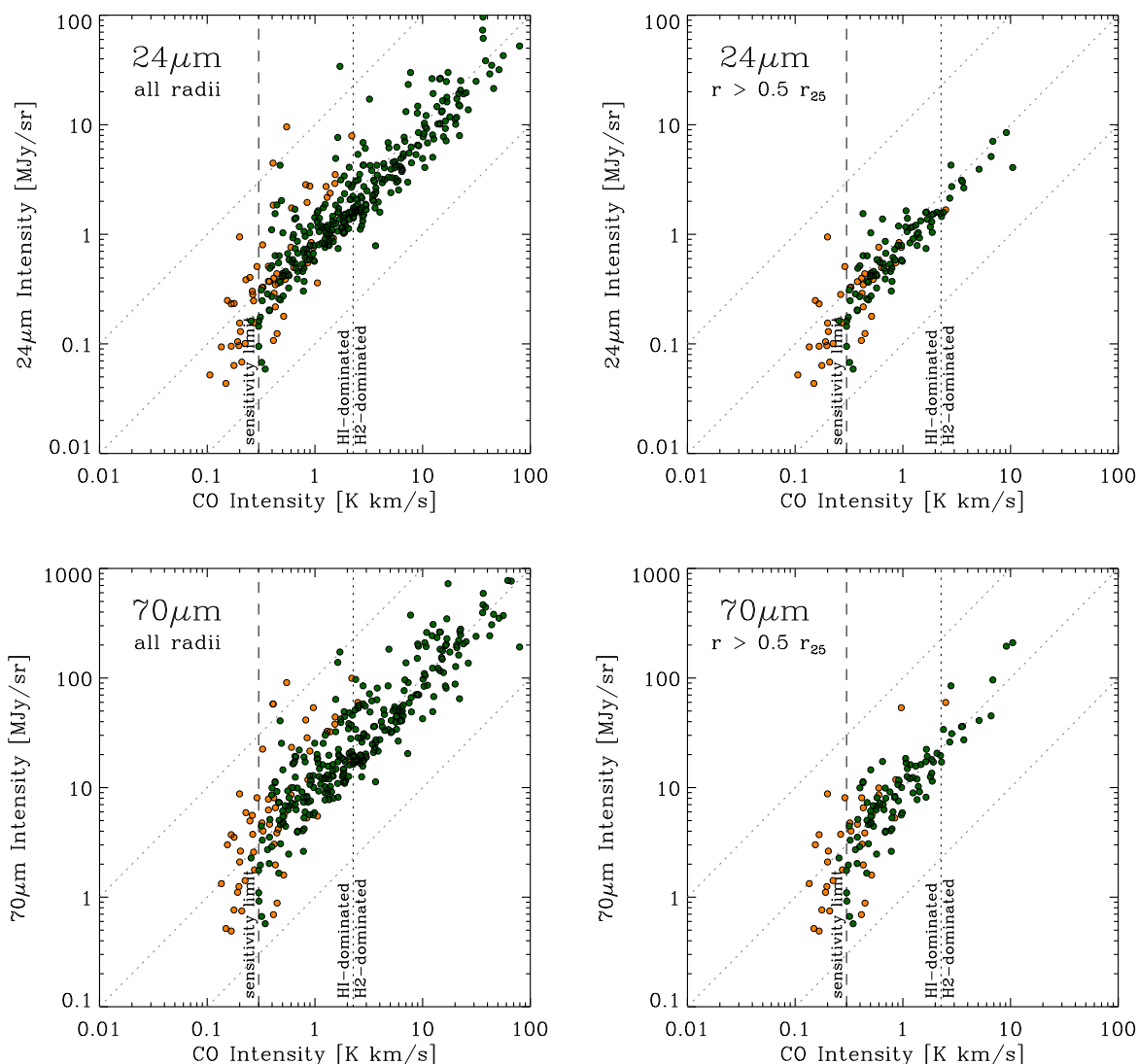


Figure 4.4 Observed IR intensities (y -axis) as a function of integrated CO(2 \rightarrow 1) intensity (x -axis). Each point corresponds to a stacked average in a tilted ring 15'' wide. Green and orange symbols indicate CO measurements of high or marginally significance; radial rings with only upper limits on the CO intensity (not shown here) are located exclusively to the left of the long-dashed line. The top panels shows the relation of 24 μm versus CO, the bottom panels shows 70 μm versus CO. The left panels show data for all radii, whereas the right panels show only data outside $0.5 r_{25}$, where the ISM is typically H I-dominated. The short-dashed vertical line indicates a typical CO intensity at which $\Sigma_{\text{H}_2} \sim \Sigma_{\text{H I}}$; data to the left of this line will usually be H I-dominated. The diagonal dashed lines indicate lines of constant ratios for orientation.

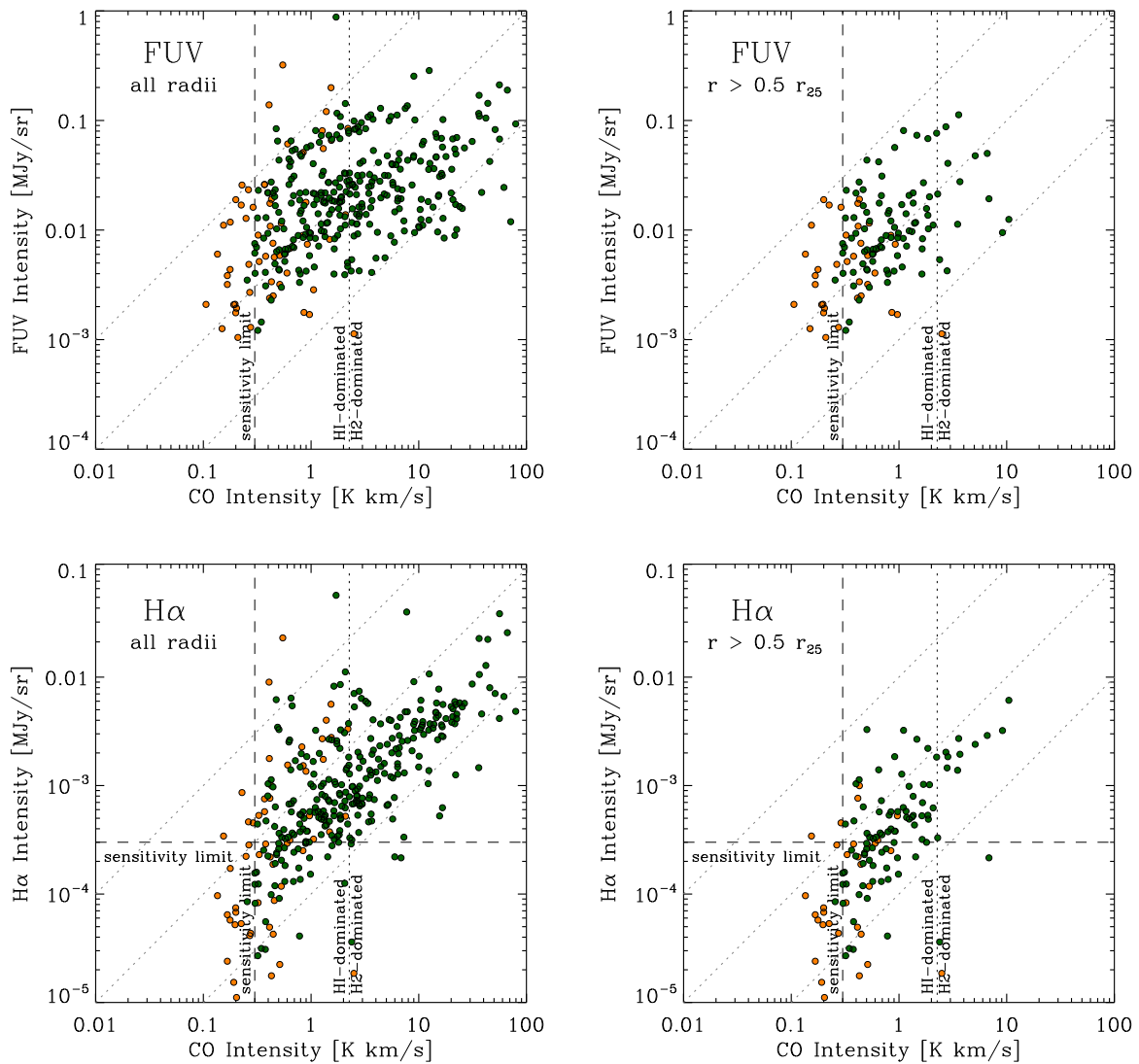


Figure 4.5 A similar plot as Figure 4.4 but this time showing the relation of FUV versus CO and H α versus CO for our two radial ranges. Note that H α intensities below a few times 10⁻⁴ MJy sr⁻¹ are affected by data quality and processing and have to be considered uncertain.

Table 4.2. Relation of IR Emission and SFR Tracers to CO

SFR Tracer	Rank Correlation	Power Law Index
24 μm		
... all data	$0.90 \pm 0.05^{\text{a}}$	$1.0 \pm 0.1^{\text{b}}$
... $r > 0.5 r_{25}$	0.87 ± 0.10	1.1 ± 0.1
70 μm		
... all data	0.87 ± 0.05	1.0 ± 0.1
... $r > 0.5 r_{25}$	0.84 ± 0.10	1.1 ± 0.2
FUV		
... all data	0.47 ± 0.05	0.8 ± 0.6
... $r > 0.5 r_{25}$	0.46 ± 0.09	1.1 ± 0.8
H α		
... all data	0.63 ± 0.05	0.9 ± 0.4
... $r > 0.5 r_{25}$	0.55 ± 0.10	1.1 ± 0.6

Note. — (a) We estimate the uncertainty in the rank correlation coefficient by taking the correlation coefficient derived from 1,000 random pairwise re-orderings of the data.

(b) The slope quoted here is from the ordinary least squares bisector with the error estimated from the spread in fitting x vs. y and y vs. x .

CO emission correlates tightly with IR emission at 24 μm and 70 μm (Figure 4.4) (rank correlation coefficient $r_{\text{corr}} = 0.9$). The correlation extends over three orders of magnitude in CO and IR intensities and crosses the H I-to-H₂ transition without substantial change in slope or normalization. Comparing the left panels (all radii) and the right panels ($r > 0.5 r_{25}$) does not reveal any significant radial dependence.

CO emission exhibits a weaker correlation with FUV and H α (Figure 4.5) ($r_{\text{corr}} = 0.5 - 0.6$) than with IR emission, i.e., both the CO-FUV and CO-H α relation show much larger scatter than the CO-IR relations. The CO-FUV relation displays a break between H I- and H₂-dominated regimes. The increased scatter and weaker correlation at least partially reflects the sensitivity of H α and FUV emission to absorption by dust. In the inner ($r \lesssim 0.5 r_{25}$), more gas rich parts of galaxies dust reprocesses most H α and FUV emission into IR emission. In this regime CO and FUV are to first order uncorrelated ($r_{\text{corr}} = 0.16$). Outside $\sim 0.5 r_{25}$ the filling factors of dense gas and dust are lower and FUV is less affected by extinction. The correlation coefficient between CO and FUV or H α is $r_{\text{corr}} = 0.45 - 0.55$ in this regime, still not as high as for the whole galaxies because of the limited dynamic range in intensity. In Section 4.6.1 we will see that the weaker correlation of CO with H α and FUV is mostly due to galaxy-to-galaxy variations, possibly reflecting different star formation histories, dust abundances, geometries, and potential changes in the CO-to-H₂ conversion factor.

We use the ordinary least squares (OLS) bisector to fit power laws to each relation. In

terms of sensitivity to a given amount of star formation, the SFR tracers are much more sensitive than our CO maps. To properly fit a relation between them we thus need to either carefully incorporate upper limits (e.g., see Blanc et al., 2009) or impose a matched sensitivity cut on the SFR tracer data. We take the latter approach, discarding data below 0.1, 1.0, 10^{-3} , and 10^{-4} MJy sr $^{-1}$ at 24 μ m, 70 μ m, FUV, and H α intensities after an initial fit⁵. Graphically, this removes the flaring towards low intensity just above our sensitivity cut seen in Figure 4.4 & 4.5, because we are not sensitive to a similar flaring towards low CO intensities.

Table 5.2 reports these fits considering all regions with CO measurements of high significance and SFR tracers above the sensitivity cut. The main result is that CO emission is consistent with being linearly proportional to IR emission both at 24 μ m and 70 μ m, down to low surface brightness. The best fits relating CO with FUV or H α emission are also consistent with a linear slope within the large uncertainties, but power laws are clearly an inadequate description of those data.

Scatter in the Scaling Relations

Each of the observed relations displays significant scatter: $I_{24\mu\text{m}}/I_{\text{CO}}$ has 1σ scatter of about 0.17 dex ($\sim 50\%$) and $I_{70\mu\text{m}}/I_{\text{CO}}$ scatters by 0.24 dex ($\sim 75\%$), whereas $I_{\text{H}\alpha}/I_{\text{CO}}$ scatters by 0.34 dex (a factor of 2.2) and $I_{\text{FUV}}/I_{\text{CO}}$ by 0.55 dex (a factor of 3.5). The origin of this scatter is of astrophysical interest. On small scales, this scatter arises from the evolution of individual star-forming regions, which vary dramatically in their ratios of CO-to-SFR tracers — leading to a breakdown of scaling relations when a resolution element corresponds to an individual region (Schruba et al., 2010). Here our azimuthal averaging washes out such small-scale variations. Each point averages over many individual star-forming regions. However, we do have the ability to distinguish scatter *within* a galaxy from scatter *among* galaxies.

To investigate the origin of the observed scatter, we remove galaxy-to-galaxy variations from the observed relation. We do so in two ways: First, we fit power-laws relating CO to IR, FUV, or H α in each galaxy and then adjust all galaxies to have the same normalization. *A priori* we do not know if the galaxy-to-galaxy variations mainly affect the measurement of our gas tracer (x -axis) or the measurements of our SFR tracers (y -axis), therefore, we repeat the exercise matching normalizations at a fixed value in y and then in x . We then compare the scatter among normalizations to the scatter about the re-normalized relation.

We also carry out a more basic test, measuring how the scatter in the ratio of SFR tracer to CO emission varies both among and within galaxies. We compare the scatter in the median ratio of SFR tracer to CO, $\langle I_{24\mu\text{m}}/I_{\text{CO}} \rangle$, among galaxies to the scatter in deviations from this median ratio within galaxies, $I_{24\mu\text{m}}/I_{\text{CO}} - \langle I_{24\mu\text{m}}/I_{\text{CO}} \rangle$.

For both approaches, we find that galaxy-to-galaxy variations dominate the scatter in the observed relation. Scatter among galaxies in Figure 4.4 & 4.5 is ~ 2 times larger than the scatter within individual galaxies. The most striking cases are H α and FUV

⁵ The result is relatively insensitive to the exact choice of sensitivity cut. Varying it by a factor of 2 affects the power law index by ~ 0.05 for the CO-IR relations and ~ 0.15 for CO-FUV or CO-H α .

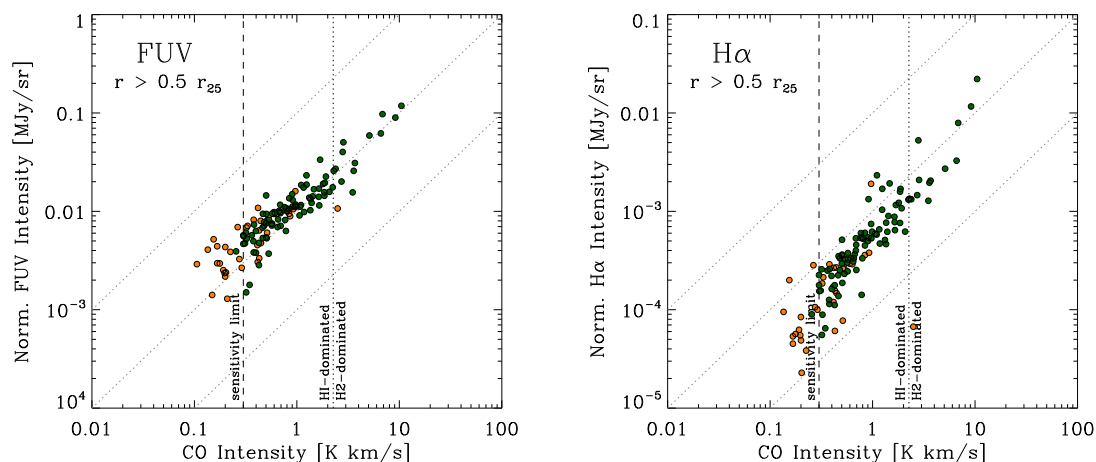


Figure 4.6 Relation between CO intensity and normalized FUV intensity (left panel) and normalized H α intensity (right panel) for outer disks, $r > 0.5 r_{25}$. For each galaxy we use power law fits to the data of high quality and normalize the relation by the FUV or H α intensity, respectively, which the fit has at 1 K km s^{-1} .

emission in the outer parts of galaxies. Figure 4.6 shows that after normalization, the relation of CO with FUV and H α emission for radii $r > 0.5 r_{25}$ becomes very strong ($r_{\text{corr}} = 0.9$) and nearly linear (power law index of 0.90 ± 0.05 for FUV and 1.1 ± 0.05 for H α). Thus in the outer parts of galaxies the FUV-to-CO and the H α -to-CO ratios vary dramatically among galaxies but are largely fixed inside each galaxy. The scatter appears driven at least in part by real systematic variations in the ratio of CO-to-SFR tracers as a function of other galaxy parameters (see below and Young et al., 1996). The case in the inner parts of galaxies is more complex because of high dust attenuations resulting in non-linear CO-FUV and CO-H α relations.

H $_2$ and Star Formation

In Figure 4.7 we combine FUV and $24 \mu\text{m}$ intensities to estimate Σ_{SFR} , which we plot as a function of Σ_{H_2} . In Figure 4.8 we instead combine H α and $24 \mu\text{m}$ to estimate Σ_{SFR} . In both Figures, the left hand panels show data for all radii, while the right hand panels show only rings with $r > 0.5 r_{25}$, where the ISM is mostly H I. As in Figure 4.4 & 4.5, a vertical dotted line shows $\Sigma_{\text{H}_2} \approx 10 \text{ M}_\odot \text{ pc}^{-2}$, a typical H $_2$ surface density where the ISM consists of equal parts H I and H $_2$.

In agreement with Bigiel et al. (2008, 2011), we observe an approximately linear scaling of Σ_{SFR} and Σ_{H_2} in regions that are dominated by molecular gas ($\Sigma_{\text{H}_2} \gtrsim 10 \text{ M}_\odot \text{ pc}^{-2}$). For Figure 4.7 this agreement does not come as a surprise because we use many of the same data and a similar approach (FUV+ $24\mu\text{m}$) to estimate recent SFR. The new results here are that (a) this trend *continues without significant changes* down to very low Σ_{H_2} , including regions strongly dominated by atomic gas, and (b) we find the same trend in Figure 4.8 using SFR(H α + $24\mu\text{m}$).

The rank correlation coefficient relating Σ_{H_2} and Σ_{SFR} for all data with at least a

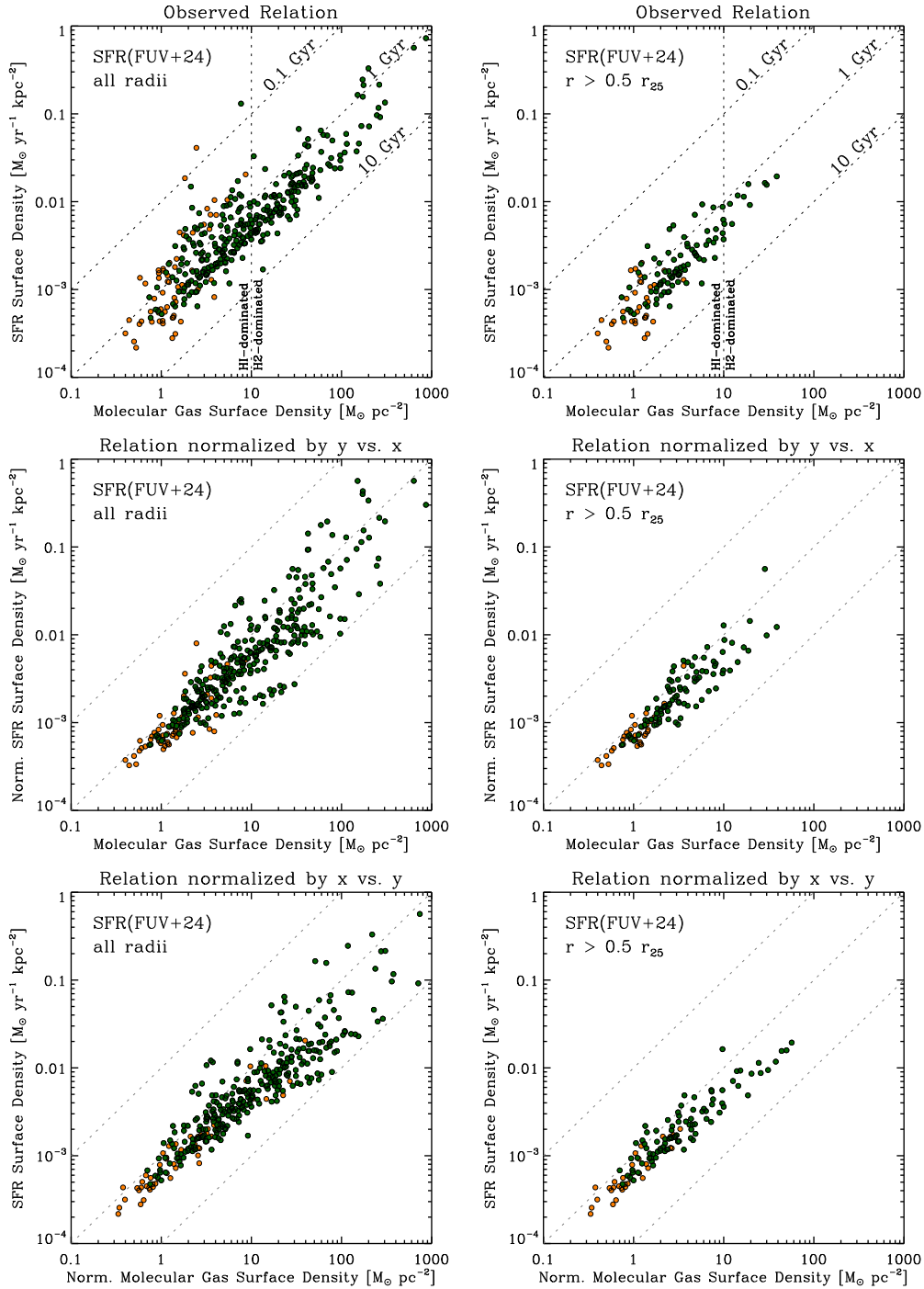


Figure 4.7 Recent star formation rate surface density estimate from FUV+24 μ m (y -axis) as a function of molecular gas surface density (x -axis). The left-hand column shows data for all radii, whereas the right-hand column shows only data where $r > 0.5 r_{25}$. The upper row presents the basic relation, which is approximately linear with average H₂ depletion time ~ 2.0 Gyr (dashed lines). The middle and bottom rows show results after we fit and remove galaxy-to-galaxy variations. These galaxy-to-galaxy variations are ~ 2 times larger than internal variations, suggesting individual galaxies each obey well-defined, though offset, relations.

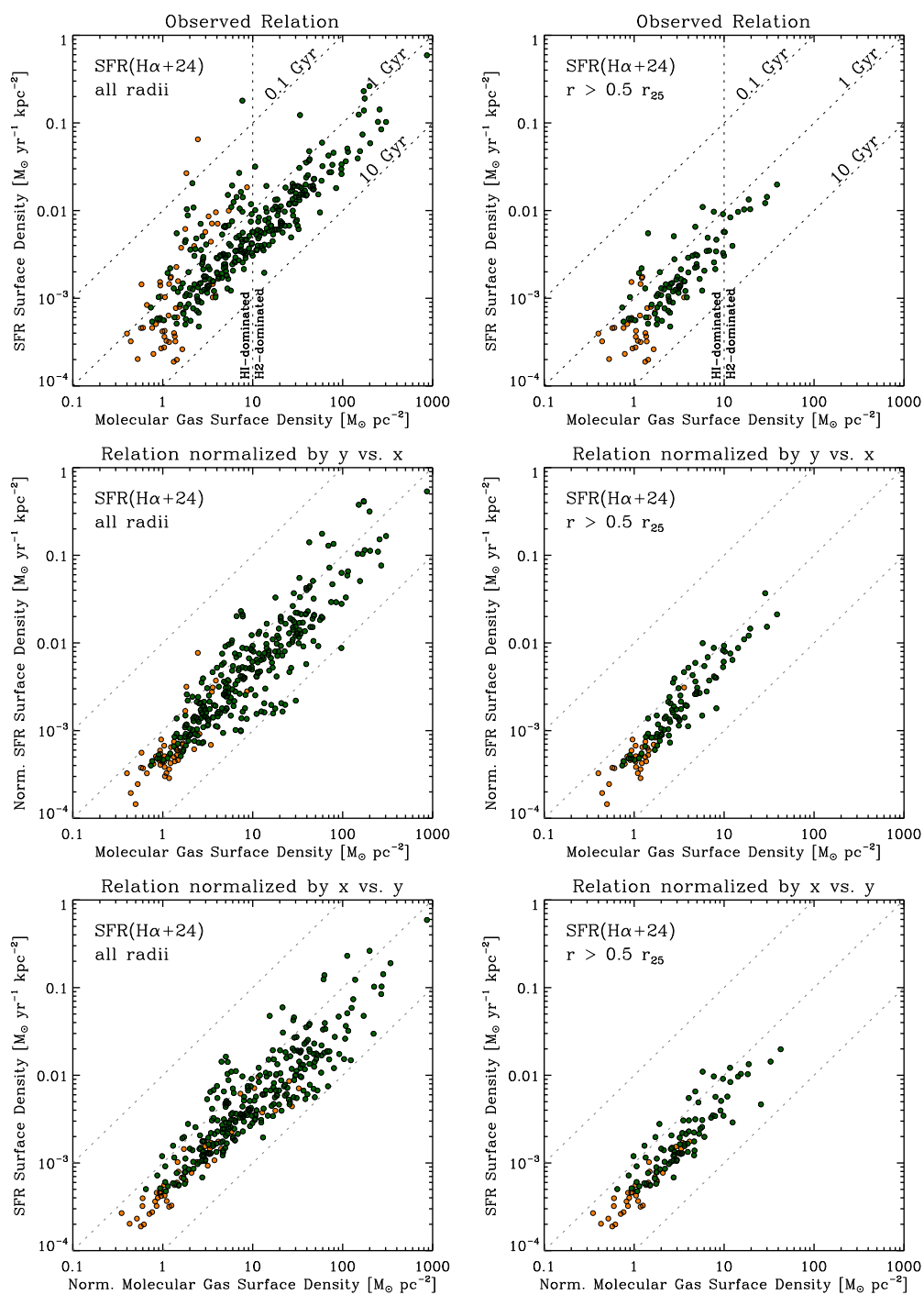


Figure 4.8 The same plot as Figure 4.7 but this time using $\text{H}\alpha+24\mu\text{m}$ to estimate Σ_{SFR} .

marginal CO measurement is $r_{\text{corr}} \approx 0.85$. The scatter about a linear relation is 0.25 dex (prior to any normalization). Both numbers resemble those derived for the CO–24 μm relation in Section 5.6.2 because 24 μm emission drives our hybrid SFR tracer over most of the area. In detail, the fractional contribution of 24 μm to SFR varies with radius and choice of hybrid tracer. Generally speaking: (a) the larger the radius the larger the contribution of the unobscured term, and (b) H α contributes fractionally more than FUV to the hybrid.

An OLS bisector fit yields a roughly linear slope and a molecular depletion time, $\tau_{\text{dep}} = \Sigma_{\text{H}_2}/\Sigma_{\text{SFR}}$, of ~ 1.8 Gyr (including a factor 1.36 to account for heavy elements; see Table 5.3 for fit parameters). This is slightly lower than $\tau_{\text{dep}} = 2$ Gyr found by Bigiel et al. (2008) and Leroy et al. (2008) for a subset of the data analyzed here and $\tau_{\text{dep}} = 2.35$ Gyr recently found by Bigiel et al. (2011) for a sample that is similar to the one analyzed here. We include (a) more starburst galaxies and (b) more low mass, low metallicity spiral galaxies that Bigiel et al. (2008) and Leroy et al. (2008) excluded from their CO analysis. Both dwarfs and starbursts have shorter τ_{dep} than large spirals (see below and Kennicutt, 1998b; Gao & Solomon, 2004; Leroy et al., 2008; Daddi et al., 2010). Moreover, our radial profiles weight these small galaxies more heavily than the pixel sampling used by Bigiel et al. (2008, 2011).

As with the scaling relations between CO and tracers of recent star formation (Figure 4.4 & 4.5), the H $_2$ –SFR relation exhibits significant scatter. We perform the same procedure to isolate galaxy–to–galaxy variations from scatter within galaxies and again find the scatter in the main relation (upper panels in Figure 4.7 & 4.8) dominated by galaxy–to–galaxy variations. We plot the relations after normalization in x and y in the middle and bottom panels of Figure 4.7 & 4.8. Once galaxy–to–galaxy scatter is removed, there is a remarkably tight, uniform linear relation linking molecular gas and star formation across almost three and a half orders of magnitude.

What drives this galaxy–to–galaxy variation? In both the H $_2$ –SFR and observed intensity relations a large part of the scatter comes from a sub–population of less massive, less metal–rich galaxies that exhibit high SFR–to–CO ratios. Figure 4.9 shows the metallicity dependence of the molecular depletion time, τ_{dep} . Massive spiral galaxies with high metallicities have considerably longer (median averaged) depletion times: ~ 2.4 Gyr for systems with metallicities of $12 + \log \text{O}/\text{H} > 8.75$ and ~ 1.7 Gyr for $12 + \log \text{O}/\text{H} = 8.65 - 8.75$, while smaller galaxies with lower metallicities have systematically shorter depletion times: ~ 0.8 Gyr for systems with $12 + \log \text{O}/\text{H} < 8.65$ ⁶. We find a similar trend for the scaling of τ_{dep} with the maximal rotation velocity, v_{flat} , that low mass systems with $v_{\text{flat}} \lesssim 140$ km s $^{-1}$ have $\tau_{\text{dep}} < 1$ Gyr. These low mass, low metallicity systems are atomic dominated ($\Sigma_{\text{HI}} \gtrsim \Sigma_{\text{H}_2}$) for most of their radii and show up prominently in the upper left panel of Figure 4.7 & 4.8 as the data points offset to shorter depletion times. Leroy et al. (2008) and Bigiel et al. (2008) labeled these galaxies “HI–dominated” and did not consider them in their H $_2$ –SFR analysis.

⁶ The absolute metallicity values that we quote should not be overemphasized, but the relative ordering of galaxies is fairly secure. See Moustakas et al. (2010) for more details.

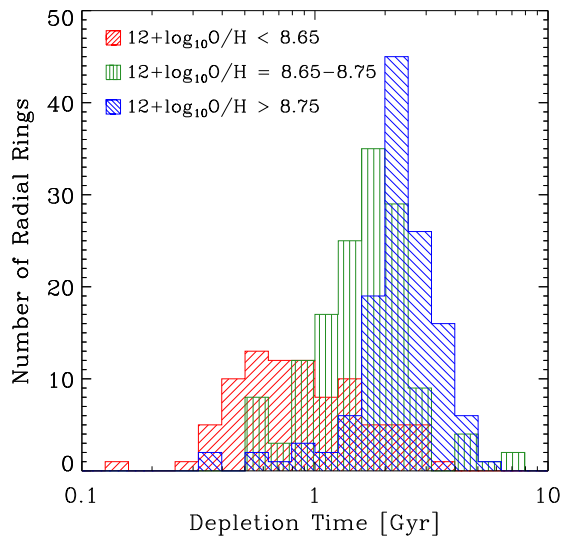


Figure 4.9 Molecular gas depletion time, $\tau_{\text{dep}} = \Sigma_{\text{H}_2}/\Sigma_{\text{SFR}}$, as function of metallicity. The depletion times shown here correspond to the ratio of the data shown in Figure 4.7 including regions with CO measurements of marginal significance. The median average τ_{dep} changes systematically with metallicity: for the low metallicity bin ~ 0.8 Gyr, for the intermediate metallicity bin ~ 1.7 Gyr, and for the high metallicity bin ~ 2.4 Gyr.

SFR, HI, and H₂

The question of which gas component — HI, H₂, or total gas — correlates best with recent star formation has received significant attention. Phrased this way, the question is not particularly well posed: the total gas surface density and the molecular gas fraction are closely related so that the different gas surface densities are not independent quantities. Therefore we do not necessarily expect a “best” correlation, only different functional forms. Still, it is illustrative to see how recent star formation relates to each gas tracer. Table 5.3 lists r_{corr} and the power law index from an OLS bisector fit between each component and Figure 4.10 shows plots for each of the three gas phases and our two SFR prescriptions. The rank correlation coefficient and the power law fits are determined for regions where we have at least a marginal CO measurement. If we restrict our analysis to high significance CO measurements, we obtain the same results within the uncertainties.

The table and figure show that recent star formation rate tracers rank-correlate approximately equally well with H₂ and HI+H₂ both across all surface densities and separately in the HI- and H₂-dominated regimes. HI does not correlate significantly with star formation in the H₂-dominated inner parts of galaxy disks, though the correlation between HI and recent star formation becomes stronger in the HI-dominated outer parts of galaxies (and further increases at even larger radii; see Bigiel et al., 2010b).

The rank correlation is a non-parametric measure of how well the relative ordering of two data sets align. A high rank correlation coefficient implies a monotonic relationship but not a fixed functional form law. For total gas, the power law index relating gas and recent star formation depends fairly strongly on the subset of data used. If we focus on

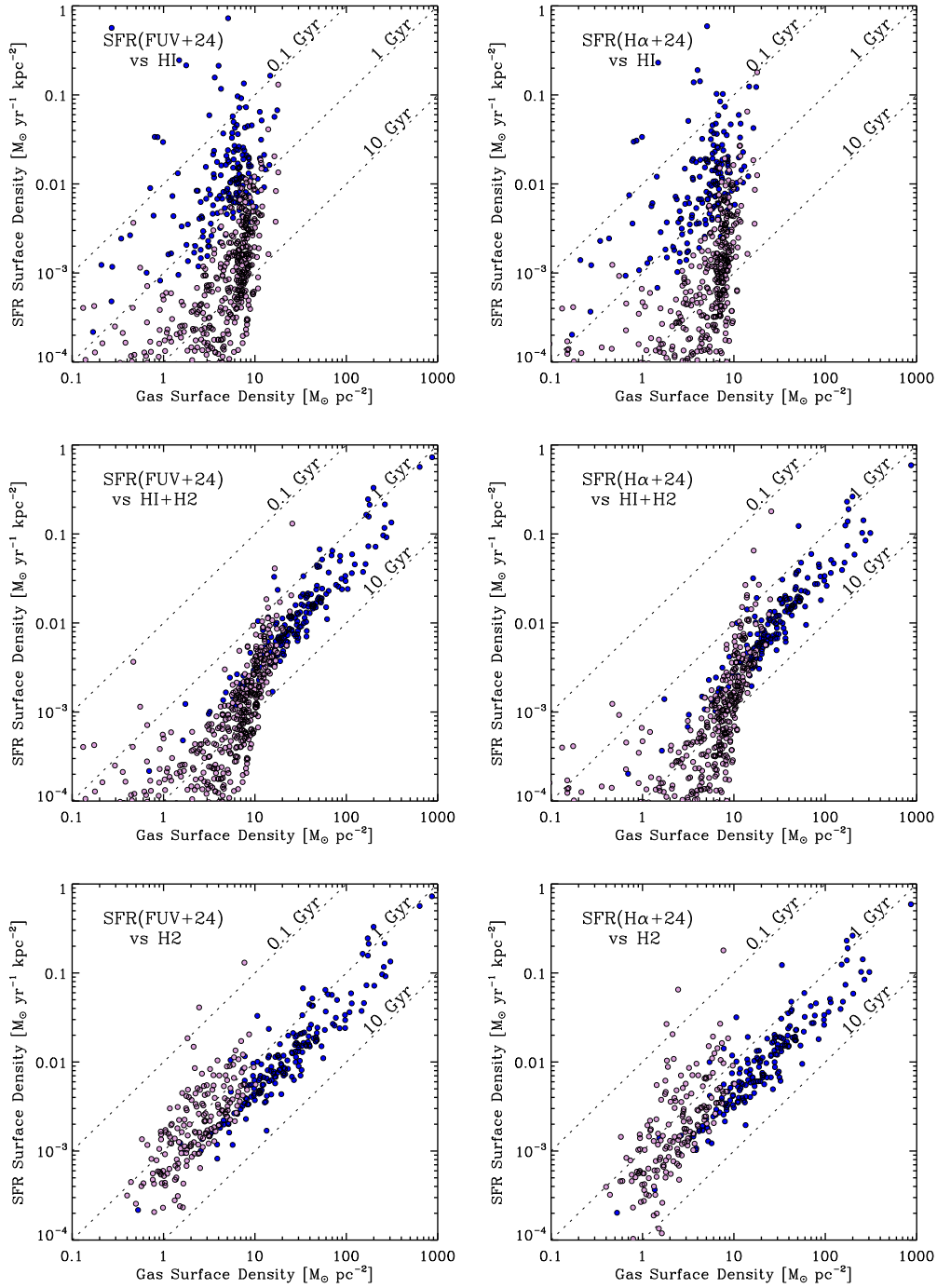


Figure 4.10 Σ_{SFR} (y -axis) from FUV+24 μm (*left*) and H α +24 μm (*right*) as a function of different gas phases: HI alone (*top*), HI+H₂ (*middle*), and H₂ alone (*bottom*). Each point in these diagrams represents a radial average in a galaxy. Regions that are H₂-dominated are plotted with dark blue symbols, regions that are HI-dominated in light red symbols. The bottom panels show only regions with at least marginal CO signal, while the top and middle panels show also regions with only an upper limit on the molecular content. Whereas SFR is not correlated to HI (in the inner galaxy disks), it correlates with H₂ and HI+H₂. The scaling with H₂ is uniform and linear for all regimes; the scaling with HI+H₂ exhibits a change in slope at the transition between HI- and H₂-dominated environments.

Table 4.3. Relation of SFR to Different Gas Phases

Gas Phase	Rank Correlation	Power Law Index
SFR(FUV+24) vs. Gas Phase		
H I		
... all data	0.23 ± 0.05^a	...
... H I-dominated	0.52 ± 0.06	...
... H ₂ -dominated	0.41 ± 0.08	...
H ₂		
... all data	0.88 ± 0.05	1.0 ± 0.1^a
... H I-dominated	0.75 ± 0.07	1.3 ± 0.5
... H ₂ -dominated	0.91 ± 0.07	1.1 ± 0.1
H I+H ₂		
... all data	0.90 ± 0.05	1.6 ± 0.2
... H I-dominated	0.78 ± 0.06	2.2 ± 0.6
... H ₂ -dominated	0.92 ± 0.07	1.2 ± 0.1
SFR(FUV+24) vs. Gas Phase		
H I		
... all data	0.21 ± 0.05^a	...
... H I-dominated	0.54 ± 0.06	...
... H ₂ -dominated	0.44 ± 0.08	...
H ₂		
... all data	0.85 ± 0.05	1.0 ± 0.1^a
... H I-dominated	0.70 ± 0.07	1.5 ± 0.7
... H ₂ -dominated	0.91 ± 0.08	1.1 ± 0.1
H I+H ₂		
... all data	0.90 ± 0.05	1.7 ± 0.2
... H I-dominated	0.79 ± 0.06	2.5 ± 0.8
... H ₂ -dominated	0.92 ± 0.08	1.3 ± 0.1

Note. — (a) Estimation of uncertainties equal to Table 5.2.

the regions where $\Sigma_{\text{HI}} > \Sigma_{\text{H}_2}$, the best-fit power law relating total gas and recent star formation (from FUV+24) has an index of 2.2 ± 0.6 . Where $\Sigma_{\text{HI}} < \Sigma_{\text{H}_2}$, the index is much shallower, 1.2 ± 0.1 . By contrast, the power law relating H_2 to recent star formation varies less across regimes, from 1.3 ± 0.5 where $\Sigma_{\text{HI}} > \Sigma_{\text{H}_2}$ to 1.1 ± 0.1 where $\Sigma_{\text{HI}} < \Sigma_{\text{H}_2}$. Both of these agree within the uncertainties with the fit to all data, which has slope 1.0 ± 0.1 . The slight steepening of the relation in the outer disks ($\Sigma_{\text{HI}} > \Sigma_{\text{H}_2}$) is driven by the interplay of two effects: the rather small dynamic range in gas surface densities and an increased dispersion in SFR-to- H_2 ratios driven by the low mass galaxies; those have high SFR-to- H_2 ratios and contribute mostly to the HI-dominated subset. The qualitative picture of a break in the total gas-SFR relation but a continuous H_2 -SFR relation remains unchanged if SFR($\text{H}\alpha$ +24) is considered, though there are small changes in the exact numbers (see the left and right panels in Figure 4.10).

Our conclusions thus match those of Bigiel et al. (2008): a single power law appears to be sufficient to relate Σ_{H_2} and Σ_{SFR} whereas the relationship between $\Sigma_{\text{HI}+\text{H}_2}$ and Σ_{SFR} varies systematically depending on the subset of data used. Because we have a dataset that includes significant CO measurements where $\Sigma_{\text{HI}} > \Sigma_{\text{H}_2}$ we can extend these findings. First, total gas and H_2 are equally well rank-correlated with recent star formation in all regimes and this correlation is always stronger than the correlation of recent star formation with HI. Second, the H_2 -SFR scaling relation extends smoothly into the regime where $\Sigma_{\text{HI}} > \Sigma_{\text{H}_2}$ whereas the total gas-SFR relation does not. Third, the result is independent of our two star formation rate tracers SFR(FUV+24) and SFR($\text{H}\alpha$ +24).

Discussion of CO-SFR Scaling Relations

Empirical Results: IR brightness at both 24 μm and 70 μm correlates strongly with CO intensity over ~ 3 orders of magnitude. Across this range, there is a nearly fixed ratio of CO to IR emission. FUV and $\text{H}\alpha$ emission show little or no correlation with CO intensity in the inner parts of galaxies, presumably due to extinction, but are found to correlate well with CO in the outer parts of galaxies after galaxy-to-galaxy scatter is removed.

A result of these empirical scaling relations is that the ratio of recent star formation rate, traced either by combining FUV and 24 μm or $\text{H}\alpha$ and 24 μm intensities, to molecular gas, traced by CO emission, does not vary strongly between the HI-dominated and H_2 -dominated ISM. This result is driven largely by the tight observed correlation between CO and 24 μm emission. The tight relation between CO and 70 μm emission suggests that the CO-IR relation actually holds for a larger range of mid-IR intensities. The tightening of the CO-FUV and CO- $\text{H}\alpha$ relation in the outer part of galaxies (after removing galaxy-to-galaxy scatter) reinforce the idea of a linear relation extending to large radii. These tight correlations are consistent with the conclusion of Leroy et al. (2008) that there is only weak variation in the SFR per unit molecular gas mass with local environment.

Galaxy-to-Galaxy Scatter: Each of the correlations we observe has significant internal scatter. Breaking this apart into scatter among galaxies and scatter within galaxies, we observe that in every case scatter among galaxies drives the overall scatter in the observed correlation. This “scatter” among galaxies is not random; less massive, less metal-rich galaxies exhibit a higher ratio of SFR tracer to CO emission (see Figure 4.9 and Young et al., 1996). There are two straightforward physical interpretations for this.

The efficiency of star formation from H_2 gas may be genuinely higher in these systems, a view advocated by Gardan et al. (2007) and Gratier et al. (2010b). Alternatively, CO emission may be depressed relative to the true amount of H_2 mass due to changes in the dust abundance. Low mass systems often have lower metallicities and correspondingly less dust, which is required to shield CO (e.g., Maloney & Black, 1988; Bolatto et al., 1999; Glover et al., 2010; Wolfire et al., 2010). A precise calibration of the CO-to- H_2 conversion factor as a function of metallicity is still lacking, so it is not possible at present to robustly distinguish between these two scenarios.

After removing these galaxy-to-galaxy variations we find a series of extraordinarily tight relationships between CO and tracers of recent star formation. The most striking — and puzzling — example of this is the emergence of a tight correlation between CO and FUV emission in the outer parts of galaxies ($r > 0.5 r_{25}$). This is puzzling because one would expect the galaxy to be mostly causally disconnected over the timescales predominantly traced by FUV emission — 20 – 30 Myr compared to a dynamical (orbital) time of a few 100 Myr. Yet, somehow the differences between galaxies affect the CO-to-FUV ratio much more than the differences between the widely separated rings represented by our data points. Galaxy-wide variations in metallicity and dust abundance probably offer the best explanation for this. These may propagate into variations in the CO-to- H_2 conversion factor and the average dust extinction. The latter may lead to scatter in estimates of SFR and both will affect τ_{dep} . An alternative explanation is that external processes, which affect the whole galaxy, play a large role in setting the star formation rate on timescales traced by FUV emission.

These strong galaxy-to-galaxy variations partially explain the unexpected lack of correlation between CO emission and recent SFR observed by Kennicutt (1998b). They averaged across whole galaxies and in doing so conceivably lost the strong internal relations that we observe but preserved the large galaxy-to-galaxy variations that offset internal relations. The result will be an apparent lack of correlation in galaxy-averaged data that obscures the strong internal relationship. Whether there is in fact a weaker relationship between H_2 and SFR in galaxy-integrated measurements than inside galaxies depends on whether the suggested variations in star formation efficiency are real or a product of a varying CO-to- H_2 conversion factor.

(The Lack of) A Molecular Star Formation Law: With improved sensitivity to CO emission we now clearly see nearly linear relations between CO and tracers of recent star formation rate spanning from the H_2 -dominated to H I -dominated parts of galaxies. Note that the relations will likely depart from these scaling relations if regions of high surface densities ($\Sigma_{\text{H}_2} > 100 M_{\odot} \text{pc}^{-2}$) or starburst galaxies are considered (e.g., Kennicutt, 1998b; Daddi et al., 2010; Genzel et al., 2010). The lack of strong variations in the scaling between these two quantities in the “non-starburst regime” reinforces that molecular gas is the key prerequisite for star formation. A nearly linear correlation over this whole range can also be restated as the absence of a strong relationship between the ratio $\Sigma_{\text{SFR}}/\Sigma_{\text{H}_2}$ and Σ_{H_2} . This implies that Σ_{H_2} averaged over a large area is not a key environmental quantity for star formation because it does not affect the rate of star formation per unit molecular gas. Apparently the global amount of H_2 directly sets the global amount of star formation but the surface density of H_2 does not affect how quickly molecular gas is

converted to stars.

By contrast, the host galaxy does appear to affect the ratio of star formation rate to at least CO intensity. This indicates important environmental variations but they are not closely linked to surface density. In this sense, Figure 4.7 & 4.8 offer a counterargument against the idea of a star formation “law” in which gas surface density alone sets the star formation rate. Instead, over the disks of normal galaxies, we see star formation governed by two processes: (a) the formation of stars in molecular gas, which varies mildly from galaxy to galaxy but appears largely fixed inside a galaxy, and (b) the conversion of HI to H₂, which does exhibit a strong dependence on environment inside a galaxy, including a strong dependence on surface density (Section 4.6.2). In the second part of this paper we will look at this second process by measuring variations in the H₂–HI balance as a function of gas surface density and radius.

Systematic Effects: We have interpreted the observed scaling relations in terms of a relationship between molecular gas and recent star formation rate. Leroy et al. (2008) demonstrated that azimuthally averaged profiles of the FUV+24 μ m combination that we use here match those of several commonly used star formation rate tracers with $\sim 50\%$ scatter. Here we have shown that using a combination of H α +24 μ m to determine the SFR leads to indistinguishable results (see Leroy et al. 2011, in prep. for more discussion). We now discuss several systematic effects that may affect the translation from observables to inferred quantities.

The most serious worry is that the IR intensity, which drives the correlations, is acting as a tracer of dust abundance and not recent star formation. Gas and dust are observed to be well mixed in the ISM, so in the extreme, this would result in plotting gas against gas times some scaling factor (the dust–to–gas ratio). A more subtle version of the same concern is that CO emission is primarily a function of dust shielding against dissociating UV radiation. If there are large variations in the abundance of dust in the ISM then it may be likely that dust emission and CO emission emerge from the same regions because that is where CO can form and evade dissociation.

A few considerations suggest that the 24 μ m and the 70 μ m emission are not primarily tracing dust abundance. First, over whole galaxies, monochromatic IR emission at 24 μ m and 70 μ m does track the SFR (with some important variations among types of galaxy; see Calzetti et al., 2010). Second, we observe a linear correlation with CO emission and not with overall gas column, which one might expect for a dust tracer. Third, both the 24 μ m and 70 μ m bands are well towards the blue side of the peak of the IR SED for dust mixed with non star-forming gas (Boulanger et al., 1996) and so are not likely to be direct tracers of the dust optical depth (mass). Still, a thorough investigation of the interplay between dust abundance, IR emission, and star formation is needed to place SFR tracers involving IR emission on firmer physical footing.

A less severe worry is that using dust and FUV emission makes us sensitive to an old stellar component that might not have formed locally. Our targets are all actively star-forming systems, so old here means mainly old relative to H α emission ($\tau \sim 4$ Myr; McKee & Williams, 1997). The appropriate timescale to use when relating star formation and gas is ambiguous. When studying an individual region, it may be desirable to use a tracer with the shortest possible time sensitivity. Averaging over large parts of galaxies, one is

implicitly trying to get at the equilibrium relation. Therefore a tracer with a somewhat longer timescale sensitivity may actually be desirable. The typical 20 – 30 Myr timescale (Salim et al., 2007) over which most UV emission (and dust heating from B stars) occurs is well matched to current estimates for the lifetimes of giant molecular clouds (Kawamura et al., 2009). This makes for a fairly symmetric measurement — with the spatial and time scales of the two axes matched — though one is comparing recent star formation with the material of future star-forming regions.

The fact that SFRs derived from FUV+24 μ m and H α +24 μ m are essentially indistinguishable indicates that the distinction between the time scale probed by H α (\sim 4 Myr) and FUV (20 – 30 Myr) is not important to this study, probably because of the large spatial scales considered by our azimuthal averages.

There may also be systematic biases in our inferred Σ_{H_2} . We have already discussed the dependence of X_{CO} on metallicity as a possible explanation for the high SFR-to-CO ratio observed in lower-mass galaxies. X_{CO} certainly depends on metallicity. Current best estimates imply a non-linear relationship, with X_{CO} sharply increasing below $12 + \log_{10} \text{O}/\text{H} \sim 8.2 - 8.4$ (Wolfire et al., 2010; Glover et al., 2010; Leroy et al., 2011). For our range of metallicities ($\sim 8.4 - 9.0$) neither the estimates of X_{CO} nor the metallicity measurements are accurate enough that we feel comfortable applying a correction to our data. Instead, under the assumption of a fixed SFR-to-H $_2$ ratio, the observed SFR-to-CO ratio can be utilized to constrain the metallicity dependence of the X_{CO} factor. Krumholz et al. (2011) adopt a version of this approach using literature data and show that the observed metallicity variation of the SFR-to-CO ratio is broadly consistent with X_{CO} predicted by Wolfire et al. (2010), though with large scatter. We therefore expect that X_{CO} does affect our results, creating much of the observed offset to higher SFR for low-mass galaxies. Subsequent analysis, especially comparison to *Herschel* dust maps, will reveal if there are also important second-order effects at play within galaxies.

Variations in the CO(2 \rightarrow 1)/CO(1 \rightarrow 0) line ratio create a second potential bias in Σ_{H_2} . We adopt a fixed ratio of 0.7 based on comparison to literature CO(1 \rightarrow 0) data. This is somewhat higher than the observed ratio in the inner part of the Milky Way (Fixsen et al., 1999), ~ 0.5 , though the uncertainties on that ratio are large. More important, Fixsen et al. (1999) suggest variations in the CO line ratios between the inner and outer Milky Way and there are well-established differences between normal disk and starburst galaxies. Although not immediately apparent from a comparison of HERACLES to literature CO(1 \rightarrow 0) data (Leroy et al., 2009), such variations could affect our derived Σ_{H_2} by as much as $\sim 50\%$. Rosolowsky et al. (2011, in prep.) will present a thorough investigation of how the line ratio varies with environment in HERACLES.

4.6.2 Distribution of Molecular Gas

The tight correlation between SFR tracers and CO emission across all regimes strongly reinforces the primary importance of molecular gas to star formation. In this section, we therefore examine the distribution of molecular gas in galaxies. In the outer parts of spiral galaxies where $\Sigma_{\text{HI}} > \Sigma_{\text{H}_2}$, the formation of molecular gas from atomic gas appears to represent the bottleneck to star formation and the relative abundance of H $_2$ and HI

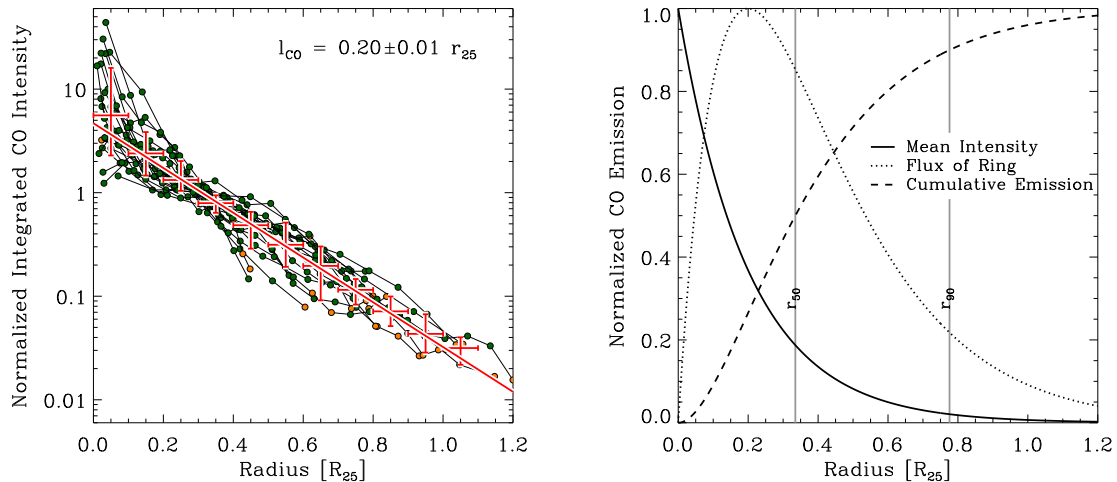


Figure 4.11 (*left*) Normalized CO intensity (y -axis) as a function of galactocentric radius (x -axis) in units of r_{25} , the 25th magnitude B -band isophote for a respective galaxy. The CO intensity is normalized so that an exponential fit to the profile has intensity 1 at $0.3 r_{25}$. Crosses mark the median and the 1σ scatter among galaxies in a series of radial bins (including only galaxies with at least marginal data in that bin). The average decline can be parametrized by an exponential with scale length of $0.2 r_{25}$ with no clear evidence of a truncation or break. (*right*) Schematic diagram for an exponential disk with scale length $0.2 r_{25}$. We plot mean intensity, flux in each ring, and enclosed luminosity as functions of radius. Gray lines show r_{50} and r_{90} , the radii at which 50 and 90% of the flux are enclosed.

is key to setting the star formation rate (e.g., Leroy et al., 2008; Bigiel et al., 2010a). We can apply the large dynamic range in H_2 -to-HI ratios achieved by stacking to make improved measurements of how this key quantity varies across galaxies.

Radial Distribution of CO Intensity

Many previous studies have shown that azimuthally averaged CO emission decreases with increasing galactocentric radius (e.g., Young & Scoville, 1991; Young et al., 1995; Regan et al., 2001; Schuster et al., 2007). Whereas galaxy centers often exhibit deviations from the large scale trend, CO emission outside the centers declines approximately uniformly with radius (Young et al., 1995). A first analysis of the HERACLES data revealed a characteristic exponential decline of CO emission in the inner parts of galaxy disks, with the scale length of CO emission similar to that of old stars and tracers of recent star formation (Leroy et al., 2009). With the increased sensitivity from stacking and a larger sample, we can revisit this question and ask if this radial decline in CO intensity continues smoothly out to $\sim 1 r_{25}$.

From exponential fits to the high-significance CO data of each galaxy⁷ (solid-dashed

⁷ We exclude the following galaxies from the analysis because (a) their emission is compact compared to our beam: NGC 337, 3049, 3077, 4625; (b) they are barely detected: NGC 4214, 4559; (c) their

lines in the lower panels of Figures A.1), excluding the galaxy centers (inner $30''$) we find a median exponential scale length, l_{CO} , of $0.21 r_{25}$ with 68% of all l_{CO} between $0.16 - 0.28 r_{25}$. This value agrees well with typical scale lengths found in previous studies (e.g., Young et al., 1995) and the individual galaxy scale lengths agree well with previous work on the HERACLES sample (Leroy et al., 2009).

The normalizations of these fits reflect galaxy-to-galaxy variations in the total molecular gas content. In the left panel of Figure 4.11 we show all profiles aligned to a common normalization. We plot the radius in units of r_{25} , the 25th magnitude B -band isophote, and normalize each profile so that the exponential fits have intensity 1 at $r_{\text{gal}} = 0.3 r_{25}$. The figure thus shows the radial variation of CO intensity across our sample, controlled for the overall CO luminosity and absolute size of each galaxy. Thick crosses mark the median CO intensity and the 68th percentile range in bins $0.1 r_{25}$ wide. The same exponential decline seen in individual profiles is even more evident here, with $l_{\text{CO}} = 0.20 \pm 0.01 r_{25}$ for the average of the sample.

The left panel in Figure 4.11 shows that the radial decline of the CO profiles observed previously for the inner part of galaxies extends without significant changes out to our last measured data points. In most galaxies there is no clear evidence for a sharp cutoff or a change in slope. As long as the normalized profiles are above the sensitivity limit the decline appears to continue (without significant deviation) with $l_{\text{CO}} = 0.20 r_{25}$ on average. This smooth exponential decline in CO intensity with increasing radius suggests that the observed decline in star formation rate from the inner to outer parts of galaxy disks is driven by a continuous decrease in the supply of molecular gas, rather than a sharp threshold of some kind.

There are several galaxies which deviate from this median exponential trend. We already noted above that we do not fit exponential profiles to NGC 2798, 2976, 4725 because their gas (HI and CO) radial profiles are insufficiently parametrized by exponentials. There are three galaxies (NGC 2146, 2903, 4569) that we do fit and determine small exponential scale lengths, $l_{\text{CO}} \lesssim 0.1 r_{25}$. NGC 2146 hosts an ongoing starburst and both NGC 2903 and NGC 4569 have prominent bars that may be funneling molecular gas to their centers. For two other galaxies (NGC 2841 and 4579) we determine large exponential scale lengths, $l_{\text{CO}} \gtrsim 0.3 r_{25}$. These galaxies are better described by a flat distribution (or even a central depression) and a cutoff at larger radii.

The tight correspondence of the CO scale length, l_{CO} to r_{25} has been noted before (Young et al., 1995), while other studies have found a close correspondence between CO and near-infrared light (Regan et al., 2001; Blitz & Rosolowsky, 2004). In our sample there is a fairly good correspondence between r_{25} and the near-infrared scale length, $l_{3.6}$, measured at $3.6 \mu\text{m}$ with $r_{25} \approx 4.7 \pm 0.8 l_{3.6}$ (Leroy et al., 2008, a treatment of a larger sample suggests a slightly lower ratio of ~ 4.1 with similar error bars). The near-infrared light should approximately trace the distribution of stellar mass, so that our measured scale length is very similar to that of the stellar mass. This tight coupling has been interpreted to indicate the importance of the stellar potential well to collecting star-forming material (Blitz & Rosolowsky, 2006). Here we see this correspondence to continue into the regime where the molecular gas is not the dominant gas component,

morphology is not well parametrized by an exponential: NGC 2798, 2976, 4725.

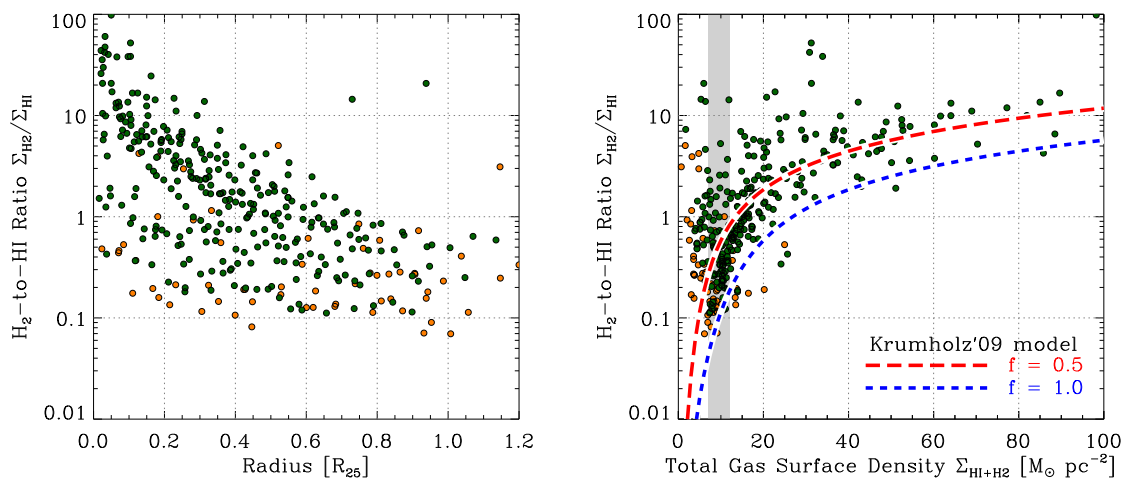


Figure 4.12 The molecular–atomic ratio, $R_{\text{H}_2} = \Sigma_{\text{H}_2}/\Sigma_{\text{HI}}$ as function of galactocentric radius (left panel), and total gas surface density, $\Sigma_{\text{HI}+\text{H}_2}$ (right panel). The dotted line in the right panel shows R_{H_2} as predicted by a theoretical model by Krumholz et al. (2009a, see text). The gray shaded area indicates data that are shown as function of radius in Figure 4.13. We observe large variations in R_{H_2} as function of radius and total gas surface density, however neither quantity is sufficient to parametrize the observed trend.

confirming that molecular gas formation is the bottleneck to star formation.

The right panel in Figure 4.11 shows the distribution of enclosed luminosity, mean intensity, and flux at each radius for an exponential disk with scale length of $0.2 r_{25}$. The brightest individual ring for such a disk lies at $0.2 r_{25}$ and half the flux is enclosed within $r_{50} \approx 0.3 r_{25}$. This value, r_{50} , is fairly close to the radius at which $\Sigma_{\text{HI}} \approx \Sigma_{\text{H}_2}$ in a typical disk galaxy (see the left panel of Figure 4.12 and Leroy et al., 2008), so that CO emission is about evenly split between the H_2 -dominated and HI-dominated parts of such a galaxy. Meanwhile, 90% of the flux lies within $r_{90} \sim 0.8 r_{25}$ a value that is very similar to the threshold radius identified by Martin & Kennicutt (2001). We do not find evidence to support a true break at this radius, but as an “edge” to the star-forming disk, a 90% contour may have utility.

The H_2 -to-HI Ratio

In the outer parts of galaxy disks — and thus over most of the area in galaxy disks — we have $\Sigma_{\text{HI}} \gtrsim \Sigma_{\text{H}_2}$, implying that star-forming H_2 gas does not make up most of the interstellar medium. In this regime the relative abundance of H_2 and HI is a key quantity to regulate the star formation rate. Observations over the last decade have revealed strong variations of the fraction of gas in the molecular phase as a function of galactocentric radius, total gas surface density, stellar surface density, disk orbital time, and interstellar pressure (Wong & Blitz, 2002; Heyer et al., 2004; Blitz & Rosolowsky, 2006; Leroy et al., 2008; Wong et al., 2009). In Figure 4.12 we show the two most basic of these trends, the H_2 -to-HI ratio, $R_{\text{H}_2} = \Sigma_{\text{H}_2}/\Sigma_{\text{HI}}$, as a function of normalized galactocentric radius

(left panel) and total gas surface density (right panel). We focus on R_{H_2} because it is more easily separated in discrete observables than the fraction of gas that is molecular, $f_{\text{H}_2} = \Sigma_{\text{H}_2}/(\Sigma_{\text{HI}} + \Sigma_{\text{H}_2}) = R_{\text{H}_2}/(1 + R_{\text{H}_2})$. This makes it easier to interpret uncertainties and systematic effects like changes in the CO-to-H₂ conversion factor.

The left panel of Figure 4.12 shows R_{H_2} as function of galactocentric radius in units of r_{25} for all data detected with high or marginal significance. For clarity, we do not plot R_{H_2} for regions where we determined only upper limits in CO intensity; for the inner parts ($r < 0.6 r_{25}$) these upper limits are bounded by $R_{\text{H}_2} \lesssim 0.3$, whereas for outer parts ($r > 0.6 r_{25}$) the upper limits in Σ_{H_2} are typically of comparable magnitude as measurements of Σ_{HI} and upper limits are bounded by $R_{\text{H}_2} \lesssim 1$. In agreement with Wong & Blitz (2002), Heyer et al. (2004), Bigiel et al. (2008), and Leroy et al. (2008) we find R_{H_2} to decline with increasing galactocentric radius, a variation that reflects the distinct radial profiles of atomic and molecular gas. However, radial variations alone do not explain the full range of observed molecular fractions because R_{H_2} can vary by up to two orders of magnitude at any given galactocentric radius.

A significant part of the variations in R_{H_2} at a given galactocentric radius corresponds to systematic variations between galaxies. These are mainly caused by variations in the absolute molecular gas content of a galaxy and can be removed by a normalization procedure similar to one applied in the left panel of Figure 4.11. The result is similar to that seen for the radial profiles of CO: the relationship tightens and we can see that most of the decline of R_{H_2} inside a galaxy occurs radially. However, there is significantly more scatter remaining in R_{H_2} versus radius than we observed for the normalized CO radial profiles, highlighting the importance of parameters other than a combination of radius and host galaxy to set R_{H_2} .

In addition to declining with increasing galactocentric radius, R_{H_2} increases as the total gas surface density, $\Sigma_{\text{gas}} = \Sigma_{\text{HI}} + \Sigma_{\text{H}_2}$, increases. The more gas that is present along a line of sight, the larger the fraction of gas that is molecular. The right panel of Figure 4.12 shows this result, plotting R_{H_2} as function of the total gas surface density, Σ_{gas} . R_{H_2} increases with increasing Σ_{gas} , with regions of high surface density, $\Sigma_{\text{gas}} \gtrsim 20 M_{\odot} \text{pc}^{-2}$, being predominately molecular, $R_{\text{H}_2} \gtrsim 1$.

At high Σ_{gas} , the right panel of Figure 4.12 is largely a way of visualizing the ‘‘saturation’’ of Σ_{HI} on large scales in galaxies. A number of authors have found that averaged over hundreds of parsecs to kpc scales, Σ_{HI} rarely exceeds $\sim 10 M_{\odot} \text{pc}^{-2}$ (Wong & Blitz, 2002). This limit is clearly violated at high spatial resolution (e.g. Kim et al., 1999; Stanimirovic et al., 1999; Brinks & Shane, 1984) and may vary among classes of galaxies. Several recent theoretical works have aimed at reproducing this behavior. Krumholz et al. (2009a) focused on shielding of H₂ inside individual atomic–molecular complexes, whereas Ostriker et al. (2010) examined the interplay between large–scale thermal and dynamical equilibria.

The right panel in Figure 4.12 includes also the predicted solar–metallicity $\Sigma_{\text{gas}}-R_{\text{H}_2}$ relation from Krumholz et al. (2009a, their Equations 38 & 39). They model individual atomic–molecular complexes, however these complexes have a filling factor substantially less than 1 inside our beam. The appropriate Σ_{gas} to input into their model is therefore the average surface densities of the complexes, Σ_{comp} , within our beam, which will be

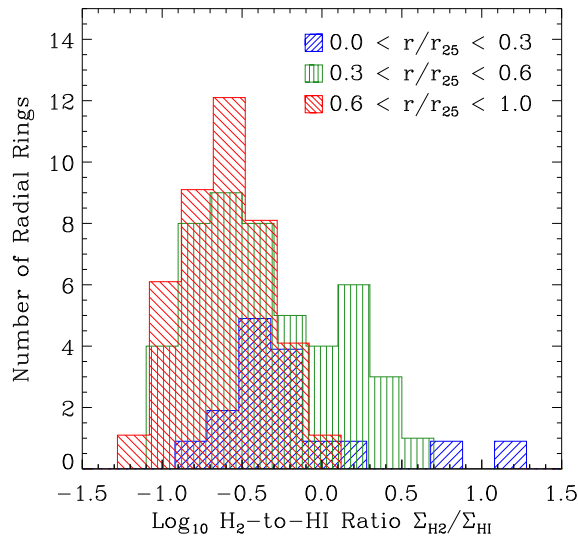


Figure 4.13 The radial dependence of R_{H_2} for regions with comparable total gas surface density, $\Sigma_{\text{HI}+\text{H}_2} = 7 - 12 \text{ M}_\odot \text{ pc}^{-2}$. The data are taken from the gray highlighted region in the left panel of Figure 4.12. R_{H_2} is not sufficiently determined by the total gas surface density but shows also a radial dependence.

related to our observed surface density, Σ_{gas} , by the filling factor, f , namely: $\Sigma_{\text{gas}} = f \Sigma_{\text{comp}}$. The model curve (blue short-dashed line) with a filling factor $f = 1$ is offset towards higher Σ_{gas} (shifted right) or lower R_{H_2} (shifted down) compared to our data. To have the model curve intersect our data (red long-dashed line) requires a filling factor of $f \approx 0.5 - 1$, so that atomic-molecular complexes fill about half the areas in our beam. This is before any accounting for the presence of diffuse HI not in star-forming atomic-molecular complexes and is assuming a fixed filling factor, both of which are likely oversimplifications. Nonetheless, the Krumholz et al. (2009a) curve does show an overall good correspondence to our data.

As with the radius, the total gas surface density predicts some of the broad behavior of R_{H_2} but knowing Σ_{gas} does not uniquely specify the amount of molecular gas, particularly at low Σ_{gas} . This is visible as the large scatter in R_{H_2} at low surface densities in the right panel of Figure 4.12. The scatter reflects a dependence of R_{H_2} on environmental factors other than gas surface density. Figure 4.13 shows R_{H_2} over the small range $\Sigma_{\text{gas}} = 7 - 12 \text{ M}_\odot \text{ pc}^{-2}$, i.e., the data from the gray highlighted region in Figure 4.12. We plot histograms for several radial bins which are clearly offset, indicating an additional radial dependence of R_{H_2} . At small radii ($r \lesssim 0.3 r_{25}$) we observe a large scatter in R_{H_2} for $\Sigma_{\text{gas}} = 7 - 12 \text{ M}_\odot \text{ pc}^{-2}$ whereas at large radii ($r \gtrsim 0.6 r_{25}$) gas with this surface density is always predominantly HI.

As was the case in SFR- H_2 space, distinct populations of galaxies are responsible for some of the variations in the right panel of Figure 4.12. Early type (Sab-Sb) spirals (e.g., NGC 2841, 3351, 3627, 4736) often show large molecular fractions, $R_{\text{H}_2} \gtrsim 0.5$, but typically have low HI and H_2 surface densities, Σ_{HI} and $\Sigma_{\text{H}_2} \approx 1 - 5 \text{ M}_\odot \text{ pc}^{-2}$. By contrast, massive Sc galaxies (e.g., NGC 4254, 4321, 5194, 6946) can have comparably high

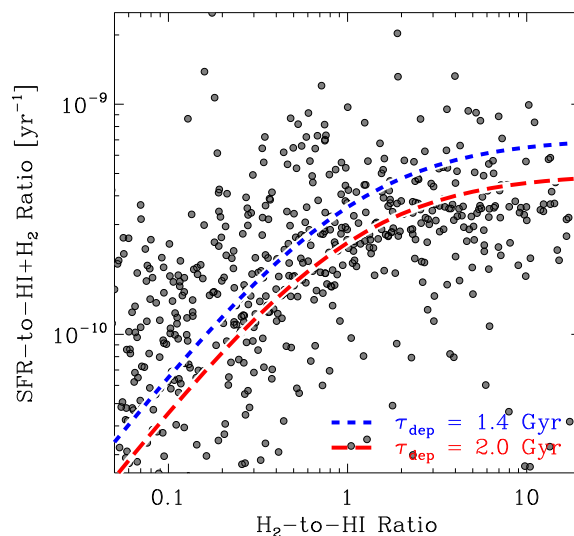


Figure 4.14 The recent star formation rate per unit total gas, $\Sigma_{\text{SFR}}/\Sigma_{\text{HI}+\text{H}_2}$ (the inverse of the total gas depletion time; y -axis), as function of the molecular-atomic gas ratio, $R_{\text{H}_2} = \Sigma_{\text{H}_2}/\Sigma_{\text{HI}}$ (x -axis). A fixed ratio of SFR-to- H_2 is shown by the blue dotted line for a *molecular* gas depletion time of $\tau_{\text{dep}} \approx 1.4$ Gyr and by the red dashed line for $\tau_{\text{dep}} \approx 2$ Gyr. In regions dominated by molecular gas ($R_{\text{H}_2} > 1$) the $\Sigma_{\text{SFR}}/\Sigma_{\text{HI}+\text{H}_2}$ ratio approximates a value corresponding to the constant molecular depletion time, τ_{dep} . In regions of small molecular gas fraction ($R_{\text{H}_2} < 1$) the $\Sigma_{\text{SFR}}/\Sigma_{\text{HI}+\text{H}_2}$ ratio decreases significantly indicating that the total gas does not scale uniformly with the recent star formation rate.

molecular fractions, $R_{\text{H}_2} \approx 0.35-1$, but have higher surface density HI disks, $\Sigma_{\text{HI}} \approx 5-10 M_{\odot} \text{pc}^{-2}$, so that these fractions occur at higher Σ_{gas} . A trend with metallicity is not immediately obvious in the data but these differences may reflect the more substantial stellar surface densities found in the earlier-type galaxies. This increased stellar surface density results in a stronger gravitational field, which could lead to a higher midplane gas pressure (Blitz & Rosolowsky, 2006) and a low fraction of diffuse HI gas (Ostriker et al., 2010).

Discussion of R_{H_2}

Following several recent studies we observe strong systematic variations in the H_2 -HI balance across galaxies. Two of the strongest behaviors are an approximately exponential decrease in R_{H_2} with increasing galactocentric radius and a steady increase in R_{H_2} with increasing gas surface density. Our improved sensitivity shows these trends extending to low surface densities and our expanded sample makes clear that neither of these basic parametrizations adequately captures the entire range of R_{H_2} variations. The likely physical drivers for the scatter in R_{H_2} that we observe are metallicity and dust-to-gas ratio (e.g., Leroy et al., 2008; Krumholz et al., 2009a; Gnedin et al., 2009, Bolatto et al. 2011, in prep.), the dissociating radiation field (e.g., Robertson & Kravtsov, 2008), variations in interstellar gas pressure and density (e.g., Elmegreen, 1994; Wong & Blitz, 2002; Blitz

& Rosolowsky, 2006), and external perturbations that drive gas to higher densities (e.g., Blitz & Rosolowsky, 2006; Bournaud et al., 2010). Each of these quantities are observationally accessible in our sample (e.g., Leroy et al., 2008) and estimates of the relative roles of each process will be presented in Leroy et al. (2011, in prep.).

The overall relationship of total gas and star formation rate (middle panels of Figure 4.10) can be reproduced by a roughly fixed ratio of SFR-to- H_2 within galaxies (Section 4.6.1) and the observed scaling of R_{H_2} with Σ_{HI+H_2} (Section 4.6.2). This is shown in Figure 4.14, where we plot the SFR per unit total gas, $\Sigma_{SFR}/\Sigma_{HI+H_2}$ (the inverse of the *total* gas depletion time) as function of the molecular-to-atomic ratio, $R_{H_2} = \Sigma_{H_2}/\Sigma_{HI}$. At low surface densities, the R_{H_2} - Σ_{HI+H_2} relation regulates Σ_{SFR} , at high surface densities where almost all of the gas is molecular the SFR- H_2 scaling determines the observed ratio. This trend is well parametrized by a fixed SFR-to- H_2 ratio with a *molecular* gas depletion time of $\tau_{dep} \approx 1.4$ Gyr (blue dotted line) for all of our targets and $\tau_{dep} \approx 2$ Gyr (red dashed line) for big spirals (i.e. using the same sample as Bigiel et al., 2008; Leroy et al., 2008). The transition between these two regimes creates the curved shape seen in Figure 4.10 & 4.14. This offers more support for a modified version of the classical picture of a star formation threshold (Skillman, 1987; Kennicutt, 1989; Martin & Kennicutt, 2001), in which dense, mostly molecular gas forms stars but the efficiency with which such (molecular) gas forms is a strong function of environment, decreasing steadily with decreasing gas surface density and increasing galactocentric radius.

4.7 Summary

We combine HERACLES CO(2 \rightarrow 1) data with HI velocity fields, mostly from THINGS, to make sensitive measurements of CO intensity across the disks of 33 nearby star-forming galaxies. We stack CO spectra across many lines of sight by assuming that the mean HI and CO velocities are similar, an assumption that we verify in the inner parts of galaxies. This approach allows us to detect CO out to galactocentric radii $\sim 1 r_{25}$. Because we measure integrated CO intensities as low as 0.3 K km s^{-1} ($\sim 1 M_{\odot} \text{ pc}^{-2}$, before any correction for inclination) with high significance, we are able to robustly measure CO intensities in parts of galaxies where most of the ISM is atomic.

Using this approach we compare the radially averaged intensities of FUV, $H\alpha$, IR, CO, and HI emission across galaxy disks. We find an approximately linear relation between CO intensity and monochromatic IR intensity at both $24 \mu\text{m}$ and $70 \mu\text{m}$. For the first time, we show that these scaling relations continue smoothly from the H_2 -dominated to HI-dominated ISM. Extinction causes FUV and $H\alpha$ emission to display a more complex relationship with CO, especially in the inner parts of galaxies. In the outer parts of galaxy disks FUV and $H\alpha$ emission do correlate tightly with CO emission after galaxy-to-galaxy variations are removed.

We use two calibration to estimate the recent star formation rate, FUV+ $24\mu\text{m}$ and $H\alpha$ + $24\mu\text{m}$, which we compare to H_2 derived from CO. We find an approximately linear relation between Σ_{SFR} and Σ_{H_2} in the range of $\Sigma_{H_2} \approx 1 - 100 M_{\odot} \text{ pc}^{-2}$ with no notable variation between the two SFR estimates. A number of recent studies (Bigiel et al., 2008; Leroy et al., 2008; Blanc et al., 2009; Bigiel et al., 2011) have also seen a roughly

linear relationship between Σ_{SFR} and Σ_{H_2} and have argued that it implies that the surface density of H_2 averaged over large scales does not strongly affect the efficiency with which molecular gas forms stars.

We do find evidence for variations in the SFR-to-CO ratio among galaxies. Indeed, most of the scatter in the relations between CO and SFR tracers is driven by galaxy-to-galaxy variations. These variations are not random, but show the trend observed by Young et al. (1996) that lower mass, lower metallicity galaxies have higher ratios of SFR-to- H_2 than massive disk galaxies. It will take further study to determine whether these are real variations in the efficiency of star formation or reflect changes in the CO-to- H_2 conversion factor due to lower metallicities in these systems. After removing these galaxy-to-galaxy variations the composite H_2 -SFR relation is remarkably tight, reinforcing a close link between H_2 and star formation inside galaxies.

We compare the scaling between the surface densities of SFR and H I, H_2 , and total gas ($\text{H I} + \text{H}_2$). The relationship between SFR and total gas has roughly the same rank correlation coefficient as that between SFR and H_2 , but does not obey a single functional form. Where $\Sigma_{\text{H I}} > \Sigma_{\text{H}_2}$ the relationship between Σ_{SFR} and $\Sigma_{\text{H I} + \text{H}_2}$ is steep whereas where $\Sigma_{\text{H I}} < \Sigma_{\text{H}_2}$ the relationship is much flatter. Meanwhile, we observe a linear relationship between Σ_{H_2} and Σ_{SFR} for the full range of $\Sigma_{\text{H}_2} = 1 - 100 \text{ M}_\odot \text{ pc}^{-2}$. $\Sigma_{\text{H I}}$ and Σ_{SFR} are weakly correlated and exhibit a strongly nonlinear relation, except at very large radii.

The unbroken extension of the $\Sigma_{\text{SFR}} - \Sigma_{\text{H}_2}$ relation into the H I-dominated regime suggests a modified version of the classical picture of a star formation threshold (Skillman, 1987; Kennicutt, 1989; Martin & Kennicutt, 2001), in which stars form at fixed efficiency out of molecular gas, to first order independent of environment within a galaxy. The observed turn-over in the relation between SFR and *total* gas relates to the H_2 -to-H I ratio which is a strong function of environment.

We therefore investigate the distribution of H_2 traced by CO using our stacked data and compare it to the H I. On large scales we observe CO to decrease exponentially with a remarkably uniform scale length of $\sim 0.2 r_{25}$, again extending previous studies to lower surface densities. We find the normalization of this exponential decline to vary significantly among galaxies. The H_2 -to-H I ratio, traced by the ratio of CO-to-H I intensities, also varies systematically across galaxies. It exhibits significant correlations with both galactocentric radius and total gas surface density and we present high-sensitivity measurements of both of these relationships. However, neither quantity is sufficient to uniquely predict the H_2 -to-H I ratio on its own.

It is a pleasure to thank my collaborators on this project:

Adam Leroy (MPIA, NRAO), Fabian Walter (MPIA), Frank Bigiel (UC Berkeley), Elias Brinks (University of Hertfordshire), Erwin de Blok (University of Cape Town), Gaelle Dumas (MPIA), Carsten Kramer (IRAM), Erik Rosolowsky (University of Okanagan), Karin Sandstrom (MPIA), Karl Schuster (IRAM), Antonio Usero (Observatorio Astronómico Nacional, Madrid), Axel Weiss (MPIfR), and Helmut Wiesemeyer (IRAM)

5 Low CO Luminosities in Dwarf Galaxies

5.1 Context

In the previous Chapter we studied the ISM phase balance and the star formation relation in azimuthally-averaged radial profiles. This study has been successful to determine the radial distribution of CO emission in spiral galaxies but resulted in non-detections for a dozen of dwarf galaxies (which have therefore been neglected in the previous Chapter). In this Chapter now, we come back to these dwarf galaxies to perform a more detailed search for CO emission. Many previous studies have tried to detect CO in dwarf galaxies and many of those have failed. Because of the general faintness of CO, most studies concentrated on (single) pointed observations. However, these observations are inadequate to constrain the total CO luminosity of dwarf galaxies. Contrary to previous CO observations in dwarf galaxies, the HERACLES survey did map large parts of dwarf galaxies using the most sensitive instrument available and thus for the first time offers the prospect to constrain the total CO luminosity of dwarf galaxies. In this Chapter we will use the stacking method introduced in the previous Chapter to carefully search for CO emission in dwarf galaxies ranging from individual lines-of-sight, stacking the data of all star-forming regions, and up to the entire galaxy (or map) extent.

5.2 Abstract¹

We present maps of $^{12}\text{CO } J = 2 - 1$ emission covering the whole star-forming disk of 16 nearby dwarf galaxies observed by the IRAM HERACLES survey. The data have $13''$ angular resolution, ~ 250 pc at our average distance of $D = 4$ Mpc, and sample the galaxies by $10 - 1000$ resolution elements. We apply stacking techniques to perform the first sensitive search for CO emission in dwarf galaxies outside the Local Group ranging from individual lines-of-sight, stacking over IR-bright regions of embedded star formation, and stacking over the whole galaxy. We detect 5 galaxies in CO with total CO luminosities of $L_{\text{CO}2-1} = 3 - 28 \times 10^6 \text{ K km s}^{-1} \text{ pc}^2$. The other 11 galaxies remain undetected in CO even in the stacks and have $L_{\text{CO}2-1} \lesssim 0.4 - 8 \times 10^6 \text{ K km s}^{-1} \text{ pc}^2$. We combine our sample of dwarf galaxies with a large sample of spiral galaxies from the literature to study scaling relations of $L_{\text{CO}2-1}$ with M_{B} and metallicity. We find that dwarf galaxies with metallicities

¹ This Chapter will be submitted as: Schrubba, A, Leroy, A. K., Walter, F., Bigiel, F., Brinks, E., de Blok, W. J. G., Dumas, G., Kramer, C., Rosolowsky, E., Sandstrom, K., Schuster, K., Usero, A., Weiss, A., Wiese Meyer, H., 2011, AJ

of $Z \approx 1/2 - 1/10 Z_{\odot}$ have $L_{\text{CO}2-1}$ of 2 – 4 orders of magnitude smaller than massive spiral galaxies and that their $L_{\text{CO}2-1}$ per unit L_{B} is 1 – 2 orders of magnitude smaller. A comparison with tracers of star formation (FUV and $24\mu\text{m}$) shows that $L_{\text{CO}2-1}$ per unit SFR is 1 – 2 orders of magnitude smaller in dwarf galaxies. While this may indicate that dwarf galaxies form stars much more efficiently, we argue that the low $L_{\text{CO}2-1}/\text{SFR}$ ratio is due to the fact that the CO-to- H_2 conversion factor, α_{CO} , changes significantly in low metallicity environments. Assuming that a constant H_2 depletion time of $\tau_{\text{dep}} = 1.8$ Gyr holds in dwarf galaxies (as found for a large sample of nearby spirals) implies α_{CO} values for dwarf galaxies with $Z \approx 1/2 - 1/10 Z_{\odot}$ that are more than one order of magnitude higher than those found in solar metallicity spiral galaxies. Such a significant increase of α_{CO} at low metallicity is consistent with previous studies, in particular those of Local Group dwarf galaxies which model dust emission to constrain H_2 masses. Even though it is difficult to parametrize the dependence of α_{CO} on metallicity given the currently available data the results suggest that CO is increasingly difficult to detect at lower metallicities. This has direct consequences for the detectability of star-forming galaxies at high redshift which presumably have on average sub-solar metallicity.

5.3 Introduction

Robust knowledge of the molecular (H_2) gas distribution is indispensable to understand star formation in galaxies. Observations in the Milky Way and nearby galaxies suggest that stars form in clouds consisting predominantly of H_2 (Lada & Lada, 2003; Fukui & Kawamura, 2010). Because H_2 is almost impossible to observe directly under typical conditions of the cold interstellar medium (ISM), its abundance and distribution has to be inferred using indirect methods. Observations of low rotational lines of carbon monoxide (CO) have been the standard method to do so as CO is the second most abundant molecule and easily excited in the cold ISM. Over the last decades on the order hundred galaxies in the local Universe have been successfully detected in CO. Over the last years CO has been detected throughout the Universe out to cosmological distances (Solomon & Vanden Bout, 2005). These CO observations have greatly enhanced our knowledge of H_2 in galaxies, the phase balance of the ISM, and its interplay with star formation.

Despite great advances in studying H_2 in massive star-forming galaxies, our knowledge of H_2 in star-forming dwarf galaxies remains poor. The CO emission in these systems has proven to be extremely faint and most studies targeting metal-poor dwarf galaxies have resulted in non-detections. For sensitivity reasons, surveys of dwarf galaxies have tended to target only a few systems and used mostly single pointings (Israel et al., 1995; Young et al., 1995; Taylor et al., 1998; Barone et al., 2000; Böker et al., 2003; Sauty et al., 2003; Albrecht et al., 2004; Leroy et al., 2005). These data are very heterogeneous as they target different CO transitions, different regions, have different beam sizes, different sensitivities, and different filling factors. Thus, conclusive results for basic quantities as the total CO luminosity of dwarf galaxies have not been reached and comparison to other observables have been complicated by these systematic effects.

CO observations are currently — and will remain — our most accessible tracer of cold H_2 in the local and distant Universe. It is thus important to obtain deep knowledge of the

connection between CO and H₂ in different environments. Inside individual molecular clouds, this dependence has proven to be highly complicated and influenced by many factors (e.g., Shetty et al., 2011a,b). Many of these dependencies average out on scales larger than individual clouds, however, metallicity will not. Metallicity may thus be the most important factor determining the CO/H₂ ratio on large scales. This makes a robust calibration of the CO/H₂ ratio as function of metallicity a viable input for all observational studies which use CO as a tracer of H₂. The need becomes strengthened as observations start probing the H₂ content of galaxies in the distant Universe where most stars presumably formed in environments with sub-solar metallicity.

To understand the environmental dependencies of the CO/H₂ ratio requires good knowledge of the CO content of all types of galaxies, even in those where we worry that CO may not trace H₂ in the same way as it does in massive spiral galaxies. This makes sensitive, wide-field CO maps of dwarf galaxies an important undertaking. The HERACLES survey (partly published in Leroy et al., 2009) has obtained those CO maps for a large set of nearby star-forming galaxies ranging from massive spirals down to low-mass, low-metallicity dwarfs. In conjunction with an extensive set of multi-wavelength data, this survey lead to a vast improvement of our knowledge of the relation between H I, CO, H₂, and star formation.

In this paper, we present sensitive measurements of CO emission of 16 nearby, low-mass, low-metallicity, star-forming dwarf galaxies from the HERACLES survey using stacking techniques. We use these data to study the relation between CO emission and other galaxy parameters, especially star formation rate (SFR) and H₂ mass. Then we analyze the CO/H₂ ratio as function of metallicity. In Section 5.4 we introduce our multi-wavelength data and summarize their basic properties. In Section 5.5 we make a careful search for CO emission for individual lines-of-sight, IR-bright regions, and whole galaxies. In Section 5.6 we compare these CO measurements to other galaxy parameters and compare the relationships found for dwarf galaxies to those of massive spiral galaxies. In Section 5.7 we study the metallicity dependence of the CO/H₂ ratio. We use observed SFRs to infer H₂ masses and thus constrain CO/H₂ and compare our results to results derived from other methods. In Section 5.8 we summarize our findings.

5.4 Data

We study 16 nearby, low-mass, star-forming galaxies from the HERACLES survey (Leroy et al., 2009); see Figure 5.1 for poster stamps of these galaxies. These data have been largely neglected in previous work on the HERACLES sample as their CO emission has rarely been robustly detected in the pixel-based studies of Bigiel et al. (2008, 2011) and Leroy et al. (2008) or the radial stacking analysis of Schruba et al. (2011); but see Leroy et al. (2009) for a description of the data of Ho I, Ho II, DDO 154, IC 2574, NGC 2976, and NGC 4214. Table 5.1 lists our sample of dwarf galaxies along with adopted distances, inclination, position angle, optical radius, metallicity, *B*-band optical magnitude, H I mass, and total star formation rate (SFR). These values are taken from Walter et al. (2008) where possible and from LEDA (Prugniel & Heraudeau, 1998) and NED elsewhere.

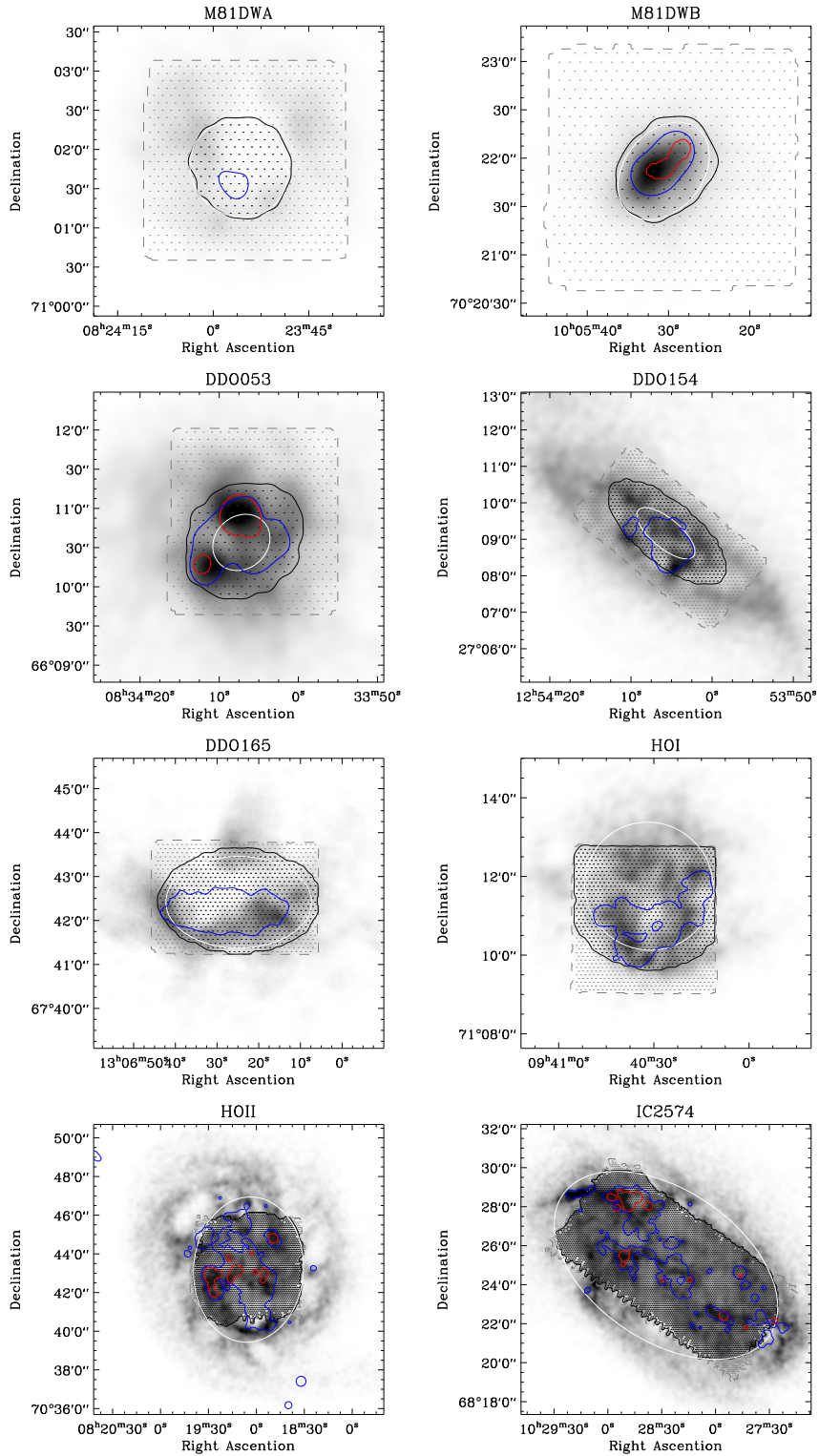


Figure 5.1 *Coverage of CO Observations.* For each HERACLES dwarf galaxy we show the coverage of our CO data (gray dashed line), the HI surface density (grayscale) at linear scale between 0–30 $M_{\odot} \text{pc}^{-2}$, the 24 μ m intensity (red contour) at 0.2 MJy sr^{-1} , the FUV intensity (blue contour) at 0.01 MJy sr^{-1} , and a galactocentric radius $R = 1 R_{25}$ (white contour). We determine the CO intensity at each sampling point (dot), and stack the data for the whole galaxy (inside black contour) and for IR-bright regions (red contour).

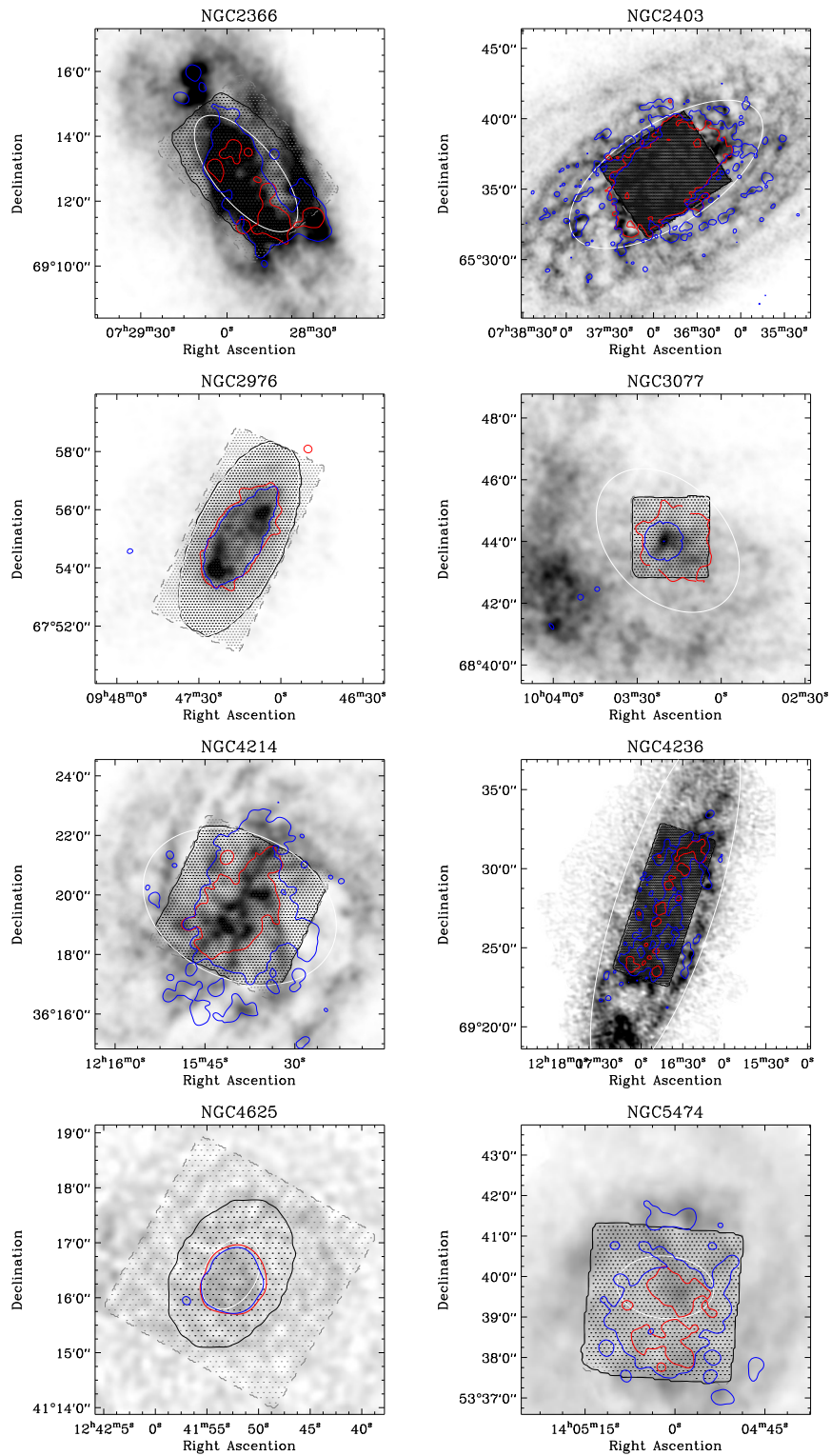


Figure 5.1 (Continued)

Table 5.1. Properties of Galaxy Sample

Name	Alt. Name	D (Mpc)	Incl. ($^{\circ}$)	P.A. ($^{\circ}$)	R_{25} ($'$)	Metal. ^a 12+logO/H	M_B^b (mag)	M_{HI}^c ($10^8 M_{\odot}$)	SFR ^d ($M_{\odot} \text{ yr}^{-1}$)
M81 Dw A		3.6	23	49	0.64	7.50	-11.4	0.12	0.0005
M81 Dw B	UGC 5423	5.3	44	321	0.56	8.02	-13.8	0.25	0.0023
DDO 053	UGC 4459	3.6	31	132	0.39	7.80	-13.9	0.60	0.0035
DDO 154	UGC 8024	4.3	66	230	0.98	7.78	-15.4	3.58	0.0056
DDO 165	UGC 8201	4.6	51	90	1.66	7.84	-14.1	6.33	0.0100
HO I	UGC 5139	3.8	12	50	1.65	7.83	-16.8	1.39	0.0100
HO II	UGC 4305	3.4	41	177	3.76	7.93	-12.5	5.95	0.0455
IC 2574	UGC 5666	4.0	53	56	6.41	8.05	-17.2	14.80	0.0718
NGC 2366	UGC 3851	3.4	64	40	2.20	7.96	-16.2	6.49	0.0605
NGC 2403	UGC 3918	3.2	63	124	7.87	8.57	-18.6	25.80	0.4140
NGC 2976	UGC 5221	3.6	65	335	3.60	8.67	-16.5	1.36	0.0895
NGC 3077	UGC 5398	3.8	46	45	2.70	8.64	-17.3	8.81	0.0838
NGC 4214	UGC 7278	2.9	44	65	3.40	8.25	-17.1	4.08	0.1208
NGC 4236	UGC 7306	4.4	75	162	11.99	8.46	-18.1	34.60	0.1409
NGC 4625	UGC 7861	9.5	47	330	0.69	8.70	-17.0	11.80	0.0716
NGC 5474	UGC 9013	6.8	50	85	1.20	8.57	-17.3	15.50	0.1069

Note. — (a) Oxygen abundance from Moustakas et al. (2010).

(b) B -band magnitude from HERACLES.

(c) M_{HI} from Walter et al. (2008).

(d) SFR(FUV+24) from this work.

5.4.1 CO Data

We take CO data from the HERACLES survey which mapped the $^{12}\text{CO } J = 2 \rightarrow 1$ emission line in 48 nearby galaxies using the IRAM 30m telescope (Leroy et al., 2009). The observations are designed to cover large parts of the galaxies and extend to 1 – 1.5 times the optical radius, R_{25} , for large spirals and up to 2 – 3 R_{25} for small galaxies. The final data cubes have an angular resolution (FWHM) of $13''$ and a spectral resolution (channel separation) of 2.6 km s^{-1} . The signal-to-noise is 20 – 30 mK per resolution element and per channel.

Whenever possible we compare our observed CO(2-1) data to literature measurements, for that we convert them to CO(1-0) intensities. We assume a constant line ratio, $R_{21} = I_{\text{CO } 2-1} / I_{\text{CO } 1-0} = 0.7$ (following Bigiel et al., 2011; Schruba et al., 2011). This is the average ratio found for all HERACLES galaxies (E. Rosolowsky et al., in preparation). We will discuss the CO-to- H_2 conversion factor extensively in Section 5.7 but note that a typical Galactic CO(1-0)-to- H_2 conversion factor is $X_{\text{CO}} = 2.0 \times 10^{20} \text{ cm}^{-2} (\text{K km s}^{-1})^{-1}$ (Strong & Mattox, 1996; Dame et al., 2001; Abdo et al., 2010) which translates to $\alpha_{\text{CO}} = 4.38 M_{\odot} \text{ pc}^{-2} (\text{K km s}^{-1})^{-1}$ when including a factor of 1.36 to account for heavy elements.

5.4.2 HI Data

We draw HI data mostly from the VLA THINGS survey (Walter et al., 2008). The HI data for NGC 4236, NGC 4626, and NGC 5474 are from the VLA programs AL 731, AL 735, and the archive. The HI data for DDO 165 is from the LITTLE THINGS survey (D. Hunter et al., in preparation). The angular resolution of these data is $\sim 10 - 20''$, the velocity resolution is $2.6 - 5.2 \text{ km s}^{-1}$ for the THINGS and LITTLE THINGS data, and $5.2 - 10 \text{ km s}^{-1}$ for the other data. The sensitivity of these data is sufficiently high to never limit our analysis.

5.4.3 Star Formation Tracers

We estimate the star formation rate (SFR) using a combination of FUV and $24\mu\text{m}$ emission following the approach introduced in Bigiel et al. (2008); Leroy et al. (2008) and intensively studied in A. K. Leroy et al. (in preparation). The SFR surface density is given by $\Sigma_{\text{SFR}} [\text{M}_{\odot} \text{ yr}^{-1} \text{ kpc}^{-2}] = 0.081 (I_{\text{FUV}} + 0.04 I_{24\mu\text{m}}) [\text{MJy sr}^{-1}] \times \cos i$. The FUV data are taken from the *GALEX* Nearby Galaxy Survey (Gil de Paz et al., 2007) or alternatively from the NASA Multimission Archive at STScI. They cover a wavelength range of $1350 - 1750 \text{ \AA}$, have angular resolution $\sim 4.5''$, and sufficient sensitivity to determine FUV intensities with high signal-to-noise throughout the star-forming disk. The IR data are taken from the *Spitzer* SINGS (Kennicutt et al., 2003a) and Local Volume Legacy (LVL) surveys (Dale et al., 2009). These data have $\sim 6''$ resolution; their sensitivity is sufficient to detect $24\mu\text{m}$ emission in most of our galaxies except the lowest mass and lowest metallicity dwarf galaxies. We apply some processing to the FUV and $24\mu\text{m}$ maps (i.e., mask foreground stars and flatten background) as described in A. K. Leroy et al. (in preparation).

5.4.4 Metallicities

Gas phase oxygen abundances (metallicities) are taken from Moustakas et al. (2010). For galaxy-integrated data we use the average of their “characteristic” metallicities (their Table 9) derived from a theoretical calibration (KK04 values) and an empirical calibration (PT05 values). In some plots we also show the radial stacking results from Schruba et al. (2011) for which we use the metallicity gradients from Moustakas et al. (2010, Table 8) again averaging the two calibrations. The “characteristic” metallicity of a galaxy corresponds to the value of the metallicity gradient at radius $R = 0.4 R_{25}$.

5.4.5 Sampling

We convolve all our data to a common resolution of $13''$ (limited by the CO data) and sample them by a hexagonally packed grid spaced by half a beam size ($6.5''$). For each line-of-sight we collect observed intensities of CO, HI, FUV, and $24\mu\text{m}$, and determined local gas masses and SFRs. We also store the HI mean velocity, the original CO spectrum, and the galactocentric radius. Figure 5.1 shows for each galaxy in our sample the HI distribution as grayscale, the FUV and $24\mu\text{m}$ intensity as contour, the CO map coverage,

and our sampling grid as dots. See Figure 5.2 for integrated CO intensity maps for a subset of our galaxies.

5.4.6 Literature Sample

Throughout the paper we will compare our new measurements for dwarf galaxies to a larger sample of nearby galaxies. This sample is taken from the literature compilation of Krumholz et al. (2011) which includes the more massive HERACLES galaxies and some additional Local Group and nearby galaxies. Table 5.2 lists their names together with adopted distances, metallicities, *B*-band magnitudes, total CO(1-0) luminosity, and total SFR with references to the original literature. The compilation aims at maximizing homogeneity of used data and methodology. We supplement the Krumholz et al. compilation by adding absolute *B*-band magnitudes adjusted at our adopted distances. We also update the total CO luminosities using the most recent HERACLES data (converted to CO(1-0) luminosities) and SFRs derived from combining FUV and 24 μ m maps. The metallicities had already been given following our approached adopt.

5.5 CO Emission in HERACLES Dwarf Galaxies

To derive the most meaningful possible constrains on CO content, we search for CO emission on three different spatial scales: individual lines-of-sight, stacked over the entire galaxy, and stacked over regions bright at 24 μ m.

5.5.1 Individual Lines of Sight

We start with searching for significant CO emission over individual lines-of-sight. For the dwarf galaxies in HERACLES the noise per channel map in the full resolution ($13'' \times 2.6$ km s⁻¹) cubes is $\sigma = 21 \pm 3$ mK. We search the whole cube in each galaxy for regions with signal-to-noise ratio (SNR) > 4 over two consecutive velocity channels. This corresponds to a CO point sources with luminosity $L_{\text{CO } 2-1} = 2.1 \times 10^4 (\sigma/20 \text{ mK}) (D/4 \text{ Mpc})^2$ K km s⁻¹ pc². For comparison, Table 5.3 lists CO(1-0) luminosities of the brightest clouds in M 33, LMC, SMC, IC 10, and values for the Milky Way Orion-Monoceros complex, Orion A, and Taurus. We are sensitive to detect those clouds (except Taurus) at our average source distance of $D = 4$ Mpc.

Figure 5.2 shows maps of integrated CO intensity for the more massive dwarf galaxies of our sample. Five galaxies, NGC 2403, NGC 2976, NGC 3077, NGC 4214, and NGC 4625, show emission exceeding our point source sensitivity within ± 50 km s⁻¹ of the local mean HI velocity. A point source of 1.5 times our point source sensitivity will show up completely black at the chosen linear grayscale. For all other galaxies we detect no such point sources. The non-detection of bright CO clouds in most of our targets is most likely linked to their low metallicity, $12 + \log \text{O}/\text{H} \lesssim 8.0$, while the reference sample in Table 5.3 has higher metallicities, $8.2 \lesssim 12 + \log \text{O}/\text{H} \lesssim 8.8$.

Table 5.2. Properties of Literature Galaxy Sample

Name	D (Mpc)	Ref.	Metal. 12+logO/H	Ref.	M_B (mag)	Ref.	$\log L_{CO\ 1-0}$ (K km s ⁻¹ pc ²)	Ref.	$\log SFR$ (M_\odot yr ⁻¹)	Ref.
SMC	0.06	L11	8.00	D84; MA10	-16.2	L11	5.20	M06	-1.30	W04
LMC	0.05	L11	8.30	D84; MA10	-17.6	L11	6.50	F08	-0.70	H09
IC 10	0.95	H01	8.20	L79; L03	-16.5	H01	6.30	L06	-1.03	L06
M 33	0.84	G04	8.30	R08	-18.9	NED	7.60	H04	0.00	H04
I ZW 18	14.00	I04	7.22	T05	-14.7	G03	< 0.10	L07	-1.00	L07
II ZW 40	9.20	C10	8.10	E08; C10	-17.9	NED	6.20	T98	-0.19	C10
NGC 0628	7.30	W08	8.69	MO10	-20.0	W08	8.45	HERA	-0.08	HERA
NGC 0925	9.20	W08	8.52	MO10	-20.0	W08	7.47	HERA	-0.24	HERA
NGC 1482	22.00	C10	8.53	MO10	-18.8	NED	8.80	Y95	0.53	C10
NGC 1569	3.36	G08	8.10	M97	-18.1	NED	5.55	T98	-0.40	P11
NGC 2146	12.80	W08	8.70	E08; C10	-20.6	W08	9.06	HERA	0.93	C10
NGC 2537	6.90	L11	8.40	MA10	-16.4	L11	5.50	T98	-1.05	C10
NGC 2782	40.00	C10	8.60	E08; C10	-20.9	NED	9.00	Y95	0.72	C10
NGC 2798	24.70	W08	8.69	MO10	-19.4	W08	8.73	HERA	0.49	C10
NGC 2841	14.10	W08	8.88	MO10	-21.2	W08	8.34	HERA	-0.10	HERA
NGC 2903	8.90	W08	8.90	MA10	-20.1	L11	8.82	HERA	0.32	HERA
NGC 3034	3.60	W08	8.82	MO10	-18.5	L11	8.94	HERA	0.90	C10
NGC 3079	21.80	C10	8.60	E08; C10	-21.7	NED	9.40	Y95	0.50	C10
NGC 3184	11.10	W08	8.83	MO10	-19.9	W08	8.56	HERA	-0.01	HERA
NGC 3198	13.80	W08	8.62	MO10	-20.7	W08	8.15	HERA	-0.01	HERA
NGC 3310	21.30	C10	8.20	E08; C10	-20.5	NED	8.20	Y95	0.92	C10
NGC 3351	10.10	W08	8.90	MO10	-19.5	L11	8.41	HERA	-0.01	HERA
NGC 3368	10.52	L11	9.00	MA10	-20.0	L11	8.30	Y95	-0.45	C10
NGC 3521	10.70	W08	8.70	MO10	-20.3	L11	8.96	HERA	0.34	HERA
NGC 3627	9.30	W08	8.66	MO10	-20.1	L11	8.84	HERA	0.36	HERA
NGC 3628	9.40	L11	9.00	MA10	-19.6	L11	9.20	Y95	0.33	C10
NGC 3938	12.20	W08	8.70	E08; C10	-19.6	W08	8.41	HERA	-0.07	HERA
NGC 4194	42.00	C10	8.70	E08; C10	-20.5	NED	8.90	Y95	1.13	C10
NGC 4254	20.00	W08	8.79	MO10	-21.3	W08	9.50	HERA	0.83	HERA
NGC 4321	14.30	W08	8.84	MO10	-20.9	W08	9.20	HERA	0.45	HERA
NGC 4449	4.20	W08	8.30	M97	-18.1	L11	7.01	B03	-0.45	C10
NGC 4450	27.10	C10	8.90	C10; MA10	-21.7	NED	8.90	Y95	-0.18	C10
NGC 4536	14.50	W08	8.60	MO10	-19.7	W08	8.60	HERA	0.42	HERA
NGC 4569	20.00	W08	8.90	E08; C10	-22.1	W08	9.14	HERA	0.29	HERA
NGC 4579	20.60	W08	9.00	C10; MA10	-21.4	W08	8.94	HERA	0.11	HERA
NGC 4631	8.90	W08	8.43	MO10	-19.9	L11	8.72	HERA	0.40	C10
NGC 4725	9.30	W08	8.73	MO10	-20.2	W08	7.85	HERA	-0.43	HERA
NGC 4736	4.70	W08	8.66	MO10	-19.4	L11	8.14	HERA	-0.29	HERA
NGC 4826	7.50	W08	8.87	MO10	-20.0	L11	8.10	H03	-0.50	C10
NGC 5033	14.80	MO10	8.66	MO10	-20.8	NED	9.30	H03	0.10	K03
NGC 5055	10.10	W08	8.77	MO10	-20.7	L11	9.10	HERA	0.34	HERA
NGC 5194	8.00	W08	8.86	MO10	-20.6	L11	9.20	HERA	0.49	HERA
NGC 5236	4.50	W08	9.00	MO10	-20.1	L11	8.90	Y95	0.37	C10
NGC 5253	3.15	L11	8.20	MA10	-16.6	L11	5.80	T98	-0.22	C10
NGC 5713	26.50	W08	8.64	MO10	-20.9	W08	9.17	HERA	0.76	HERA
NGC 5866	15.10	C10	8.70	C10; MA10	-20.2	NED	8.10	Y95	-0.60	C10
NGC 5953	35.00	C10	8.70	E08; C10	-20.0	NED	9.00	Y95	0.38	C10
NGC 6822	0.49	G10	8.11	LE06	-15.2	NED	5.15	G10	-1.85	E11
NGC 6946	5.90	W08	8.73	MO10	-19.2	L11	9.04	HERA	0.57	HERA
NGC 7331	14.70	W08	8.68	MO10	-21.7	NED	9.10	HERA	0.49	HERA

References. — B03 = Böttner et al. (2003); C10 = Calzetti et al. (2010); D84 = Dufour (1984); E08 = Engelbracht et al. (2008); E11 = Efremova et al. (2011); F08 = Fukui et al. (2008); G03: Gil de Paz et al. (2003); G04: Galletti et al. (2004); G08 = Grocholski et al. (2008); G10 = Gratier et al. (2010a); H01 = Hunter (2001); H03 = Helfer et al. (2003); H04 = Heyer et al. (2004); H09 = Harris & Zaritsky (2009); I97 = Israel (1997); I04 = Izotov & Thuan (2004); K03 = Kennicutt et al. (2003a); L79 = Lequeux et al. (1979); L03 = Lee et al. (2003); LE06 = Lee et al. (2006); L06 = Leroy et al. (2006); L07 = Leroy et al. (2007); L11 = Lee et al. (2011); M97 = Martin (1997); M06 = Mizuno et al. (2006); MA10 = Marble et al. (2010); MO10 = Moustakas et al. (2010); P11 = Pasquali et al. (2011); R08 = Rosolowsky & Simon (2008); T98 = Taylor et al. (1998); T05 = Thuan & Izotov (2005); W04 = Wilke et al. (2004); W08 = Walter et al. (2008); Y95 = Young et al. (1995); HERA = HERACLES collaboration.

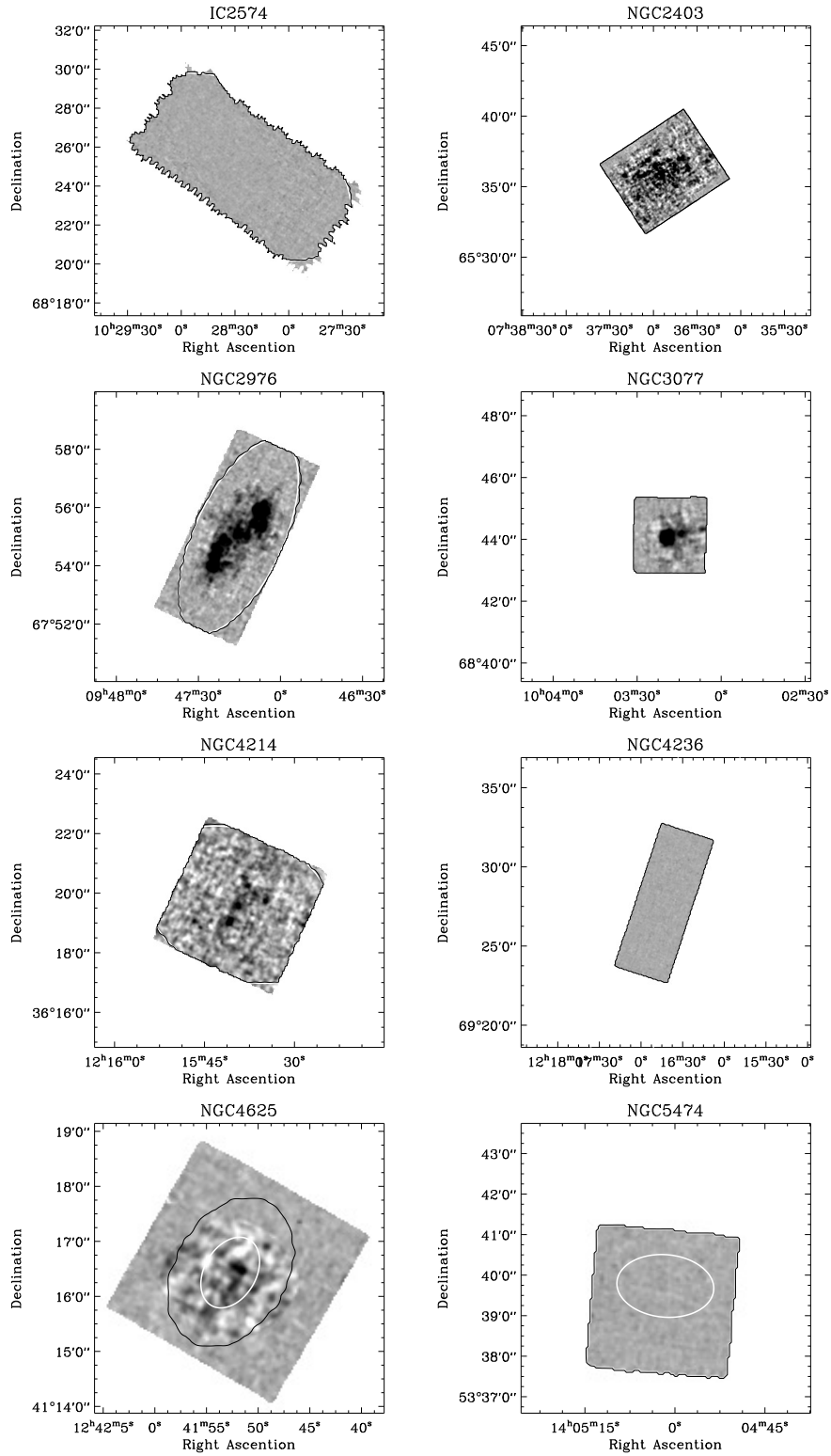


Figure 5.2 *CO Intensity Maps*. Integrated CO(2-1) intensity maps for a subsample of the HERACLES dwarf galaxies at linear scale from -0.3 to 0.7 K km s^{-1} . The galactocentric radius $R = 1 R_{25}$ is shown as white contour, the region selected to determine the integrated CO intensity for the whole galaxy as black contour. The remaining HERACLES dwarf galaxies are non-detections.

Table 5.3. CO Luminosities of Molecular Clouds

Name	$L_{\text{CO } 1-0}$ (K km s ⁻¹ pc ²)	Reference
M 33 EPRB 1	1.8×10^5	Rosolowsky et al. (2003)
LMC N 197	7.0×10^5	Fukui et al. (2008)
SMC N 84	1.3×10^4	Mizuno et al. (2001)
IC 10 B11a	7.6×10^4	Leroy et al. (2006)
Orion-Monoceros	8.6×10^4	Wilson et al. (2005)
Orion A	2.7×10^4	Wilson et al. (2005)
Taurus	5.6×10^3	Goldsmith et al. (2008)

5.5.2 Improve Sensitivity by Stacking

The large map size of the HERACLES maps and the fine (13'') resolution as compared to the angular extent of the galaxies allows us to search for CO emission at many different locations inside the galaxies. To do that we apply the stacking technique developed and described in detail in Schruba et al. (2011). This method accounts for the velocity shift in the observed CO spectrum due to galaxy rotation or other bulk motion. This is done by re-adjusting the velocity axis of the CO spectra for each line-of-sight such that the local HI mean velocity appears at a common (zero) velocity in the shifted spectrum. Under the assumption that the mean velocities of HI and CO closely correspond to each other (confirmed in the bright inner disk of spiral galaxies), the CO line peaks in the shifted spectra by construction at zero velocity across each galaxy (and across the sample). By averaging these shifted spectra we can decrease the noise and coherently add up the spectral line at known (zero) velocity.

To determine the line intensity we fit the stacked spectrum by a Gaussian profile with center restricted to be within ± 50 km s⁻¹ of zero velocity, FWHM to be larger than 15 km s⁻¹, and the amplitude to be positive. In cases where the fitted Gaussian has peak intensity below 3σ or the integrated intensity is less than 5 times its uncertainty we determine an upper limit instead. The upper limit is defined as the integrated intensity of a Gaussian profile with FWHM set to 18 km s⁻¹ and amplitude fixed to 3σ . Figure 5.3 shows stacked CO spectra determined over the whole galaxy for the targets shown in Figure 5.2.

In an ideal world the rms noise, σ_{rms} , decreases proportional to $N^{-1/2}$ by stacking where N is the number of independent resolution elements. For our data σ_{rms} does improve by stacking but at somewhat slower rate and saturates at ~ 1 mK km s⁻¹ after averaging over $\sim 500 - 1000$ resolution elements. It is further instructive to note that the size of the selected stacking region plays an important role as we have to deal with non-detections. While our ability to derive a strong upper limit on I_{CO} does improve proportional to $N^{-1/2}$ by increasing the stacking region, upper limits on L_{CO} degrade by $N^{1/2}$ by increasing the stacking region, and it is the absolute quantity L_{CO} that we are inevitably interested in.

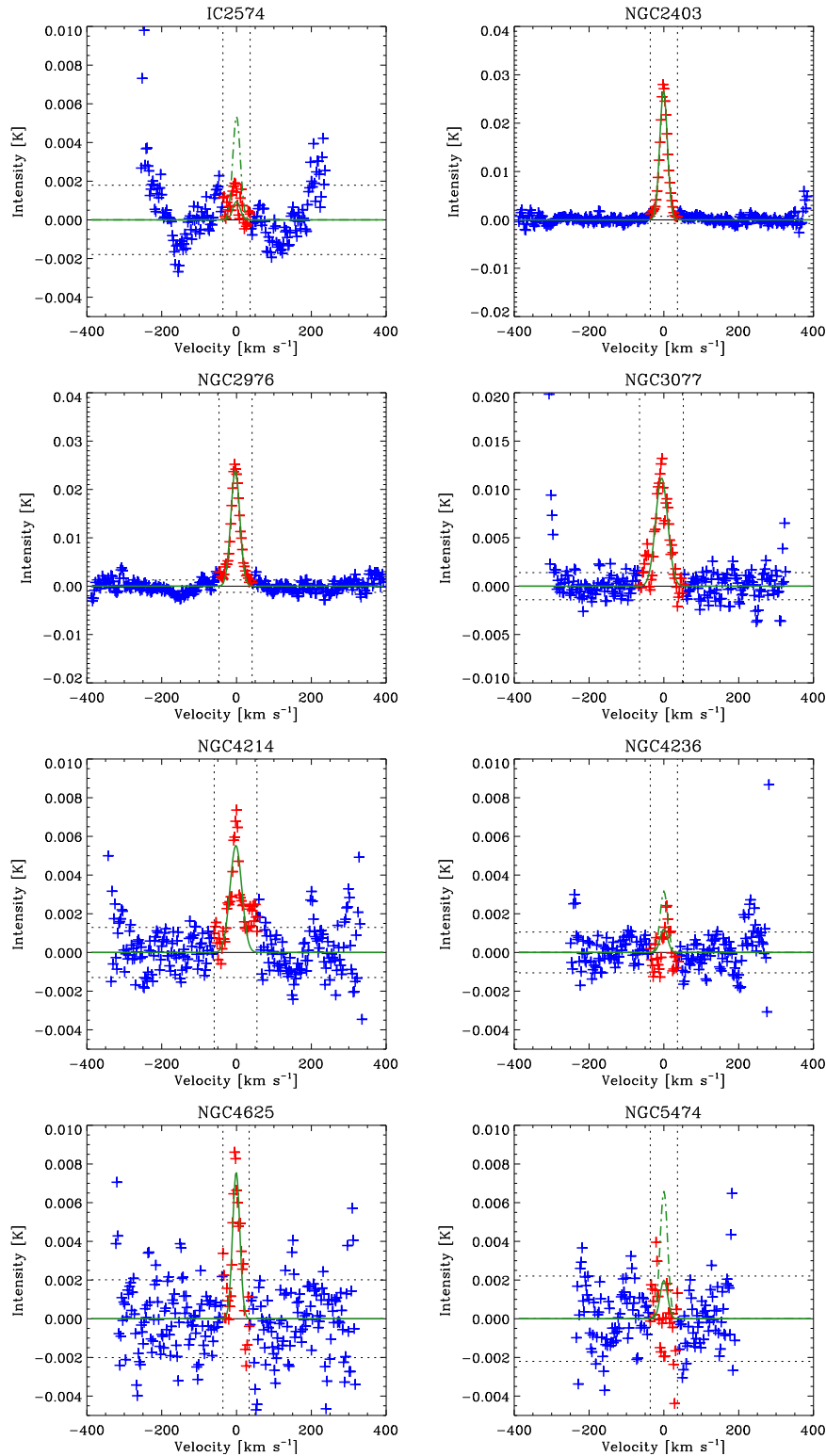


Figure 5.3 *Stacked CO Spectra*. The resulting mean CO(2-1) spectrum after stacking all data over the whole galaxy (black contours in Figures 5.1 & 5.2). The spectra are shifted to the local mean HI velocity and expected to peak at zero velocity (see text). We fit Gaussian profiles (green lines) to the data within ± 50 km s⁻¹ (vertical dotted lines) to determine the integrated CO intensity (or 3σ upper limit). The horizontal dotted lines show the 1σ rms noise of the stacked spectra.

Table 5.4. Stacking of Whole Galaxy

Name	Area ^a (kpc ²)	$L_{\text{CO } 2-1}$ ^b ($10^6 \text{ K km s}^{-1} \text{ pc}^2$)	SFR ^c ($M_{\odot} \text{ yr}^{-1}$)
M 81 Dw A	1.33	< 0.38	0.0004
M 81 Dw B	1.79	< 0.64	0.0022
DDO 053	1.75	< 0.37	0.0035
DDO 154	7.74	< 1.00	0.0054
DDO 165	11.47	< 1.46	0.0093
HO I	12.37	< 1.81	0.0093
HO II	26.69	< 2.83	0.0379
IC 2574	83.85	< 8.20	0.0670
NGC 2366	12.23	< 0.86	0.0532
NGC 2403	39.40	26.79 ± 0.31	0.3131
NGC 2976	19.21	13.89 ± 0.29	0.0908
NGC 3077	7.78	3.54 ± 0.15	0.0689
NGC 4214	14.75	3.21 ± 0.25	0.1041
NGC 4236	59.54	< 3.53	0.1063
NGC 4625	31.19	5.73 ± 0.65	0.0664
NGC 5474	39.19	< 4.92	0.0683

Note. — (a) Unprojected area sampled from this work.

(b) $L_{\text{CO}(2-1)}$ in sampled area from this work.

(c) SFR(FUV+24) in sampled area from this work.

Stacking of Whole Galaxy

We start with stacking the CO spectra over the whole galaxy extent. For that we use the SFR distribution as guideline for the (most likely) distribution of molecular gas and CO emission. Unfortunately, this method does not provide definite sizes. FUV emission (the main tracer of SFR in dwarf galaxies outside massive star-forming regions) typically starts to flatten as function of galactocentric radius before reaching the background level. We therefore select for each galaxy a maximal galactocentric radius (typically between $1 - 2 R_{25}$) that includes most ($\sim 95\%$) of the galaxy-integrated SFR. The thus selected regions are highlighted by black contours in Figures 5.1 & 5.2.

We will see that for some galaxies the selected region (a) does not fully sample the region subtended by a fixed galactocentric radius and/or (b) does miss a significant fraction ($\lesssim 10 - 30\%$) of the total SFR given in Table 5.1. This is especially true for NGC 5474 and NGC 2403, and to a minor extend for Ho II, NGC 2366, NGC 3077, NGC 4214, and NGC 4236. It is however not straightforward how to correct for that. In the remaining paper we will therefore continue to refer to our measured L_{CO} as the total galaxy-integrated luminosity but keep in mind that the true value may be up to $\sim 30\%$ higher for a subset of our sample. The given uncertainties on L_{CO} include only the statistical uncertainties

Table 5.5. Stacking of 24 μ m-bright Regions^a

Name	Area (kpc ²)	$L_{24\mu\text{m}}^{\text{b}}$ (10 ⁶ MJy sr ⁻¹ pc ²)	$L_{\text{CO } 2-1}$ (10 ⁶ K km s ⁻¹ pc ²)	SFR (M_{\odot} yr ⁻¹)
M81 Dw A
M81 Dw B
DDO 053	0.31	0.20	< 0.16	0.0016
DDO 154
DDO 165
HO I
HO II	1.82	1.35	< 0.38	0.0136
IC 2574	2.39	1.54	< 0.52	0.0158
NGC 2366	2.80	7.25	< 0.39	0.0403
NGC 2403	33.01	50.87	26.04 \pm 0.28	0.3021
NGC 2976	7.63	17.78	12.10 \pm 0.16	0.0856
NGC 3077	6.13	19.10	3.53 \pm 0.13	0.0679
NGC 4214	5.99	15.73	2.33 \pm 0.12	0.0934
NGC 4236	7.15	5.75	< 1.01	0.0500
NGC 4625	9.48	10.33	5.12 \pm 0.31	0.0592
NGC 5474	7.64	3.16	< 2.19	0.0375

Note. — (a) Includes all lines-of-sight with $I_{24\mu\text{m}} \geq 0.2$ MJy sr⁻¹ at 13'' resolution.
(b) These (unusual) units allow comparison to Figure 5.4.

of fitting the stacked spectrum with Gaussian profiles. Uncertainties in the calibration may affect L_{CO} by up to 30% and uncertainties in the distance will enter to the power of 2 — both are not included.

Figure 5.3 shows the resulting spectra when stacking over the whole galaxy (for the galaxies shown in Figure 5.2). Table 5.4 lists the (unprojected) area and the included L_{CO} and SFR. Five galaxies, NGC 2403, NGC 2976, NGC 3077, NGC 4214, and NGC 4625 are robustly detected. These are the same galaxies that already showed emission for individual lines-of-sight (Section 5.5.1). One galaxy, NGC 4236, may show a tentative signal which extends from -8 to $+20$ km s⁻¹, has peak intensity ~ 2.4 mK ($\sim 2.3\sigma$) over 2 channels, $I_{\text{CO } 2-1} \approx 0.035$ K km s⁻¹, and $L_{\text{CO}, 2-1} \approx 2.1 \times 10^6$ K km s⁻¹ pc², a factor 0.6 below our quoted upper limit. This emission is not point like because with a point source sensitivity of $L_{\text{CO}} \sim 2.5 \times 10^4$ K km s⁻¹ pc² for this galaxy we would have easily identified it. All other galaxies remain undetected.

There are three galaxies, IC 2574, Ho II, and NGC 5474, where we may have expected to see signal as these galaxies have properties similar to detected galaxies. The stacked spectrum of IC 2574 shows an enhancement at $\sim 0 - 5$ km s⁻¹ over a velocity range $\sim 16 - 18$ km s⁻¹, and peak intensity ~ 4 mK ($\sim 1\sigma$) for the 24 μ m-selected regions or ~ 1.3 mK ($\sim 0.8\sigma$) over the whole galaxy. While the match between CO and HI velocities is encouraging, the strength of this enhancement is too low to differentiate it

from spurious emission. The stacked spectra of Ho II and NGC 5474 show no signs of signal at a noise level of 1.9 and 2.2 mK per 2.6 km s^{-1} channel, respectively.

Stacking of $24 \mu\text{m}$ -bright Regions

We make a final attempt to search for faint CO emission by stacking over regions that likely have the highest probability to contain molecular gas and are bright in CO. These are regions rich in dust and showing signs of embedded high-mass star formation. We use the $24 \mu\text{m}$ intensity, $I_{24 \mu\text{m}}$, as a tracer of these conditions and select all lines-of-sight that have $I_{24 \mu\text{m}} \geq 0.2 \text{ MJy sr}^{-1}$ at $13''$ resolution. The adopted $24 \mu\text{m}$ level does not have a specific physical interpretation, but it is well ($\sim 4\sigma$) above the noise level of the $24 \mu\text{m}$ maps. IR emission tends to be faint in these targets (e.g. Walter et al., 2007) and this low contour effectively separates the star-forming peaks from the rest of the galaxy. Because the smallest galaxies in our sample do not reach this intensity, we omit them from this calculation. The regions thus selected are highlighted by red contours in Figure 5.1.

Table 5.5 lists the results when stacking over these $24 \mu\text{m}$ -bright regions: the (unprojected) area, $24 \mu\text{m}$ and CO luminosity, and included SFR. This method does not lead to new CO detections in addition to those galaxies already detected at individual lines-of-sight and over the whole galaxy. However, for non-detected galaxies it results in stronger upper limits on L_{CO} and to lower L_{CO}/SFR ratios.

5.6 Scaling Relations for CO Luminosity

5.6.1 Comparison to Magellanic Clouds

We begin with a comparison of our CO measurements (upper limits) as listed in Table 5.4 & 5.5 to the Magellanic Clouds. These are essentially the only low-metallicity systems that are well detected over the full galaxy extent; their properties are included in Table 5.2. We also list previous CO observations of our targets in Table 5.6. A direct comparison to our CO measurements is however not straightforward as previous observations covered only very small fractions of the star-forming disk (often just a single pointing) and were strongly limited by sensitivity. The large scatter between individual literature measurements and compared to our values indicate that previous pointed observations have not been adequate to robustly constrain the galaxy-integrated CO luminosity.

The galaxies that we detect in CO are comparable (or exceed) in M_{HI} , M_{B} , SFR, and metallicity the LMC, but we are able to detect them at distances $D = 2.9 - 9.5 \text{ Mpc}$. Galaxies that have not been detected when stacking over the whole galaxy extent, have $L_{\text{CO } 2-1}$ upper limits 0.1 – 2.6 times the CO luminosity of the LMC, $L_{\text{CO } 1-0}^{\text{LMC}} = 3.2 \times 10^6 \text{ K km s}^{-1} \text{ pc}^2$ (Fukui et al., 2008). Our data is not sensitive enough to detect a CO luminosity comparable to the SMC, $L_{\text{CO } 1-0}^{\text{SMC}} = 1.6 \times 10^5 \text{ K km s}^{-1} \text{ pc}^2$ (Mizuno et al., 2006) if it is spread over many resolution elements. For the IR-selected regions, our CO sensitivity improved and is always sufficient to detect $L_{\text{CO } 1-0}^{\text{LMC}}$ and reaches down to 1 – 10 times $L_{\text{CO } 1-0}^{\text{SMC}}$. For individual lines-of-sight we would have easily detected $L_{\text{CO } 1-0}^{\text{SMC}}$ but detect no such point sources for 11 of our galaxies.

Table 5.6. Previous CO Observations of our Galaxy Sample

Name	Beam (arcsec)	$L_{\text{CO } 1-0^{\text{a}}}$ ($10^6 \text{ K km s}^{-1} \text{ pc}^2$)	Reference
M 81 Dw A	45	< 0.16	Young et al. (1995)
M 81 Dw B
DDO 053	55	< 0.94	Leroy et al. (2005)
DDO 154	65	< 3.2	Morris & Lo (1978)
DDO 165	65	< 5.6	Taylor et al. (1998)
Ho I	65	< 3.8	Taylor et al. (1998)
Ho II	13×65	< 9.9	Elmegreen et al. (1980)
	45	< 0.24	Young et al. (1995)
	55	< 1.2	Leroy et al. (2005)
IC 2574	10×65	< 10	Elmegreen et al. (1980)
	55	1.1	Leroy et al. (2005)
NGC 2366	3×65	< 1.9	Elmegreen et al. (1980)
	22	< 0.50	Hunter & Sage (1993)
	22	< 0.04	Albrecht et al. (2004)
	55	< 1.3	Leroy et al. (2005)
NGC 4214	45	0.38	Young et al. (1995)
	60	0.56	Israel (1997)
	4×55	0.73	Taylor et al. (1998)
NGC 4236	11×45	< 9.4	Young et al. (1995)
NGC 4625	22	4.4	Böker et al. (2003)
	22	4.2	Albrecht et al. (2004)
	55	16	Leroy et al. (2005)
NGC 5474	55	< 1.5	Leroy et al. (2005)

Note. — (a) Luminosities are given on main beam temperature scale (T_{mb}) and are calculated assuming our adopted distances; line width and upper limit ($3-4\sigma$) on peak intensity are taken from reference.

5.6.2 Scaling Relations of L_{CO} with M_{B} and Metallicity

We use our robust estimates of the galaxy-integrated CO luminosity of dwarf galaxies to examine the relationship between L_{CO} , B -band magnitude, M_{B} , and metallicity in Figure 5.4 & 5.5. In conjunction with our literature compilation our galaxy sample covers 5 orders of magnitude in L_{CO} , 4 orders of magnitude in L_{B} , 1.5 orders of magnitude in metallicity, 5 orders of magnitude in star formation rate ($\text{SFR} = 10^{-4} - 10^1 M_{\odot} \text{ yr}^{-1}$), and 3 orders of magnitude in HI mass ($M_{\text{HI}} = 10^7 - 10^{10} M_{\odot}$).

The top panel of Figure 5.4 shows L_{CO} as function of M_{B} . For guidance we show the solid line which highlights a constant scaling between L_{CO} and L_{B} , set to intersect the bright galaxies. In the bright galaxies ($M_{\text{B}} < -18$), L_{CO} and M_{B} track one another with a more-or-less fixed ratio, $\log_{10} L_{\text{CO}}[\text{K km s}^{-1} \text{ pc}^2] / L_{\text{B}}[L_{\odot}] = -1.5 \pm 0.4$, as one might expect for a simple scaling with galaxy mass (Young & Scoville, 1991; Leroy et al., 2005; Lisenfeld et al., 2011). The dwarf galaxies ($M_{\text{B}} \geq -18$) on the other hand lie below the solid line. They are “underluminous” in CO, i.e., their ratios are systematically smaller, -2.7 ± 0.6 , than those of massive galaxies. Despite this trend, L_{CO} and M_{B} are strongly correlated with (absolute) rank correlation coefficient $r_{\text{corr}} = 0.79$.

The bottom panel of Figure 5.4 shows L_{CO} as function of metallicity. There is a dramatic drop in L_{CO} by 3 – 4 orders of magnitude over a small range of metallicities. This drop is to first order caused by the much smaller mass and size of dwarf galaxies. However, due to the strong luminosity–metallicity relation for dwarf irregulars (e.g., Lee et al., 2006; Guseva et al., 2009), it is also correlated to M_{B} (i.e., the top panel). The rank correlation coefficient is $r_{\text{corr}} = 0.60$.

Figure 5.5 shows the ratio $L_{\text{CO}}/L_{\text{B}}$ as function of metallicity. Plotting $L_{\text{CO}}/L_{\text{B}}$ should remove most of the mass and size dependence seen in the above panels. The decreasing trend of $L_{\text{CO}}/L_{\text{B}}$ with decreasing metallicity clearly shows that dwarf galaxies are also “underluminous” in CO in a normalized sense.

From the study of a large sample of literature CO data, Taylor et al. (1998) suggested a “detection threshold” for CO below $12 + \log \text{O}/\text{H} \approx 8.0$, about the metallicity of the SMC. Our data do not overcome this threshold: All of our galaxies with lower metallicity remain undetected. However, given the decreasing trend of $L_{\text{CO}}/L_{\text{B}}$ with decreasing metallicity and the fact that our data is not sensitive enough to detect a SMC at distance $D = 4$ Mpc leaves the question open if the proposed threshold is of observational and/or physical origin.

5.6.3 CO and Tracers of Star Formation

Figure 5.6 shows the relationship between CO emission and tracers of recent star formation, FUV and $24\mu\text{m}$, together with a combination of FUV and $24\mu\text{m}$ often used to estimate SFR (see Section 5.4.3). Panels in the left column show the correlations between observables I_{CO} , I_{FUV} , and $I_{24\mu\text{m}}$, panels in the right column show the ratios of I_{CO} and I_{FUV} or $I_{24\mu\text{m}}$ as function of metallicity. For our dwarf galaxies (bigger symbols) we show both the stacking results derived over the whole galaxy (colored by metallicity) as well as the values derived from stacking over the $24\mu\text{m}$ -bright regions (gray symbols). For comparison we also show azimuthally averaged radial intensity profiles for spiral galaxies

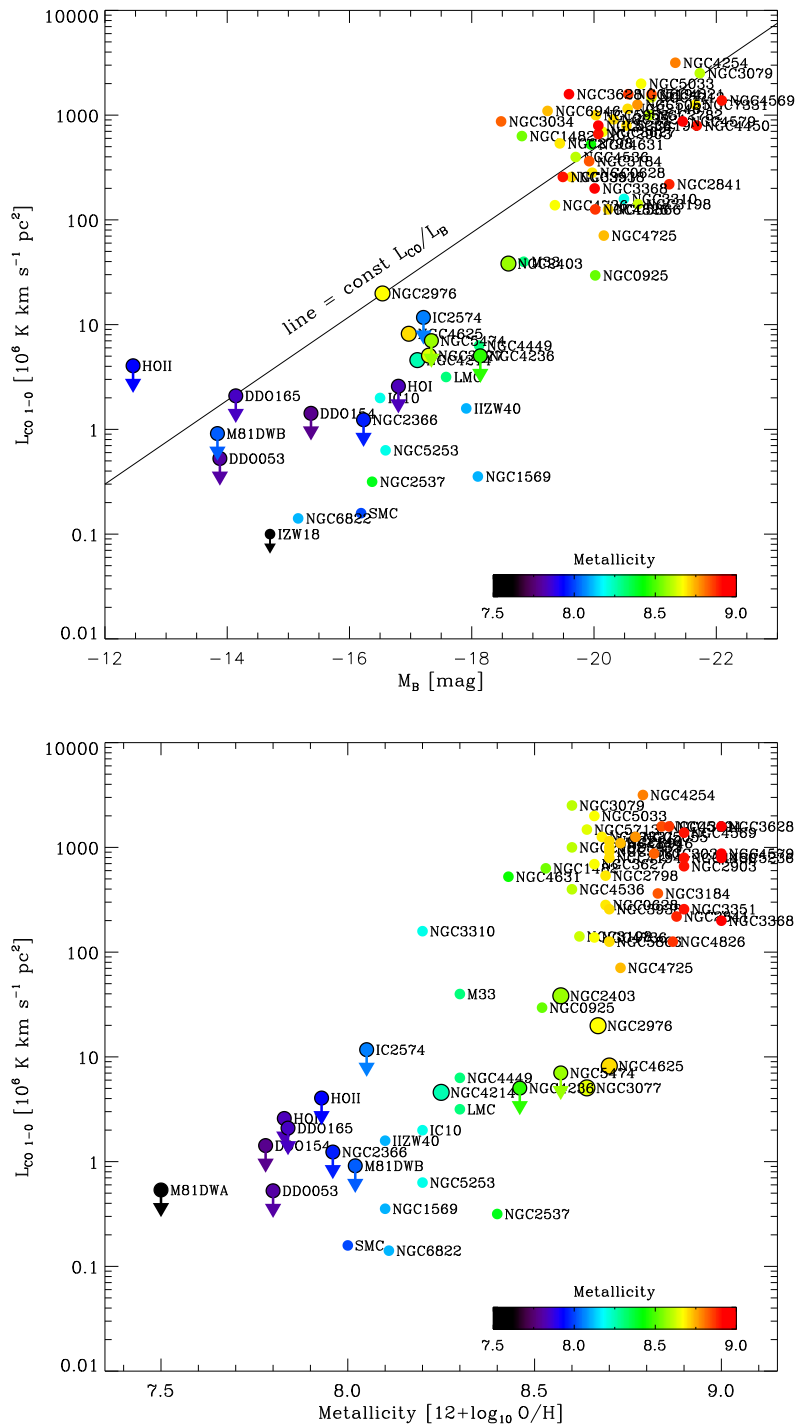


Figure 5.4 *Scaling Relations for CO Luminosity*. Galaxy-integrated CO(1-0) luminosity as function of B -band magnitude (top) and metallicity (bottom). Bigger symbols show stacking results of this work, smaller symbols show a compilation of literature measurements. Color highlights metallicity. The solid line in the top panel shows a constant L_{CO}/L_B ratio intersecting the bright galaxies. The trends are correlated by the well established luminosity-metallicity relation.

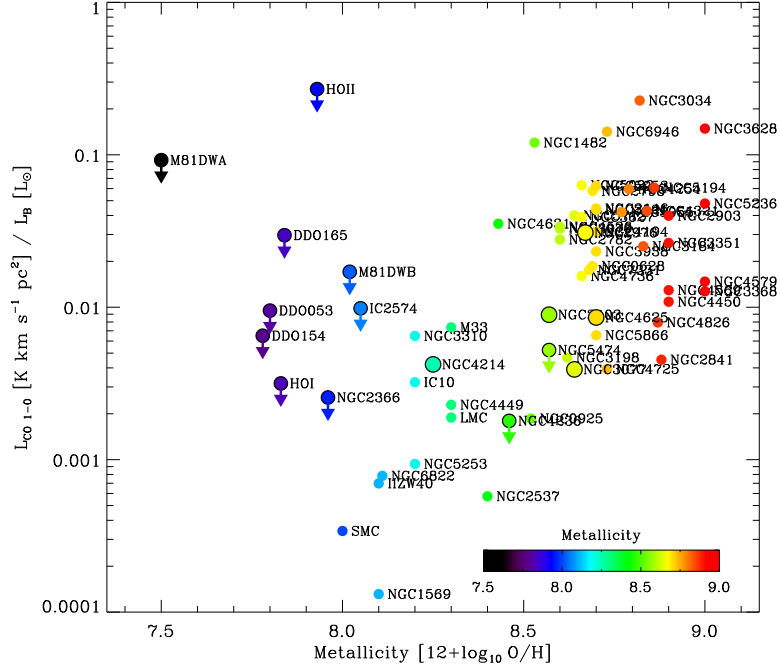


Figure 5.5 *Metallicity dependence of L_{CO}/L_B* . The L_{CO}/L_B ratio is a strongly decreasing function of decreasing metallicity. This suggests that CO abundance is genuinely low in low-mass, low-metallicity galaxies.

(smaller colored symbols) which are taken from Schruba et al. (2011). The plots shown here are similar to plots of the “star formation law”, i.e., plots of Σ_{SFR} versus Σ_{H_2} , though they are typically presented with axes in reverse ordering and show data that are corrected for inclination (which we have not done here).

One of the results from Schruba et al. (2011) was that spiral galaxies exhibit a strong correlation between I_{CO} and $I_{24\mu m}$ (see middle panel in left column). This has been interpreted as a direct link between molecular gas as traced by CO emission and SFR, which is mostly deeply embedded and traced by $24\mu m$ emission. The ratio of CO/ $24\mu m$ is roughly constant inside galaxies and shows only small variation between galaxies and as function of metallicity where CO is detected (middle panels). The ratio of CO/FUV also shows only little scatter inside individual galaxies but can vary significantly between galaxies (upper panels). The large scatter in CO/FUV and the strong scaling with metallicity reflects the strong susceptibility of FUV emission to dust attenuation. In low metallicity environments CO/FUV is low because CO abundance and thus I_{CO} is low and at the same time, low dust abundance and low attenuation cause high I_{FUV} . The ratio of $I_{CO}/(I_{FUV}+0.04I_{24\mu m})$ which is proportional to the H_2 depletion time, τ_{dep} , is also to first order constant ~ 1.8 Gyr for environments with $12+\log_{10} O/H = 8.7$ and shows only little dependence on metallicity in environments with about solar metallicity (see also Bigiel et al., 2008, 2011; Leroy et al., 2011).

Our dwarf galaxies however do show deviations from the trends observed for radial profiles of more massive galaxies. The CO, FUV, and $24\mu m$ intensities measured in the

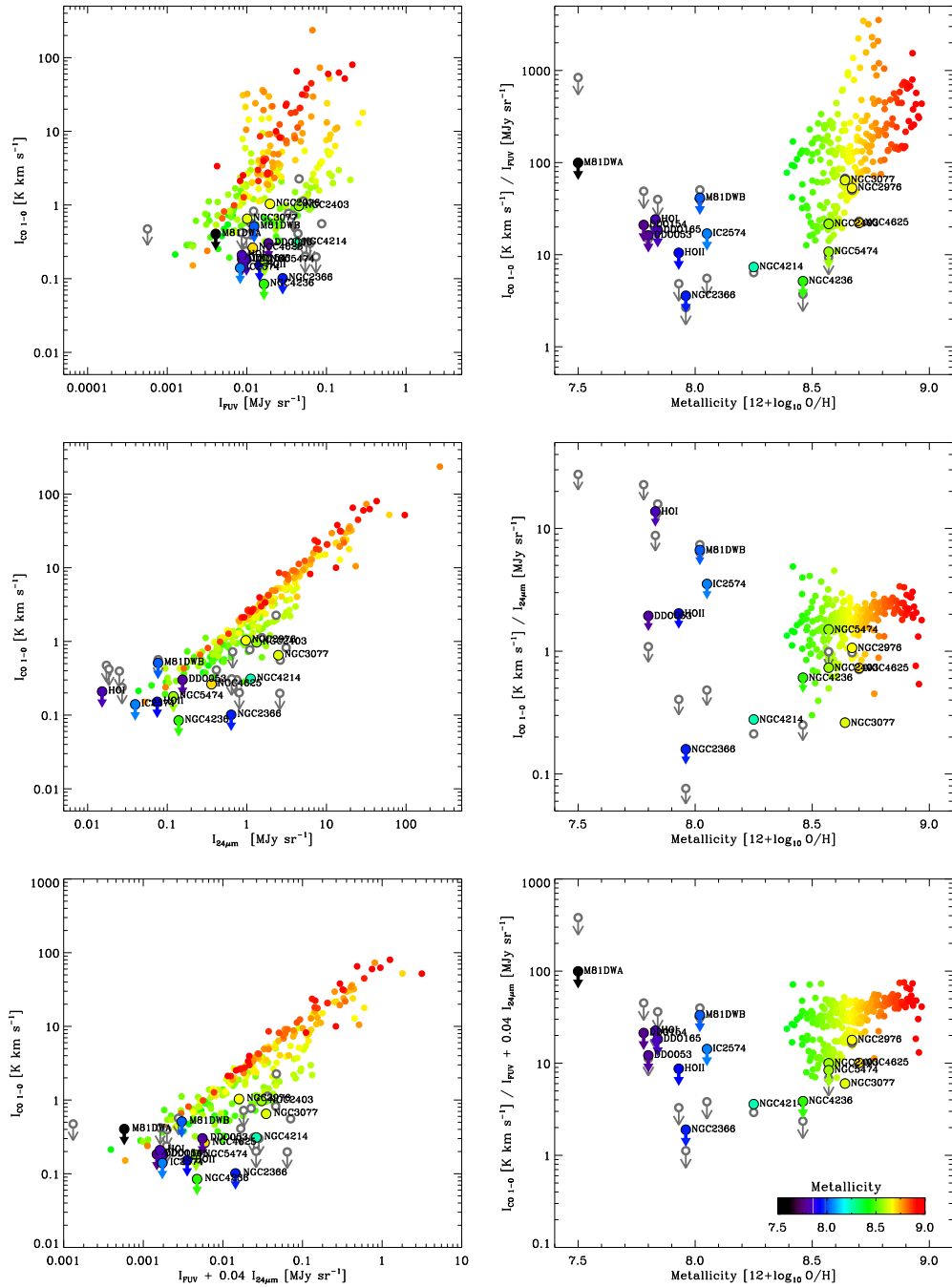


Figure 5.6 *CO Emission and Tracers of Star Formation.* Left column: CO(1-0) intensity as function of FUV and $24\mu\text{m}$ intensity, and a combination of FUV and $24\mu\text{m}$ used to determine SFR. Right column: Intensity ratios of CO and FUV or $24\mu\text{m}$ as function of metallicity. Bigger symbols show stacking results for dwarf galaxies derived over the whole galaxy extent (colored symbols) or over $24\mu\text{m}$ -bright regions (gray symbols). Smaller symbols show azimuthally averaged radial profiles in massive spiral galaxies. CO emission is well correlated with emission of SFR tracers, especially with $24\mu\text{m}$. The ratios CO/FUV and CO/ $24\mu\text{m}$ show systematically smaller values in low-intensity, low-metallicity environments as is typical for dwarf galaxies.

dwarf galaxies are close to the lowest intensities measured in the radial annuli of more massive galaxies. In addition, the ratios of CO/FUV and CO/24 μ m are shifted to smaller values. For our detected galaxies the ratios are a factor 5 – 10 below the ratios found in more massive galaxies. The data of our undetected galaxies are scattered but for galaxies with sensitive CO upper limits they are also shifted toward low CO/FUV and CO/24 μ m ratios. Dwarf galaxies exhibit enhanced signatures of star formation (both embedded and unobscured) per unit CO brightness as compared to large star-forming galaxies.

5.7 Implications for CO-to-H₂ Conversion Factor

A serious complication in studying the molecular content of dwarf galaxies arises in how to relate the observed CO luminosities to H₂ masses. Applying a Galactic CO-to-H₂ conversion factor, $\alpha_{\text{CO,Gal}}$, to dwarf galaxies that have been detected in CO results in very low H₂ masses (Taylor et al., 1998; Mizuno et al., 2001; Leroy et al., 2007). The resulting H₂ masses are so low that to explain the observed SFRs the conversion of H₂ to stars would need to be on average 10 – 100 times more efficient than in Galactic environments — a condition that seems unlikely (e.g., Bolatto et al., 2011).

The detection of excess ionized carbon and infrared to millimeter dust emission around star-forming regions (Madden et al., 1997; Pak et al., 1998; Rubin et al., 2009; Cormier et al., 2010; Israel & Maloney, 2011) indicates that CO may not trace all H₂ at low metallicity (Maloney & Black, 1988; Israel, 1997; Bolatto et al., 1999; Wolfire et al., 2010). Because H₂ can self-shield, its abundance is basically a function of its formation time (which depends on metallicity), however, CO cannot self-shield and exists only in regions that are sufficiently shielded by dust from the interstellar radiation field (Glover et al., 2010; Glover & Mac Low, 2011). α_{CO} is therefore assumed to be a strong function of metallicity and radiation field strength, though, robust functional parametrizations of these dependences are still lacking (but see Shetty et al., 2011a,b; Narayanan et al., 2011, for recent theoretical attempts).

In the following we will discuss three different methods that have been applied to estimate α_{CO} in external galaxies. In particular we are interested in the metallicity dependence of α_{CO} . Whenever possible, we parametrize this dependence by power laws of the form $\alpha_{\text{CO}} = A \times (12 + \log \text{O}/\text{H} - 8.7)^N$ where the normalization A corresponds to the α_{CO} value at $12 + \log_{10} \text{O}/\text{H} = 8.7$ and N is the power law slope.

Before we begin, we have to caution the reader that gas phase metallicities bear considerable uncertainty. Different empirical and theoretical calibrations can result in systematic discrepancies in estimated metallicities as large as 0.1 – 0.7 dex (Kewley & Ellison, 2008). Though, once selecting a specific calibration the relative ordering of individual galaxies and derived power law slopes are more robust. For our new data and our literature compilation we have tried to maximize homogeneity of metallicity estimates. The compilation of α_{CO} parametrizations from the literature however relies on a variety of different calibrations that can also vary within individual studies. Without a full reanalysis of their data there is no straightforward method to correct for this. We thus include these studies as they were given in the original literature and concentrate our discussion on the slope of those parametrizations.

5.7.1 Different Methods to Estimate the CO-to-H₂ Conversion Factor

Virial Method

The classic method to derive α_{CO} uses high resolution CO observations that are capable of resolving individual molecular clouds (e.g., Solomon et al., 1987). Under the assumption that a CO-bright core is in virial equilibrium, its observed linewidth and size can be converted into a virial mass, M_{vir} , and from that $\alpha_{\text{CO}} \equiv M_{\text{vir}}/L_{\text{CO}}$. Early work by Wilson (1995); Arimoto et al. (1996); Boselli et al. (2002) have applied this method to a handful of Local Group galaxies and predicted a weak metallicity dependence of α_{CO} with power law slopes flatter than -1 . This metallicity dependence however has not been confirmed by the recent studies of Blitz et al. (2007); Bolatto et al. (2008). They re-analyze a large set of literature data aiming at maximizing homogeneity of their analysis and carefully correcting for finite spatial and spectral resolution. They derive a distribution of α_{CO} values that scatters without systematic trend around $0.5 - 5 \alpha_{\text{CO,Gal}}$; the green striped region in Figure 5.8. It has to be emphasized that the virial method is only sensitive to H₂ that is also CO-bright and thus does significantly underestimate the total H₂ mass of (low metallicity) galaxies.

Dust Modeling

This method uses IR observations and dust modeling to estimate the gas mass and distribution which has the advantage to be independent of CO emission (Thronson et al., 1988; Israel, 1997; Dame et al., 2001; Leroy et al., 2007, 2009, 2011; Gratier et al., 2010b; Bolatto et al., 2011). It builds on the assumption that gas and dust are well mixed and α_{CO} is derived from $M_{\text{dust}} \equiv \text{DGR} \times (M_{\text{HI}} + \alpha_{\text{CO}}L_{\text{CO}})$. By modeling the dust distribution the local H₂ mass can be inferred from M_{dust} (after subtraction of local H I) by either fixing the DGR in quiescent regions (assumed to be H₂-free) or by simultaneous optimizing α_{CO} and DGR such that the scatter between $M_{\text{dust}}/\text{DGR}$ and $M_{\text{HI}} + \alpha_{\text{CO}}L_{\text{CO}}$ gets minimized. Early work by Israel (1997) implied a strong metallicity dependence of α_{CO} with slope of -2.7 ± 0.3 . Recent work by Gratier et al. (2010b); Leroy et al. (2011); Bolatto et al. (2011) did confirm a strong increase of α_{CO} at low metallicities, though their values vary in absolute terms, proposed functional form, and are systematically smaller than the α_{CO} values derived by Israel (1997). The α_{CO} values derived by these studies lie within the blue striped region in Figure 5.8. The lowest metallicity galaxy to which this method has been applied is the SMC, for which large amounts of H₂ have been predicted implying α_{CO} values 10 – 100 times the Galactic value (Leroy et al., 2011; Bolatto et al., 2011).

Disadvantages of this method are that it is susceptible to variations of the FIR emissivity of dust grains and variations in DGR between dense, star-forming regions and low density, quiescent regions. There are indications that the emissivity is enhanced in dense regions (e.g. Paradis et al., 2009; Planck Collaboration et al., 2011) which would cause an overprediction of α_{CO} on scales of individual star-forming regions. Second, because dust enrichment of the ISM by stars seems insufficient to explain observed dust abundances, it is proposed that most dust forms in the ISM, presumably in the densest regions (Dwek, 1998; Draine et al., 2007). If this dust is only slowly transported into the lower

density ISM then this would also lead to an overprediction of α_{CO} . The need for sensitive, matched high resolution data to make the analysis robust limits this method to very nearby galaxies and makes observations time demanding.

Constant SFE

An alternative method to constrain the H₂ mass is to assume that the conversion of H₂ to stars is independent of environment, i.e., assuming a constant H₂ depletion time, τ_{dep} , or a constant star formation efficiency (SFE; the inverse of τ_{dep}). α_{CO} is then given by $\alpha_{\text{CO}} \equiv \tau_{\text{dep}} \times \text{SFR}/L_{\text{CO}}$. This approach has already been applied in times when it was still considered very uncertain how to relate CO to H₂ in our Galaxy (Rana & Wilkinson, 1986) and we will apply to our sample of nearby galaxies in the remainder of this paper. The idea is encouraged by several observations: (a) the accumulating evidence that star formation in molecular clouds is largely decoupled from environment as indicated by the similarity of molecular cloud properties in our and nearby galaxies (Blitz et al., 2007; Bolatto et al., 2008; Fukui & Kawamura, 2010), the universality of SFE per free-fall time of clouds of different mass and density (Krumholz & Tan, 2007), and evidence in favor of a universal initial stellar mass function (Bastian et al., 2010); and (b) the remarkably constant scaling between H₂ and SFR on \sim kpc scales observed in a large set of nearby galaxies (e.g., Bigiel et al., 2008, 2011; Leroy et al., 2008; Schruba et al., 2011). A drawback of this method is that it requires that the correlation between H₂ and SFR established (for a range of environments) in spiral galaxies continues to hold in dwarf galaxies. This makes the method less rigorous than direct attempts to trace H₂ but also makes it available for a much larger sample of galaxies including distant galaxies.

Currently we are not able to definitely conclude that τ_{dep} is truly constant. Observation of strongly variable star formation histories and starbursts readily indicate that it does not hold in all environments (e.g. Lee et al., 2009; Weisz et al., 2011). However, recent theoretical considerations by Krumholz et al. (2011); Glover & Clark (2011) provide motivation in favor of a constant H₂-SFR ratio. Though some of these studies do questioned if H₂ is fundamental for star formation, they also argue that H₂ will be a good tracer of star-forming regions. This is because the H I to H₂ transition and the drop in gas temperature which makes clouds susceptible to gravitational instabilities occur under similar conditions that are to first order set by shielding of the interstellar radiation field. Because of this, H₂ is suggested to be a good tracer of regions that are able to form stars independent of metallicity and/or radiation field, even though it may not be a prerequisite for star formation.

5.7.2 New & Literature Measurements

In the following we explore the implications for α_{CO} if τ_{dep} is indeed constant. We set $\tau_{\text{dep}} = 1.8$ Gyr, the average value for spiral galaxies in the HERACLES sample with about solar metallicity (Schruba et al., 2011). Figure 5.7 shows the resulting α_{CO} values as function of metallicity. In this plot we show galaxy-integrated values, bigger symbols show our measurements of dwarf galaxies (Table 5.4) and smaller symbols show data from

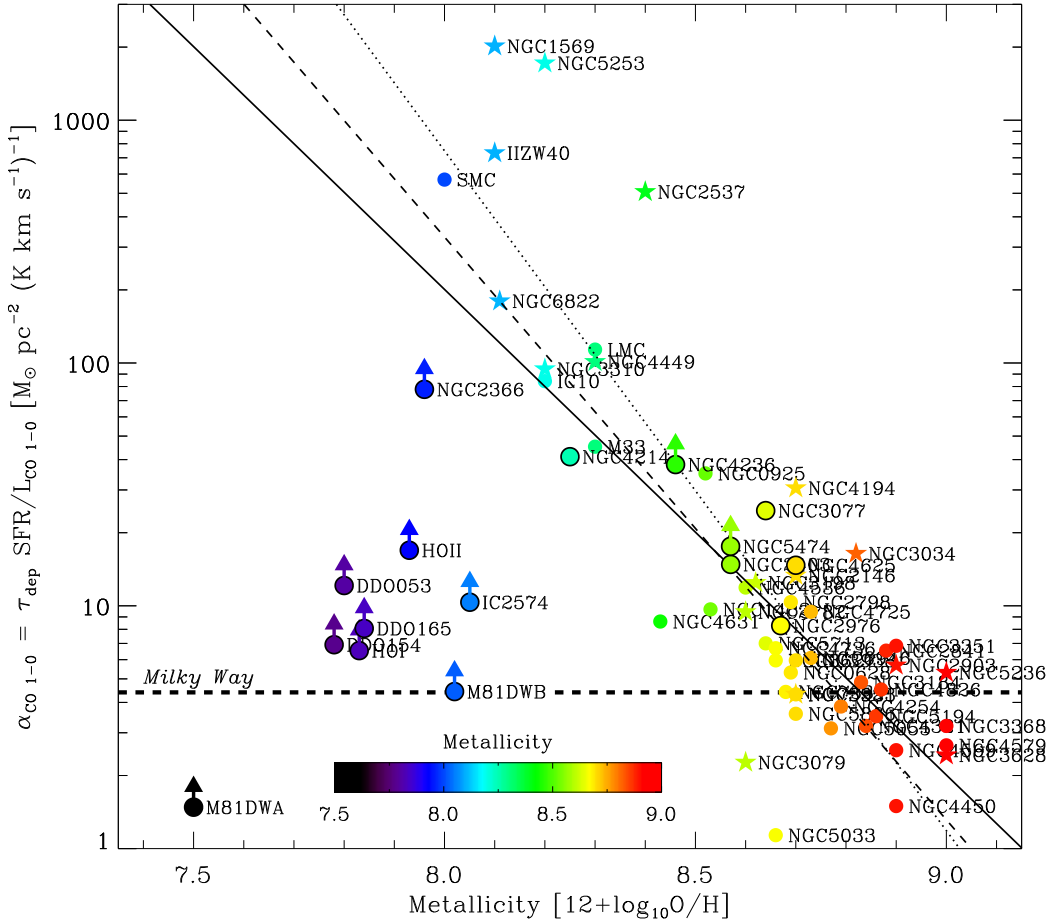


Figure 5.7 *Metallicity Dependence of the CO-to- H_2 Conversion Factor.* α_{CO} is derived from the ratio of observed SFR scaled by a constant H_2 depletion time, $\tau_{\text{dep}} = 1.8 \text{ Gyr}$, and the observed CO luminosity, L_{CO} . Bigger symbols show galaxy-integrated measurements of dwarf galaxies from this work, smaller symbols show data for our literature compilation with starbursts highlighted by stars. The horizontal dashed line shows the Galactic conversion factor, the diagonal lines power law fits: to all galaxies (dotted line), to all non-starburst galaxies (dashed line), and exclusively to the HERACLES sample (solid line).

Table 5.7. Metallicity Dependence of α_{CO} assuming constant SFE^a

Selected Data	Value at 12+logO/H=8.7	Slope of Power Law	Scatter (dex)
complete sample			
• all galaxies	8.2 ± 1.0	-2.8 ± 0.2	0.13
• non-starbursts	6.9 ± 1.0	-2.4 ± 0.3	0.10
HERACLES sample			
• all galaxies	8.0 ± 1.3	-2.0 ± 0.4	0.10
• non-starbursts	7.1 ± 1.2	-2.0 ± 0.4	0.09

Note. — (a) Using bisecting linear regression of $\log_{10} \alpha_{\text{CO}}$ as function of 12+log₁₀ O/H; uncertainties are determined by repeatedly adding random noise of 0.1 dex to x -axis and 0.3 dex to y -axis data values.

our literature compilation (Table 5.2). Color coding highlights metallicity as in previous plots. Star symbols indicate galaxies that are labeled in the literature as starbursts.

The derived α_{CO} values strongly depend on metallicity. For galaxies with 12+log₁₀ O/H \gtrsim 8.6, we find $\alpha_{\text{CO}} \sim \alpha_{\text{CO,Gal}}$ although with \sim 0.3 dex (factor 2) scatter. For galaxies with lower metallicity, α_{CO} increases strongly with decreasing metallicity. For dwarf galaxies with 12+log₁₀ O/H \lesssim 8.6, though most of them remain undetected in CO, we can readily exclude $\alpha_{\text{CO}} \sim \alpha_{\text{CO,Gal}}$. The few dwarf galaxies with CO detection suggest $\alpha_{\text{CO}} \gtrsim 10 \alpha_{\text{CO,Gal}}$ at 12+log₁₀ O/H \lesssim 8.4. We emphasize that the derived α_{CO} values for dwarf galaxies with $Z/Z_{\odot} \sim 1/2 - 1/10$ are by 1 – 2 orders of magnitude higher than α_{CO} values derived for massive spirals with $Z/Z_{\odot} \sim 1$.

We attempt to parametrize this dependence by fitting power laws of the form $\alpha_{\text{CO}} = A \times (12+\log \text{O}/\text{H} - 8.7)^N$. We use a bisecting linear regression to determine the best fitting function. Uncertainties are determined from a Monte Carlo analysis. We have repeatedly added Gaussian noise to α_{CO} with lognormal standard deviation of 0.1 dex and to 12+log₁₀ O/H with standard deviation of 0.3 dex and re-fitted the perturbed data. The quoted uncertainties correspond to the standard deviation of 100 such derived best-fit parameters. Table 5.7 lists the resulting normalizations and power law slopes together with the scatter of the data orthogonal to the best-fit power law. We divide our galaxy sample in two groups: “starbursts” and “non-starbursts”, and evaluate the HERACLES galaxies and the complete sample separately. This may help to minimize biases due to inhomogeneous data sets. We expect the smallest systematics for the HERACLES sample including only non-starburst galaxies. We separate the starbursts because they likely violate our assumption of a constant τ_{dep} having SFR in excess of their H₂ content.

The best-fit power law depend somewhat on the particular galaxy sample; see Figures 5.7 and Table 5.7. For the HERACLES sample we determine a slope of -2.0 ± 0.4 roughly independent of including or excluding starbursts (solid line) but having larger uncertainties due to the relative small dynamic range sampled by the detected galaxies.

For the complete galaxy sample, the slope is steeper. We determine a slope of -2.4 ± 0.2 for the non-starbursts (dashed line) and -2.9 ± 0.2 for all galaxies (dotted line). We consider the latter result uncertain and potentially biased high because it is driven by a handful galaxies that currently undergo a starburst and have CO measurements from Taylor et al. (1998), measurements that have not been confirmed yet. The scatter of the data to the best-fit relations is $0.09 - 0.12$ dex ($\sim 30\%$) which is significant smaller than the scatter of ~ 0.3 dex in the ratio $\alpha_{\text{CO}}/\alpha_{\text{CO,Gal}}$ for galaxies with $12+\log_{10} \text{O/H} \gtrsim 8.6$. In this sense a steep increase of α_{CO} with decreasing metallicity is much in favor as compared to a constant value. The trend fitted to the “complete, non-starburst” sample and its associated uncertainty is indicated as red striped region in Figure 5.8.

The recent study by Genzel et al. (2011) also applied the assumption of a constant SFE. They analyzed a sample of star-forming galaxies at redshift $z \sim 1 - 2$ and determined a slope of -1.9 ± 0.67 ; the orange striped region² in Figure 5.8. They also combined their distant galaxy sample with the dust-inferred α_{CO} measurements from Leroy et al. (2011) which reduces their slope to -1.3 ± 0.25 . Though, the decrease in slope is basically driven by two galaxies, M31 and SMC, and their result may be affected by combining two different methods.

5.7.3 Comparison

Approximate trends for the metallicity dependence of α_{CO} derived from the three discussed methods and their intrinsic scatter are indicated in Figure 5.8. At solar metallicities the three method give roughly consistent results within their uncertainties. Toward lower metallicities the three methods however predict different trends for the dependence of α_{CO} on metallicity. The α_{CO} values derived from the virial method (the green striped region in Figure 5.8) show no systematic trend with metallicity and exhibit roughly an order of magnitude scatter. The dust-inferred α_{CO} values (blue striped region) and the α_{CO} values derived from scaling the SFR (red and orange striped regions) however do show a strong systematic increase toward lower metallicities. For dwarf galaxies with $Z/Z_{\odot} \sim 1/2 - 1/10$ the dust-inferred α_{CO} values are roughly a factor 10 larger than a Galactic value but with ~ 1 order magnitude scatter, for the SFR-scaled α_{CO} values they are a factor 10 – 100 larger.

The discrepancy between α_{CO} values derived from the viral method and those derived from dust or SFR at low metallicities can be explained by the spatial scale which these methods operate on. The virial method operates on the small spatial scales of CO-bright cores of molecular clouds. At low metallicity these CO cores shrink as CO in low density gas gets dissociated while H_2 can survive there via self-shielding. Applying such α_{CO} values to the total CO luminosity of a galaxy thus traces only the H_2 mass within the high density CO-bright cores and at low metallicity will inevitably fail to predict the total H_2 mass. On the other hand, the α_{CO} values derived from dust or SFR are sensitive to

² Note that we changed the normalizations of the Genzel et al. parametrizations to match the data plotted in their Figure 3. For the high redshift sample we increased the normalization by 0.3 dex, for the combined sample we decreased it by 0.07 dex.

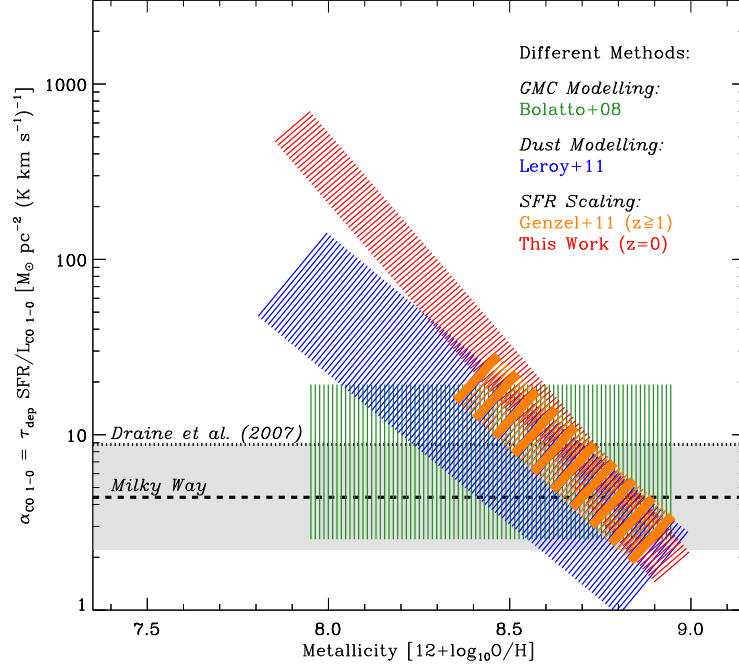


Figure 5.8 *Trends of the Metallicity Dependence of the CO-to-H₂ conversion factor α_{CO} .* Striped regions indicate the range of α_{CO} values derived from different methods (see text). The width in the trend lines indicate roughly the scatter of individual measurements.

CO-dark H₂ and can trace H₂ on spatial scales of the size of star-forming regions or larger.

But why are the α_{CO} values derived from dust and SFR different? We infer α_{CO} under the assumption of a fixed H₂/SFR ratio that spans from massive spirals to low-mass, low-metallicity dwarfs. If this assumption breaks down then we will mis-attribute variations in H₂/SFR to variations in α_{CO} . In models in which the star formation efficiency is set by the free-fall time, metallicity can affect H₂/SFR. This is pointed out by Gnedin et al. (2009); Gnedin & Kravtsov (2011); Feldmann et al. (2011); they show that the gas densities containing H₂ vary strongly with metallicity and radiation field, and thus free-fall times of clouds containing H₂ are not constant. While this can cause significant scatter in H₂/SFR on cloud scales, on large (\sim kpc) scales variations are expected to be much smaller. In environments with metallicity $Z/Z_{\odot} \sim 1/10$ and radiation field $U/U_{\odot} \sim 10 - 100$, free-fall times and thus H₂/SFR are reduced by (only) a factor 2 – 3. This is consistent with Krumholz et al. (2011); they find $\Sigma_{\text{SFR}}/\Sigma_{\text{H}_2}$ to be constant within factor 2 for ranges of $\Sigma_{\text{H}_2} = 0.1 - 100 \text{ M}_{\odot} \text{ pc}^{-2}$ and $Z/Z_{\odot} = 1 - 1/10$.

In the handful of studies that attempt to account for α_{CO} variations and measure H₂/SFR in low-metallicity galaxies (e.g., Gratier et al., 2010a,b; Bolatto et al., 2011), there are suggestions that H₂/SFR is up to 2–5 times lower in local dwarfs at $Z/Z_{\odot} \sim 1/5$. A factor of $\sim 2 - 5$ adjustment will not perfectly reconcile the various α_{CO} measurements at the lowest metallicities but can provide rough agreement at $Z/Z_{\odot} \sim 1/2 - 1/5$. In this case Figure 5.8 and similar plots combine two important trends: variations in α_{CO} and in τ_{dep} . More detailed work comparing SFR to H₂ estimated via independent tracers like

dust, CII, or gamma rays will be needed to refine this approach.

As noted above, the relative alignment of our galaxy sample along the x -axis (metallicity) in Figure 5.8 and preceding are fairly secure. However the absolute calibration of metallicities measured for extragalactic systems remains *very* uncertain. Therefore the relationship to solar metallicity remains somewhat tenuous, as does the alignment of the three methods.

Another concern is that the ratios of CO, H₂, and SFR vary with time. On small scales this shows as offsets between H α , a tracers of recent star formation, and CO, and induced large scatter in the respective ratios (e.g., Schrubba et al., 2010; Onodera et al., 2010) which can be linked to the evolution of star-forming regions (Kawamura et al., 2009). Numerical simulations even suggest that the ratios may never be constant inside a cloud because chemical equilibrium is not reached during most/all of a cloud’s lifetime (Glover et al., 2010; Glover & Mac Low, 2011; Shetty et al., 2011a,b; Feldmann & Gnedin, 2011). On galaxy scales however Pelupessy & Papadopoulos (2009); Papadopoulos & Pelupessy (2010) suggest that the ratios are roughly constant after dynamical equilibrium between ISM phases and stars is established ($t \sim 1$ Gyr). Only during (early) times of strong galaxy evolution when the ISM phases and star formation are out of equilibrium, larger deviations between CO, H₂, and SFR occur ($t \lesssim 0.2 - 0.3$ Gyr). Though gas-rich and/or low-metallicity galaxies can show strong periodic variations throughout their evolution. Such variations are strongest in the smallest dwarf galaxies ($M_B > -15$) and less common and strong in (more) massive dwarfs and spirals (Lee et al., 2009). Some galaxies of our literature sample do experience a current starburst (e.g., NGC 2366, NCG 4449, and NGC 5253) or are in a post-starburst phase (e.g., NGC 1569). These bursts can last for a few 100 Myr (McQuinn et al., 2010) and may show a strong sequence in the brightness of their molecular gas and star formation tracers: starting with being bright in CO, followed by a phase being bright in CO and IR (a sign of embedded star formation), and finally being bright in IR and FUV (sensitive to stellar populations of age $\lesssim 100$ Myr; Salim et al., 2007). Our literature samples, including SINGS, LVL, THINGS, and HERACLES have often an implicit or explicit bias to select IR-bright galaxies, and thus actively star-forming systems which means that we infer high α_{CO} . Robust volume-limited surveys or otherwise unbiased sampled are needed to remedy this bias.

5.8 Summary

This paper presents sensitive maps of ¹²CO $J = 2 - 1$ emission for 16 nearby star-forming dwarf galaxies from the HERACLES survey (for a first presentation of a subsample our galaxies see Leroy et al., 2009). The large map coverage ($\sim 2 - 5 R_{25}$) and fine ($13''$) angular resolution, ~ 250 pc at our average distance of $D = 4$ Mpc, sample our targets by 10 – 1000 resolution elements.

We apply the stacking techniques developed in Schrubba et al. (2011) to perform the most sensitive search for CO emission in low-metallicity galaxies across the whole star-forming disk. We search for CO emission on three spatial scales: individual lines-of-sight, stacking over IR-bright regions indicating embedded star-formation and thus regions likely to contain molecular gas, and stacking over whole galaxies. Our point source sensitivity

is $L_{\text{CO}2-1} \sim 2 \times 10^4 \text{ K km s}^{-1} \text{ pc}^2$, sufficient to detect a CO-bright cloud with luminosity comparable to Orion A or the brightest cloud in the SMC but at distance $D = 4 \text{ Mpc}$. When stacking over the whole galaxy our data have sufficient sensitivity to detect the LMC at $D = 4 \text{ Mpc}$; but not the SMC. We detect 5 galaxies in CO with total CO luminosities of $L_{\text{CO}2-1} = 3 - 28 \times 10^6 \text{ K km s}^{-1} \text{ pc}^2$. The other 11 galaxies remain undetected in CO even in the stacks and have $L_{\text{CO}2-1} \lesssim 0.4 - 8 \times 10^6 \text{ K km s}^{-1} \text{ pc}^2$.

We combine our dwarf galaxy sample with a large sample of spiral galaxies from the literature to study the relations between $L_{\text{CO}2-1}$, M_B , and metallicity. We find that dwarf galaxies with metallicities $Z/Z_\odot \approx 1/2 - 1/10$ have $L_{\text{CO}2-1}$ of 2 – 4 orders of magnitude smaller than massive spiral galaxies with $Z/Z_\odot \sim 1$ and that their $L_{\text{CO}2-1}$ per unit L_B is 1 – 2 orders of magnitude smaller. Dwarf galaxies are thus significantly fainter in CO than a simple linear scaling with galaxy mass would suggest.

We also compare $L_{\text{CO}2-1}$ with tracers of recent star formation (FUV and $24\mu\text{m}$ intensity) and find that $L_{\text{CO}2-1}$ per unit SFR is 1 – 2 orders of magnitude smaller in dwarf galaxies as compared to massive spiral galaxies. The low $L_{\text{CO}2-1}/\text{SFR}$ ratios in dwarf galaxies may either indicate intrinsically small H_2 masses coupled with high star formation efficiencies or that CO emission becomes an increasingly poor tracer of H_2 . The two are degenerate, however, we argue that the latter, i.e., significant changes in the CO-to- H_2 conversion factor, α_{CO} , at low metallicity is the dominant driver.

To estimate α_{CO} and study its metallicity dependence we apply an idea recently proposed by Genzel et al. (2011) which assumes the conversion of H_2 to stars to be constant and infer H_2 masses and α_{CO} values by scaling the observed total SFRs. We assume an H_2 depletion time of $\tau_{\text{dep}} = M_{\text{H}_2}/\text{SFR} = 1.8 \text{ Gyr}$, the average value found for massive spirals in the HERACLES sample (Schruba et al., 2011). With this assumption we derive α_{CO} values for dwarf galaxies with $Z/Z_\odot \approx 1/2 - 1/10$ more than one order of magnitude larger than those found in massive spiral galaxies with solar metallicity. This strong increase of α_{CO} at low metallicity is consistent with previous studies, in particular those of Local Group dwarf galaxies which model dust emission to constrain H_2 masses (Leroy et al., 2011; Bolatto et al., 2011). Even though it is difficult to parametrize the dependence of α_{CO} on metallicity given the currently available data the results suggest that CO is increasingly difficult to detect at lower metallicities. This has direct consequences for the detectability of star-forming galaxies at high redshift which presumably have on average sub-solar metallicity.

It is a pleasure to thank my collaborators on this project:

Adam Leroy, (MPIA, NRAO), Fabian Walter (MPIA), Frank Bigiel (UC Berkeley), Elias Brinks (University of Hertfordshire), Erwin de Blok (University of Cape Town), Gaelle Dumas (MPIA), Carsten Kramer (IRAM), Erik Rosolowsky (University of Okanagan), Karin Sandstrom (MPIA), Karl Schuster (IRAM), Antonio Usero (Observatorio Astronómico Nacional, Madrid), Axel Weiss (MPIfR), and Helmut Wiesemeyer (IRAM)

6 Concluding Remarks & Outlook

6.1 Concluding Remarks

The basic question that has driven this work is the question what sets the star formation rate in a galaxy. This is a long standing question of astronomy and has been pursued by astronomers for over 50 years by now. A basic goal of many studies has been to characterize the (functional) relationship between star formation rate and gas abundance and search for potential environmental dependencies. To truly understand star formation in galaxies, we however also require answers to a number of closely related questions: we need to characterize the gas phase that is directly associated with star formation; find out if this “star-forming” gas makes the bulk gas reservoir of a galaxy, or alternatively how it is assembled from that and what processes are responsible or delimitate this assembly; we have to understand how the “star-forming” gas is converted into stars; and finally assess the role of stellar feedback that may quench or trigger further star formation.

This forms an ambitious set of questions as it covers processes as small as the formation of individual stars from molecular cores observable in the Solar Neighborhood, the larger agglomerations of gas and star formation in GMCs observable in our and the most nearby galaxies, and finally whole galaxies which can have vastly different properties as found throughout the Universe. Thanks to the multi-wavelength data described here, and others like them, we know today that this relationship is complex even on galaxy scales and does not just depend on a single parameter (i.e., the total gas mass) as once assumed. Isolating the processes that underlie this complex behavior, however, is a complicated task as many processes act in a correlated way, at least on large scales that are easiest observable. To break these degeneracies and dissect the most relevant processes, astronomers have investigated more and more of the cosmic electromagnetic and particle spectrum, pushed their observations to finer and finer resolution toward the small scales where star formation is actually happening, and expanded their surveys to include more and more galaxies and thus extend the range of environments probed.

New high resolution multi-wavelength surveys suggest different modes of star formation: (a) The “star-forming or disk sequence” in which star formation is most closely related to the amount of molecular gas, roughly linearly in regions with $\Sigma_{\text{gas}} \approx 10 - 100 M_{\odot} \text{ pc}^{-2}$ in which star formation proceeds in isolated regions (i.e., GMCs) that are largely decoupled from their ambient gas, and with super-linear slope in regions with $\Sigma_{\text{gas}} \gtrsim 100 M_{\odot} \text{ pc}^{-2}$ where star-forming regions progressively lose their isolated character and form a more persistent turbulent star-forming medium. (b) The “starburst sequence” in which star formation proceeds much more rapidly as suggestive from the amount of (low density) molecular gas, likely connected to external influences (e.g., major mergers) that provoke the concentration of large amounts of gas to high densities and (temporarily) boost star

formation. (c) The “hampered regimes” in which star formation proceeds at much lower rate than suggested by the available total gas content with the processes responsible for that low star formation tied to suppressed formation of a molecular phase out of atomic.

This work concentrates on understanding the star formation process in nearby galaxies. In particular it explores the limits of the star formation law — the relationship between star formation rate and gas surface density — and explores regimes in which observational or physical reasons lead to a (apparent) breakdown of this “law”. We look at how it breaks at high resolution (due to the evolution of individual star-forming regions; Chapter 3), in H I-dominated parts of galaxies (as H₂ formation becomes the bottleneck of star formation; Chapter 4), and in environments of low metallicity (likely due to changes in the CO-to-H₂ conversion factor; Chapter 5).

To perform this study, an comprehensive collection of multi-wavelength data for a large sample of nearby spiral and dwarf irregular galaxies has been assembled (Chapter 2 and Appendix Figures). This database stands out by its homogeneous coverage with tracers of atomic and molecular gas and obscured and unobscured star formation with unprecedented resolution and sensitivity over the entire galaxies (sometimes though limited for the HERACLES data). To exploit these data at their best, a novel machinery has been developed to stack spectra over large regions inside one or many galaxies and push the sensitivity limit to the faintest regions (Section 4.5). This machinery has then been used to extract the most sensitive measurements of molecular gas as traced by CO emission for such a large sample of galaxies by to date. For spiral galaxies (Chapter 4), we could thus trace more than 90% of the total (exponential) molecular gas disk. For dwarf galaxies (Chapter 5), we could determine the first sensitive measurements of the total CO luminosity over all star-forming regions significantly improving the information value of previous pointed observations. This comprehensive database will be made public in the near future and can be used to test all sorts of theories invoked to describe the star formation law and the phase balance of the interstellar medium. They can also be used to complement high resolution interferometric observations.

In the following list we highlight a few of the key results obtained by this work, for a complete description we refer to the summary sections at the end of the previous chapters.

- The molecular gas in spiral galaxies is distributed in an exponential disk with scale length $l_{\text{CO}} \sim 0.2 R_{25}$ extending out to the optical radius, R_{25} , similar to that of star formation but also that of older stars (Section 4.6.2).
- The molecular gas disk shows no break or truncation in the H I-dominated outer parts of spirals galaxies and thus provides no evidence of a threshold of star formation according to same critical surface density of radius (Section 4.6.1 & 4.6.2)
- Azimuthally-averaged radial profiles of CO (i.e., H₂) and extinction-corrected SFR scale with one another and have approximately constant ratios inside of galaxies independent of the local atomic gas mass (Section 4.6.1).
- The relation between SFR and H₂ and total gas (H I+H₂) has about the same rank correlation coefficient but SFR–H₂ can be parametrized by a single linear function while SFR–(H I+H₂) shows a strong break between H I- and H₂-dominated regions.

Inside the regimes studied, we find no correlation between SFR and H I (Section 4.6.1).

- For a combined sample of 33 galaxies, we find evidence for systematic variations in the CO/SFR ratio between galaxies with systematically lower ratios for lower mass, lower metallicity galaxies. These variations dominate the scatter in CO–SFR space (Section 4.6.1 & 5.6.3).
- CO luminosity in dwarf galaxies with $Z/Z_{\odot} \approx 1/2 - 1/10$ is low, both in absolute sense (by factor of $10^2 - 10^4$) as well as normalized by SFR or B -band luminosity (by more than an order of magnitude). It is suggestive that this indicates a significant increase in the CO-to-H₂ conversion factor at low metallicities (Section 5.6.2).
- The star formation relation shows substantial scatter on small scales. On a 75 pc scale in M33, the CO/H α ratio varies by factor $\gtrsim 10$ when targeting either CO-bright or H α -bright regions. This scatter is likely associated with the evolution of individual star-forming regions. It is significantly reduced when averaging over several star-forming regions (Section 3.6 & 3.7).

6.2 Outlook

The “star formation law” still holds many fundamental questions. We have yet to fully grasp the physical processes that control the atomic to molecular gas conversion, the nature of star formation in diffuse low density environments of outer disks and dwarf galaxies, but also the processes that control gas density distribution and star formation in starburst galaxies. Our current ability to quantify gas masses and star formation rates is likely not better than an accuracy of ~ 2 , so that 50% level changes in the star formation efficiency and physical conditions are easily possible. Another intriguing question that becomes addressable now is if the star formation process has been different in the early Universe. Both the studies of nearby and distant galaxies will be revolutionized by observations from the fully operational ALMA and EVLA. Indeed, both fields of research are already now developing vigorously, thanks in large part to the execution of systematic and homogeneous multi-wavelength surveys to which also this thesis work contributed.

A natural extension of the current surveys would be to target a statistically and/or volumetric complete sample of galaxies. The THINGS/HERACLES surveys are biased toward bright galaxies (as the underlying SINGS survey is) and the majority of targets are Sb-Sc spiral galaxies, though these surveys do include a smaller number of Sd-Sdm spiral and dwarf irregular galaxies. The systematic comparison of previous studies has shown that much of the confusion about the parametrization of the star formation law or the relevant gas phase has been caused by observations of different ISM and SFR tracers, different methodologies of data reduction and applied conversion factors. A homogeneous survey and analysis of a statistical sample of galaxies naturally overcomes this confusion and holds the prospect to isolate the relevant processes that control star formation.

Nearby galaxies can be well resolved down to sub-kiloparsec scales (e.g., $10'' \Leftrightarrow 500$ pc at $D = 10$ Mpc) with current telescopes which let us divide a galaxy into few hundred

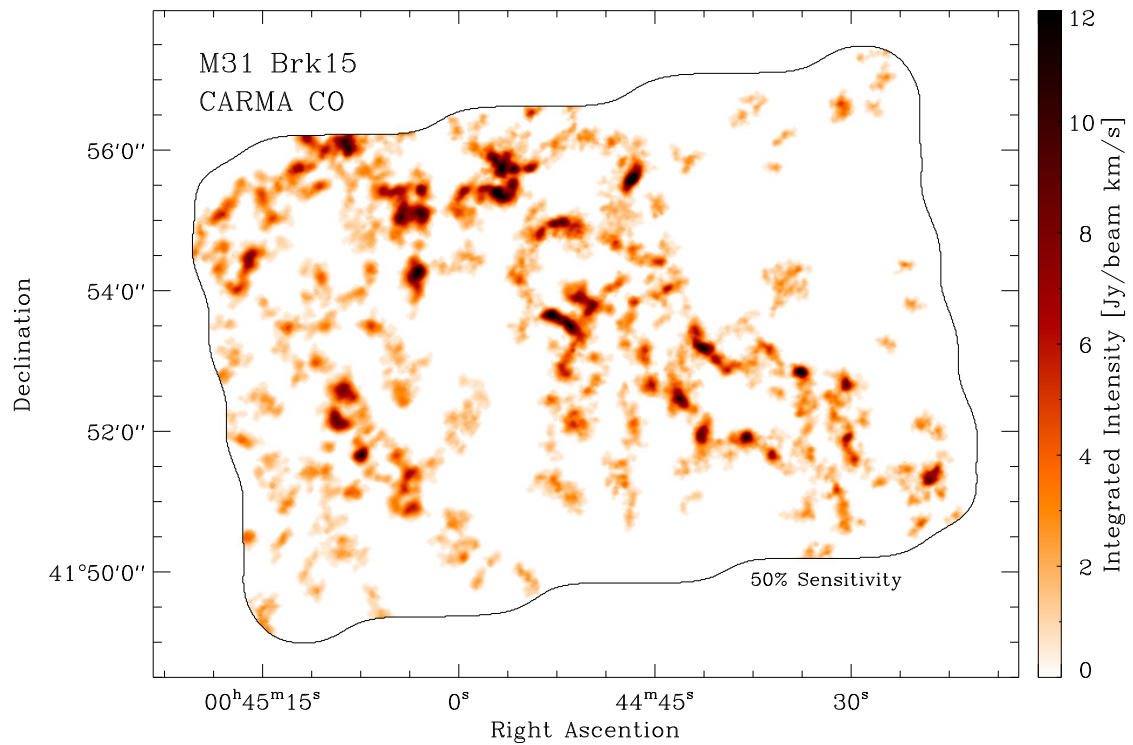


Figure 6.1 CARMA CO map of a $6' \times 9'$ region of the nearby Andromeda galaxy M31. These data have ~ 20 pc linear resolution. Thus, each dark spot is a giant molecular cloud, the sites where stars are forming. In the future, with ALMA these kind of observations will be possible throughout the (near) Universe promising new insights in our understanding of the conversion of gas to star. [This data is part of a recently started large CARMA project led by me.]

elements and determine their individual properties. Such surveys have been performed for volume-limited samples at optical wavelengths (including narrow-band imaging of $H\alpha$) using ground-based telescopes, in the ultraviolet with *Galex*, or in the infrared with *Spitzer*. Until today it has not been possible to perform similar high resolution surveys for such a large sample through mapping of the interstellar medium. Most of the currently high-resolution and high-sensitivity data in the radio regime are from the THINGS / HERACLES surveys presented here but that comprises “only” ~ 50 galaxies. However, ALMA and current developments of a second generation of multi-beam for receivers single-dish radio telescopes will advance these kind of surveys within the next years.

Totally new worlds are opening up just at the moment with the completion of ALMA and the EVLA. These two instruments should usher in a new golden age of radio astronomy and have the prospect to revolutionize many areas of astrophysics. Concerning the science of this work, these instruments will allow studies of the star formation law on cloud scale across a large number of nearby galaxies as well as resolved studies of galaxies throughout the entire Universe. For nearby galaxies, this includes studies of GMC



Figure 6.2 This image shows the center of the merging Antennae galaxy NGC 4038 / 4039 highlighting the wealth of detail becoming visible by current new instruments as ALMA and the EVLA. Young stars are shown in blue-white, surrounded H II regions in pink. Atomic gas as traced by the ELVA is blue. Sites of current massive star formation are visible at mm/sub-mm wavelengths observed by ALMA. Image credit: (NRAO/AUI/NSF); ALMA (ESO/NAOJ/NRAO); HST (NASA, ESA, and B. Whitmore (STScI))

properties that will help to determine by which extent the star formation process in these clouds does depend on environment. Much more detailed studies of the ISM become feasible, increased sensitivity (and bandwidth) will allow to observed many high-density gas tracers (e.g., HCN, HCO⁺, etc.). In combination with high-resolution dust maps (from sub-millimeter continuum) we will be able to determine the chemical, thermal, and density structure of the ISM and the processes that control them. The question how GMCs form is just one of many interesting questions that can be studied. With the EVLA we are able to robustly measure star formation rates (from free-free and/or synchrotron radiation) and study the star formation law on cloud scales. These studies will be further stimulated by the JWST and ground-based extremely large telescopes as these will be able to detect and characterize individual stars outside the Local Group (the current limit for studies with HST) and thus provide essential information on the age and energy output of stars which will let us determine the energy balance of the ISM, the lifetime of GMCs, and the process of triggered star formation.

Just as an appetizer, Figure 6.1 shows a CARMA CO map of a 6' × 9' region in our neighboring galaxy M31 with linear resolution of ~ 20 pc with the prospect to detect

~ 100 GMCs (from a ongoing 160 hour project recently started by me at CARMA). For the same galaxy (field) the PHAT project (PI: J. Dalcanton) using HST has mapped individual stars down to $5 M_{\odot}$ providing detailed knowledge on the stellar populations. In this galaxy, we can start to address the above highlighted questions already today. In the near future, we will be able to perform these kind of studies across many more galaxies and environments.

The star formation relation is observed to steepen, i.e., become super-linear, in regions of high gas (surface) density (see Figures 1.4 & 1.5). This kind of steepening is barely visible in the centers of some of the HERACLES galaxies but seems to be a general feature of galaxies in the high redshift Universe (at least for those galaxies that we can detect with current instrumentation). The morphology of the gas and star formation and the processes that control them are basically unknown today. ALMA and the EVLA will allow high resolution observations that unveil the nature of the star formation process in these regimes and will give a better indication which fraction of stars has formed under these conditions of enhanced star formation efficiency throughout the Universe. The possibility of these kind of studies has been very recently highlighted by first ALMA observations of the Antennae galaxy (see Figure 6.2).

Another field which has been studied in this work and which may look forward to stimulating new insights is the study of the ISM and star formation in dwarf galaxies. The work presented here constitutes the most sensitive search for CO emission in dwarfs, however to make progress we had to average many data to achieve high sensitivity and still ended up mostly with non-detections. This limitation will drastically improve with more sensitive instruments (e.g., ALMA) in the near future. Observations of dwarf galaxies will provide an essential test of the impact of intense radiation fields and low metal abundance on the star formation process, knowledge that is critical for our understanding of how star formation has proceeded in the early Universe.

Today, astronomers are privileged to look forward to an extremely exciting time of research that promises ground-breaking new observations and will revolutionize our insight into the processes that determine the evolution of the Universe and its constituents. This will require hard work and we will inevitably face the moment when we have to give up much-loved though out-dated conceptions. In those moments we have to remember that spending our time to think about the Universe is by far the most compelling work possible and that the only principle that we are never allowed to abandon is our curiosity!

Atlas of Galaxies and Radial Profiles

Here we present integrated intensity maps and radial profiles for all galaxies from the HERACLES survey studied in this work. Each page shows the data of one of our galaxies. The upper four panels show maps of integrated intensity for H I, CO $J = 2 \rightarrow 1$, FUV, and $24\mu\text{m}$. All data is at our working resolution of $13''$ (except the *Spitzer* $70\mu\text{m}$ and very few H I data). The dashed ellipse shows the galactocentric radius $R = 1 R_{25}$, the radius of the 25^{th} magnitude *B*-Band isophote. For details on the surveys, data processing, and conversion factors we refer to Chapter 5.4. Galaxy parameter such as distance, inclination, position angle, and R_{25} are given in Tables 4.1 & 5.1.

The lower two panels show radial profiles of H I, CO, FUV, $\text{H}\alpha$, and IR at 24 and $70\mu\text{m}$ used to generate the plots in Chapter 4. For details on the exact method we refer to this Chapter. The applied conversion factors are given in Section 2.2. In summary, we average the data in $15''$ wide tilted rings. For the CO data, we stack the shifted spectra over this area and determine the integrated CO intensity from fitting line profiles to the stacked spectrum. For the H I, FUV, $\text{H}\alpha$, and IR data we use two-dimensional maps of intensity. We determine the 1σ scatter from the 68^{th} percentile from the data inside each ring. We plot these as error bars but note the distinction from the uncertainty in the mean. Note that the extend of all radial profiles is limited to a galactocentric radius at which the radial annulus is still sampled by more than 50% of its area by the HERACLES CO maps. Emission in other wavelengths (especially of H I) may extend to larger radii.

For each galaxy we present two panels of radial profiles: The lower left panel shows CO and H I both in units of observed intensities (K km s^{-1} , left-hand y -axis) and converted to mass surface densities ($\text{M}_{\odot} \text{pc}^{-2}$, right-hand y -axis) of H_2 and H I. The color of the CO points indicates the significance with which we could determine the integrated CO intensities: green for high significance measurements, orange for measurements of marginal significance and red for 3σ upper limits. To have H_2 and H I on the same mass surface density scale, we multiplied the observed 21cm line intensities by a factor of 312.5 (the ratio of Equations (4.1) and (4.2)). We also plot the star formation rate (SFR) surface density ($\text{M}_{\odot} \text{yr}^{-1} \text{kpc}^{-2}$) determined from $\text{H}\alpha+24\mu\text{m}$ and FUV+ $24\mu\text{m}$. Black solid-dashed lines show our exponential fit to the radial CO profile. We fit all high significance data excluding galaxy centers, defined as the the inner $30''$. The derived exponential scale lengths (in units of R_{25}), appear in the lower left corner. The lower right panel shows observed intensities (in MJy sr^{-1}) of our SFR tracers — $\text{H}\alpha$, FUV, 24 and $70\mu\text{m}$ emission.

6 Concluding Remarks & Outlook

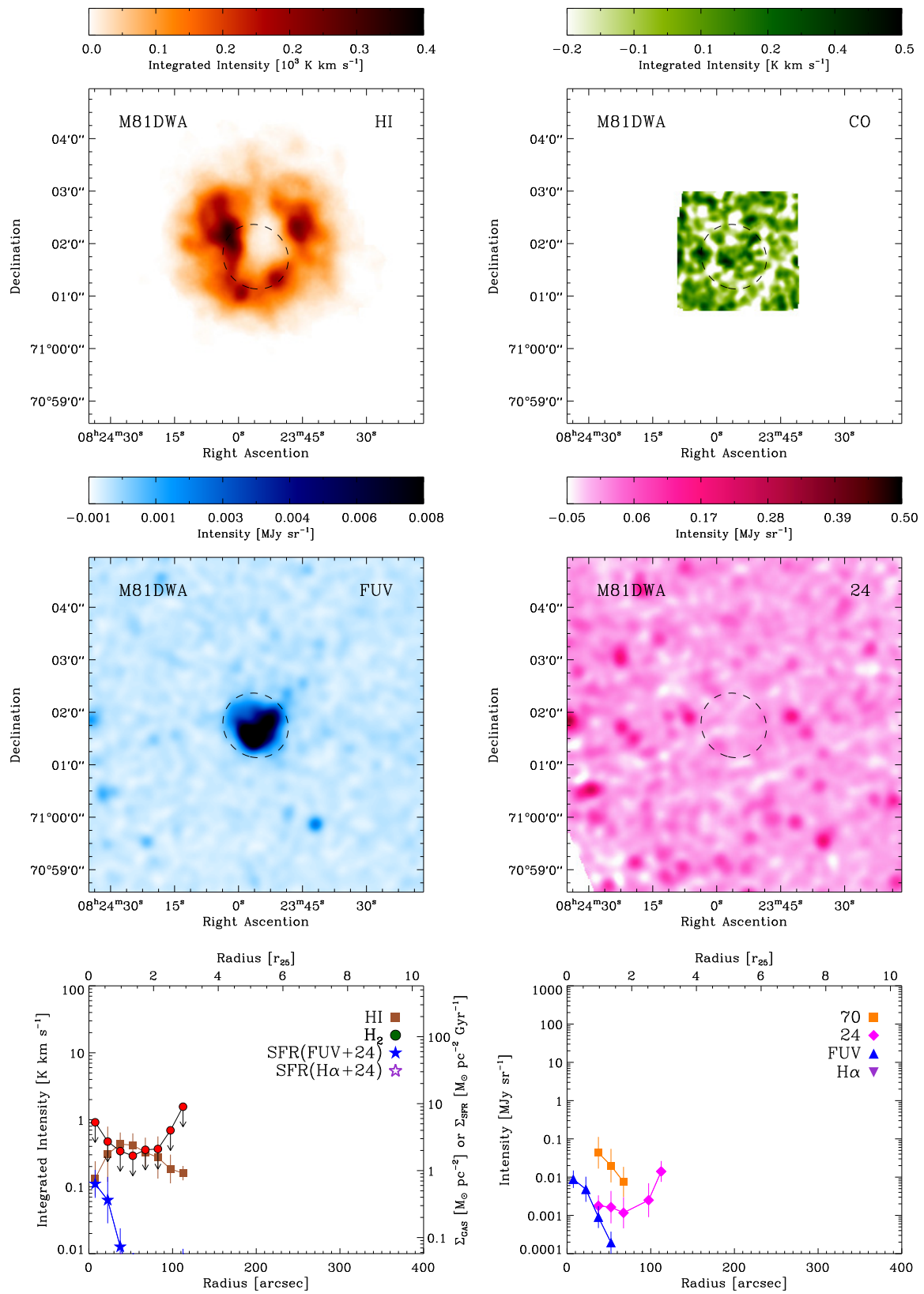


Figure A.1 Atlas of Galaxy Poster Stamps — M81 dw A

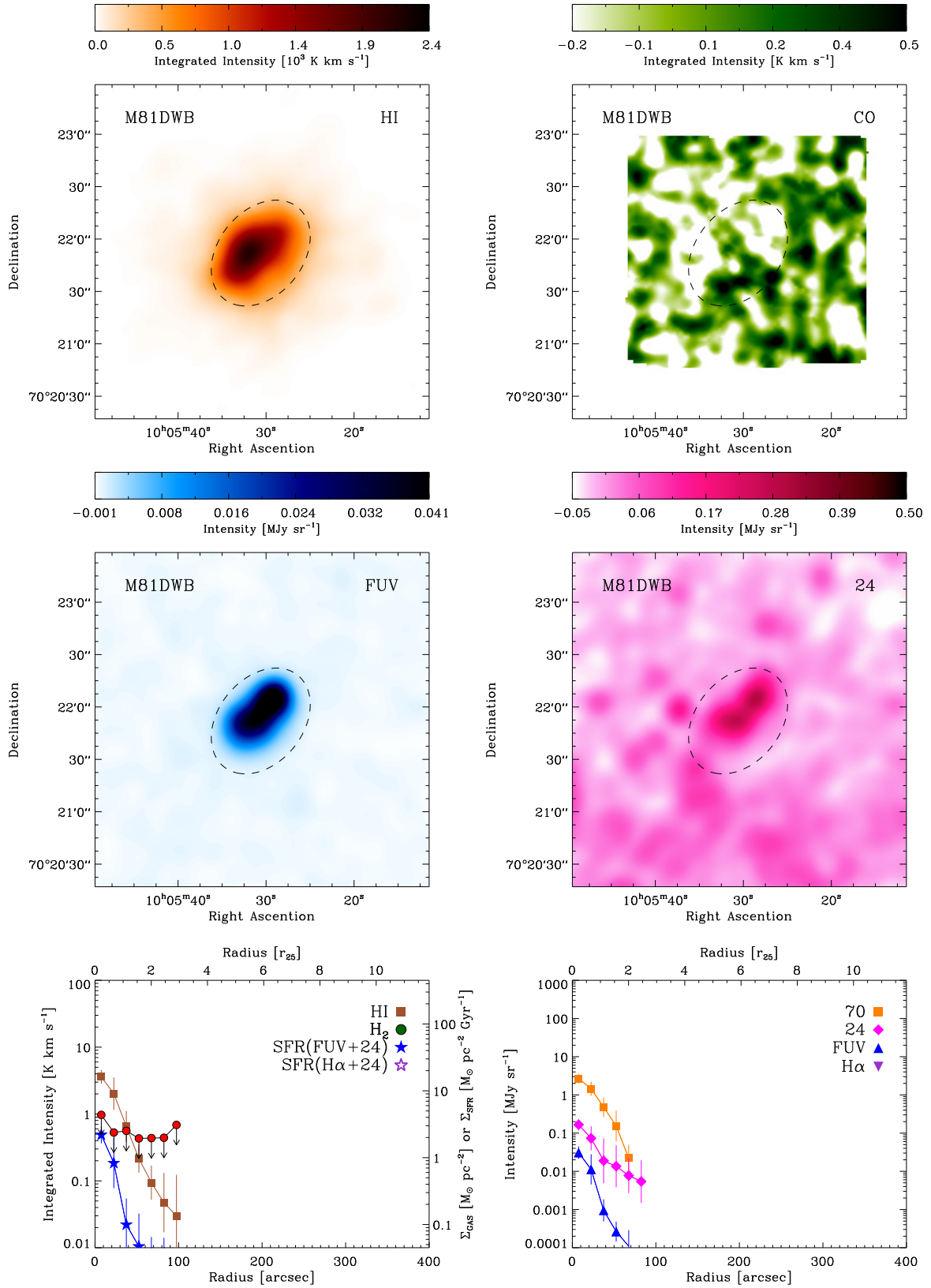


Figure A.1 (Continued) Atlas of Galaxy Poster Stamps — M81 dw B

6 Concluding Remarks & Outlook

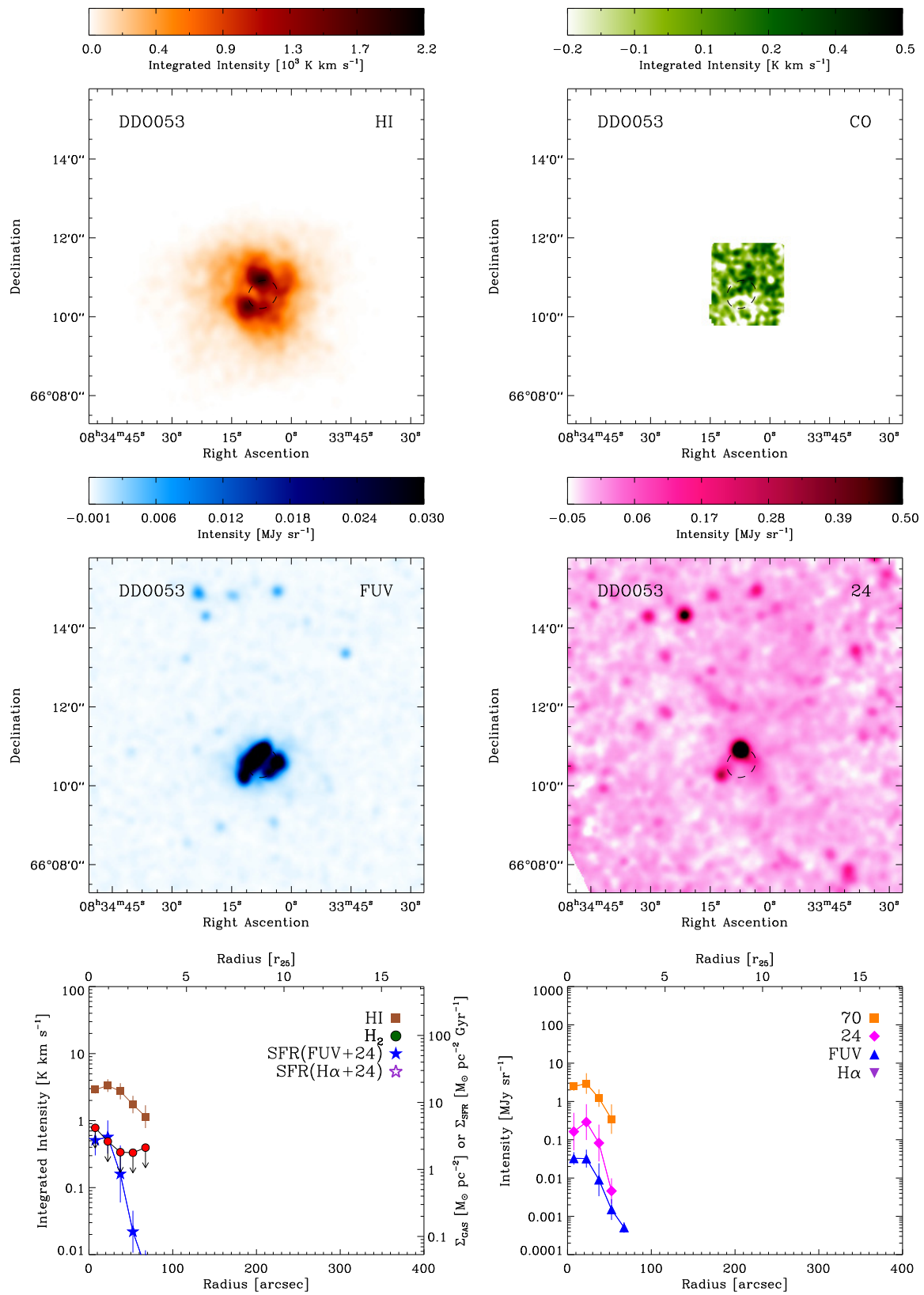


Figure A.1 (Continued) Atlas of Galaxy Poster Stamps — DDO 53

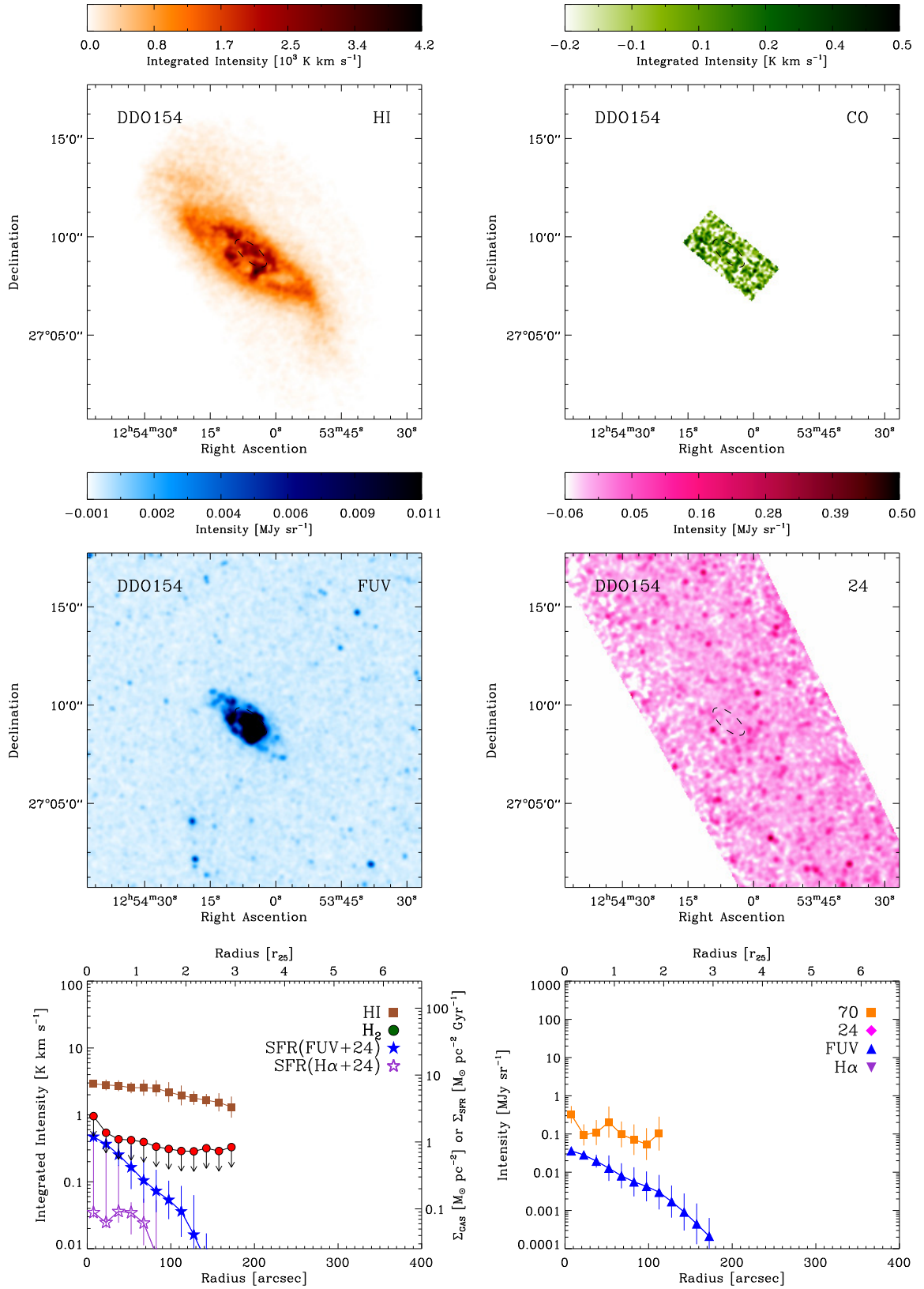


Figure A.1 (Continued) Atlas of Galaxy Poster Stamps — DDO 154

6 Concluding Remarks & Outlook

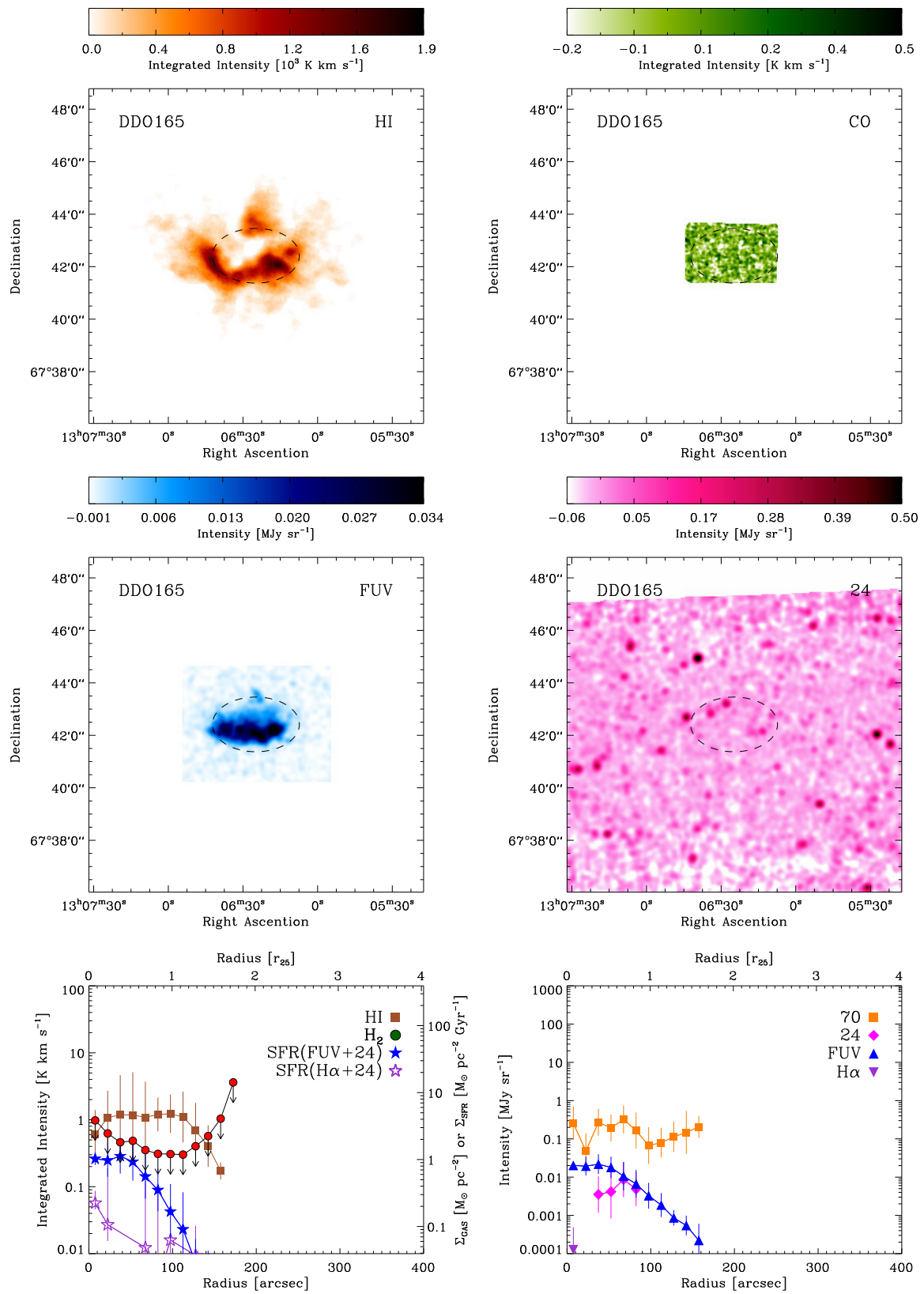


Figure A.1 (Continued) Atlas of Galaxy Poster Stamps — DDO 165

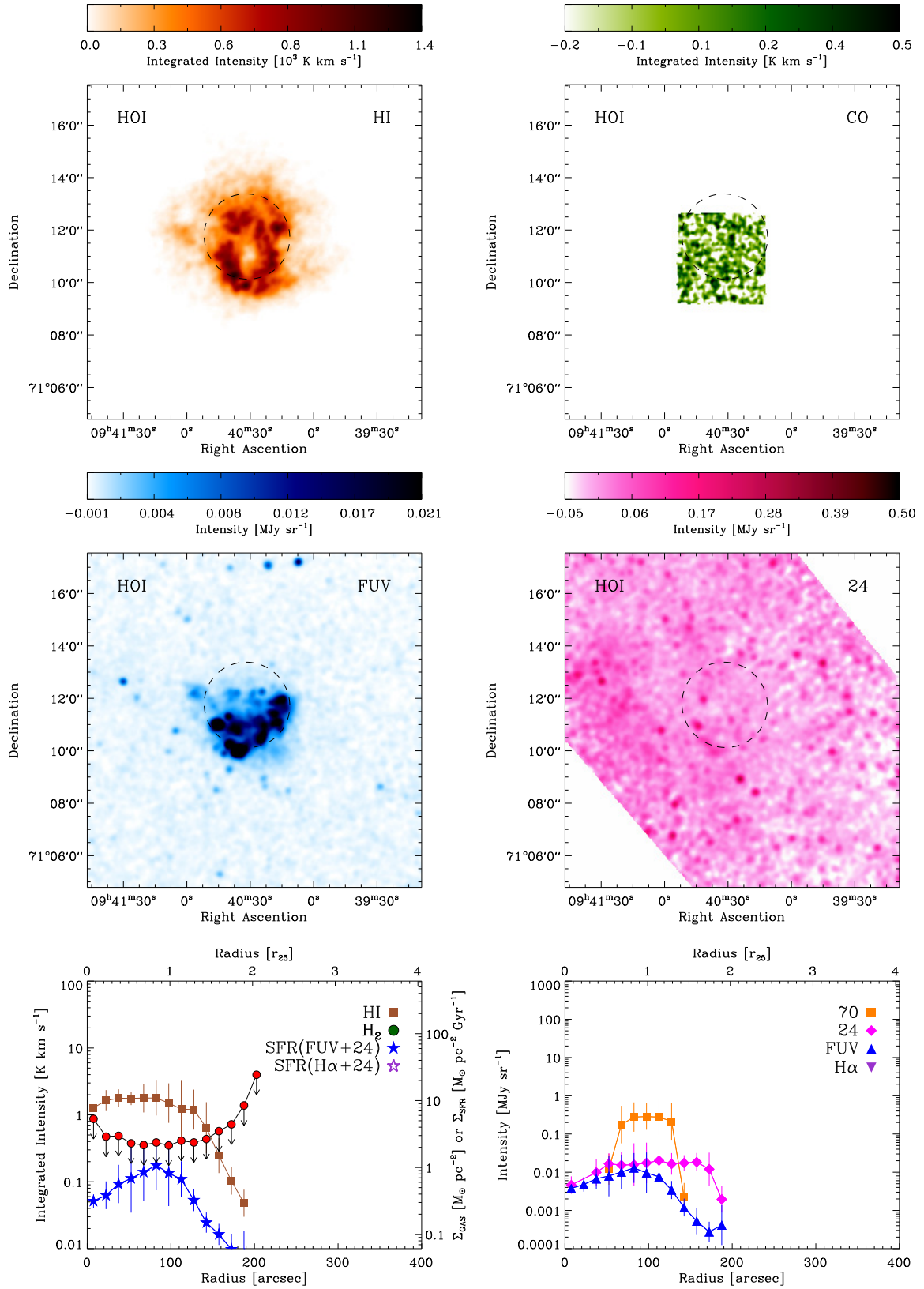


Figure A.1 (Continued) Atlas of Galaxy Poster Stamps — Ho I

6 Concluding Remarks & Outlook

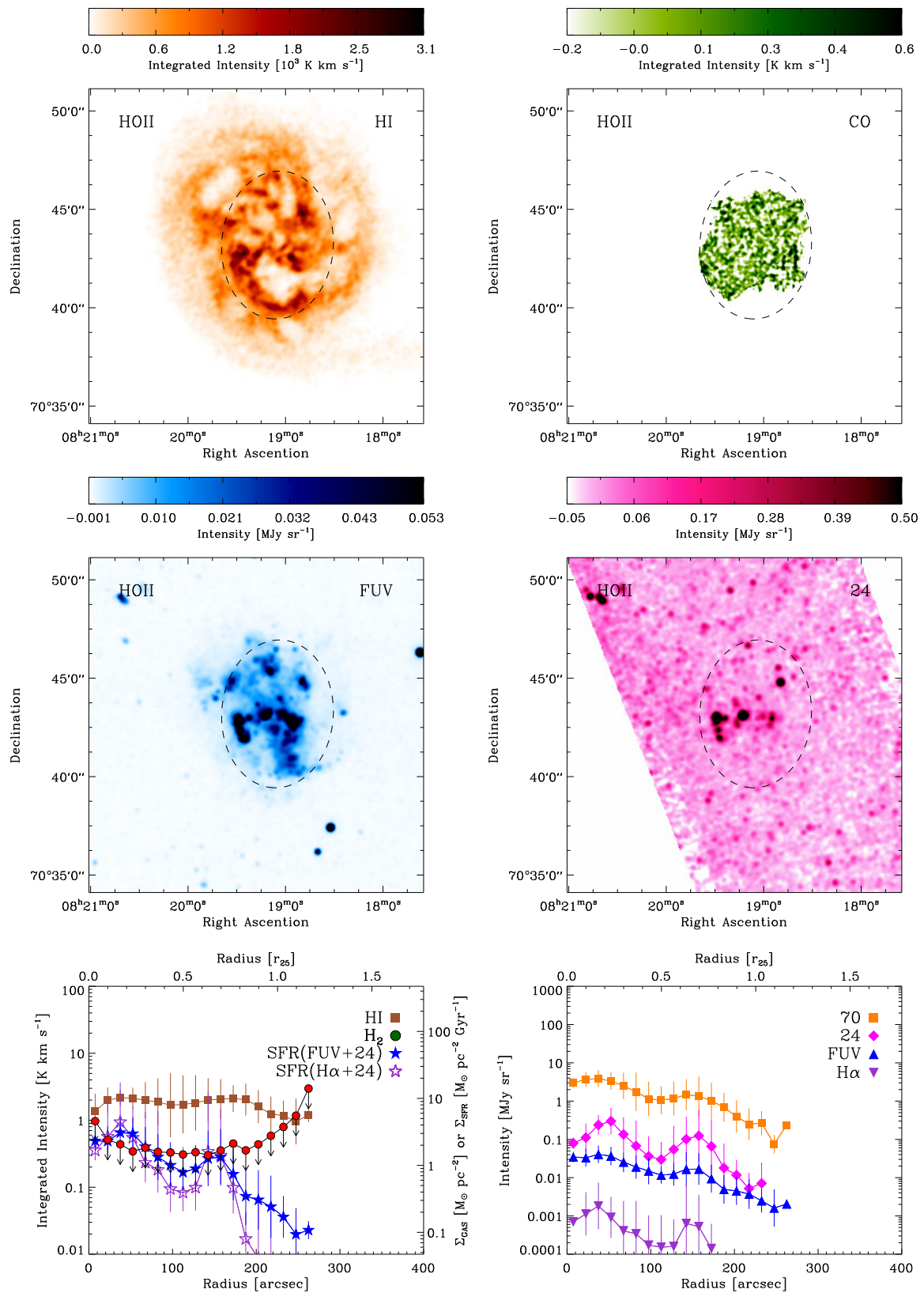


Figure A.1 (Continued) Atlas of Galaxy Poster Stamps — Ho II

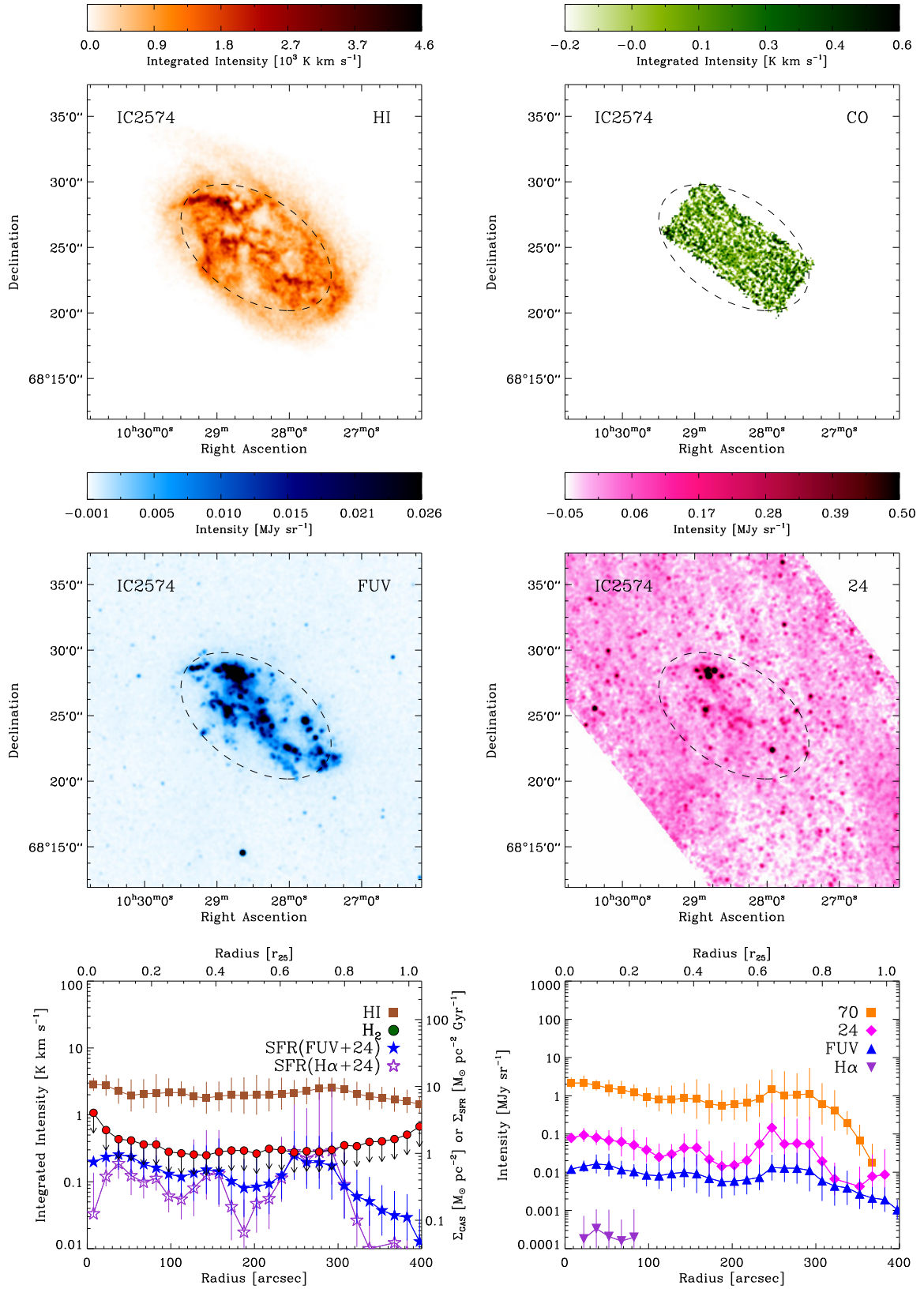


Figure A.1 (Continued) Atlas of Galaxy Poster Stamps — IC 2574

6 Concluding Remarks & Outlook

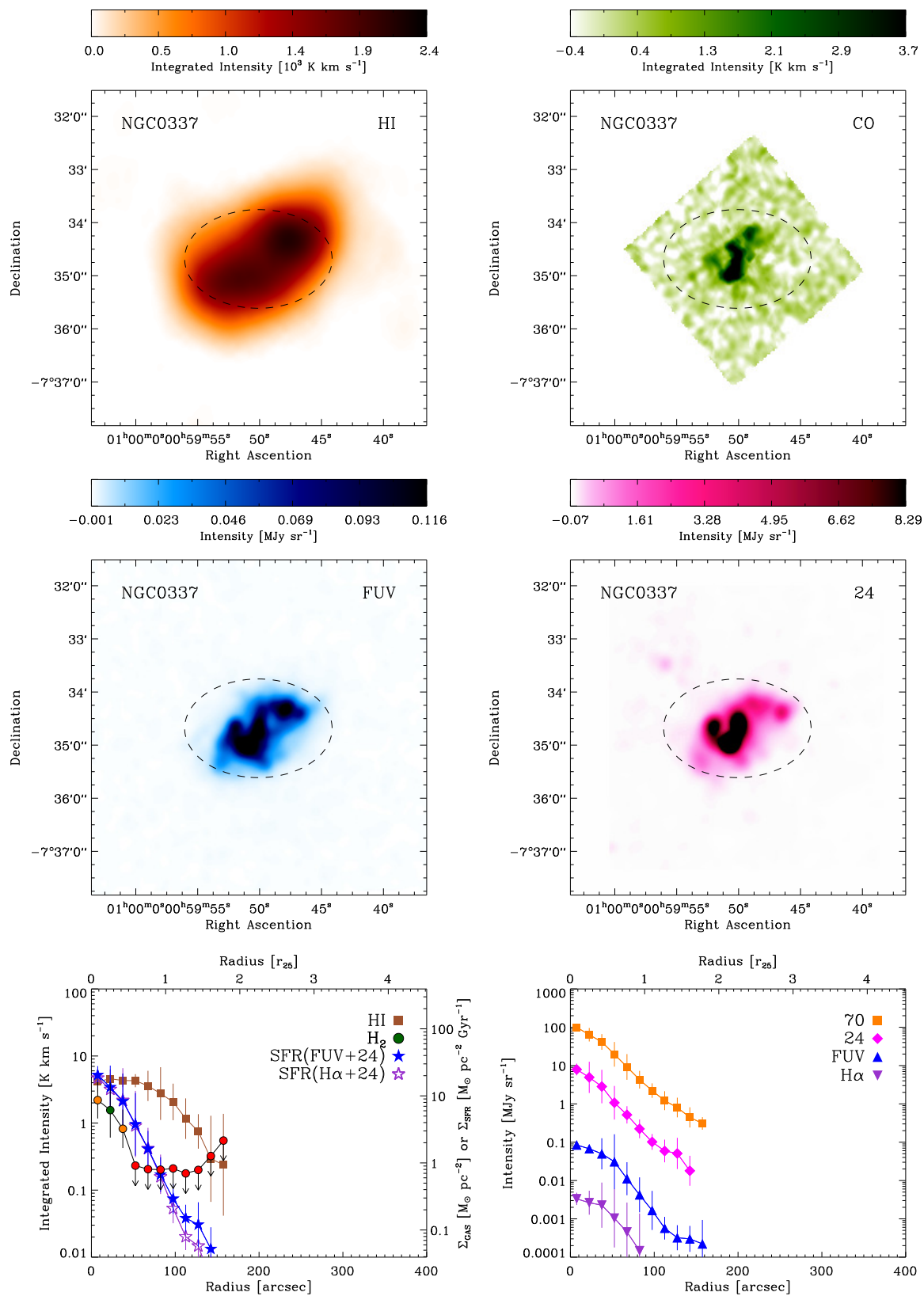


Figure A.1 (Continued) Atlas of Galaxy Poster Stamps — NGC 337

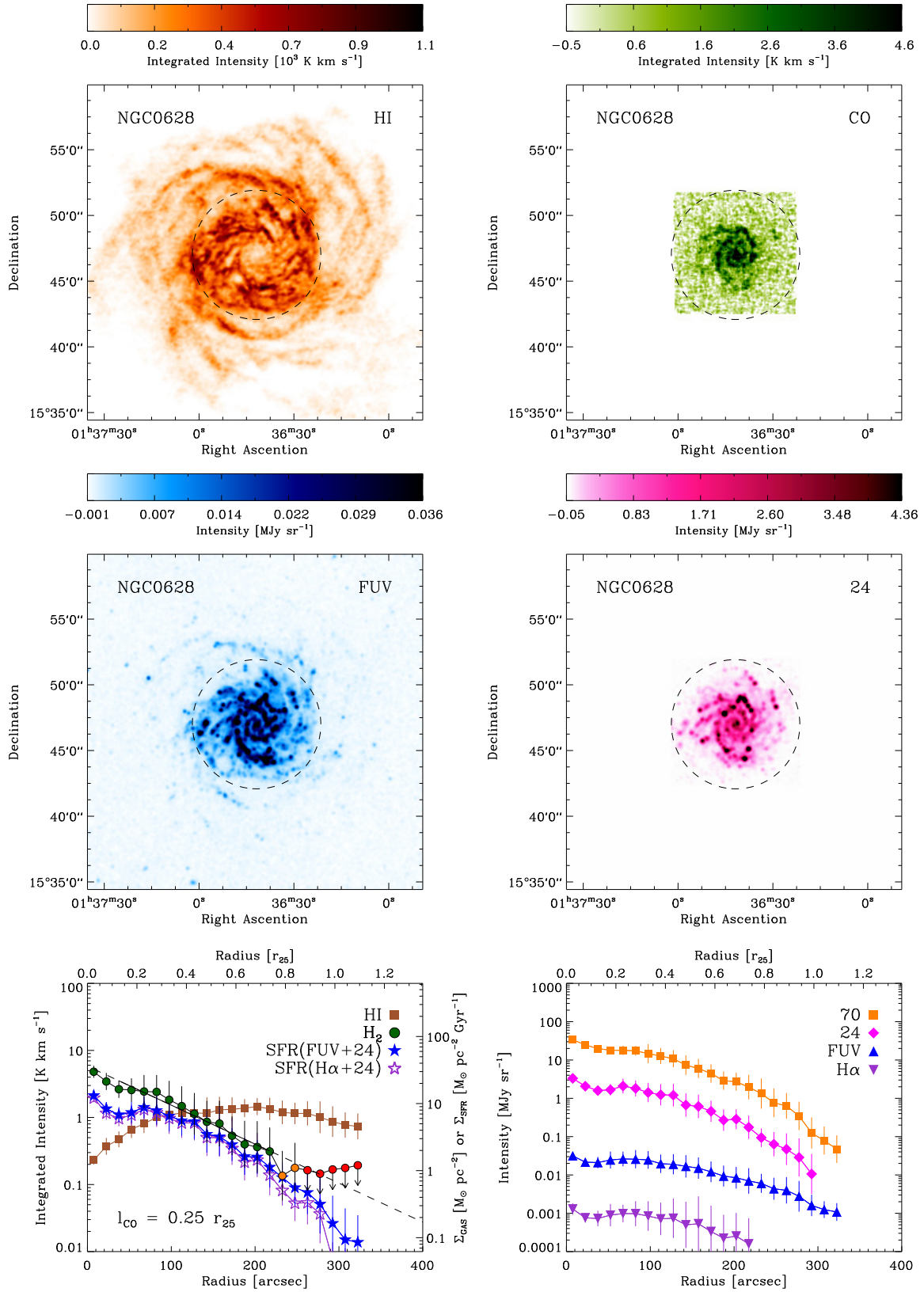


Figure A.1 (Continued) Atlas of Galaxy Poster Stamps — NGC 628 (M 74)

6 Concluding Remarks & Outlook

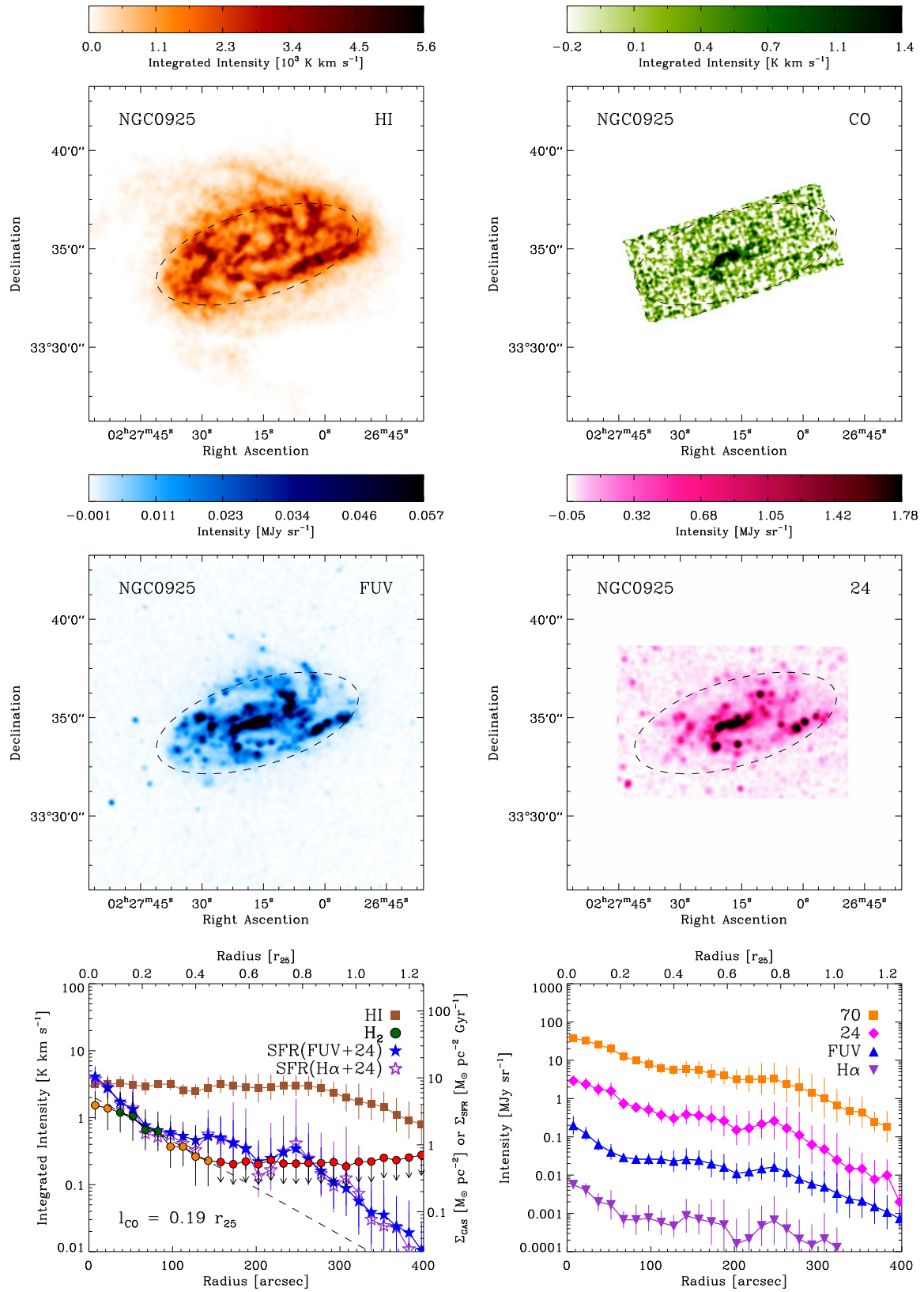


Figure A.1 (Continued) Atlas of Galaxy Poster Stamps — NGC 925

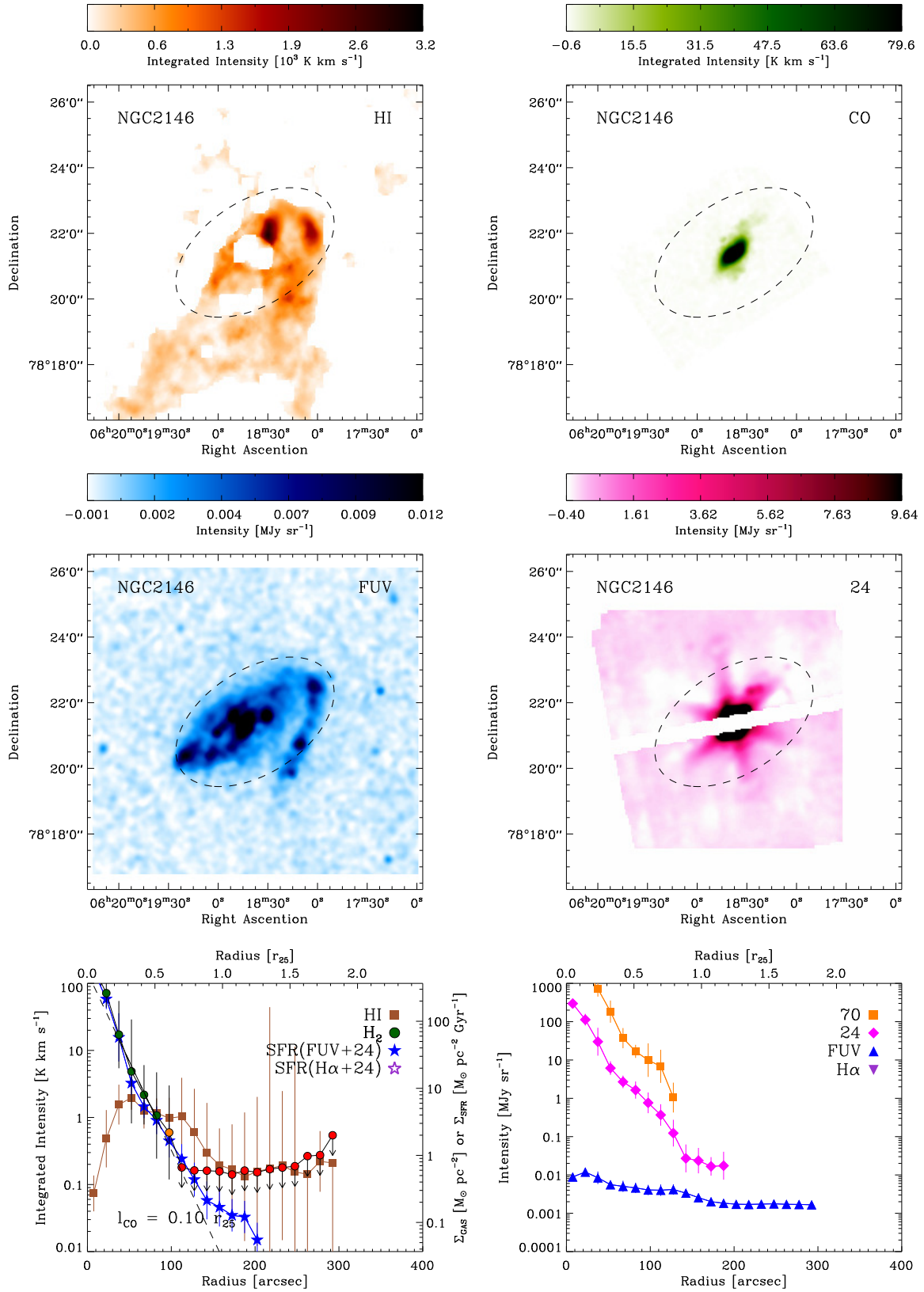


Figure A.1 (Continued) Atlas of Galaxy Poster Stamps — NGC 2146

6 Concluding Remarks & Outlook

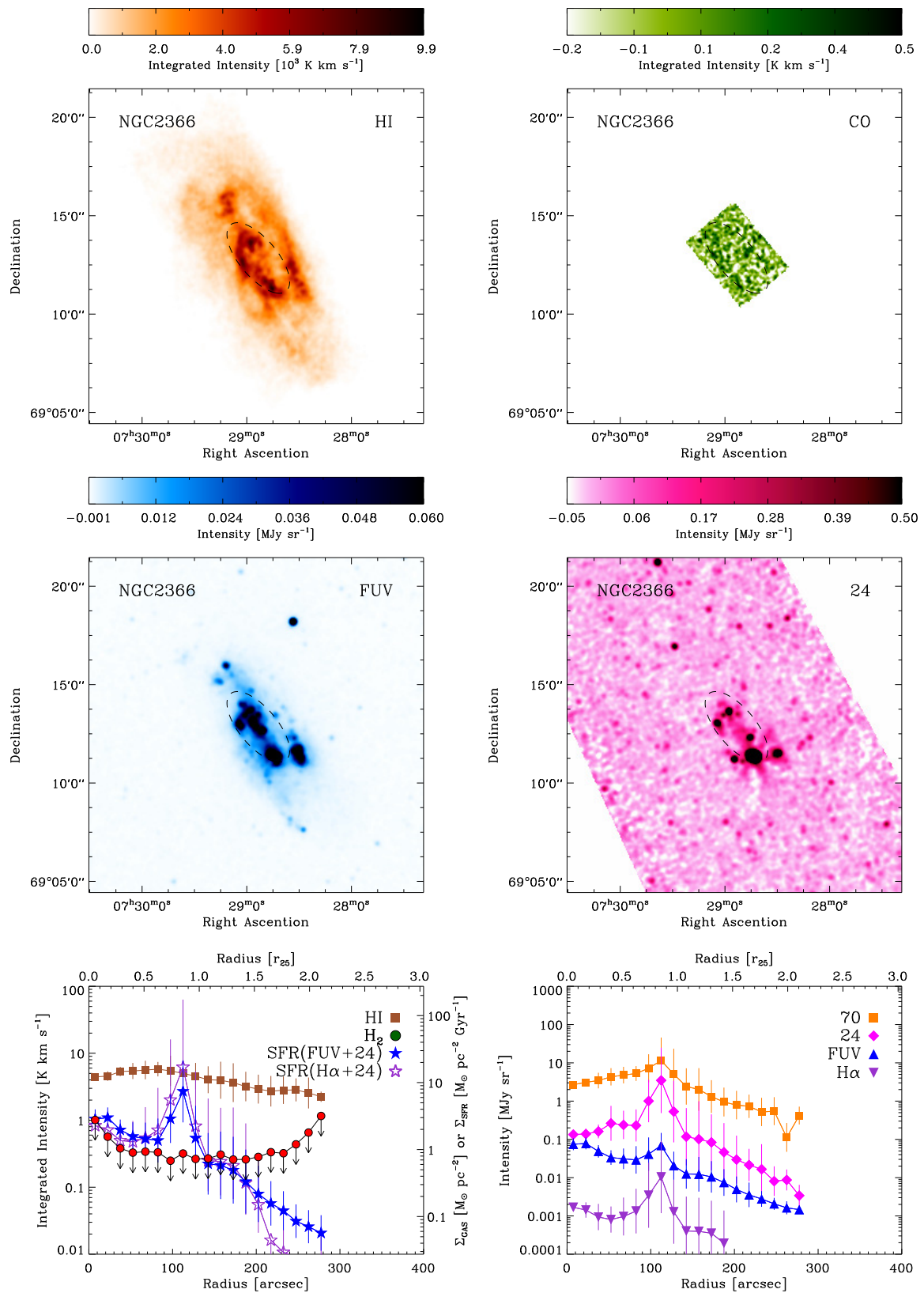


Figure A.1 (Continued) Atlas of Galaxy Poster Stamps — NGC 2366

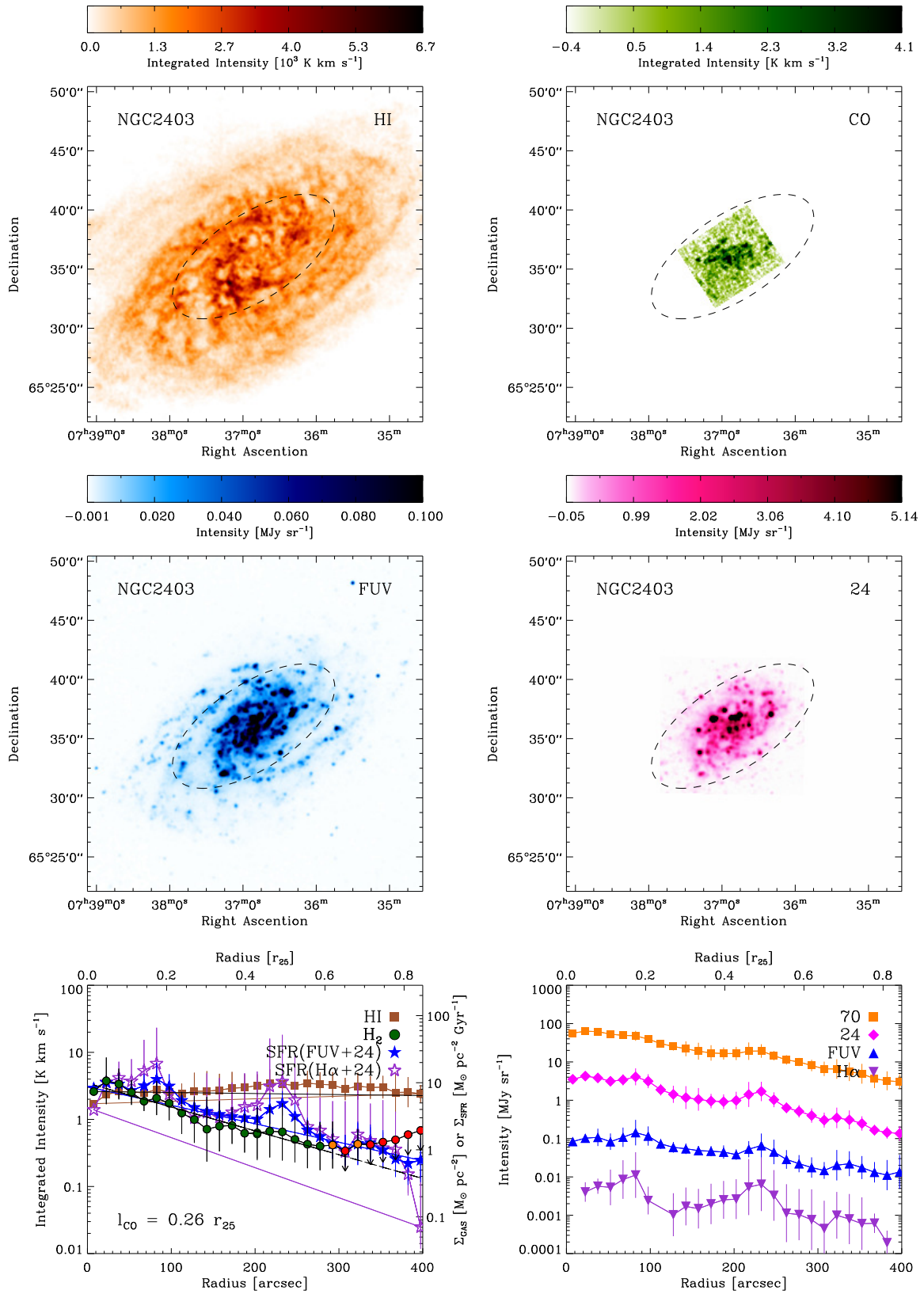


Figure A.1 (Continued) Atlas of Galaxy Poster Stamps — NGC 2403

6 Concluding Remarks & Outlook

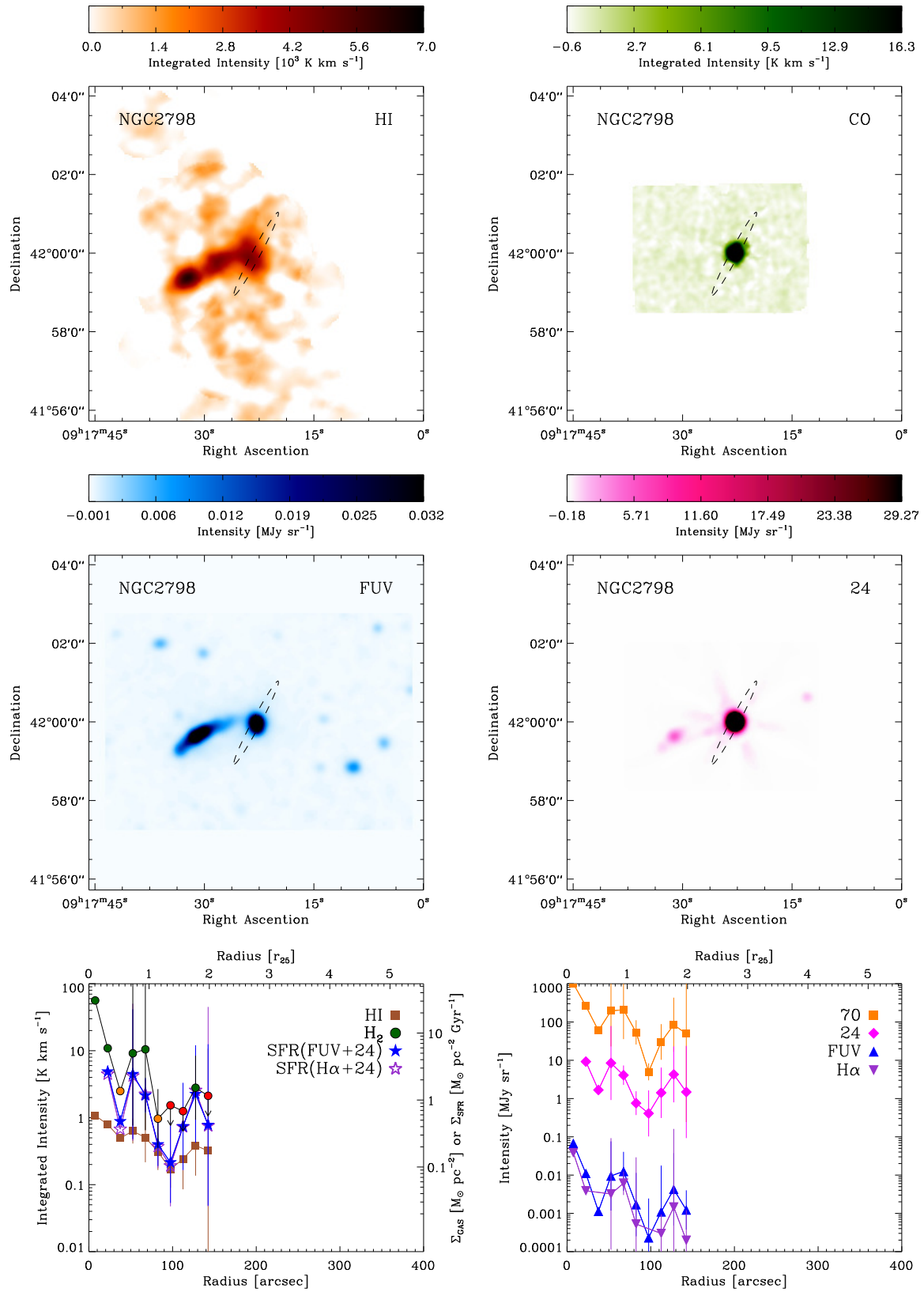


Figure A.1 (Continued) Atlas of Galaxy Poster Stamps — NGC 2798

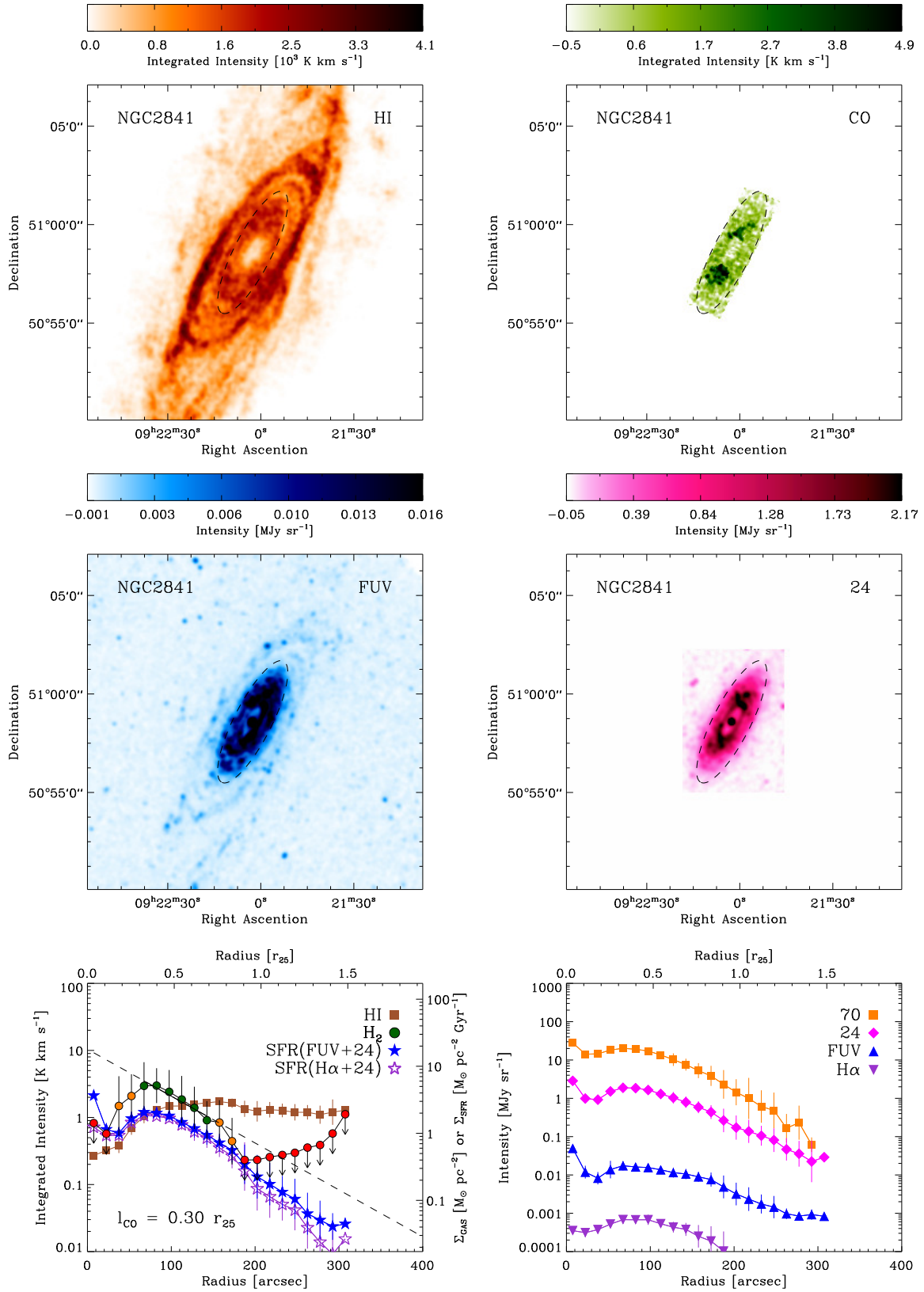


Figure A.1 (Continued) Atlas of Galaxy Poster Stamps — NGC 2841

6 Concluding Remarks & Outlook

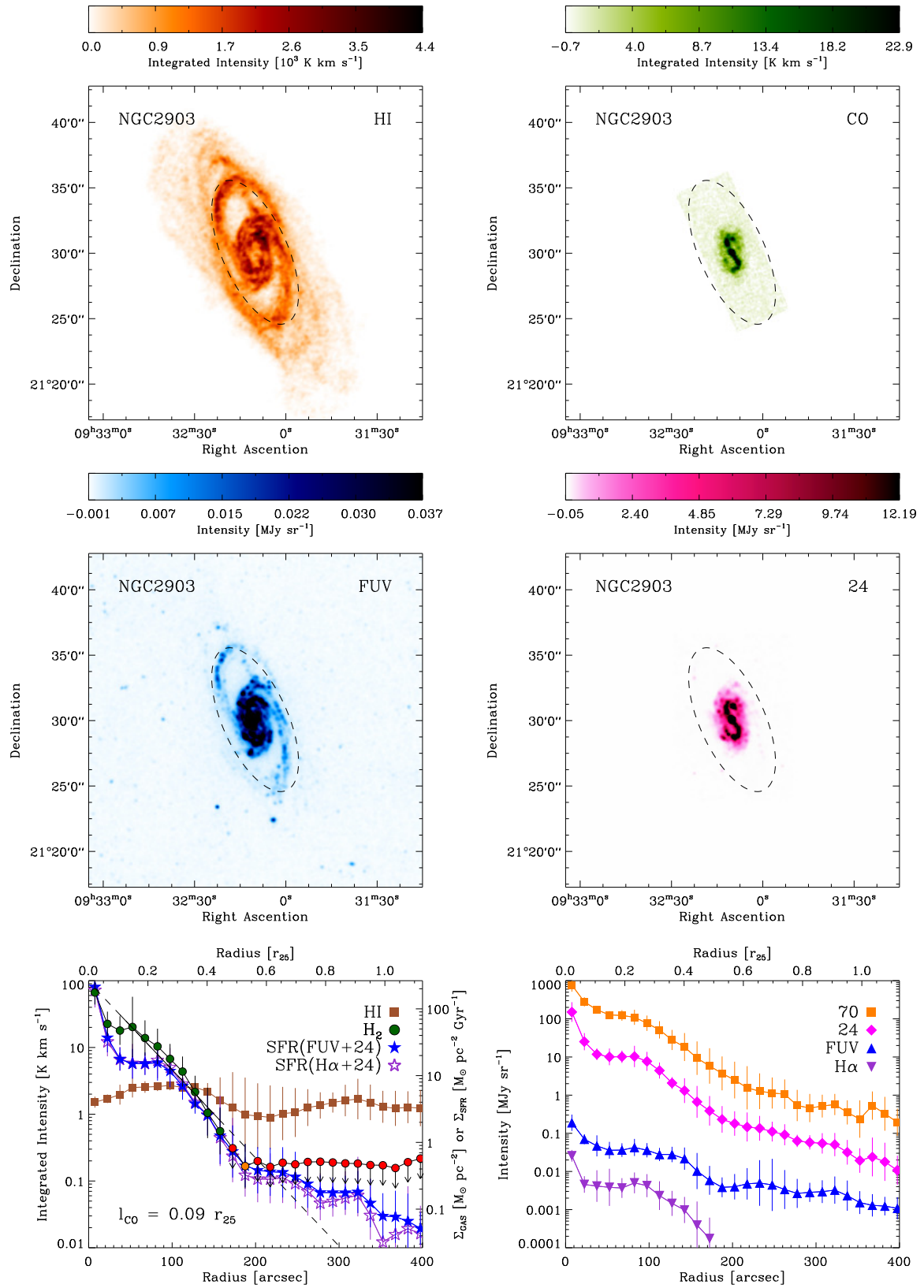


Figure A.1 (Continued) Atlas of Galaxy Poster Stamps — NGC 2903

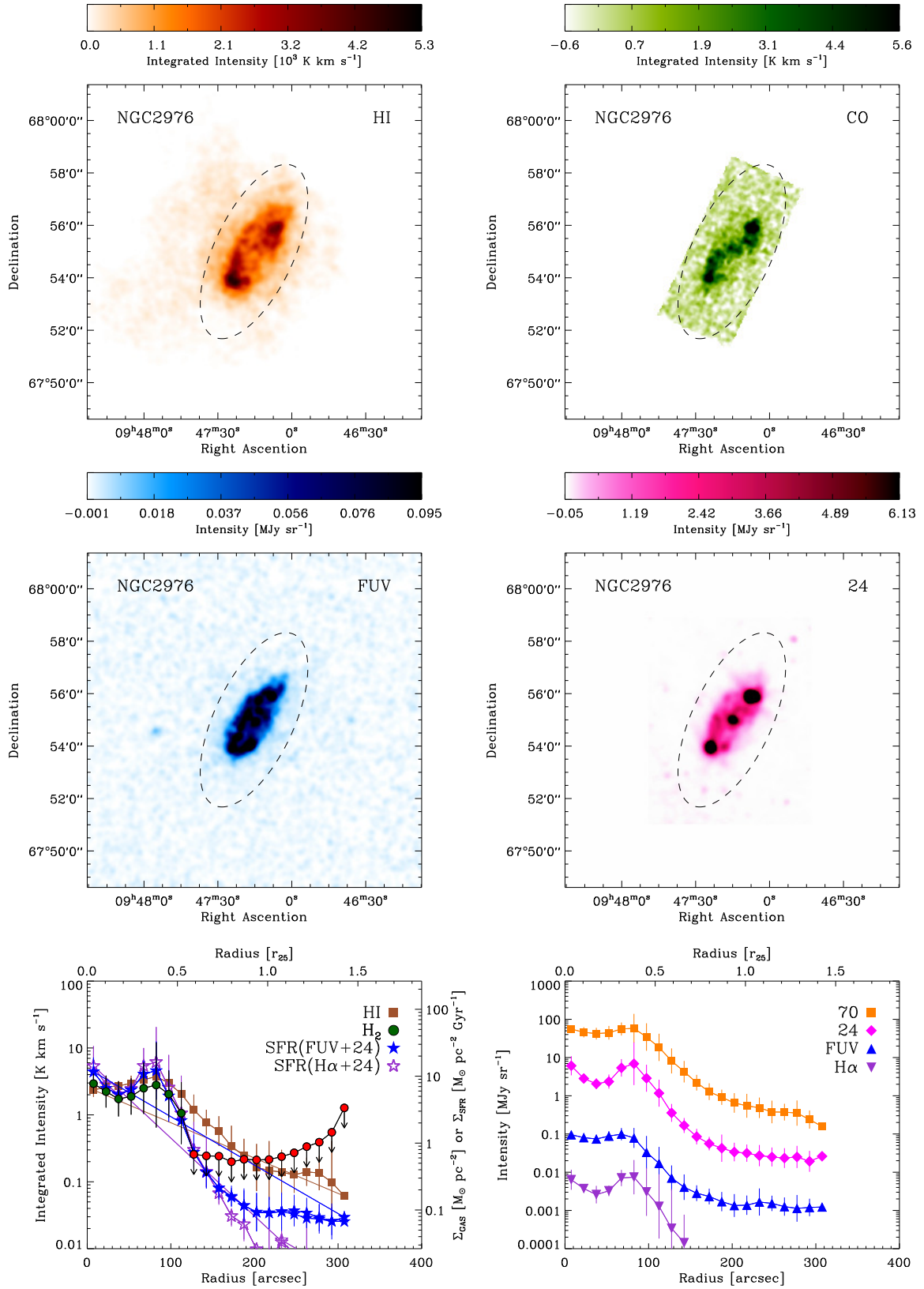


Figure A.1 (Continued) Atlas of Galaxy Poster Stamps — NGC 2976

6 Concluding Remarks & Outlook

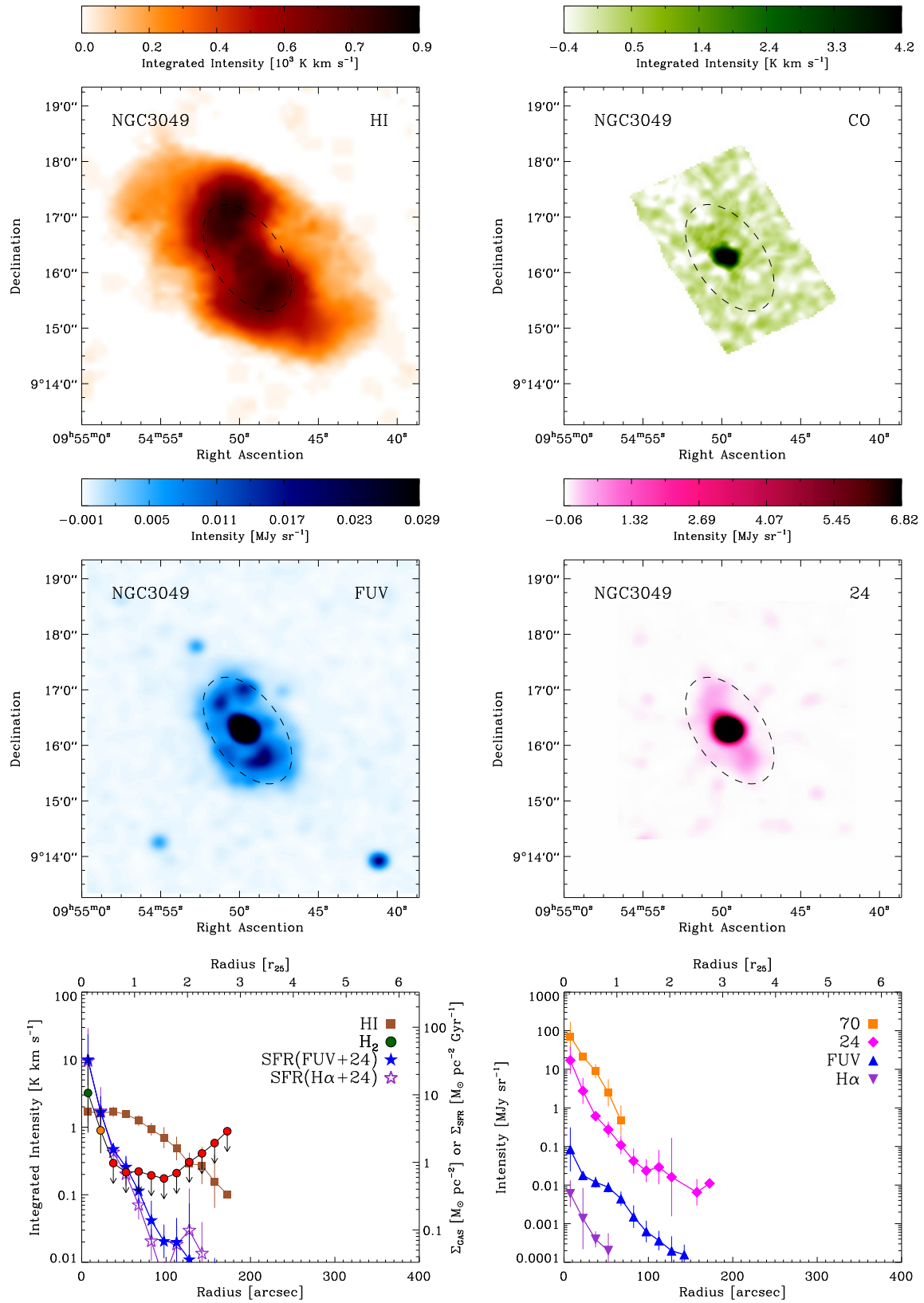


Figure A.1 (Continued) Atlas of Galaxy Poster Stamps — NGC 3049

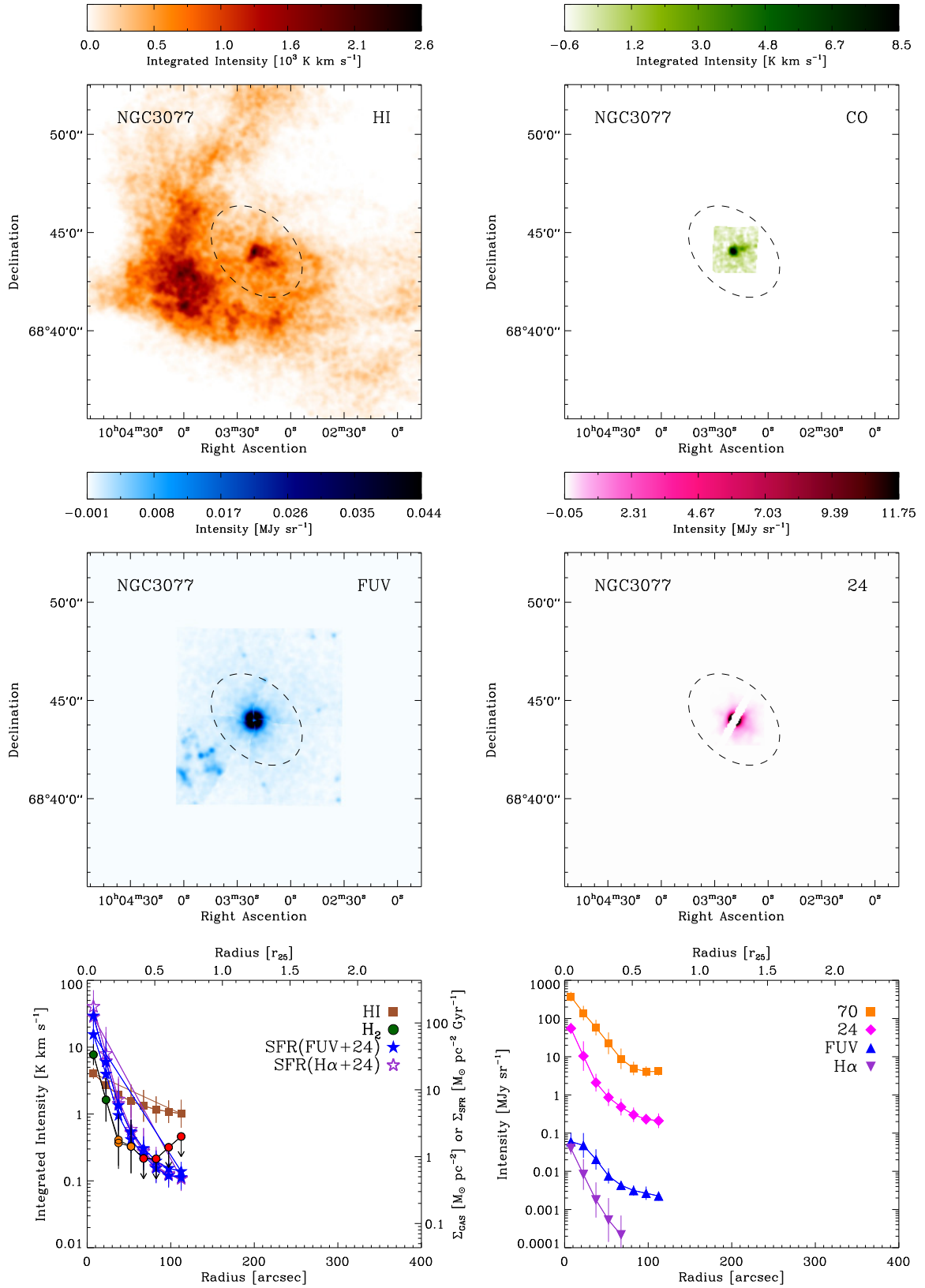


Figure A.1 (Continued) Atlas of Galaxy Poster Stamps — NGC 3077

6 Concluding Remarks & Outlook

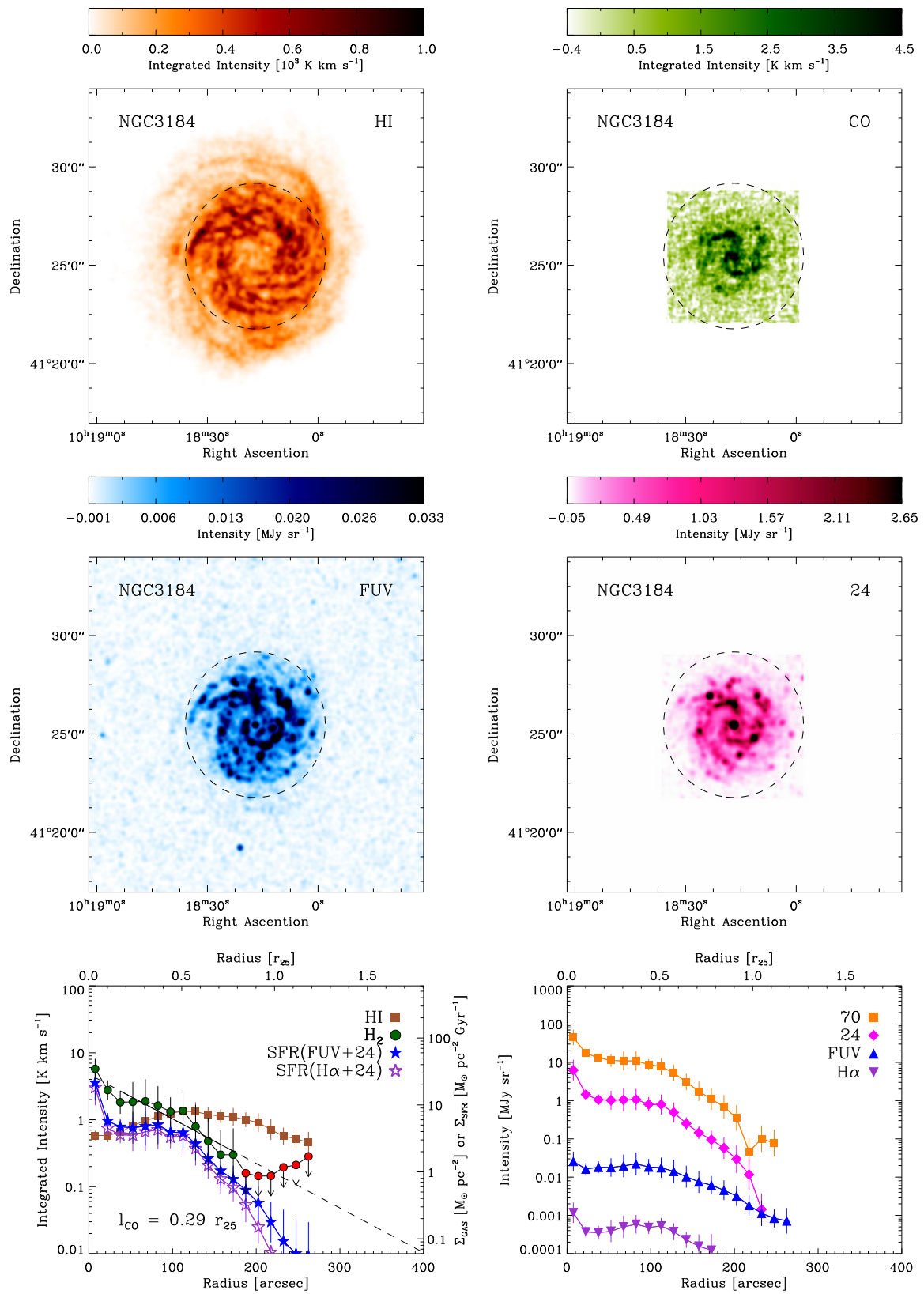


Figure A.1 (Continued) Atlas of Galaxy Poster Stamps — NGC 3184

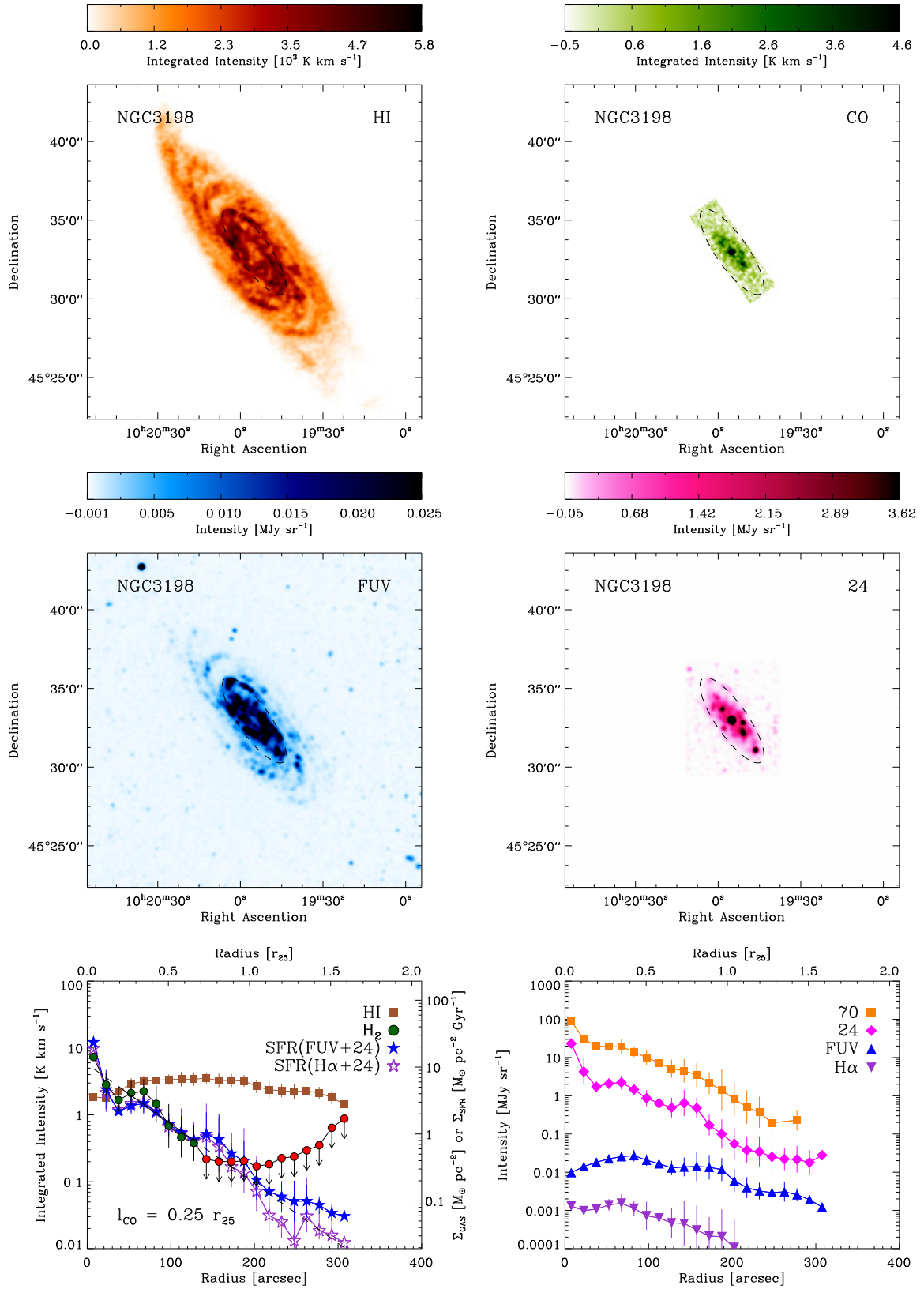


Figure A.1 (Continued) Atlas of Galaxy Poster Stamps — NGC 3198

6 Concluding Remarks & Outlook

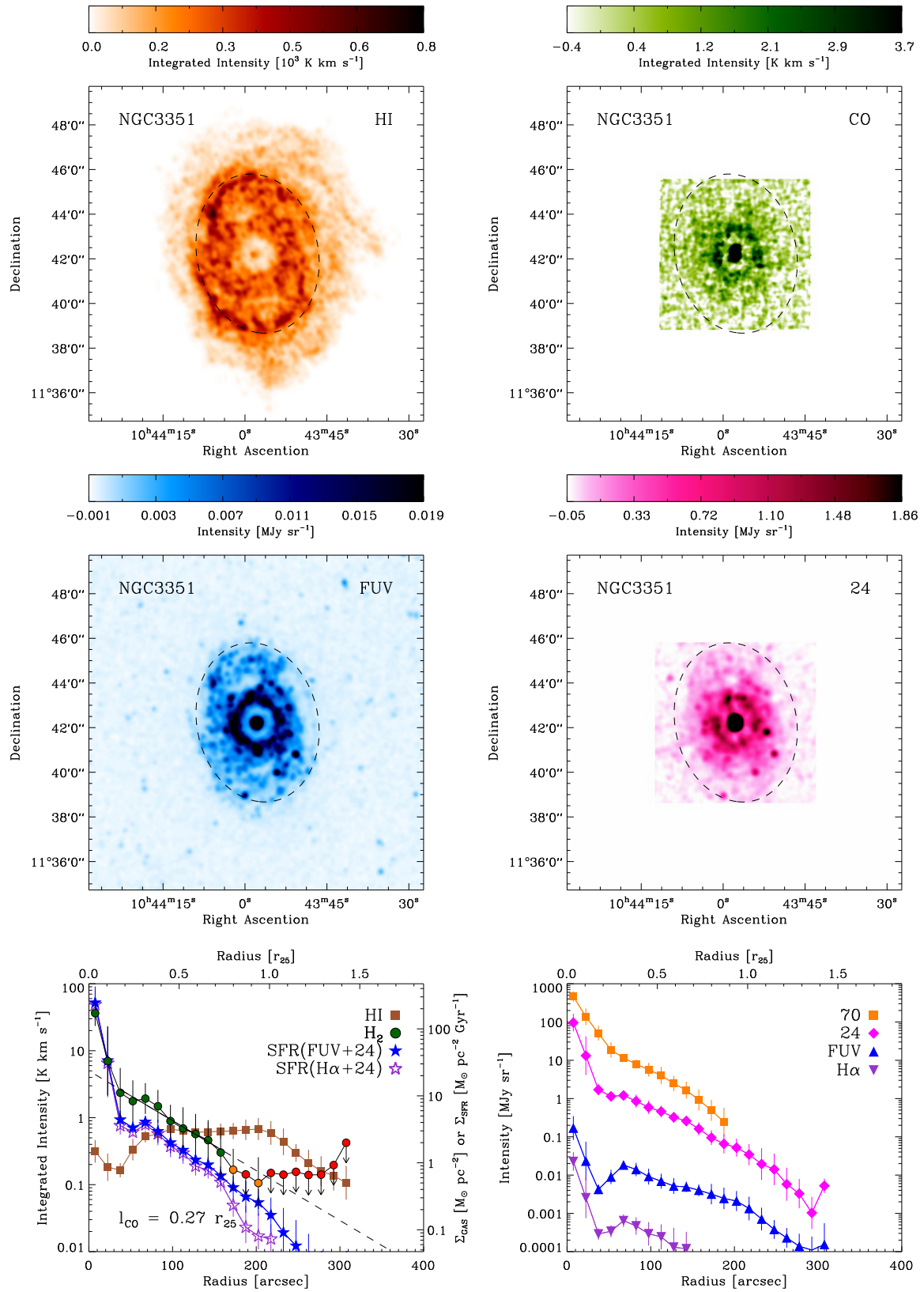


Figure A.1 (Continued) Atlas of Galaxy Poster Stamps — NGC 3351 (M 95)

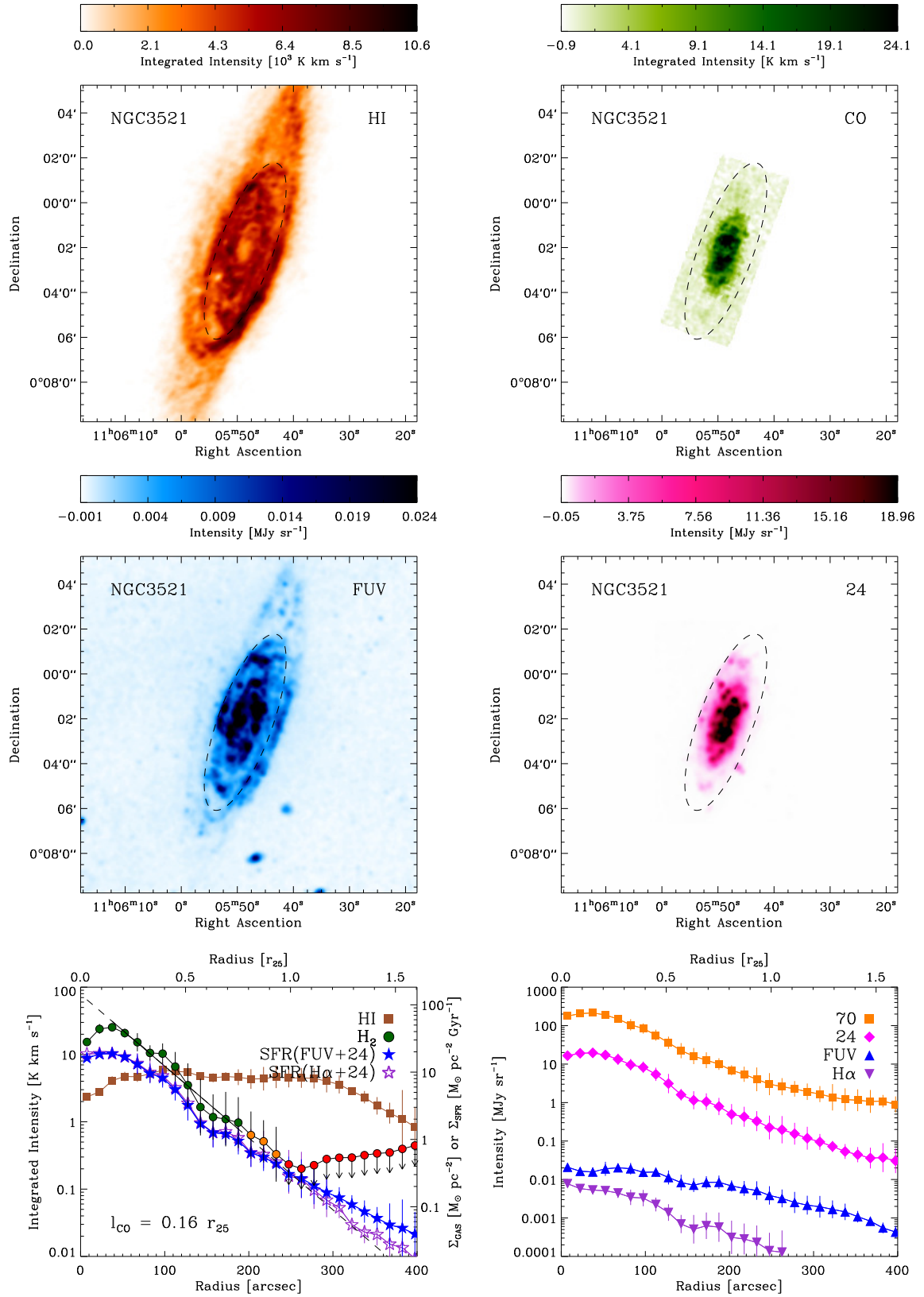


Figure A.1 (Continued) Atlas of Galaxy Poster Stamps — NGC 3521

6 Concluding Remarks & Outlook

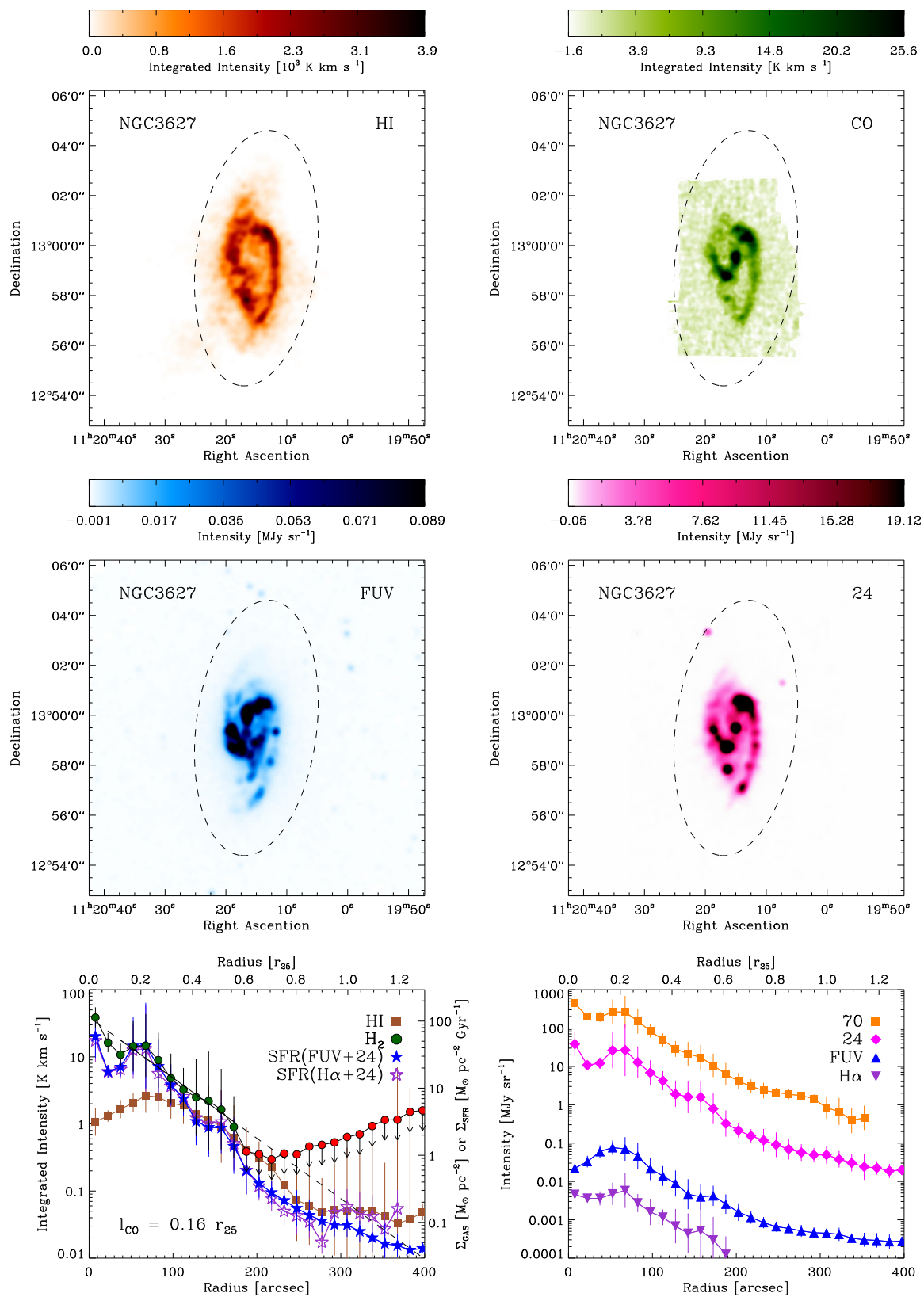


Figure A.1 (Continued) Atlas of Galaxy Poster Stamps — NGC 3627 (M 66)

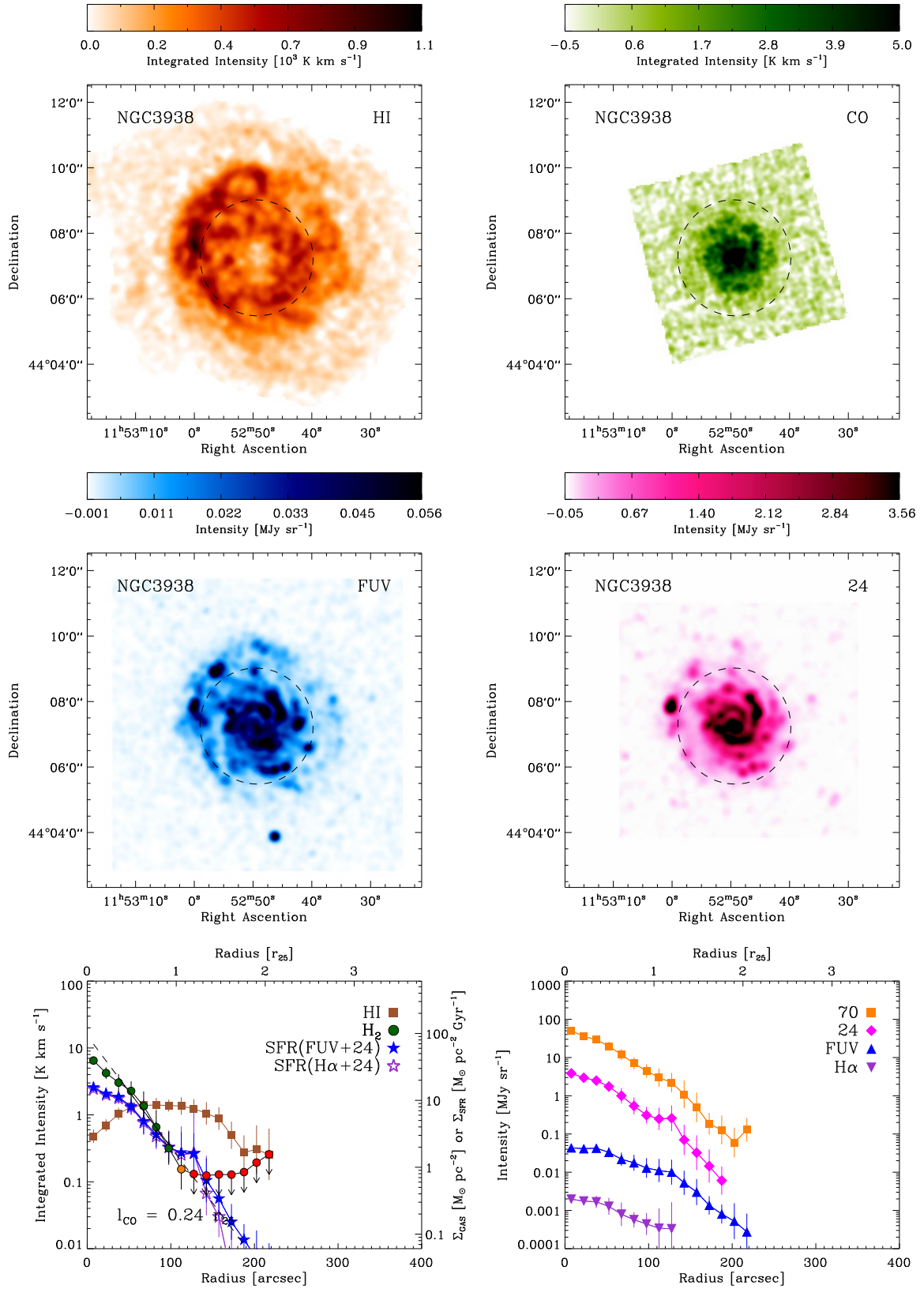


Figure A.1 (Continued) Atlas of Galaxy Poster Stamps — NGC 3938

6 Concluding Remarks & Outlook

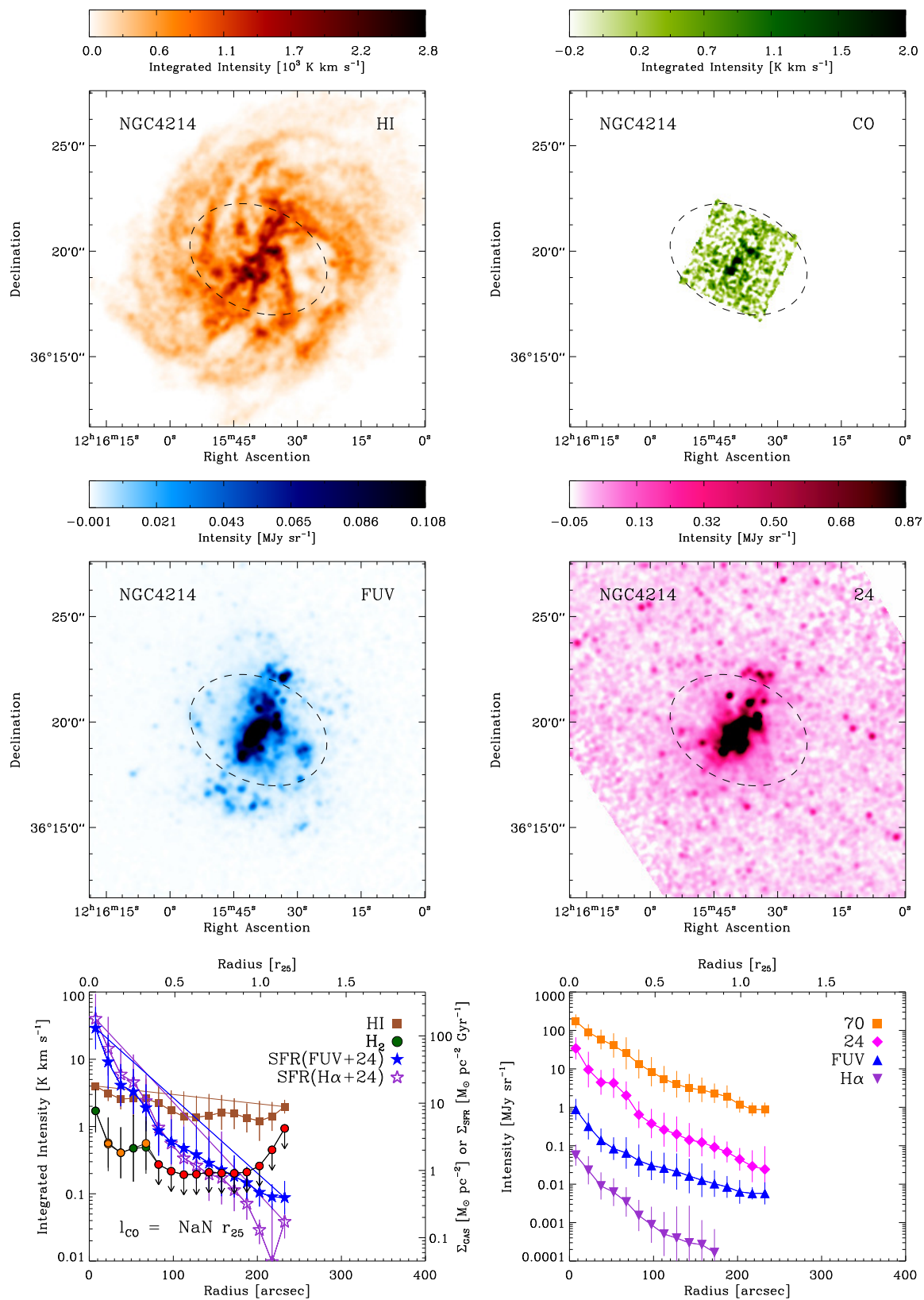


Figure A.1 (Continued) Atlas of Galaxy Poster Stamps — NGC 4214

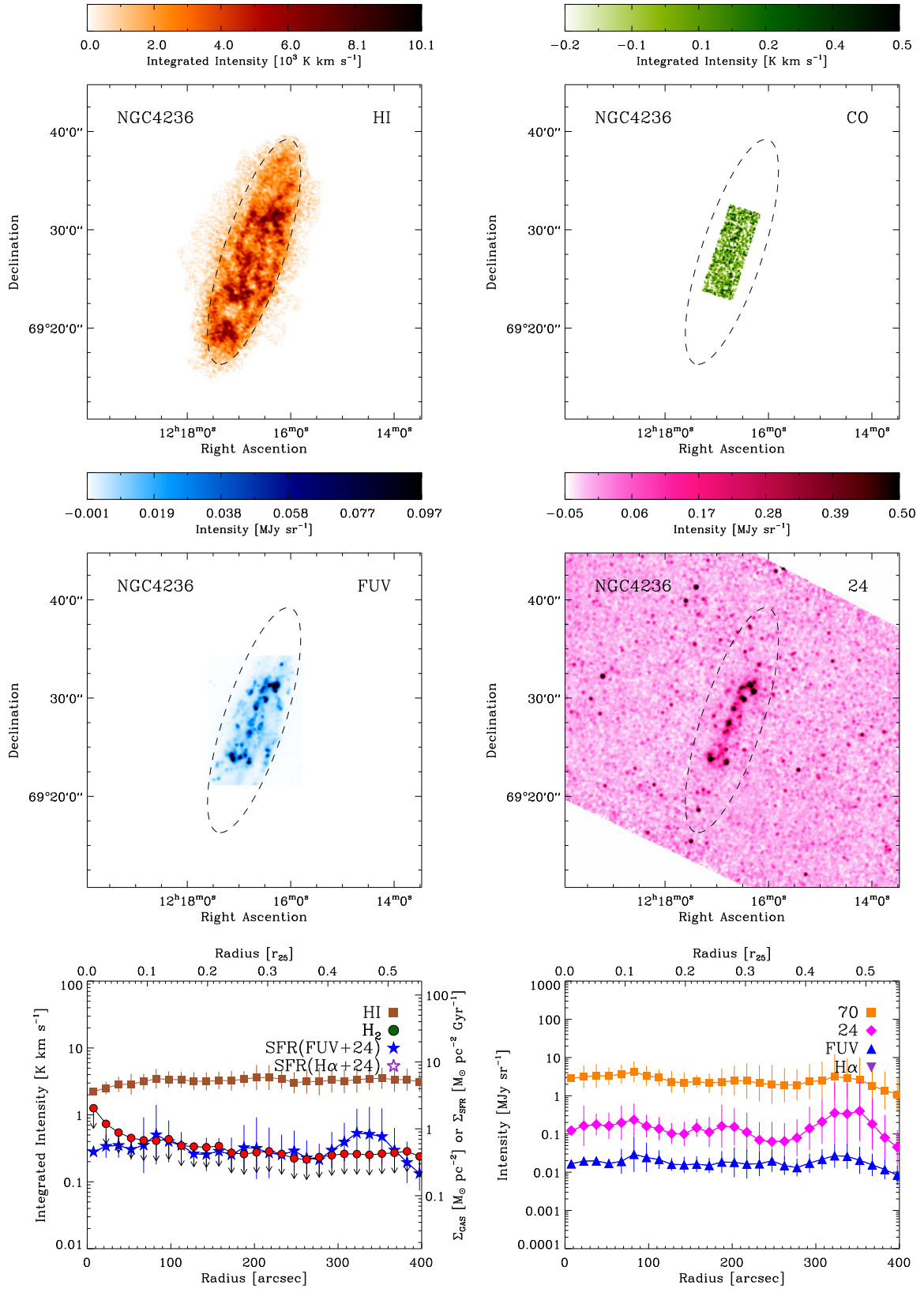


Figure A.1 (Continued) Atlas of Galaxy Poster Stamps — NGC 4236

6 Concluding Remarks & Outlook

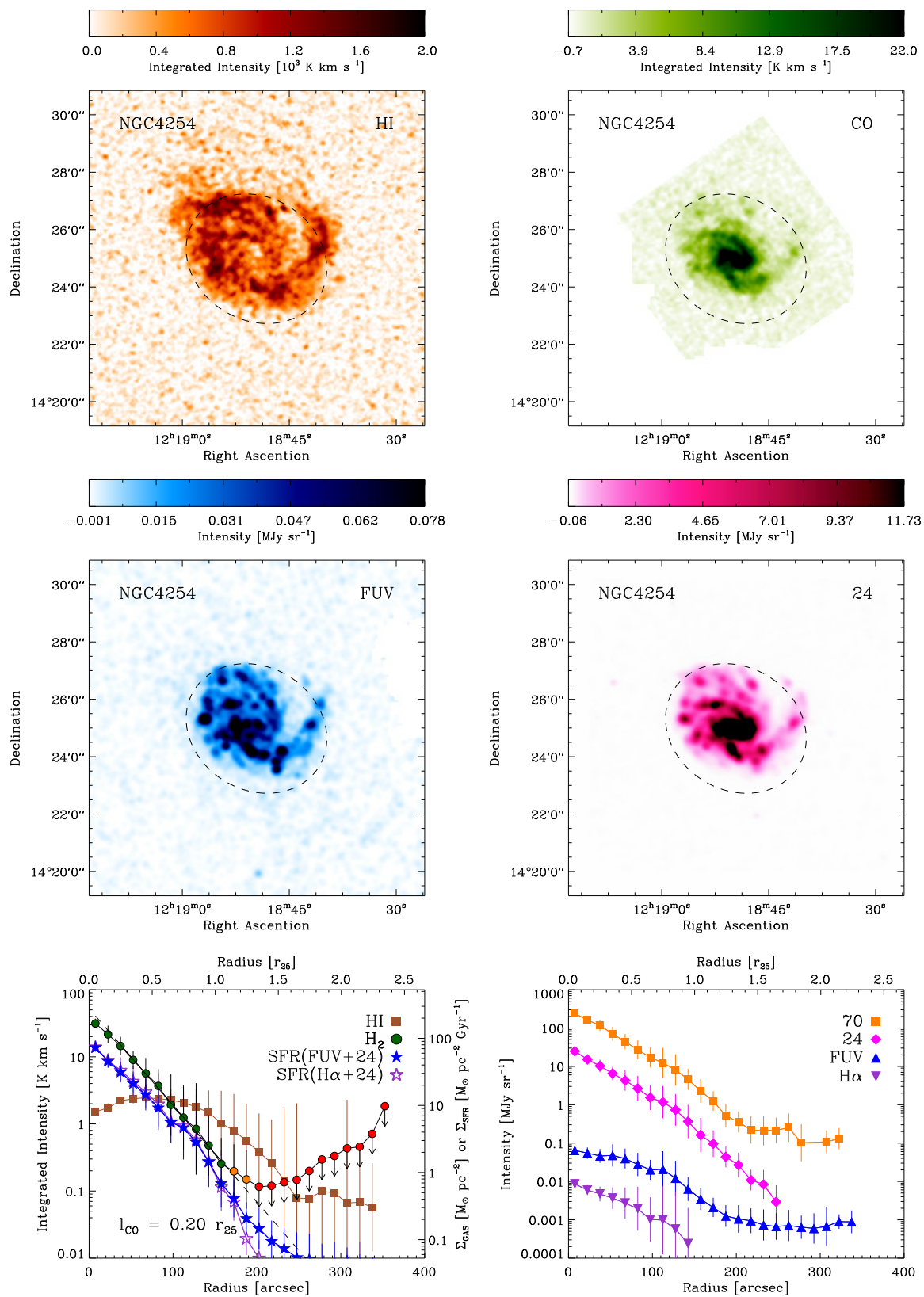


Figure A.1 (Continued) Atlas of Galaxy Poster Stamps — NGC 4254 (M 99)

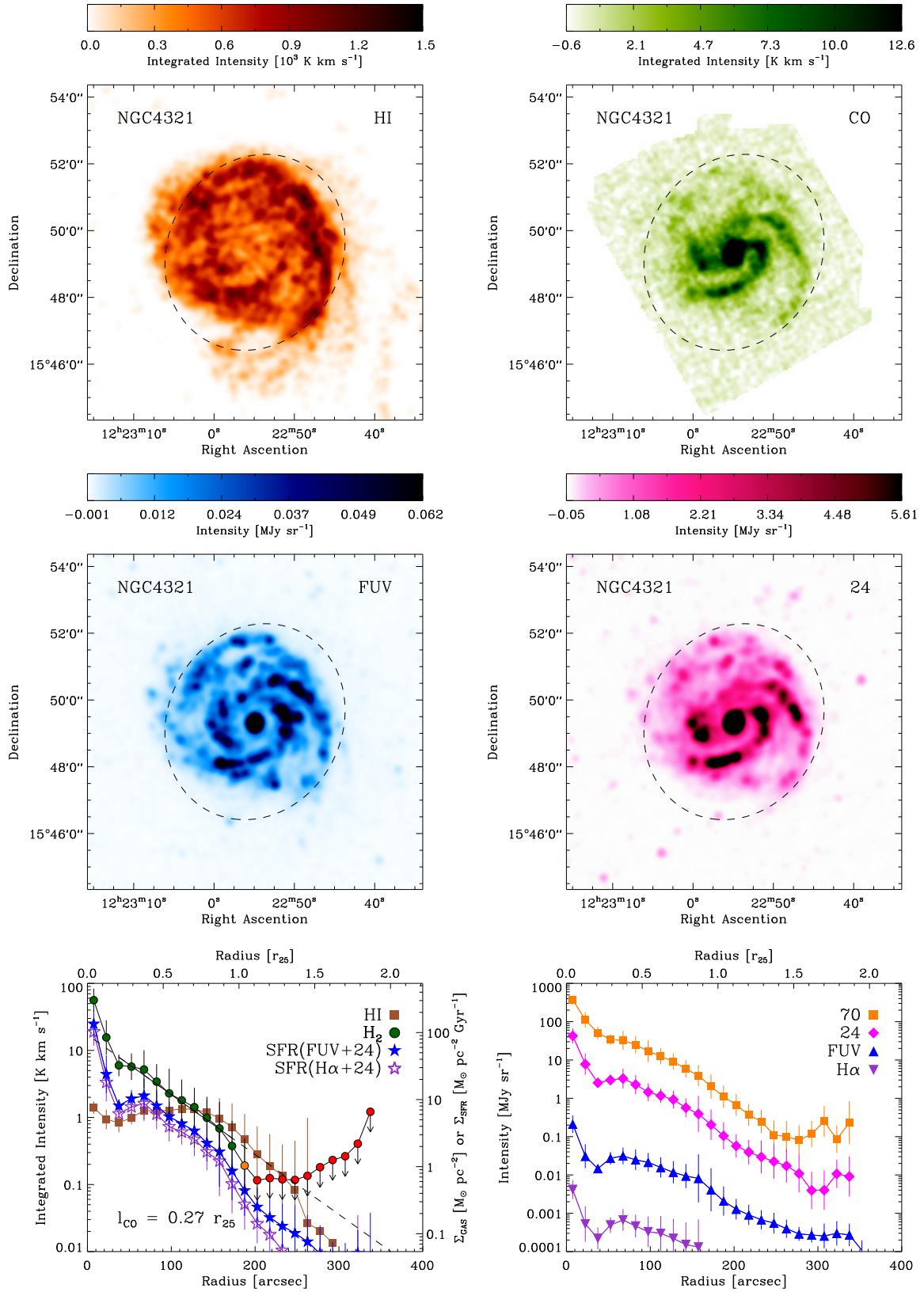


Figure A.1 (Continued) Atlas of Galaxy Poster Stamps — NGC 4321 (M 100)

6 Concluding Remarks & Outlook

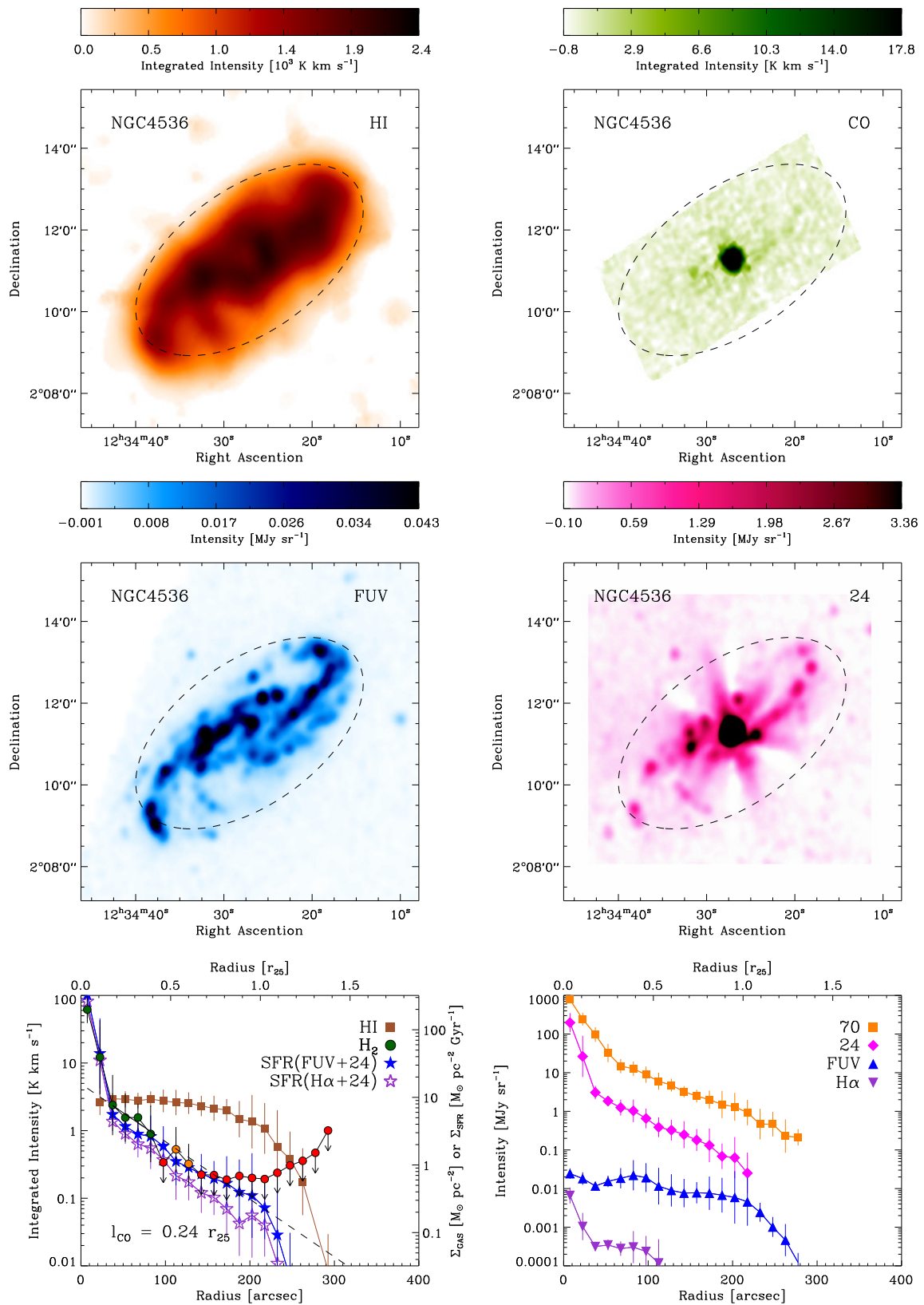


Figure A.1 (Continued) Atlas of Galaxy Poster Stamps — NGC 4536

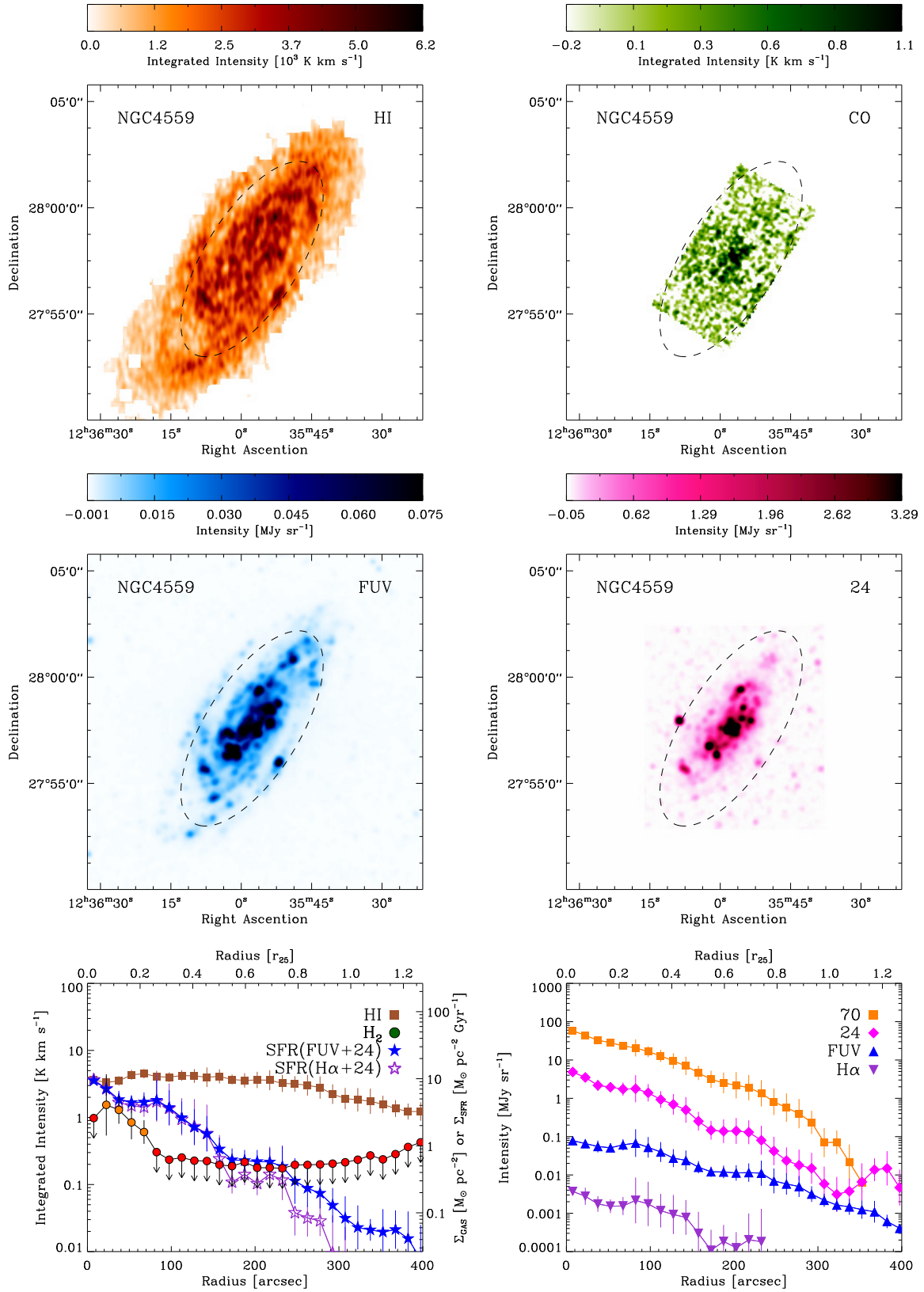


Figure A.1 (Continued) Atlas of Galaxy Poster Stamps — NGC 4559

6 Concluding Remarks & Outlook

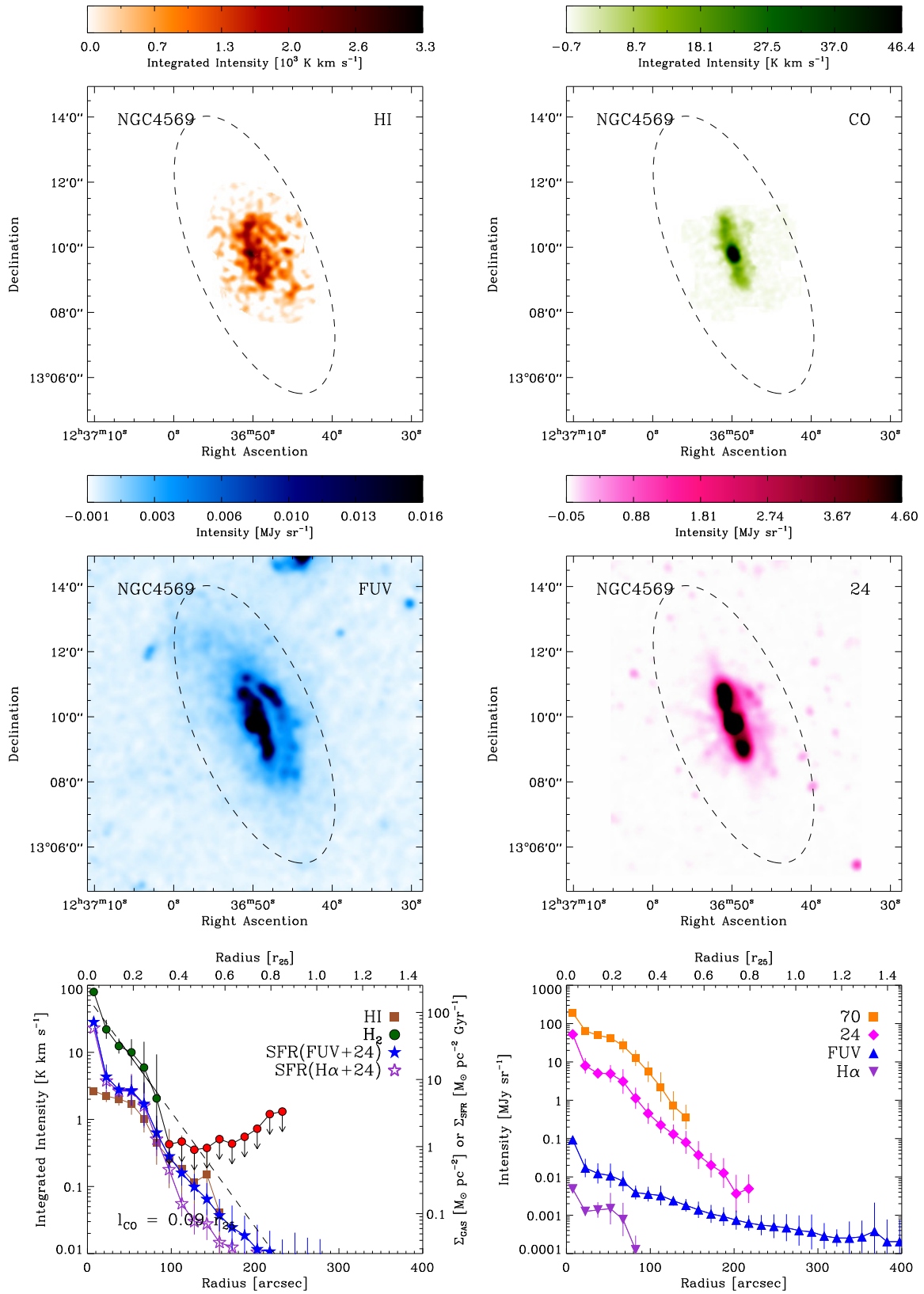


Figure A.1 (Continued) Atlas of Galaxy Poster Stamps — NGC 4569 (M 90)

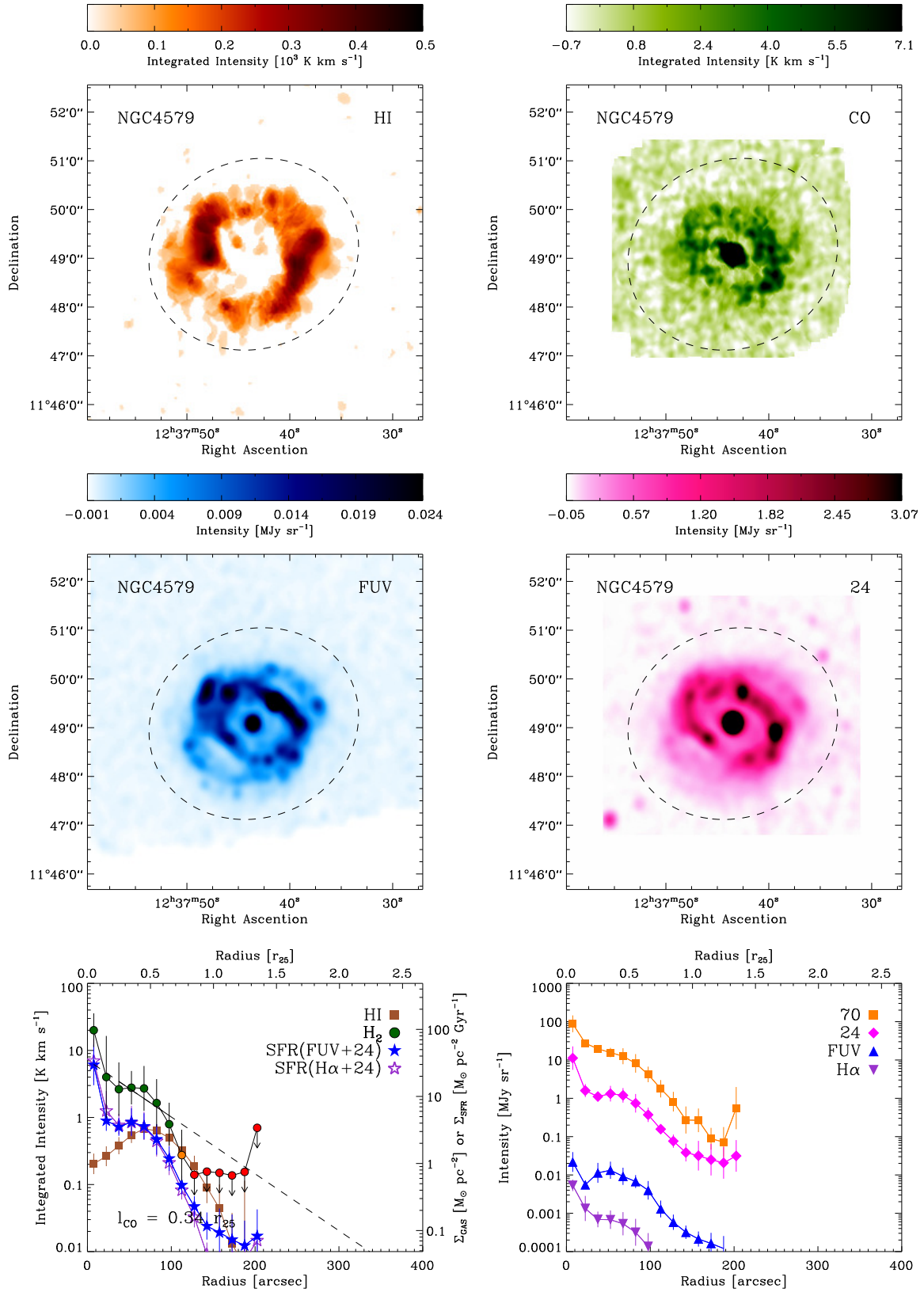


Figure A.1 (Continued) Atlas of Galaxy Poster Stamps — NGC 4579 (M 58)

6 Concluding Remarks & Outlook

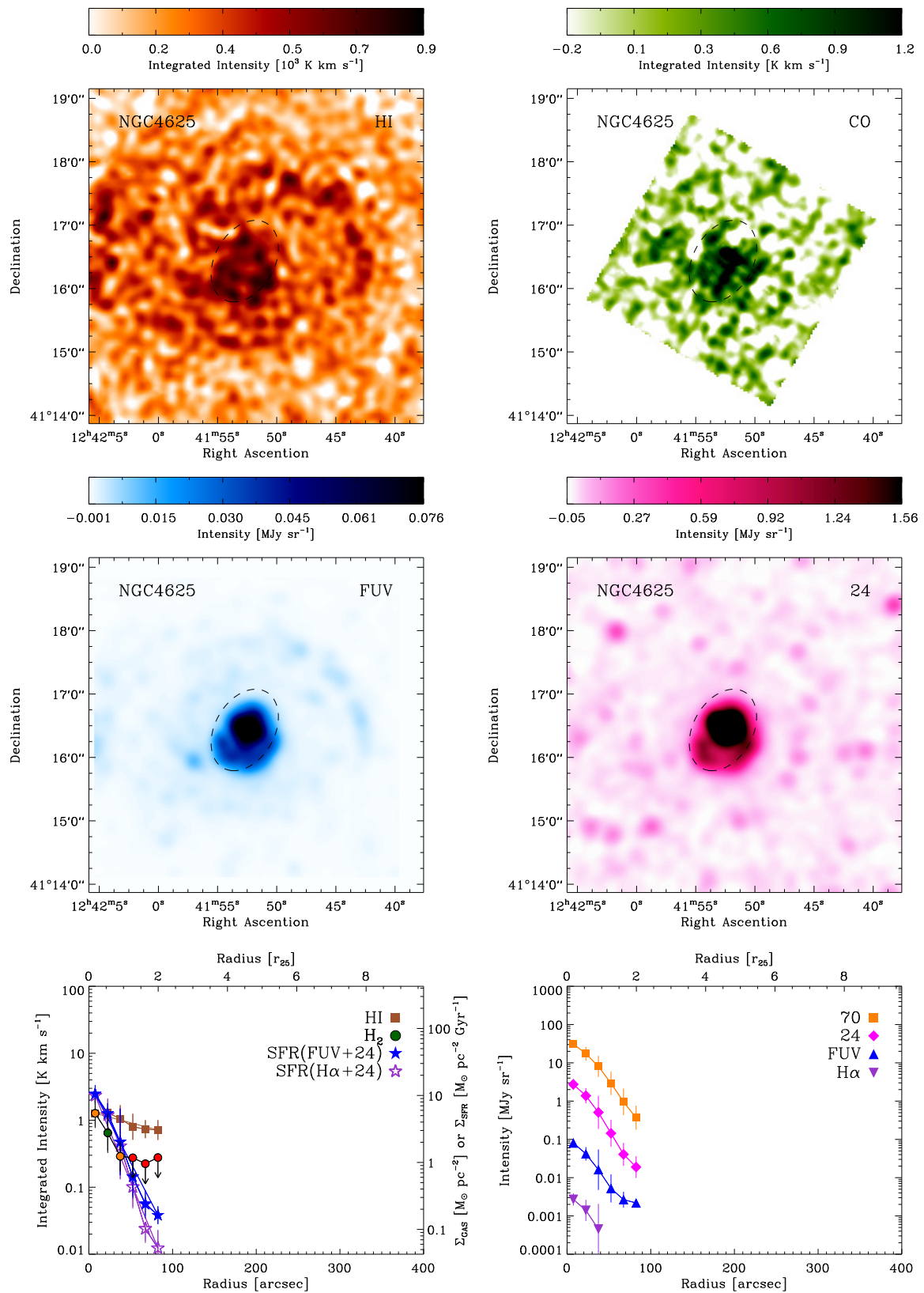


Figure A.1 (Continued) Atlas of Galaxy Poster Stamps — NGC 4625

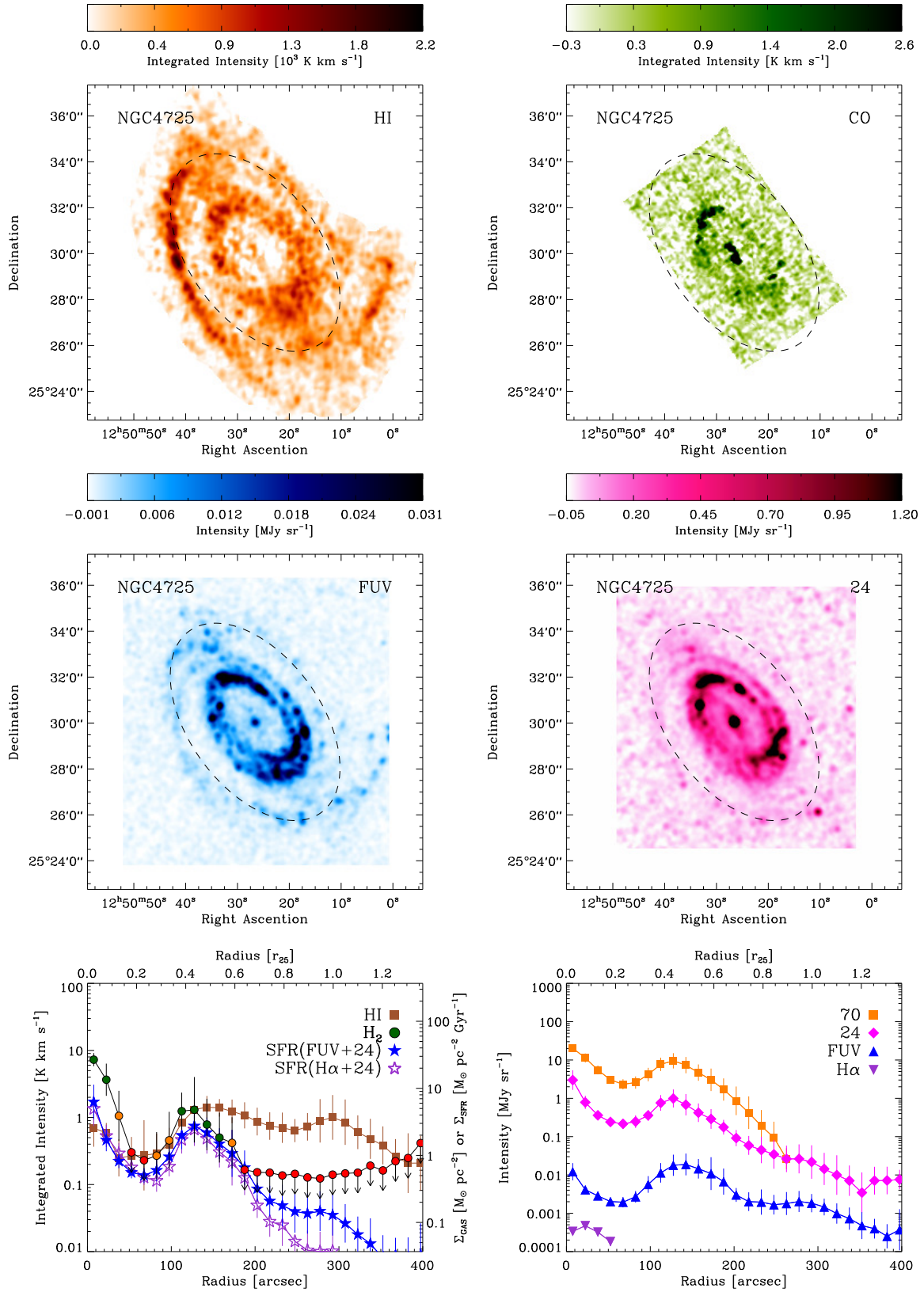


Figure A.1 (Continued) Atlas of Galaxy Poster Stamps — NGC 4725

6 Concluding Remarks & Outlook

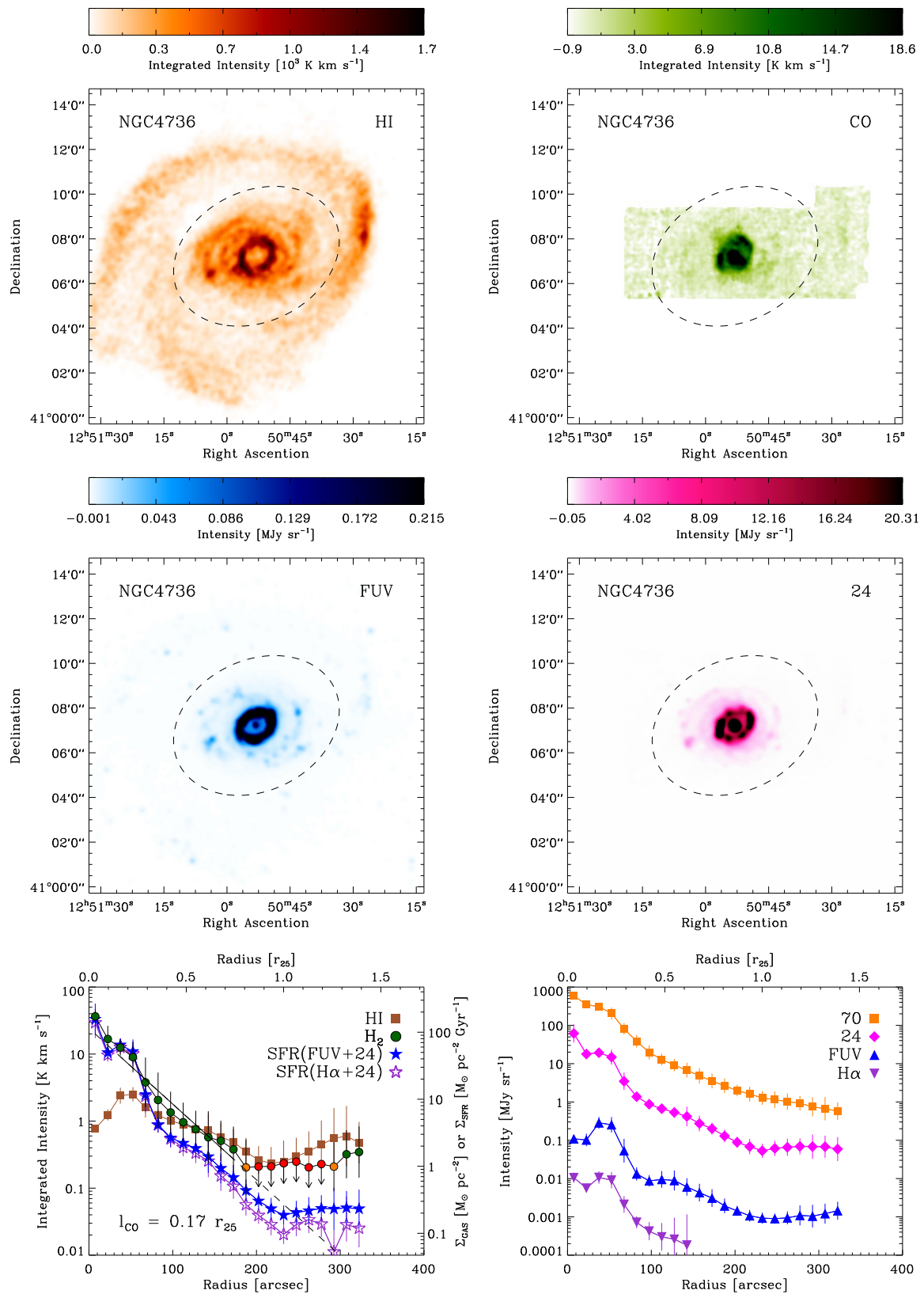


Figure A.1 (Continued) Atlas of Galaxy Poster Stamps — NGC 4736 (M 94)

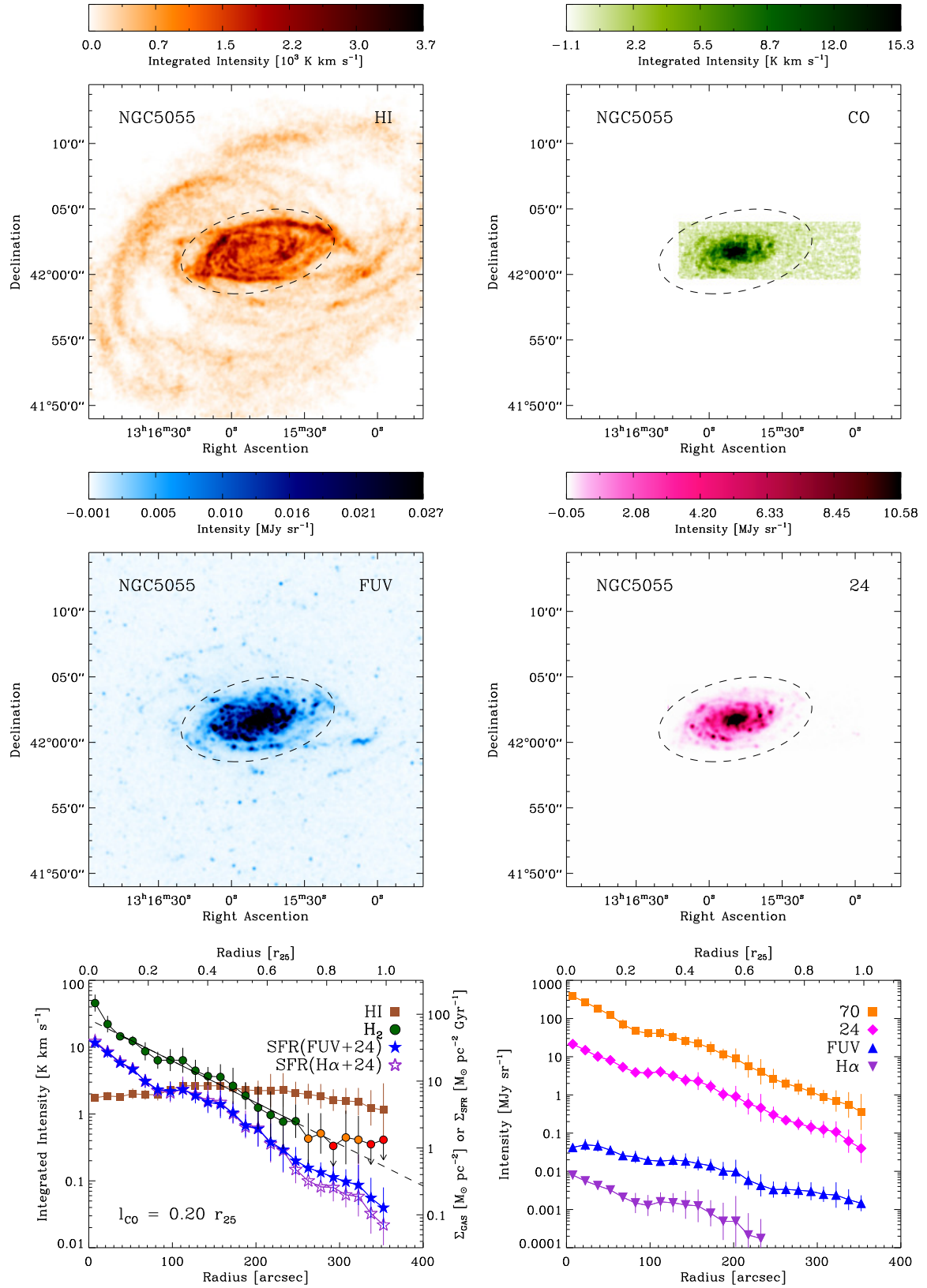


Figure A.1 (Continued) Atlas of Galaxy Poster Stamps — NGC 5055 (M 63)

6 Concluding Remarks & Outlook

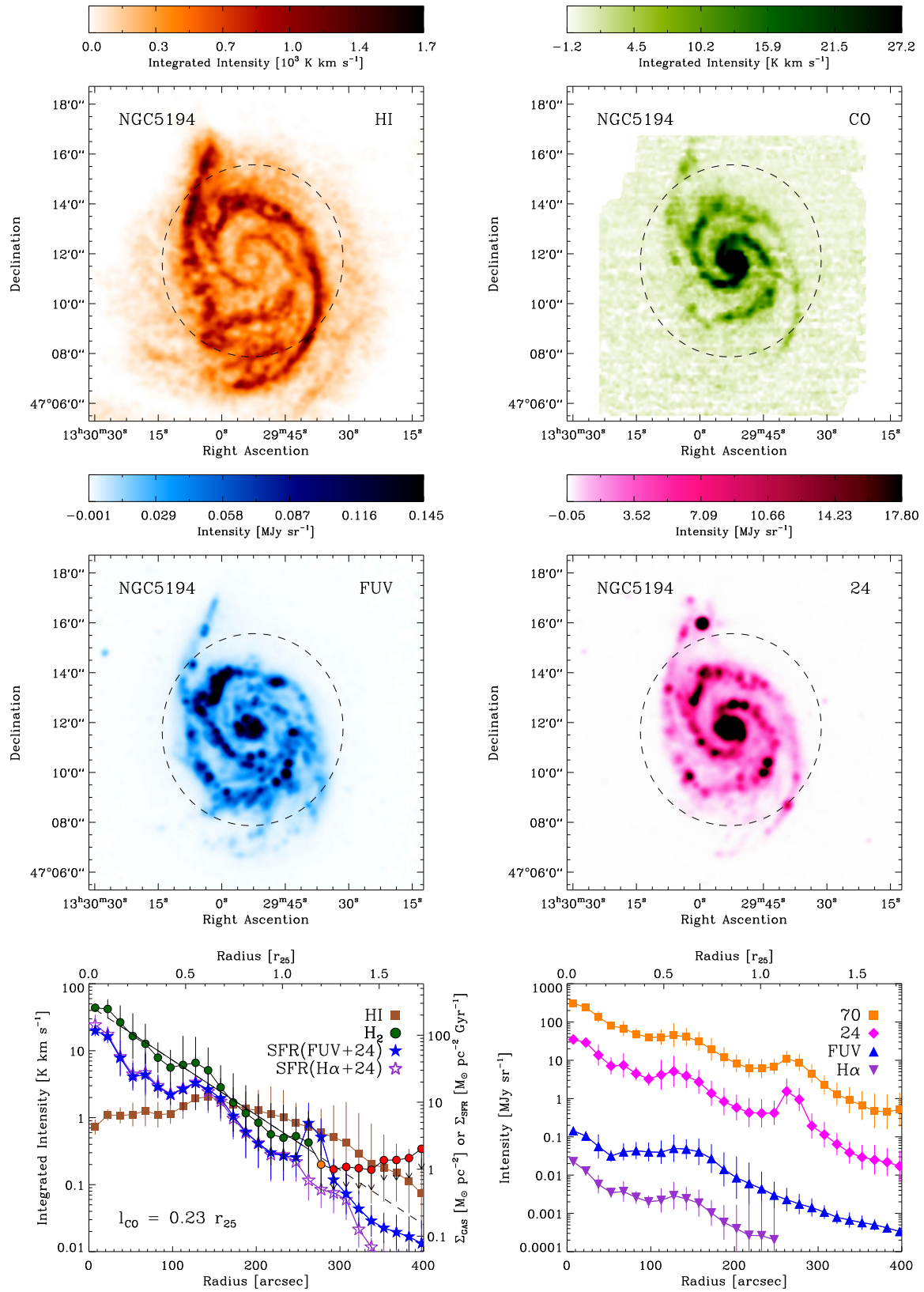


Figure A.1 (Continued) Atlas of Galaxy Poster Stamps — NGC 5194 (M 51)

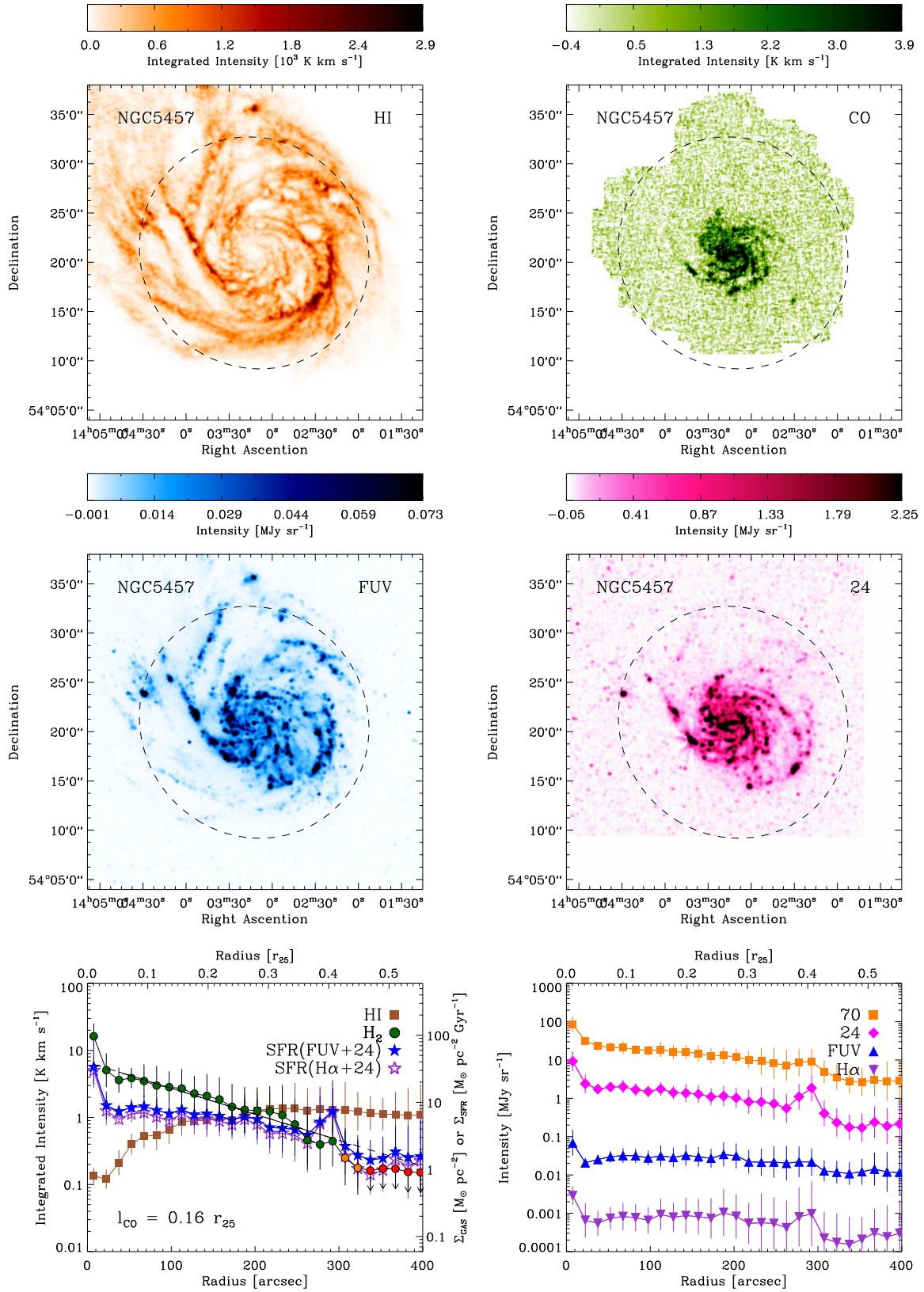


Figure A.1 (Continued) Atlas of Galaxy Poster Stamps — NGC 5457 (M 101)

6 Concluding Remarks & Outlook

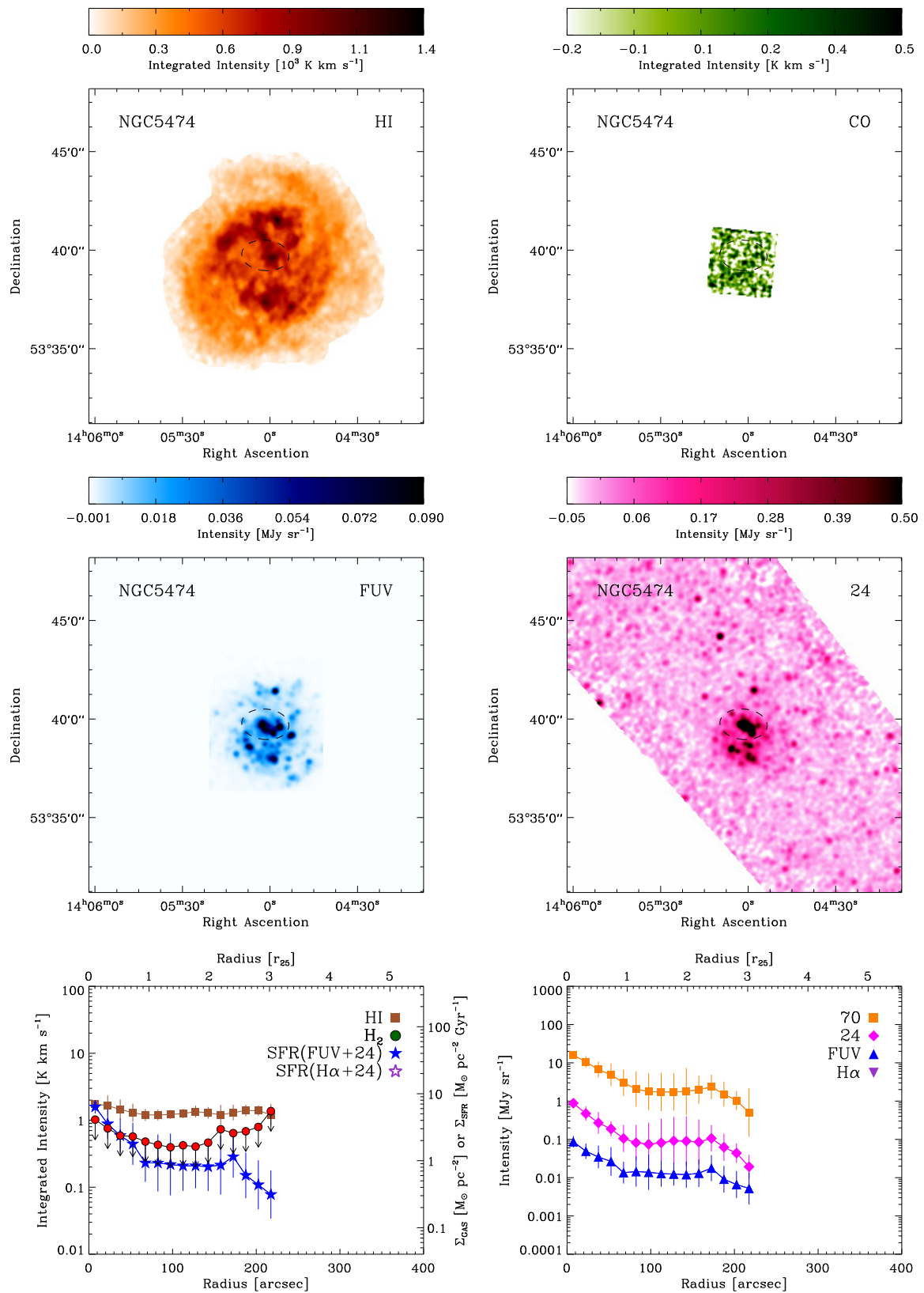


Figure A.1 (Continued) Atlas of Galaxy Poster Stamps — NGC 5474

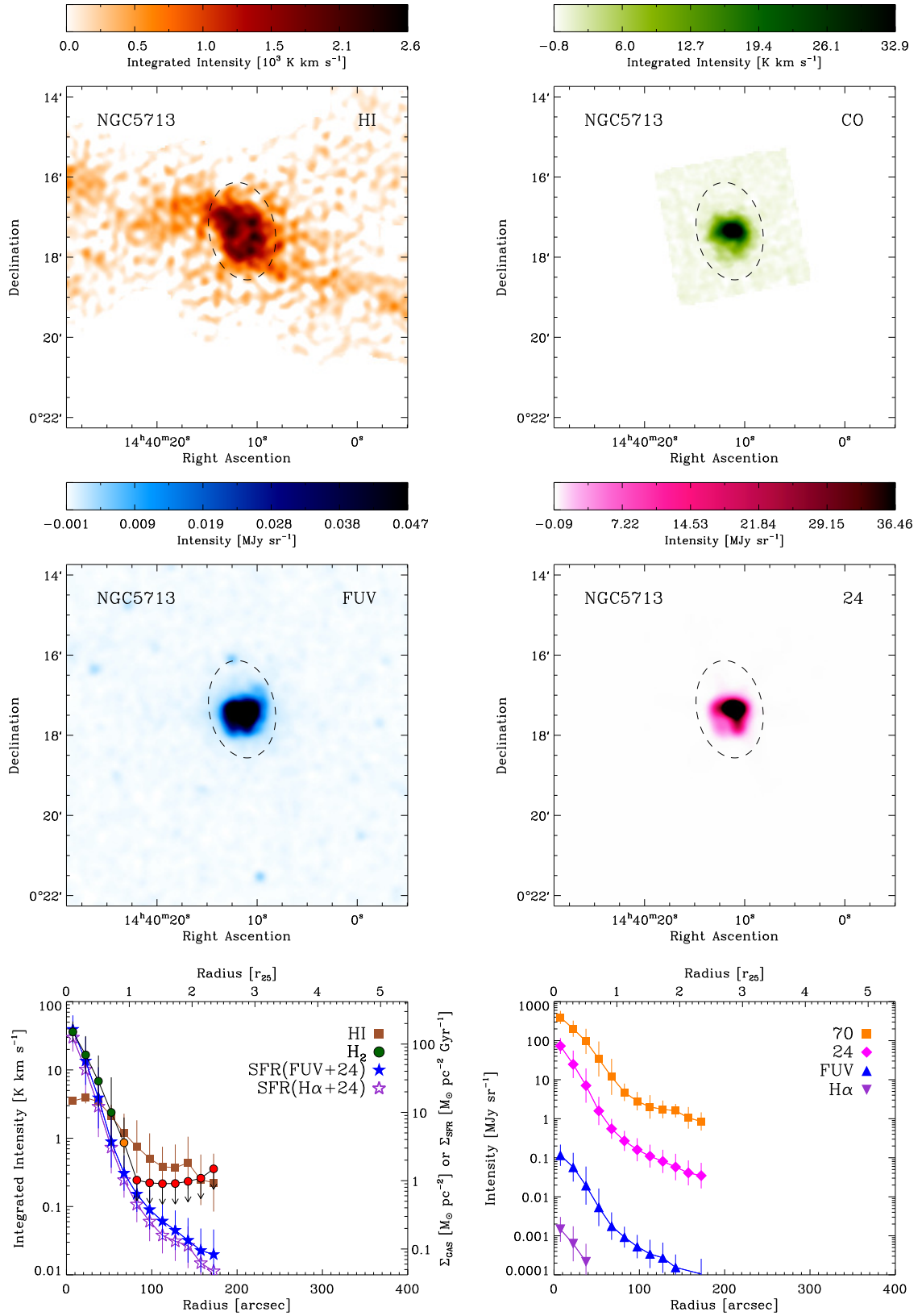


Figure A.1 (Continued) Atlas of Galaxy Poster Stamps — NGC 5713

6 Concluding Remarks & Outlook

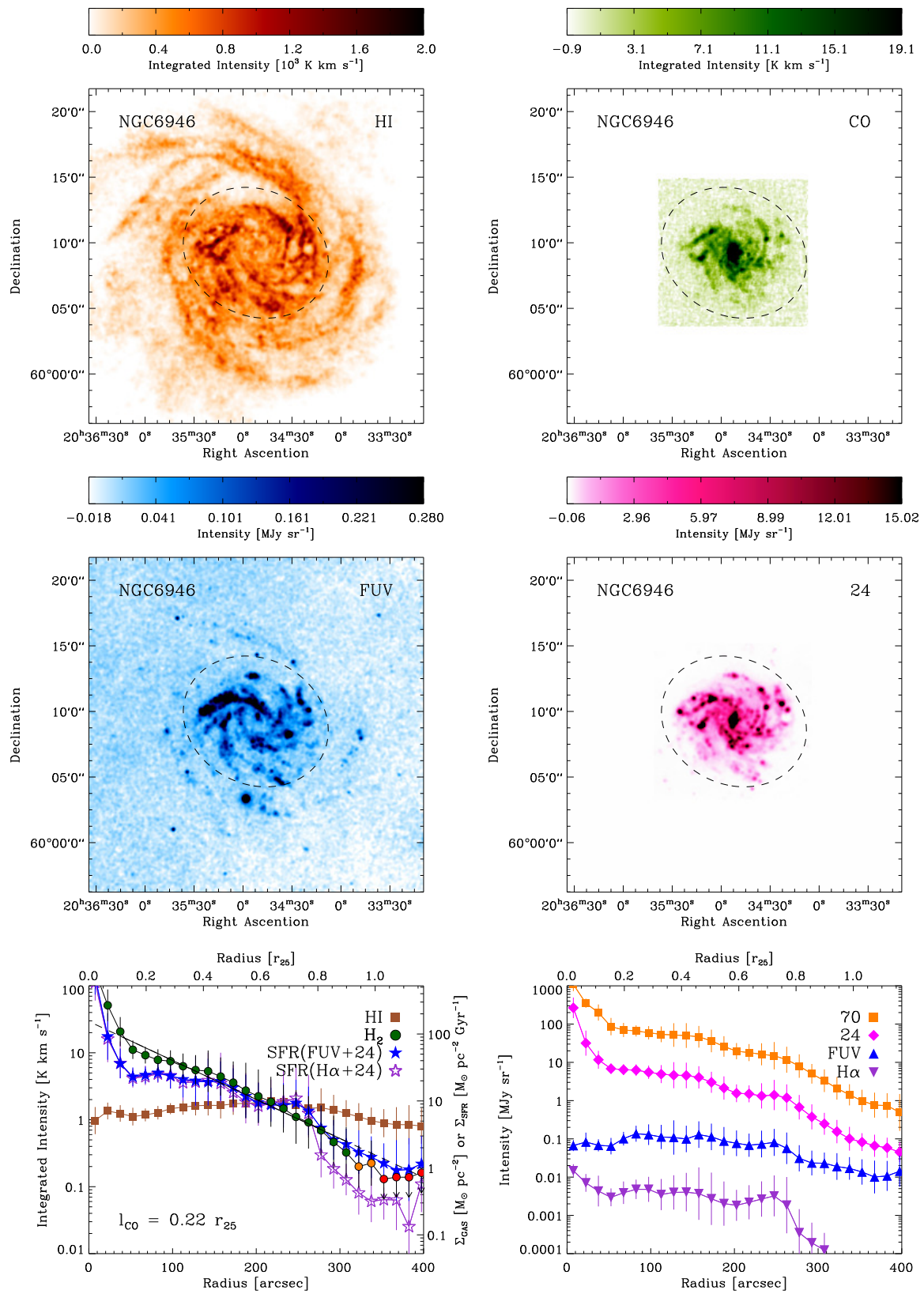


Figure A.1 (Continued) Atlas of Galaxy Poster Stamps — NGC 6946

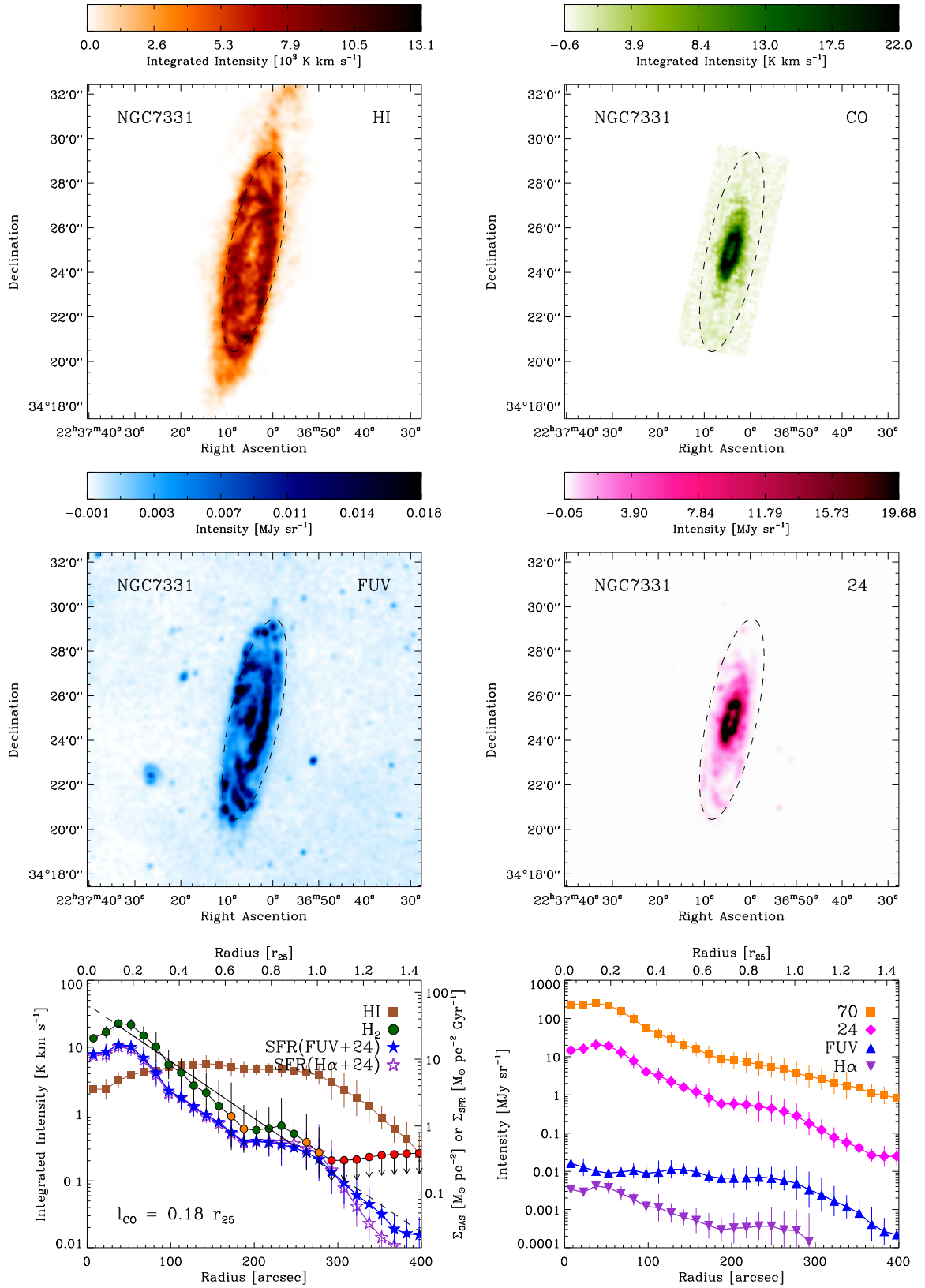


Figure A.1 (Continued) Atlas of Galaxy Poster Stamps — NGC 7331

Bibliography

Abdo, A. A., Ackermann, M., Ajello, M., Baldini, L., Ballet, J., Barbiellini, G., Bastieri, D., Baughman, B. M., Bechtol, K., Bellazzini, R., Berenji, B., Bloom, E. D., Bonamente, E., Borgland, A. W., Bregeon, J., Brez, A., Brigida, M., Bruel, P., Burnett, T. H., Buson, S., Caliandro, G. A., Cameron, R. A., Caraveo, P. A., Casandjian, J. M., Cecchi, C., Çelik, Ö., Chekhtman, A., Cheung, C. C., Chiang, J., Ciprini, S., Claus, R., Cohen-Tanugi, J., Cominsky, L. R., Conrad, J., Dermer, C. D., de Palma, F., Digel, S. W., Silva, E. d. C. e., Drell, P. S., Dubois, R., Dumora, D., Farnier, C., Favuzzi, C., Fegan, S. J., Focke, W. B., Fortin, P., Frailis, M., Fukazawa, Y., Funk, S., Fusco, P., Gargano, F., Gehrels, N., Germani, S., Giavitto, G., Giebels, B., Giglietto, N., Giordano, F., Glanzman, T., Godfrey, G., Grenier, I. A., Grondin, M.-H., Grove, J. E., Guillemot, L., Guiriec, S., Harding, A. K., Hayashida, M., Horan, D., Hughes, R. E., Jackson, M. S., Jóhannesson, G., Johnson, A. S., Johnson, W. N., Kamae, T., Katagiri, H., Kataoka, J., Kawai, N., Kerr, M., Knödlseider, J., Kuss, M., Lande, J., Latronico, L., Lemoine-Goumard, M., Longo, F., Loparco, F., Lott, B., Lovellette, M. N., Lubrano, P., Makeev, A., Mazziotta, M. N., McEnery, J. E., Meurer, C., Michelson, P. F., Mitthumsiri, W., Mizuno, T., Monte, C., Monzani, M. E., Morselli, A., Moskalenko, I. V., Murgia, S., Nolan, P. L., Norris, J. P., Nuss, E., Ohsugi, T., Okumura, A., Omodei, N., Orlando, E., Ormes, J. F., Paneque, D., Pelassa, V., Pepe, M., Pesce-Rollins, M., Piron, F., Porter, T. A., Rainò, S., Rando, R., Razzano, M., Reimer, A., Reimer, O., Reposeur, T., Rodriguez, A. Y., Ryde, F., Sadrozinski, H. F.-W., Sanchez, D., Sander, A., Saz Parkinson, P. M., Sgrò, C., Siskind, E. J., Smith, P. D., Spandre, G., Spinelli, P., Starck, J.-L., Strickman, M. S., Strong, A. W., Suson, D. J., Takahashi, H., Tanaka, T., Thayer, J. B., Thayer, J. G., Thompson, D. J., Tibaldo, L., Torres, D. F., Tosti, G., Tramacere, A., Uchiyama, Y., Usher, T. L., Vasileiou, V., Vilchez, N., Vitale, V., Waite, A. P., Wang, P., Winer, B. L., Wood, K. S., Ylinen, T., Ziegler, M., & Fermi/LAT Collaboration. 2010, *ApJ*, 710, 133

Albrecht, M., Chini, R., Krügel, E., Müller, S. A. H., & Lemke, R. 2004, *A&A*, 414, 141

Arimoto, N., Sofue, Y., & Tsujimoto, T. 1996, *PASJ*, 48, 275

Barone, L. T., Heithausen, A., Hüttemeister, S., Fritz, T., & Klein, U. 2000, *MNRAS*, 317, 649

Bastian, N., Covey, K. R., & Meyer, M. R. 2010, *ARA&A*, 48, 339

Bigiel, F., Leroy, A., Seibert, M., Walter, F., Blitz, L., Thilker, D., & Madore, B. 2010a, *ApJ*, 720, L31

- Bigiel, F., Leroy, A., Walter, F., Blitz, L., Brinks, E., de Blok, W. J. G., & Madore, B. 2010b, *AJ*, 140, 1194
- Bigiel, F., Leroy, A., Walter, F., Brinks, E., de Blok, W. J. G., Madore, B., & Thornley, M. D. 2008, *AJ*, 136, 2846
- Bigiel, F., Leroy, A. K., Walter, F., Brinks, E., de Blok, W. J. G., Kramer, C., Rix, H. W., Schrubba, A., Schuster, K.-F., Usero, A., & Wiesemeyer, H. W. 2011, *ApJ*, 730, L13+
- Blanc, G. A., Heiderman, A., Gebhardt, K., Evans, N. J., & Adams, J. 2009, *ApJ*, 704, 842
- Blitz, L., Fukui, Y., Kawamura, A., Leroy, A., Mizuno, N., & Rosolowsky, E. 2007, *Protostars and Planets V*, 81
- Blitz, L., & Rosolowsky, E. 2004, *ApJ*, 612, L29
- . 2006, *ApJ*, 650, 933
- Bloemen, J. B. G. M., Deul, E. R., & Thaddeus, P. 1990, *A&A*, 233, 437
- Boissier, S., Gil de Paz, A., Boselli, A., Madore, B. F., Buat, V., Cortese, L., Burgarella, D., Muñoz-Mateos, J. C., Barlow, T. A., Forster, K., Friedman, P. G., Martin, D. C., Morrissey, P., Neff, S. G., Schiminovich, D., Seibert, M., Small, T., Wyder, T. K., Bianchi, L., Donas, J., Heckman, T. M., Lee, Y., Milliard, B., Rich, R. M., Szalay, A. S., Welsh, B. Y., & Yi, S. K. 2007, *ApJS*, 173, 524
- Boissier, S., Prantzos, N., Boselli, A., & Gavazzi, G. 2003, *MNRAS*, 346, 1215
- Böker, T., Lisenfeld, U., & Schinnerer, E. 2003, *A&A*, 406, 87
- Bolatto, A. D., Jackson, J. M., & Ingalls, J. G. 1999, *ApJ*, 513, 275
- Bolatto, A. D., Leroy, A. K., Jameson, K., Ostriker, E., Gordon, K., Lawton, B., Stanimirovic, S., Israel, F. P., Madden, S. C., Hony, S., Sandstrom, K. M., Bot, C., Rubio, M., Winkler, P. F., Roman-Duval, J., van Loon, J. T., Oliveira, J. M., & Indebetouw, R. 2011, *ArXiv e-prints*
- Bolatto, A. D., Leroy, A. K., Rosolowsky, E., Walter, F., & Blitz, L. 2008, *ApJ*, 686, 948
- Boquien, M., Lisenfeld, U., Duc, P.-A., Braine, J., Bournaud, F., Brinks, E., & Charmandaris, V. 2011, *A&A*, 533, A19+
- Boselli, A., Lequeux, J., & Gavazzi, G. 2002, *A&A*, 384, 33
- Böttner, C., Klein, U., & Heithausen, A. 2003, *A&A*, 408, 493
- Boulanger, F., Abergel, A., Bernard, J., Burton, W. B., Desert, F., Hartmann, D., Lagache, G., & Puget, J. 1996, *A&A*, 312, 256

- Bournaud, F., Elmegreen, B. G., Teyssier, R., Block, D. L., & Puerari, I. 2010, MNRAS, 1400
- Braun, R., Thilker, D. A., Walterbos, R. A. M., & Corbelli, E. 2009, ApJ, 695, 937
- Brinks, E., & Shane, W. W. 1984, A&AS, 55, 179
- Calzetti, D., Kennicutt, R. C., Engelbracht, C. W., Leitherer, C., Draine, B. T., Kewley, L., Moustakas, J., Sosey, M., Dale, D. A., Gordon, K. D., Helou, G. X., Hollenbach, D. J., Armus, L., Bendo, G., Bot, C., Buckalew, B., Jarrett, T., Li, A., Meyer, M., Murphy, E. J., Prescott, M., Regan, M. W., Rieke, G. H., Roussel, H., Sheth, K., Smith, J. D. T., Thornley, M. D., & Walter, F. 2007, ApJ, 666, 870
- Calzetti, D., Kennicutt, Jr., R. C., Bianchi, L., Thilker, D. A., Dale, D. A., Engelbracht, C. W., Leitherer, C., Meyer, M. J., Sosey, M. L., Mutchler, M., Regan, M. W., Thornley, M. D., Armus, L., Bendo, G. J., Boissier, S., Boselli, A., Draine, B. T., Gordon, K. D., Helou, G., Hollenbach, D. J., Kewley, L., Madore, B. F., Martin, D. C., Murphy, E. J., Rieke, G. H., Rieke, M. J., Roussel, H., Sheth, K., Smith, J. D., Walter, F., White, B. A., Yi, S., Scoville, N. Z., Polletta, M., & Lindler, D. 2005, ApJ, 633, 871
- Calzetti, D., Wu, S., Hong, S., Kennicutt, R. C., Lee, J. C., Dale, D. A., Engelbracht, C. W., van Zee, L., Draine, B. T., Hao, C., Gordon, K. D., Moustakas, J., Murphy, E. J., Regan, M., Begum, A., Block, M., Dalcanton, J., Funes, J., Gil de Paz, A., Johnson, B., Sakai, S., Skillman, E., Walter, F., Weisz, D., Williams, B., & Wu, Y. 2010, ApJ, 714, 1256
- Chabrier, G. 2003, PASP, 115, 763
- Chen, C., Indebetouw, R., Chu, Y., Gruendl, R. A., Testor, G., Heitsch, F., Seale, J. P., Meixner, M., & Sewilo, M. 2010, ArXiv e-prints
- Combes, F., Young, L. M., & Bureau, M. 2007, MNRAS, 377, 1795
- Cormier, D., Madden, S. C., Hony, S., Contursi, A., Poglitsch, A., Galliano, F., Sturm, E., Doublier, V., Feuchtgruber, H., Galametz, M., Geis, N., de Jong, J., Okumura, K., Panuzzo, P., & Sauvage, M. 2010, A&A, 518, L57+
- Crocker, A. F., Bureau, M., Young, L. M., & Combes, F. 2011, MNRAS, 410, 1197
- Crosthwaite, L. P., & Turner, J. L. 2007, AJ, 134, 1827
- Daddi, E., Cimatti, A., Renzini, A., Fontana, A., Mignoli, M., Pozzetti, L., Tozzi, P., & Zamorani, G. 2004, ApJ, 617, 746
- Daddi, E., Elbaz, D., Walter, F., Bournaud, F., Salmi, F., Carilli, C., Dannerbauer, H., Dickinson, M., Monaco, P., & Riechers, D. 2010, ApJ, 714, L118

- Dale, D. A., Cohen, S. A., Johnson, L. C., Schuster, M. D., Calzetti, D., Engelbracht, C. W., Gil de Paz, A., Kennicutt, R. C., Lee, J. C., Begum, A., Block, M., Dalcanton, J. J., Funes, J. G., Gordon, K. D., Johnson, B. D., Marble, A. R., Sakai, S., Skillman, E. D., van Zee, L., Walter, F., Weisz, D. R., Williams, B., Wu, S., & Wu, Y. 2009, *ApJ*, 703, 517
- Dame, T. M., Hartmann, D., & Thaddeus, P. 2001, *ApJ*, 547, 792
- Deul, E. R., & van der Hulst, J. M. 1987, *A&AS*, 67, 509
- Dopita, M. A., & Ryder, S. D. 1994, *ApJ*, 430, 163
- Draine, B. T., Dale, D. A., Bendo, G., Gordon, K. D., Smith, J. D. T., Armus, L., Engelbracht, C. W., Helou, G., Kennicutt, Jr., R. C., Li, A., Roussel, H., Walter, F., Calzetti, D., Moustakas, J., Murphy, E. J., Rieke, G. H., Bot, C., Hollenbach, D. J., Sheth, K., & Teplitz, H. I. 2007, *ApJ*, 663, 866
- Dufour, R. J. 1984, in *IAU Symposium*, Vol. 108, *Structure and Evolution of the Magellanic Clouds*, ed. S. van den Bergh & K. S. D. de Boer, 353–360
- Dwek, E. 1998, *ApJ*, 501, 643
- Efremova, B. V., Bianchi, L., Thilker, D. A., Neill, J. D., Burgarella, D., Wyder, T. K., Madore, B. F., Rey, S.-C., Barlow, T. A., Conrow, T., Forster, K., Friedman, P. G., Martin, D. C., Morrissey, P., Neff, S. G., Schiminovich, D., Seibert, M., & Small, T. 2011, *ApJ*, 730, 88
- Elmegreen, B. G. 1989, *ApJ*, 338, 178
- . 1993, *ApJ*, 411, 170
- . 1994, *ApJ*, 427, 384
- Elmegreen, B. G., Morris, M., & Elmegreen, D. M. 1980, *ApJ*, 240, 455
- Engargiola, G., Plambeck, R. L., Rosolowsky, E., & Blitz, L. 2003, *ApJS*, 149, 343
- Engelbracht, C. W., Rieke, G. H., Gordon, K. D., Smith, J., Werner, M. W., Moustakas, J., Willmer, C. N. A., & Vanzi, L. 2008, *ApJ*, 678, 804
- Evans, N. J., Dunham, M. M., Jørgensen, J. K., Enoch, M. L., Merín, B., van Dishoeck, E. F., Alcalá, J. M., Myers, P. C., Stapelfeldt, K. R., Huard, T. L., Allen, L. E., Harvey, P. M., van Kempen, T., Blake, G. A., Koerner, D. W., Mundy, L. G., Padgett, D. L., & Sargent, A. I. 2009, *ApJS*, 181, 321
- Feldmann, R., & Gnedin, N. Y. 2011, *ApJ*, 727, L12+
- Feldmann, R., Gnedin, N. Y., & Kravtsov, A. V. 2011, *ApJ*, 732, 115
- Fixsen, D. J., Bennett, C. L., & Mather, J. C. 1999, *ApJ*, 526, 207

- Fukui, Y., & Kawamura, A. 2010, *ARA&A*, 48, 547
- Fukui, Y., Kawamura, A., Minamidani, T., Mizuno, Y., Kanai, Y., Mizuno, N., Onishi, T., Yonekura, Y., Mizuno, A., Ogawa, H., & Rubio, M. 2008, *ApJS*, 178, 56
- Fukui, Y., Mizuno, N., Yamaguchi, R., Mizuno, A., Onishi, T., Ogawa, H., Yonekura, Y., Kawamura, A., Tachihara, K., Xiao, K., Yamaguchi, N., Hara, A., Hayakawa, T., Kato, S., Abe, R., Saito, H., Mano, S., Matsunaga, K., Mine, Y., Moriguchi, Y., Aoyama, H., Asayama, S., Yoshikawa, N., & Rubio, M. 1999, *PASJ*, 51, 745
- Galleti, S., Bellazzini, M., & Ferraro, F. R. 2004, *A&A*, 423, 925
- Gao, Y., & Solomon, P. M. 2004, *ApJ*, 606, 271
- Gardan, E., Braine, J., Schuster, K. F., Brouillet, N., & Sievers, A. 2007, *A&A*, 473, 91
- Gehrz, R. D., Polomski, E., Woodward, C. E., McQuinn, K., Boyer, M., Humphreys, R. M., Brandl, B., van Loon, J. T., Fazio, G., Willner, S. P., Barmby, P., Ashby, M., Pahre, M., Rieke, G., Gordon, K., Hinz, J., Engelbracht, C., Alonso-Herrero, A., Misselt, K., Pérez-González, P. G., & Roellig, T. 2005, in *Bulletin of the American Astronomical Society*, Vol. 37, *Bulletin of the American Astronomical Society*, 451–+
- Genzel, R., Tacconi, L. J., Combes, F., Bolatto, A., Neri, R., Sternberg, A., Cooper, M. C., Bouche, N., Bournaud, F., Burkert, A., Comerford, J., Cox, P., Davis, M., Foerster Schreiber, N. M., Garcia-Burillo, S., Gracia-Carpio, J., Lutz, D., Naab, T., Newman, S., Saintonge, A., Shapiro, K., Shapley, A., & Weiner, B. 2011, *ArXiv e-prints*
- Genzel, R., Tacconi, L. J., Gracia-Carpio, J., Sternberg, A., Cooper, M. C., Shapiro, K., Bolatto, A., Bouché, N., Bournaud, F., Burkert, A., Combes, F., Comerford, J., Cox, P., Davis, M., Schreiber, N. M. F., Garcia-Burillo, S., Lutz, D., Naab, T., Neri, R., Omont, A., Shapley, A., & Weiner, B. 2010, *MNRAS*, 407, 2091
- Gil de Paz, A., Boissier, S., Madore, B. F., Seibert, M., Joe, Y. H., Boselli, A., Wyder, T. K., Thilker, D., Bianchi, L., Rey, S.-C., Rich, R. M., Barlow, T. A., Conrow, T., Forster, K., Friedman, P. G., Martin, D. C., Morrissey, P., Neff, S. G., Schiminovich, D., Small, T., Donas, J., Heckman, T. M., Lee, Y.-W., Milliard, B., Szalay, A. S., & Yi, S. 2007, *ApJS*, 173, 185
- Gil de Paz, A., Madore, B. F., & Pevunova, O. 2003, *ApJS*, 147, 29
- Glover, S. C. O., & Clark, P. C. 2011, *ArXiv e-prints*
- Glover, S. C. O., Federrath, C., Mac Low, M.-M., & Klessen, R. S. 2010, *MNRAS*, 404, 2
- Glover, S. C. O., & Mac Low, M.-M. 2011, *MNRAS*, 412, 337
- Gnedin, N. Y., & Kravtsov, A. V. 2011, *ApJ*, 728, 88
- Gnedin, N. Y., Tassis, K., & Kravtsov, A. V. 2009, *ApJ*, 697, 55

- Goldsmith, P. F., Heyer, M., Narayanan, G., Snell, R., Li, D., & Brunt, C. 2008, *ApJ*, 680, 428
- Gordon, K. D., Rieke, G. H., Engelbracht, C. W., Muzerolle, J., Stansberry, J. A., Misselt, K. A., Morrison, J. E., Cadien, J., Young, E. T., Dole, H., Kelly, D. M., Alonso-Herrero, A., Egami, E., Su, K. Y. L., Papovich, C., Smith, P. S., Hines, D. C., Rieke, M. J., Blaylock, M., Pérez-González, P. G., Le Floc'h, E., Hinz, J. L., Latter, W. B., Hesselroth, T., Frayer, D. T., Noriega-Crespo, A., Masci, F. J., Padgett, D. L., Smylie, M. P., & Haegel, N. M. 2005, *PASP*, 117, 503
- Gratier, P., Braine, J., Rodriguez-Fernandez, N. J., Israel, F. P., Schuster, K. F., Brouillet, N., & Gardan, E. 2010a, *A&A*, 512, A68+
- Gratier, P., Braine, J., Rodriguez-Fernandez, N. J., Schuster, K. F., Kramer, C., Xilouris, E. M., Tabatabaei, F. S., Henkel, C., Corbelli, E., Israel, F., van der Werf, P. P., Calzetti, D., Garcia-Burillo, S., Sievers, A., Combes, F., Wiklind, T., Brouillet, N., Herpin, F., Bontemps, S., Aalto, S., Koribalski, B., van der Tak, F., Wiedner, M. C., Röllig, M., & Mookerjee, B. 2010b, *A&A*, 522, A3+
- Greenawalt, B. E. 1998, PhD thesis, AA(New Mexico State University)
- Grocholski, A. J., Aloisi, A., van der Marel, R. P., Mack, J., Annibali, F., Angeretti, L., Greggio, L., Held, E. V., Romano, D., Sirianni, M., & Tosi, M. 2008, *ApJ*, 686, L79
- Guseva, N. G., Papaderos, P., Meyer, H. T., Izotov, Y. I., & Fricke, K. J. 2009, *A&A*, 505, 63
- Hamajima, K., & Tosa, M. 1975, *PASJ*, 27, 561
- Harris, J., & Zaritsky, D. 2009, *AJ*, 138, 1243
- Hartwick, F. D. A. 1971, *ApJ*, 163, 431
- Helfer, T. T., Thornley, M. D., Regan, M. W., Wong, T., Sheth, K., Vogel, S. N., Blitz, L., & Bock, D. C.-J. 2003, *ApJS*, 145, 259
- Heyer, M., Krawczyk, C., Duval, J., & Jackson, J. M. 2009, *ApJ*, 699, 1092
- Heyer, M. H., Corbelli, E., Schneider, S. E., & Young, J. S. 2004, *ApJ*, 602, 723
- Hitschfeld, M., Kramer, C., Schuster, K. F., Garcia-Burillo, S., & Stutzki, J. 2009, *A&A*, 495, 795
- Hodge, P. W., Skelton, B. P., & Ashizawa, J., eds. 2002, *Astrophysics and Space Science Library*, Vol. 221, *An Atlas of Local Group Galaxies*
- Hoopes, C. G., & Walterbos, R. A. M. 2000, *ApJ*, 541, 597
- . 2003, *ApJ*, 586, 902

- Hunter, D. A. 2001, *ApJ*, 559, 225
- Hunter, D. A., & Elmegreen, B. G. 2004, *AJ*, 128, 2170
- Hunter, D. A., Elmegreen, B. G., & Baker, A. L. 1998, *ApJ*, 493, 595
- Hunter, D. A., & Sage, L. 1993, *PASP*, 105, 374
- Israel, F. P. 1997, *A&A*, 328, 471
- Israel, F. P., & Maloney, P. R. 2011, *A&A*, 531, A19+
- Israel, F. P., Tacconi, L. J., & Baas, F. 1995, *A&A*, 295, 599
- Izotov, Y. I., & Thuan, T. X. 2004, *ApJ*, 616, 768
- Jogee, S., Scoville, N., & Kenney, J. D. P. 2005, *ApJ*, 630, 837
- Juneau, S., Narayanan, D. T., Moustakas, J., Shirley, Y. L., Bussmann, R. S., Kennicutt, Jr., R. C., & Vanden Bout, P. A. 2009, *ApJ*, 707, 1217
- Kawamura, A., Mizuno, Y., Minamidani, T., Filipović, M. D., Staveley-Smith, L., Kim, S., Mizuno, N., Onishi, T., Mizuno, A., & Fukui, Y. 2009, *ApJS*, 184, 1
- Kennicutt, R. C., Hao, C., Calzetti, D., Moustakas, J., Dale, D. A., Bendo, G., Engelbracht, C. W., Johnson, B. D., & Lee, J. C. 2009, *ApJ*, 703, 1672
- Kennicutt, Jr., R. C. 1989, *ApJ*, 344, 685
- . 1998a, *ARA&A*, 36, 189
- . 1998b, *ApJ*, 498, 541
- Kennicutt, Jr., R. C., Armus, L., Bendo, G., Calzetti, D., Dale, D. A., Draine, B. T., Engelbracht, C. W., Gordon, K. D., Grauer, A. D., Helou, G., Hollenbach, D. J., Jarrett, T. H., Kewley, L. J., Leitherer, C., Li, A., Malhotra, S., Regan, M. W., Rieke, G. H., Rieke, M. J., Roussel, H., Smith, J., Thornley, M. D., & Walter, F. 2003a, *PASP*, 115, 928
- Kennicutt, Jr., R. C., Bresolin, F., & Garnett, D. R. 2003b, *ApJ*, 591, 801
- Kennicutt, Jr., R. C., Calzetti, D., Walter, F., Helou, G., Hollenbach, D. J., Armus, L., Bendo, G., Dale, D. A., Draine, B. T., Engelbracht, C. W., Gordon, K. D., Prescott, M. K. M., Regan, M. W., Thornley, M. D., Bot, C., Brinks, E., de Blok, E., de Mello, D., Meyer, M., Moustakas, J., Murphy, E. J., Sheth, K., & Smith, J. D. T. 2007, *ApJ*, 671, 333
- Kennicutt, Jr., R. C., Lee, J. C., Funes, José G., S. J., Sakai, S., & Akiyama, S. 2008, *ApJS*, 178, 247
- Kewley, L. J., & Ellison, S. L. 2008, *ApJ*, 681, 1183

- Kim, S., Dopita, M. A., Staveley-Smith, L., & Bessell, M. S. 1999, *AJ*, 118, 2797
- Komugi, S., Sofue, Y., Nakanishi, H., Onodera, S., & Egusa, F. 2005, *PASJ*, 57, 733
- Krumholz, M. R. 2011, ArXiv e-prints
- Krumholz, M. R., Leroy, A. K., & McKee, C. F. 2011, *ApJ*, 731, 25
- Krumholz, M. R., & McKee, C. F. 2005, *ApJ*, 630, 250
- Krumholz, M. R., McKee, C. F., & Tumlinson, J. 2008, *ApJ*, 689, 865
- . 2009a, *ApJ*, 693, 216
- . 2009b, *ApJ*, 699, 850
- Krumholz, M. R., & Tan, J. C. 2007, *ApJ*, 654, 304
- Lada, C. J., & Lada, E. A. 2003, *ARA&A*, 41, 57
- Larson, R. B. 1981, *MNRAS*, 194, 809
- Lee, H., McCall, M. L., Kingsburgh, R. L., Ross, R., & Stevenson, C. C. 2003, *AJ*, 125, 146
- Lee, H., Skillman, E. D., Cannon, J. M., Jackson, D. C., Gehrz, R. D., Polomski, E. F., & Woodward, C. E. 2006, *ApJ*, 647, 970
- Lee, J. C., Gil de Paz, A., Kennicutt, Jr., R. C., Bothwell, M., Dalcanton, J., José G. Funes S., J., Johnson, B. D., Sakai, S., Skillman, E., Tremonti, C., & van Zee, L. 2011, *ApJS*, 192, 6
- Lee, J. C., Kennicutt, Jr., R. C., Funes, S. J. J. G., Sakai, S., & Akiyama, S. 2009, *ApJ*, 692, 1305
- Lequeux, J., Peimbert, M., Rayo, J. F., Serrano, A., & Torres-Peimbert, S. 1979, *A&A*, 80, 155
- Leroy, A., Bolatto, A., Stanimirovic, S., Mizuno, N., Israel, F., & Bot, C. 2007, *ApJ*, 658, 1027
- Leroy, A., Bolatto, A., Walter, F., & Blitz, L. 2006, *ApJ*, 643, 825
- Leroy, A., Bolatto, A. D., Simon, J. D., & Blitz, L. 2005, *ApJ*, 625, 763
- Leroy, A. K., Bolatto, A., Gordon, K., Sandstrom, K., Gratier, P., Rosolowsky, E., Engelbracht, C. W., Mizuno, N., Corbelli, E., Fukui, Y., & Kawamura, A. 2011, ArXiv e-prints
- Leroy, A. K., Walter, F., Bigiel, F., Usero, A., Weiss, A., Brinks, E., de Blok, W. J. G., Kennicutt, R. C., Schuster, K.-F., Kramer, C., Wiesemeyer, H. W., & Roussel, H. 2009, *AJ*, 137, 4670

- Leroy, A. K., Walter, F., Brinks, E., Bigiel, F., de Blok, W. J. G., Madore, B., & Thornley, M. D. 2008, *AJ*, 136, 2782
- Lisenfeld, U., Espada, D., Verdes-Montenegro, L., Kuno, N., Leon, S., Sabater, J., Sato, N., Sulentic, J., Verley, S., & Yun, M. S. 2011, *ArXiv e-prints*
- Mac Low, M.-M., & Klessen, R. S. 2004, *Reviews of Modern Physics*, 76, 125
- Madden, S. C., Poglitsch, A., Geis, N., Stacey, G. J., & Townes, C. H. 1997, *ApJ*, 483, 200
- Madore, B. F. 1977, *MNRAS*, 178, 1
- Madore, B. F., van den Bergh, S., & Rogstad, D. H. 1974, *ApJ*, 191, 317
- Maloney, P., & Black, J. H. 1988, *ApJ*, 325, 389
- Marble, A. R., Engelbracht, C. W., van Zee, L., Dale, D. A., Smith, J. D. T., Gordon, K. D., Wu, Y., Lee, J. C., Kennicutt, R. C., Skillman, E. D., Johnson, L. C., Block, M., Calzetti, D., Cohen, S. A., Lee, H., & Schuster, M. D. 2010, *ApJ*, 715, 506
- Martin, C. L. 1997, *ApJ*, 491, 561
- Martin, C. L., & Kennicutt, Jr., R. C. 2001, *ApJ*, 555, 301
- McKee, C. F., & Krumholz, M. R. 2010, *ApJ*, 709, 308
- McKee, C. F., & Ostriker, E. C. 2007, *ARA&A*, 45, 565
- McKee, C. F., & Williams, J. P. 1997, *ApJ*, 476, 144
- McQuinn, K. B. W., Skillman, E. D., Cannon, J. M., Dalcanton, J., Dolphin, A., Hidalgo-Rodríguez, S., Holtzman, J., Stark, D., Weisz, D., & Williams, B. 2010, *ApJ*, 724, 49
- Meurer, G. R., Wong, O. I., Kim, J. H., Hanish, D. J., Heckman, T. M., Werk, J., Bland-Hawthorn, J., Dopita, M. A., Zwaan, M. A., Koribalski, B., Seibert, M., Thilker, D. A., Ferguson, H. C., Webster, R. L., Putman, M. E., Knezek, P. M., Doyle, M. T., Drinkwater, M. J., Hoopes, C. G., Kilborn, V. A., Meyer, M., Ryan-Weber, E. V., Smith, R. C., & Staveley-Smith, L. 2009, *ApJ*, 695, 765
- Mizuno, N., Muller, E., Maeda, H., Kawamura, A., Minamidani, T., Onishi, T., Mizuno, A., & Fukui, Y. 2006, *ApJ*, 643, L107
- Mizuno, N., Rubio, M., Mizuno, A., Yamaguchi, R., Onishi, T., & Fukui, Y. 2001, *PASJ*, 53, L45
- Morganti, R., de Zeeuw, P. T., Oosterloo, T. A., McDermid, R. M., Krajnović, D., Cappellari, M., Kenn, F., Weijmans, A., & Sarzi, M. 2006, *MNRAS*, 371, 157
- Morris, M., & Lo, K. Y. 1978, *ApJ*, 223, 803

- Moustakas, J., Kennicutt, Jr., R. C., Tremonti, C. A., Dale, D. A., Smith, J., & Calzetti, D. 2010, *ApJS*, 190, 233
- Muñoz-Mateos, J. C., Gil de Paz, A., Zamorano, J., Boissier, S., Dale, D. A., Pérez-González, P. G., Gallego, J., Madore, B. F., Bendo, G., Boselli, A., Buat, V., Calzetti, D., Moustakas, J., & Kennicutt, Jr., R. C. 2009, *ApJ*, 703, 1569
- Murgia, M., Crapsi, A., Moscadelli, L., & Gregorini, L. 2002, *A&A*, 385, 412
- Narayanan, D., Krumholz, M., Ostriker, E. C., & Hernquist, L. 2011, *ArXiv e-prints*
- Onodera, S., Kuno, N., Tosaki, T., Kohno, K., Nakanishi, K., Sawada, T., Muraoka, K., Komugi, S., Miura, R., Kaneko, H., Hirota, A., & Kawabe, R. 2010, *ApJ*, 722, L127
- Ostriker, E. C., McKee, C. F., & Leroy, A. K. 2010, *ApJ*, 721, 975
- Pak, S., Jaffe, D. T., van Dishoeck, E. F., Johansson, L. E. B., & Booth, R. S. 1998, *ApJ*, 498, 735
- Papadopoulos, P. P., & Pelupessy, F. I. 2010, *ApJ*, 717, 1037
- Paradis, D., Bernard, J.-P., & Mény, C. 2009, *A&A*, 506, 745
- Pasquali, A., Bik, A., Zibetti, S., Ageorges, N., Seifert, W., Brandner, W., Rix, H.-W., Jütte, M., Knierim, V., Buschkamp, P., Feiz, C., Gemperlein, H., Germeroth, A., Hofmann, R., Laun, W., Lederer, R., Lehmitz, M., Lenzen, R., Mall, U., Mandel, H., Müller, P., Naranjo, V., Polsterer, K., Quirrenbach, A., Schäffner, L., Storz, C., & Weiser, P. 2011, *AJ*, 141, 132
- Pelupessy, F. I., & Papadopoulos, P. P. 2009, *ApJ*, 707, 954
- Planck Collaboration, Abergel, A., Ade, P. A. R., Aghanim, N., Arnaud, M., Ashdown, M., Aumont, J., Baccigalupi, C., Balbi, A., Banday, A. J., Barreiro, R. B., Bartlett, J. G., Battaner, E., Benabed, K., Benoît, A., Bernard, J. ., Bersanelli, M., Bhatia, R., Bock, J. J., Bonaldi, A., Bond, J. R., Borrill, J., Bouchet, F. R., Boulanger, F., Bucher, M., Burigana, C., Cabella, P., Cardoso, J. ., Catalano, A., Cayón, L., Challinor, A., Chamballu, A., Chiang, L. ., Chiang, C., Christensen, P. R., Clements, D. L., Colombi, S., Couchot, F., Coulais, A., Crill, B. P., Cuttaia, F., Danese, L., Davies, R. D., Davis, R. J., de Bernardis, P., de Gasperis, G., de Rosa, A., de Zotti, G., Delabrouille, J., Delouis, J. ., Désert, F. ., Dickinson, C., Dobashi, K., Donzelli, S., Doré, O., Dörl, U., Douspis, M., Dupac, X., Efstathiou, G., Enßlin, T. A., Eriksen, H. K., Finelli, F., Forni, O., Frailis, M., Franceschi, E., Galeotta, S., Ganga, K., Giard, M., Giardino, G., Giraud-Héraud, Y., González-Nuevo, J., Górski, K. M., Gratton, S., Gregorio, A., Gruppuso, A., Guillet, V., Hansen, F. K., Harrison, D., Henrot-Versillé, S., Herranz, D., Hildebrandt, S. R., Hivon, E., Hobson, M., Holmes, W. A., Hovest, W., Hoyland, R. J., Huppenberger, K. M., Jaffe, A. H., Jones, A., Jones, W. C., Juvela, M., Keihänen, E., Keskitalo, R., Kisner, T. S., Kneissl, R., Knox, L., Kurki-Suonio, H., Lagache, G., Lamarre, J. ., Lasenby, A., Laureijs, R. J., Lawrence, C. R., Leach, S., Leonardi, R.,

- Leroy, C., Linden-Vørnle, M., López-Caniego, M., Lubin, P. M., Macías-Pérez, J. F., MacTavish, C. J., Maffei, B., Mandolesi, N., Mann, R., Maris, M., Marshall, D. J., Martin, P., Martínez-González, E., Masi, S., Matarrese, S., Matthai, F., Mazzotta, P., McGehee, P., Meinhold, P. R., Melchiorri, A., Mendes, L., Mennella, A., Mitra, S., Miville-Deschênes, M. ., Moneti, A., Montier, L., Morgante, G., Mortlock, D., Munshi, D., Murphy, A., Naselsky, P., Natoli, P., Netterfield, C. B., Nørgaard-Nielsen, H. U., Noviello, F., Novikov, D., Novikov, I., Osborne, S., Pajot, F., Paladini, R., Pasian, F., Patanchon, G., Perdureau, O., Perotto, L., Perrotta, F., Piacentini, F., Piat, M., Plaszczynski, S., Pointecouteau, E., Polenta, G., Ponthieu, N., Poutanen, T., Prézeau, G., Prunet, S., Puget, J. ., Reach, W. T., Rebolo, R., Reinecke, M., Renault, C., Ricciardi, S., Riller, T., Ristorcelli, I., Rocha, G., Rosset, C., Rubiño-Martín, J. A., Rusholme, B., Sandri, M., Santos, D., Savini, G., Scott, D., Seiffert, M. D., Shellard, P., Smoot, G. F., Starck, J. ., Stivoli, F., Stolyarov, V., Sudiwala, R., Sygnet, J. ., Tauber, J. A., Terenzi, L., Toffolatti, L., Tomasi, M., Torre, J. ., Tristram, M., Tuovinen, J., Umama, G., Valenziano, L., Verstraete, L., Vielva, P., Villa, F., Vittorio, N., Wade, L. A., Wandelt, B. D., Yvon, D., Zacchei, A., & Zonca, A. 2011, ArXiv e-prints
- Prugniel, P., & Heraudeau, P. 1998, *A&AS*, 128, 299
- Quirk, W. J. 1972, *ApJ*, 176, L9+
- Rahman, N., Bolatto, A. D., Wong, T., Leroy, A. K., Walter, F., Rosolowsky, E., West, A. A., Bigiel, F., Ott, J., Xue, R., Herrera-Camus, R., Jameson, K., Blitz, L., & Vogel, S. N. 2011, *ApJ*, 730, 72
- Rana, N. C., & Wilkinson, D. A. 1986, *MNRAS*, 218, 721
- Regan, M. W., Thornley, M. D., Helfer, T. T., Sheth, K., Wong, T., Vogel, S. N., Blitz, L., & Bock, D. 2001, *ApJ*, 561, 218
- Relaño, M., & Kennicutt, R. C. 2009, *ApJ*, 699, 1125
- Rieke, G. H., Young, E. T., Engelbracht, C. W., Kelly, D. M., Low, F. J., Haller, E. E., Beeman, J. W., Gordon, K. D., Stansberry, J. A., Misselt, K. A., Cadien, J., Morrison, J. E., Rivlis, G., Latter, W. B., Noriega-Crespo, A., Padgett, D. L., Stapelfeldt, K. R., Hines, D. C., Egami, E., Muzerolle, J., Alonso-Herrero, A., Blaylock, M., Dole, H., Hinz, J. L., Le Floch, E., Papovich, C., Pérez-González, P. G., Smith, P. S., Su, K. Y. L., Bennett, L., Frayer, D. T., Henderson, D., Lu, N., Masci, F., Pesenson, M., Rebull, L., Rho, J., Keene, J., Stolovy, S., Wachter, S., Wheaton, W., Werner, M. W., & Richards, P. L. 2004, *ApJS*, 154, 25
- Robertson, B. E., & Kravtsov, A. V. 2008, *ApJ*, 680, 1083
- Rosolowsky, E., Engargiola, G., Plambeck, R., & Blitz, L. 2003, *ApJ*, 599, 258
- Rosolowsky, E., Keto, E., Matsushita, S., & Willner, S. P. 2007, *ApJ*, 661, 830
- Rosolowsky, E., & Simon, J. D. 2008, *ApJ*, 675, 1213

- Rownd, B. K., & Young, J. S. 1999, *AJ*, 118, 670
- Roychowdhury, S., Chengalur, J. N., Begum, A., & Karachentsev, I. D. 2009, *MNRAS*, 397, 1435
- Rubin, D., Hony, S., Madden, S. C., Tielens, A. G. G. M., Meixner, M., Indebetouw, R., Reach, W., Ginsburg, A., Kim, S., Mochizuki, K., Babler, B., Block, M., Bracker, S. B., Engelbracht, C. W., For, B.-Q., Gordon, K., Hora, J. L., Leitherer, C., Meade, M., Misselt, K., Sewilo, M., Vijh, U., & Whitney, B. 2009, *A&A*, 494, 647
- Saintonge, A. 2007, *AJ*, 133, 2087
- Salim, S., Rich, R. M., Charlot, S., Brinchmann, J., Johnson, B. D., Schiminovich, D., Seibert, M., Mallery, R., Heckman, T. M., Forster, K., Friedman, P. G., Martin, D. C., Morrissey, P., Neff, S. G., Small, T., Wyder, T. K., Bianchi, L., Donas, J., Lee, Y.-W., Madore, B. F., Milliard, B., Szalay, A. S., Welsh, B. Y., & Yi, S. K. 2007, *ApJS*, 173, 267
- Sanders, D. B., & Mirabel, I. F. 1996, *ARA&A*, 34, 749
- Sanduleak, N. 1969, *AJ*, 74, 47
- Sauty, S., Casoli, F., Boselli, A., Gerin, M., Lequeux, J., Braine, J., Gavazzi, G., Dickey, J., Kazès, I., & Fouqué, P. 2003, *A&A*, 411, 381
- Schaye, J. 2004, *ApJ*, 609, 667
- Schlegel, D. J., Finkbeiner, D. P., & Davis, M. 1998, *ApJ*, 500, 525
- Schmidt, M. 1959, *ApJ*, 129, 243
- . 1963, *ApJ*, 137, 758
- Schruba, A., Leroy, A. K., Walter, F., Bigiel, F., Brinks, E., de Blok, W. J. G., Dumas, G., Kramer, C., Rosolowsky, E., Sandstrom, K., Schuster, K., Usero, A., Weiss, A., & Wiesemeyer, H. 2011, *AJ*, 142, 37
- Schruba, A., Leroy, A. K., Walter, F., Sandstrom, K., & Rosolowsky, E. 2010, *ApJ*, 722, 1699
- Schuster, K.-F., Boucher, C., Brunswig, W., Carter, M., Chenu, J.-Y., Foullieux, B., Greve, A., John, D., Lazareff, B., Navarro, S., Perrigouard, A., Pollet, J.-L., Sievers, A., Thum, C., & Wiesemeyer, H. 2004, *A&A*, 423, 1171
- Schuster, K. F., Kramer, C., Hitschfeld, M., Garcia-Burillo, S., & Mookerjea, B. 2007, *A&A*, 461, 143
- Shapiro, K. L., Falcón-Barroso, J., van de Ven, G., de Zeeuw, P. T., Sarzi, M., Bacon, R., Bolatto, A., Cappellari, M., Croton, D., Davies, R. L., Emsellem, E., Fakhouri, O., Krajnović, D., Kuntschner, H., McDermid, R. M., Peletier, R. F., van den Bosch, R. C. E., & van der Wolk, G. 2010, *MNRAS*, 402, 2140

- Shetty, R., Glover, S. C., Dullemond, C. P., & Klessen, R. S. 2011a, *MNRAS*, 412, 1686
- Shetty, R., Glover, S. C., Dullemond, C. P., Ostriker, E. C., Harris, A. I., & Klessen, R. S. 2011b, *MNRAS*, 943
- Shi, Y., Helou, G., Yan, L., Armus, L., Wu, Y., Papovich, C., & Stierwalt, S. 2011, *ApJ*, 733, 87
- Shu, F. H., Milione, V., & Roberts, Jr., W. W. 1973, *ApJ*, 183, 819
- Silk, J. 1997, *ApJ*, 481, 703
- Skillman, E. D. 1987, in *NASA Conference Publication*, Vol. 2466, NASA Conference Publication, ed. C. J. Lonsdale Persson, 263–266
- Soifer, B. T., Helou, G., & Werner, M. 2008, *ARA&A*, 46, 201
- Solomon, P. M., Rivolo, A. R., Barrett, J., & Yahil, A. 1987, *ApJ*, 319, 730
- Solomon, P. M., & Vanden Bout, P. A. 2005, *ARA&A*, 43, 677
- Stanimirovic, S., Staveley-Smith, L., Dickey, J. M., Sault, R. J., & Snowden, S. L. 1999, *MNRAS*, 302, 417
- Strong, A. W., & Mattox, J. R. 1996, *A&A*, 308, L21
- Tamburro, D., Rix, H.-W., Leroy, A. K., Mac Low, M.-M., Walter, F., Kennicutt, R. C., Brinks, E., & de Blok, W. J. G. 2009, *AJ*, 137, 4424
- Tan, J. C. 2000, *ApJ*, 536, 173
- . 2010, *ApJ*, 710, L88
- Taylor, C. L., Kobulnicky, H. A., & Skillman, E. D. 1998, *AJ*, 116, 2746
- Temi, P., Brighenti, F., & Mathews, W. G. 2009, *ApJ*, 695, 1
- Teyssier, R., Chapon, D., & Bournaud, F. 2010, *ApJ*, 720, L149
- Thilker, D. A., Bianchi, L., Meurer, G., Gil de Paz, A., Boissier, S., Madore, B. F., Boselli, A., Ferguson, A. M. N., Muñoz-Mateos, J. C., Madsen, G. J., Hameed, S., Overzier, R. A., Forster, K., Friedman, P. G., Martin, D. C., Morrissey, P., Neff, S. G., Schiminovich, D., Seibert, M., Small, T., Wyder, T. K., Donas, J., Heckman, T. M., Lee, Y.-W., Milliard, B., Rich, R. M., Szalay, A. S., Welsh, B. Y., & Yi, S. K. 2007a, *ApJS*, 173, 538
- Thilker, D. A., Boissier, S., Bianchi, L., Calzetti, D., Boselli, A., Dale, D. A., Seibert, M., Braun, R., Burgarella, D., Gil de Paz, A., Helou, G., Walter, F., Kennicutt, Jr., R. C., Madore, B. F., Martin, D. C., Barlow, T. A., Forster, K., Friedman, P. G., Morrissey, P., Neff, S. G., Schiminovich, D., Small, T., Wyder, T. K., Donas, J., Heckman, T. M., Lee, Y.-W., Milliard, B., Rich, R. M., Szalay, A. S., Welsh, B. Y., & Yi, S. K. 2007b, *ApJS*, 173, 572

- Thilker, D. A., Hoopes, C. G., Bianchi, L., Boissier, S., Rich, R. M., Seibert, M., Friedman, P. G., Rey, S.-C., Buat, V., Barlow, T. A., Byun, Y.-I., Donas, J., Forster, K., Heckman, T. M., Jelinsky, P. N., Lee, Y.-W., Madore, B. F., Malina, R. F., Martin, D. C., Milliard, B., Morrissey, P. F., Neff, S. G., Schiminovich, D., Siegmund, O. H. W., Small, T., Szalay, A. S., Welsh, B. Y., & Wyder, T. K. 2005, *ApJ*, 619, L67
- Thilker, D. A., Walterbos, R. A. M., Braun, R., & Hoopes, C. G. 2002, *AJ*, 124, 3118
- Thronson, Jr., H. A., Greenhouse, M., Hunter, D. A., Telesco, C. M., & Harper, D. A. 1988, *ApJ*, 334, 605
- Thuan, T. X., & Izotov, Y. I. 2005, *ApJS*, 161, 240
- Toomre, A. 1964, *ApJ*, 139, 1217
- Vacca, W. D., Garmany, C. D., & Shull, J. M. 1996, *ApJ*, 460, 914
- van der Hulst, J. M. 2002, in *Astronomical Society of the Pacific Conference Series*, Vol. 276, *Seeing Through the Dust: The Detection of HI and the Exploration of the ISM in Galaxies*, ed. A. R. Taylor, T. L. Landecker, & A. G. Willis, 84–+
- Verley, S., Corbelli, E., Giovanardi, C., & Hunt, L. K. 2010, *A&A*, 510, A64+
- Verley, S., Hunt, L. K., Corbelli, E., & Giovanardi, C. 2007, *A&A*, 476, 1161
- Walter, F., Brinks, E., de Blok, W. J. G., Bigiel, F., Kennicutt, R. C., Thornley, M. D., & Leroy, A. 2008, *AJ*, 136, 2563
- Walter, F., Cannon, J. M., Roussel, H., Bendo, G. J., Calzetti, D., Dale, D. A., Draine, B. T., Helou, G., Kennicutt, Jr., R. C., Moustakas, J., Rieke, G. H., Armus, L., Engelbracht, C. W., Gordon, K., Hollenbach, D. J., Lee, J., Li, A., Meyer, M. J., Murphy, E. J., Regan, M. W., Smith, J.-D. T., Brinks, E., de Blok, W. J. G., Bigiel, F., & Thornley, M. D. 2007, *ApJ*, 661, 102
- Wang, B., & Silk, J. 1994, *ApJ*, 427, 759
- Wei, L. H., Vogel, S. N., Kannappan, S. J., Baker, A. J., Stark, D. V., & Laine, S. 2010, *ApJ*, 725, L62
- Weisz, D. R., Dalcanton, J. J., Williams, B. F., Gilbert, K. M., Skillman, E. D., Seth, A. C., Dolphin, A. E., McQuinn, K. B. W., Gogarten, S. M., Holtzman, J., Rosema, K., Cole, A., Karachentsev, I. D., & Zaritsky, D. 2011, *ApJ*, 739, 5
- Wilke, K., Klaas, U., Lemke, D., Mattila, K., Stickel, M., & Haas, M. 2004, *A&A*, 414, 69
- Wilson, B. A., Dame, T. M., Mashedier, M. R. W., & Thaddeus, P. 2005, *A&A*, 430, 523
- Wilson, C. D. 1995, *ApJ*, 448, L97+

- Wilson, C. D., Petitpas, G. R., Iono, D., Baker, A. J., Peck, A. B., Krips, M., Warren, B., Golding, J., Atkinson, A., Armus, L., Cox, T. J., Ho, P., Juvela, M., Matsushita, S., Mihos, J. C., Pihlstrom, Y., & Yun, M. S. 2008, *ApJS*, 178, 189
- Wolfire, M. G., Hollenbach, D., & McKee, C. F. 2010, *ApJ*, 716, 1191
- Wong, T., & Blitz, L. 2002, *ApJ*, 569, 157
- Wong, T., Hughes, A., Fukui, Y., Kawamura, A., Mizuno, N., Ott, J., Muller, E., Pineda, J. L., Welty, D. E., Kim, S., Mizuno, Y., Murai, M., & Onishi, T. 2009, *ApJ*, 696, 370
- Wyder, T. K., Martin, D. C., Barlow, T. A., Foster, K., Friedman, P. G., Morrissey, P., Neff, S. G., Neill, J. D., Schiminovich, D., Seibert, M., Bianchi, L., Donas, J., Heckman, T. M., Lee, Y.-W., Madore, B. F., Milliard, B., Rich, R. M., Szalay, A. S., & Yi, S. K. 2009, *ApJ*, 696, 1834
- Wyse, R. F. G. 1986, *ApJ*, 311, L41
- Wyse, R. F. G., & Silk, J. 1989, *ApJ*, 339, 700
- Yi, S. K., Yoon, S.-J., Kaviraj, S., Deharveng, J.-M., Rich, R. M., Salim, S., Boselli, A., Lee, Y.-W., Ree, C. H., Sohn, Y.-J., Rey, S.-C., Lee, J.-W., Rhee, J., Bianchi, L., Byun, Y.-I., Donas, J., Friedman, P. G., Heckman, T. M., Jelinsky, P., Madore, B. F., Malina, R., Martin, D. C., Milliard, B., Morrissey, P., Neff, S., Schiminovich, D., Siegmund, O., Small, T., Szalay, A. S., Jee, M. J., Kim, S.-W., Barlow, T., Forster, K., Welsh, B., & Wyder, T. K. 2005, *ApJ*, 619, L111
- Young, J. S., Allen, L., Kenney, J. D. P., Lesser, A., & Rownd, B. 1996, *AJ*, 112, 1903
- Young, J. S., & Scoville, N. Z. 1991, *ARA&A*, 29, 581
- Young, J. S., Xie, S., Tacconi, L., Knezek, P., Viscuso, P., Tacconi-Garman, L., Scoville, N., Schneider, S., Schloerb, F. P., Lord, S., Lesser, A., Kenney, J., Huang, Y., Devereux, N., Claussen, M., Case, J., Carpenter, J., Berry, M., & Allen, L. 1995, *ApJS*, 98, 219
- Young, L. M., Bendo, G. J., & Lucero, D. M. 2009, *AJ*, 137, 3053
- Young, L. M., Bureau, M., Davis, T. A., Combes, F., McDermid, R. M., Alatalo, K., Blitz, L., Bois, M., Bournaud, F., Cappellari, M., Davies, R. L., de Zeeuw, P. T., Emsellem, E., Khochfar, S., Krajnović, D., Kuntschner, H., Lablanche, P.-Y., Morganti, R., Naab, T., Oosterloo, T., Sarzi, M., Scott, N., Serra, P., & Weijmans, A.-M. 2011, *MNRAS*, 414, 940
- Zwaan, M. A., Briggs, F. H., Sprayberry, D., & Sorar, E. 1997, *ApJ*, 490, 173

Curriculum Vitae

ADDRESS

Max Planck Institute for Astronomy
Königstuhl 17
69117 Heidelberg, Germany

Email: schruba@mpia.de
Phone: +49 6221 528-465
Fax: +49 6221 528-246

PRESENT OCCUPATION

Max Planck Institute for Astronomy, Ph.D. Student, Aug 2008 – Nov 2011

FUTURE POSITION

California Institute of Technology, CARMA Postdoctoral Scholar, starting Dec 2011

EDUCATION

Ruprecht–Karls–Universität Heidelberg, Ph.D. Studies, Aug 2008 – Nov 2011

Advisor: Dr. Fabian Walter (Max Planck Institute for Astronomy)

Title: *"The Molecular Interstellar Medium of Nearby Star-Forming Galaxies"*

Ruprecht–Karls–Universität Heidelberg, "Diplom Physik", Grade 1.3, Oct 2003 – Apr 2008

Advisor: Prof. Christof Wetterich (Institute for Theoretical Physics)

Title: *"Constraints on the Fifth Force in Coupled Quintessence from Galaxy Rotation Curves"*

Erasmus Scholarship at Uppsala University, Sweden, Aug 2004 – Oct 2005

Institute for Physics and Astronomy, Institute for Mathematics

Ruprecht–Karls–Universität Heidelberg, "Vordiplom Physik", Grade 1.8, Apr 2002 – Oct 2003

TECHNICAL EXPERIENCE

- **Radio:** Involvement in three large VLA projects THINGS (PI: Walter), LITTLE THINGS (PI: Hunter) and VLA-ANGST (PI: Ott), intensive experience in data reduction using AIPS.
- **Millimeter:** Involvement in IRAM Large Programme HERACLES (PI: Leroy), ongoing 60 h survey of dwarf galaxies with 30m (PI: Schruba), 10 weeks of

observing experience at 30m, data reduction using GILDAS and self-written IDL code; ongoing 120h survey of M31 with CARMA (PI: Schruba), data reduction with MIRIAD.

- **Infrared:** Extensive use of *Spitzer* MIPS data from SINGS & LVL (PI: Kennicutt and Dale), and *Herschel* KINGFISH project (PI: Kennicutt), especially in low surface brightness dwarfs.
- **Optical and Ultraviolet:** Intensive scientific use of photometric data, especially *Galex* and ground-based H α data.
- **Software Skills:** Very extensive use of IDL, especially for all kinds of scientific analysis involving large sets of multi-wavelength data.

TEACHING EXPERIENCE

- Tutor for Astronomy Lab “Stellar CCD Photometry”, University of Heidelberg, 2010
- Tutor in Theoretical Physics “Classical Electrodynamics”, University of Heidelberg, 2007

ATTENDED CONFERENCES & WORKSHOPS

- DFG WORKSHOP “The HERACLES View of Molecular Gas in the Outer Disks of Galaxies” (*talk*), Bad Honnef, Germany, July 2011
- AMERICAN ASTRONOMICAL SOCIETY MEETING 217 “The HERACLES View of Molecular Gas in the Outer Disks of Galaxies” (*thesis talk*), Seattle, USA, January 2011
- MOLECULES IN GALAXIES “The HERACLES View of Molecular Gas in the Outer Disks of Galaxies” (*talk*), Oxford, Great Britain, July 2010
- FROM STARS TO GALAXIES “The Scale Dependence of the Molecular Gas Depletion Time in M33” (*poster*), Gainesville, USA, April 2010
- CONFERENCE “Infrared Emission, Interstellar Medium, and Star Formation”, Heidelberg, Germany, February 2010
- M33 WORKSHOP “The Star Formation Law from Galactic to Cloud Scale” (*talk*), Florence, Italy, September 2009
- SFR@50: FILLING THE COSMOS WITH STARS “The Resolved Star Formation Law in M33” (*talk*), Spineto, Italy, July 2009
- AMERICAN ASTRONOMICAL SOCIETY MEETING 214 “Variations in the Dust-to-Gas Ratio in Nearby Dwarf Galaxies” (*poster*), Pasadena, USA, June 2009

ATTENDED SUMMER SCHOOLS & TEAM MEETINGS

- ALMA COMMUNITY DAYS Garching, Germany, April 2011
- 7TH IRAM INTERFEROMETRY SCHOOL, Grenoble, France, October 2010
- KINGFISH TEAM MEETING “IR Emission and Dust in Dwarfs” (*talk*), Ringberg, Germany, July 2010
- NRAO CHARLOTTESVILLE Two Weeks Working Visit, April 2010
- LITTLE THINGS TEAM MEETING “Constraining the Dust Content in Low Metallicity Galaxies using Stacking Techniques” (*talk*), Heidelberg, Germany, March 2010
- HERACLES TEAM MEETING “The Power of Stacking” (*talk*), Heidelberg, Germany, February 2010
- KINGFISH TEAM MEETING in Heidelberg, Germany, February 2010
- LVL TEAM MEETING “Where is the Dust in Low Metallicity Dwarf Galaxies” (*talk*), Pasadena, USA, June 2009
- LITTLE THINGS TEAM MEETING in Socorro, USA, September 2008
- DFG SUMMER SCHOOL “Black Holes and Galaxy Evolution”, Bad Honnef, Germany, August 2008
- TRR WINTER SCHOOL “The Dark Universe”, Passo del Tonale, Italy, December 2007
- GENERAL RELATIVITY SUMMER SCHOOL, MPI for Gravitational Physics, Golm, Germany, March 2004

List of Publications

REFEREED PUBLICATIONS (FIRST AUTHOR)

- **Schruba, A.**, Leroy, A. K., Walter, F., Bigiel, F., Brinks, E., de Blok, W. J. G., Dumas, G., Kramer, C., Rosolowsky, E., Sandstrom, K., Schuster, K., Usero, A., Weiss, A., Wiesemeyer, H., “Low CO Luminosities in Dwarf Galaxies”, 2011, AJ, to be submitted
- **Schruba, A.**, Leroy, A. K., Walter, F., Bigiel, F., Brinks, E., de Blok, W. J. G., Dumas, G., Kramer, C., Rosolowsky, E., Sandstrom, K., Schuster, K., Usero, A., Weiss, A., Wiesemeyer, H., “A Molecular Star Formation Law in the Atomic-gas-dominated Regime in Nearby Galaxies”, 2011, AJ, 142, 37
- **Schruba, A.**, Leroy, A. K., Walter, F., Sandstrom, K., Rosolowsky, E., “The Scale Dependence of the Molecular Gas Depletion Time in M 33”, 2010, ApJ, 722, 1699

REFEREED PUBLICATIONS (CO-AUTHOR)

- Leroy, A., Walter, F., Munoz-Mateos, J.-C., Bolatto, A., **Schruba, A.**, Sandstrom, K., Bigiel, F., Brinks, E., de Blok, W. J. G., Schuster, K., “Estimating the Star Formation Rate at 1 kpc Scales in Nearby Galaxies”, 2011, to be submitted
- Bigiel, F., Leroy, A. K., Walter, F., Brinks, E., de Blok, W. J. G., Kramer, C., Rix, H. W., **Schruba, A.**, Schuster, K. F., Usero, A., Wiesemeyer, H., “A Constant Molecular Gas Depletion Time in Nearby Disk Galaxies”, 2011, ApJ, 730, 13

CONFERENCE CONTRIBUTIONS (FIRST AUTHOR)

- **Schruba, A.**, Leroy, A. K., Walter, F., and the HERACLES team, “The HERACLES View of Molecular Gas in the Outer Disks of Galaxies”, 2011, AAS, 217, 133.04
- **Schruba, A.**, Walter, F., Leroy, A., Kennicutt, R., Lee, J., Gil de Paz, A., Hunter, D., Ott, J., “Variations in the Dust-to-Gas Ratio in Nearby Dwarf Galaxies”, 2009, AAS, 214, 424.02

CONFERENCE CONTRIBUTIONS (CO-AUTHOR)

- Leroy, A. K., Walter, F., **Schruba, A.**, Bigiel, F., Foyle, K., and the HERACLES team, “HERACLES: The HERA CO-Line Extragalactic Survey”, 2011, AAS, 217, 246.14

- Thornley, M. D., Leroy, A. K.; **Schruba, A.**, Bagetakos, I., Portas, A., Usero, A., Bigiel, F., Foyle, K., “Structure and Dynamics in Nearby Galaxies from THINGS”, 2010, ASPC, 438
- Walter, F., Leroy, A.; Bigiel, F., **Schruba, A.**, Usero, A., Kennicutt, R., and the HERACLES team, “HERACLES: A CO Survey of Nearby Galaxies”, 2009, AAS, 214, 419.08